ABSTRACT

CALVERT, DAVID JAMES. A Study of Magnetic Fields and Stellar Evolution on Core-Collapse Supernovae. (Under the direction of Carla Fröhlich and James P. Kneller).

Massive stars end their lives in spectacular explosions known as core-collapse supernovae (CCSNe) that are responsible for the production of neutron stars, black holes, and magnetars while simultaneously enriching their host galaxies with the elements synthesized during their evolution. The conditions found within CCSNe are beyond anything we can create in a laboratory so uncovering their nature can provide insight into physics of the extreme. Understanding CCSNe in detail requires a tremendous effort across many fields of physics. Supernovae are multiscale phenomena that depend on the physics in the smallest regimes (quantum mechanics, nuclear physics) to the physics that govern objects on cosmic scales (gravity, fluid dynamics). Stars die as they lived, and as such the explosion properties can also be influenced by the properties of a star's evolution throughout its life. In this dissertation I will investigate the effects of different initial conditions on CCSNe and demonstrate that these quantities can impact the evolution and measurable outcomes of these explosions. To do this, we will first explore the role of turbulent fluid motion on the ability of CCSNe to explode and describe a new method for quantifying the effects of this turbulence. Continuing this thread of investigation, we will then use this new metric to study how the magnetic field in CCSNe impacts the turbulence. Finally, we examine how the treatments of mass loss and convective overshooting in stars throughout their lifetime drive changes to the structure of the star at the point of collapse, and how the supernova explosion exhibits properties that can be correlated with the treatments of these stellar processes.

A Study of Magnetic Fields and Stellar Evolution on Core-Collapse Supernovae

by
David James Calvert

A dissertation submitted to the Graduate Faculty of
North Carolina State University
in partial fulfillment of the
requirements for the Degree of
Doctor of Philosophy

Physics

Raleigh, North Carolina
2026

APPROVED BY:

John Blondin	Lorena Bociu
Carla Fröhlich Co-chair of Advisory Committee	James P. Kneller Co-chair of Advisory Committee

BIOGRAPHY

David Calvert was born in Toms River, NJ in 1996. He attended the Marine Academy of Technology and Environmental Sciences for his 1st year of high school before moving to Burlington, NC in 2011. After this, he attended and graduated from the North Carolina School of Science and Mathematics where he was first introduced to courses in modern physics. He obtained bachelors degrees in Physics and Applied Mathematics from North Carolina State University in 2018. During his undergraduate career he attended an REU in Germany to simulate the penetration depth of protons in time projection chambers for the T2K experiment. He then took 1 year to work in industry before returning to graduate school.

David joined the Ph.D. program at NC State University in 2019 and began working with Drs. Carla Fröhlich and Jim Kneller on simulating core-collapse supernovae in 3D and applying neutrino flavor oscillations to a 1D core-collapse supernova code. His work then continued into studying the impacts of stellar evolution parameters on core-colapse supernova outcomes.

ACKNOWLEDGEMENTS

This Ph.D. would not have been possible without the endless support from my friends and family.

I would first like to thank my advisors, Jim Kneller and Carla Fröhlich, for their patience and guidance through the most difficult portions of this degree. Their support is what made this degree possible.

Next I would like to thank my lab mates, Kelsey, Somdutta, Julien, Bibek, and Kenzie, for their tireless support and encouragement over the last several years. This degree would not have been possible without our Monday night pint nights and many games of tarot together.

I also want to thank my friends who have been by my side through this degree and have kept my spirits high when it all felt hopeless. Erik, Joe, Jordan, Ridge; you guys are my support team and this degree is as much your accomplishment as it is mine. Additionally I would like to thank the friends I've made along the way in this degree. Max, Merve, Sinan, Caroline, Andy, Michael; the adventures and time we spent together during this degree helped keep me sane over the years.

Further I would like to extend my thanks to my family, both given and chosen, for keeping me going. Specifically to my brother Michael, I want to thank you for sparking the love of space and science in me at a young age. My passion for space has been there since the beginning, and that is thanks to you. To Linda & Rick, thank you for treating me as your own son and encouraging me through it all. And a special thank you to the Davern clan for embracing me with open arms and welcoming me into the family. Jack, thank you for checking on me and encouraging me to keep writing every week. Your motivation helped pull me through to the end.

I would like to say an additional thank you to my cat Molly for her work to ensure that I was petting her as much as possible throughout this degree. Her relentless need for attention and constant love made getting this degree that much more enjoyable.

Lastly I want to thank my biggest supporter through this degree, Carolynn. No matter the circumstances you were there for me through it all, helping me make this degree possible. You encouraged me and reminded me every day that I am strong enough to achieve this goal. Your support during the long days and nights of work was invaluable to me. Thank you for your love and support in every aspect of my life and for reminding me that I don't have to be a robot all the time.

AUTHORSHIP STATEMENT

Contributions of David Calvert and coauthors are listed below for each chapter.

- Chapter 1

    1. David Calvert: sole author of Chapter 1.

- Chapter 2
  Published; David Calvert *et al* 2025 *ApJ* **995** 109

    1. **David Calvert**: Simulation benchmarking, code deployment, conceptualization, literature review, code execution, data analysis, data visualization, writing, editing
    2. Michael Redle: Data analysis, numerical analysis, conceptualization, data visualization, writing, editing
    3. Charles Stapleford: Simulation benchmarking, code deployment, conceptualization
    4. Bibek Gautam: Code execution, data analysis
    5. Carla Fröhlich, Jim Kneller: Primary advisors on the project; conceptualization, supervision, funding
    6. Matthias Liebendörfer: Original author of AGILE and ELEPHANT codes; expertise on MHD and numerical methods.

- Chapter 3

    1. **David Calvert**: Simulation benchmarking, code deployment, conceptualization, literature review, code execution, data analysis, data visualization, writing, editing
    2. Michael Redle: Data analysis, numerical analysis, conceptualization, data visualization, writing, editing
    3. Charles Stapleford: Simulation benchmarking, code deployment, conceptualization
    4. Bibek Gautam: Code execution, data analysis
    5. Carla Fröhlich, Jim Kneller: Primary advisors on the project; conceptualization, supervision, funding

6. Matthias Liebendörfer: Original author of AGILE and ELEPHANT codes; expertise on MHD and numerical methods.

- Chapter 4

1. **David Calvert**: Code development, conceptualization, code execution, debugging, data analysis, data visualization,
2. Kenzie Myers, Kelly Patton, Claire Campbell: Generated progenitor models for the study
3. Jim Kneller, Carla Fröhlich: Primary advisors on the project; conceptualization, supervision, funding

- Chapter 5

1. David Calvert: sole author of Chapter 5

No generative artificial intelligence was used to write this dissertation.

TABLE OF CONTENTS

LIST OF TABLES

LIST OF FIGURES

CHAPTER

1

INTRODUCTION

1.1 Supernova Discovery and History

Supernovae have been a subject of intrigue for astronomers for millennia. Studying these transients in detail has been beyond the reach of science until relatively recently. The first supernova recorded was in the year 185 A.D. by Chinese astronomers, who described the sudden appearance of a "guest star" that remained visible for 8-20 months after its initial appearance [1]. At the time the origin of this star was unclear, but modern astronomical observations of supernova remnants, cross-referenced with the original documentation, suggest that this event was the explosion of a star. Subsequent similar events have been recorded throughout history, with the most well studied being those in 1572 and 1604 [2]. These two Galactic supernovae were extensively documented by Tycho Brahe and Johannes Kepler, with their locations in the sky studied to arc-minute precision [3]. Brahe published his findings in his book *De Stella Nova*, introducing the term "nova" to describe the sudden appearance of new stars. For centuries, any transient stellar phenomena were classified as novae regardless of their origins. The rarity of these events [4, 5], coupled with the sheer distance and complexity of the underlying physical processes, made deeper un-

derstanding of novae a nearly impossible task. Thus, progress was not possible until the early 20th century and the advent of modern astronomy.

In 1934, Walter Baade and Fritz Zwicky identified a particularly luminous subset within the catalog of novae. These superluminous novae emitted as much energy as the Sun radiates over its entire lifetime within days of their appearance. Their light could be observed for several weeks, distinguishing them from shorter and dimmer events. For these reasons, such events earned the distinction being named as "super-novae" [6]. Baade and Zwicky proposed that the source of this incredible energy and luminosity was a product of gravitational collapse of a star [6].

Later work refined the classification of supernova into two distinct types. Minkowski denoted two categories: Type I supernovae that have no hydrogen emission lines in their spectra, and Type II that do contain them [7]. This distinction implied there were different explosion mechanisms behind each of these supernovae categories. The current understanding indicates that Type I supernovae are caused by two distinct methods of explosion and have thus been subdivided further. The first type, Type Ia, are distinguished by strong silicon emission lines and are understood to be the explosion of a carbon-oxygen (CO) white dwarf powered by a thermonuclear detonation [8]. The other two subtypes, Type Ib/c supernovae, lack silicon emission lines and are characterized by the presence of helium emission lines. The current understanding is that these subtypes of supernovae are the explosion of a star that lacks an outer envelope of hydrogen. Type II supernovae are those cases where the star has retained its outer hydrogen layer. The source of energy of Type Ib/c and Type II supernovae is the gravitational collapse of the core of a star and are, therefore collectively called core-collapse supernovae. Outlined in more detail in section 1.3, core-collapse supernovae (CCSNe) occur when a star has exhausted its nuclear fuel and explodes cataclysmically.

Given that the gravitational collapse mechanism leads to supernovae of all spectroscopic types except Type Ia, there has been a great desire to accurately understand the details of these events. In the 1960s Colgate and Johnson proposed that a key component of the core-collapse mechanism was the formation of a prompt-shock as the infalling material crashes into the proto-neutron star (PNS) that forms during the collapse of the core [9]. In this model, the shock then travels outward through the star ejecting the outer layers. However, a gap in their understanding was still present, as noted by Colgate and White in 1966. The total thermonuclear energy available to CCSNe was not sufficient to account for the energy released into the star's mantle during implosion [10]. They proposed to reconcile this discrepancy via the energy of the neutrinos that are produced during the col-

lapse. In this model, the enormous number of neutrinos emitted during collapse deposit a small fraction ($\sim 1\%$) of their energy into the supernova mantle. This can supply a sufficient amount of energy to force the shock through the outer layers of the star and produce a CCSN. However, the initial implementation of this idea in simulations was unsuccessful [11] and the shock instead stalled approximately 200 km above the PNS. The resolution came with the introduction of the "delayed neutrino-heating mechanism" [12]. Improvements in the calculation of the neutrino cross section by Tubbs and Schramm revealed that under CCSNe conditions, the neutrino is 'trapped' within the PNS and not free streaming, as Colgate and White had assumed [13]. While trapped, the neutrinos reach thermal equilibrium with the matter. The thermally coupled neutrinos can now impart sufficient energy to the material behind the shock to explode the star. This paradigm is still accepted today as the primary mechanism for shock revival.

Over the decades since the proposal of the delayed neutrino-heating mechanism, further complexities have been introduced into CCSNe modeling. Rotation, convection, turbulence, magnetic fields, and neutrino oscillations [14, 15, 16] all have been shown to affect the behavior of CCSNe. With the introduction of new physics, new explosion mechanisms beyond neutrino heating, such as those driven by magnetic fields [17, 18, 19], have been seen in some simulations. As we seek to more firmly connect supernova models with reality, the importance of this new physics to the outcome of CCSNe is still an area of intense research.

1.2 Stellar Evolution

Stars originate as over-densities of gas in molecular clouds. Gravitational self-attraction causes the diffuse material to contract and increase in density. Gravitational potential energy is converted into heat, which is radiated away in a low-opacity gas. However, once the gas density becomes large and the gas optically thick, the generated heat is retained, resulting in a rise in the temperature and pressure. Eventually the conditions in the core of the collapsing cloud of gas are sufficient to initiate the nuclear fusion of hydrogen, releasing even more energy and raising the outward pressure further. When the gravitational attraction is counterbalanced by the outward pressure gradient, the system reaches a hydrostatic equilibrium and thus begins a star's life. This equilibrium defines the onset of a stars "main-sequence" phase [20], the phase which constitutes the majority of the star's life. For the purposes of stellar modeling, the mass of the star at this point is known as the

"zero-age main sequence" (ZAMS) mass, M_{ZAMS}, and, as will be detailed later, is the key property of the star that determines its life and fate.

The newly formed star will remain in the hydrogen burning phase until the hydrogen fuel in the core has become exhausted. The length of this period is primarily dependent upon the ZAMS mass of the star, and is approximated by

$$\tau_{\mathrm{MS}} \sim (M_{\mathrm{ZAMS}})^{-2.5} \tag{1.1}$$

where τ_{MS} is the time a star spends on the main sequence [21]. While this picture becomes more refined by the inclusion of other stellar effects (e.g. convection, stellar wind, rotation), the basic relationship remains that stars of higher mass exhaust their hydrogen fuel more rapidly and diverge from the main sequence earlier than those of smaller ZAMS masses.

As the hydrogen abundance in the core becomes depleted, the star enters its next phase of evolution. The ZAMS mass is a critical determinant in the behavior of the next stages. The cores of stars with ZAMS mass greater than $\sim 2M_{\odot}$ will smoothly transition to helium burning after the core has contracted and risen in temperature; stars with less than $\sim 2M_{\odot}$ will become supported by electron degeneracy pressure before the conditions are reached to burn helium. Stars with ZAMS masses in the range $0.8M_{\odot} \lesssim M_{\mathrm{ZAMS}} \lesssim 2M_{\odot}$ will ignite helium burning in a "helium flash" while stars with ZAMS masses below this range will never ignite the helium. If helium burning commences, the star begins to create carbon/oxygen nuclei within the core. The ZAMS mass of the star will once again determine what follows the initiation of helium burning. If sufficiently massive, the core will contract, leading to an increase in temperature and the initiation of carbon burning. The transition can either occur smoothly or explosively, dependent on the conditions. In stars with a greater ZAMS mass, this process repeats itself for heavier elements. Each successive nuclear fuel is ignited at progressively higher temperatures and densities, moving up the chain and producing heavier nuclei. At each phase, if the star is able to reach sufficient ignition temperatures and densities (dictated by the ZAMS mass) before reaching the limit of the electron degeneracy pressure, fusion of the nuclei at the core will initiate. The specific energy released by the burning of each nuclear fuel becomes smaller as the atomic mass number of the fuel increases. More importantly, the energy lost by the core of the star to neutrino emission grows rapidly with density and temperature. The effect is that each burning cycle in the star becomes increasingly shorter. At this advanced stage of its life, the structure of the star is a sequence of shells each burning a different nuclear fuel: a structure that has been colloquially referred to as onion shells, as shown in Figure 1.2. While the onion-shell model

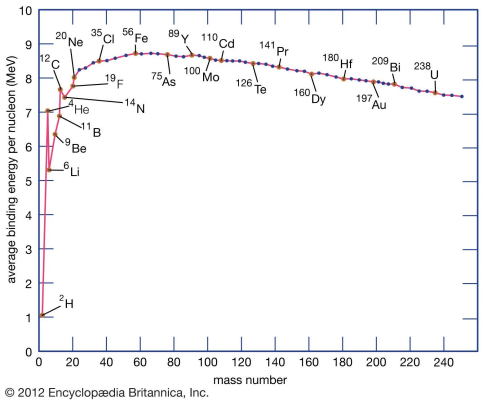

Figure 1.1: A plot of binding energy per nucleon as a function of mass number. Source: `https://www.britannica.com/science/nuclear-binding-energy`.

captures the general behavior of the burning stages, stars have a much more complex composition. Figure 1.3 shows the composition of the core of a late-stage red supergiant (RSG) model with $M_{ZAMS} = 15\ M_{\odot}$.

Nuclear burning continues until iron-group nuclei are produced. Fusion beyond this point is endothermic, requiring an input of energy rather than releasing it in the process. These nuclei have the highest binding energy per nucleon, as shown in Figure 1.1. Thus they represent the end of the nuclear energy fusion process in stars. Since iron cannot be burned, massive stars will come to possess large cores of iron-group nuclei supported by electron degeneracy pressure. When this core becomes too massive to be supported by the degeneracy pressure, it will collapse and the core-collapse supernova begins. The sequence of events during this stage will be explored in depth in §1.3.

The dynamics and structure of the stellar interior play a critical role in supernovae outcomes. Many details of stellar evolution affect the internal structure of the star at the end of its life. The dominant means of energy transport throughout the star is one such factor. Stellar interiors are broadly divided into two regimes, radiative and convective. In radiative regions, photons are the primary carriers of energy; in convective zones, energy is transported through the bulk motion of the plasma. Because of the high densities and correspondingly short photon mean free paths, radiative diffusion operates on timescales that are several orders of magnitude longer than those associated with convection. Heating of the plasma by the nuclear reactions in the core can produce hotter, lower-density material that may become buoyant relative to the material above. The stability of these zones

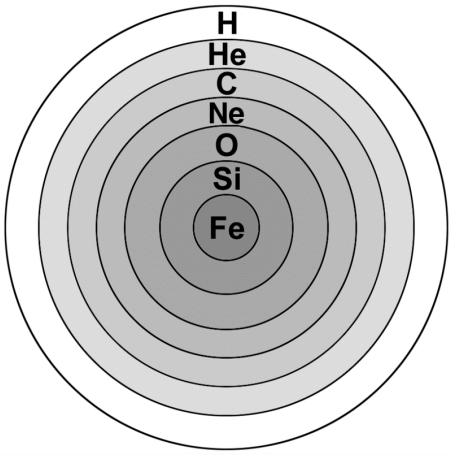

Figure 1.2: An onion-shell model of a massive star nearing the end of its lifetime.
Source: `https://imagine.gsfc.nasa.gov/educators/elements/imagine/05.html`

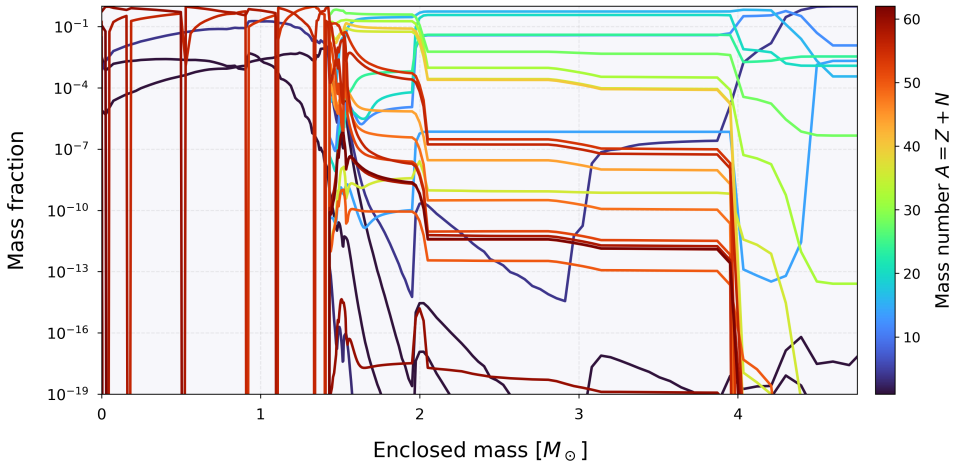

Figure 1.3: Mass fractions in the core of a $M_{ZAMS} = 15\ M_\odot$ red supergiant model at the onset of core collapse.

is determined by comparing gradients in the stellar structure, quantified as

$$\nabla_{\text{ad}} = \left(\frac{d \ln T}{d \ln P} \right)_s \tag{1.2}$$

$$\nabla_{\text{rad}} = \left(\frac{d \ln T}{d \ln P} \right)_{\text{rad}} \tag{1.3}$$

where T is temperature, P is pressure, the subscript s represents a derivative with respect to constant entropy, and ∇_{ad} and ∇_{rad} are shorthand for the gradients shown. For a homogeneous chemical composition, if the Schwarzschild criterion

$$\nabla_{\text{rad}} < \nabla_{\text{ad}} \tag{1.4}$$

is met, then the layer is stable to convection and radiation is the dominant means of energy transfer. If this criteria is not met, the region is unstable against convection and convection will dominate as the means of energy transfer within the star.

Because convective nuclear burning regions that can extend the burning phases of a stars life, distinguishing between the energy transport mechanisms is critical to stellar theory. Through convection, the products of the nuclear burning are replenished with the lighter nuclear fuel from layers above. At the boundary between radiative and convective zones, i.e. where $\nabla_{\text{rad}} = \nabla_{\text{ad}}$, stellar theory does not have an agreed-upon description for how much mixing occurs between these zones. In the mixing length theory used to model convection in stars, buoyant bubbles that are unstable to convection through the Schwarzschild criterion travel upward through the convective zone and stop at radiative boundaries [22]. As it approaches the interface between a convective and radiative zone, the convective bubble is traveling with nonzero momentum. Presumably, then, there may be some distance into the radiative zone this convective bubble will penetrate as it loses its momentum and dissipates. This applies to sinking material at the bottom of convective zones as well. The extent to which the convection "overshoots" these boundaries is not well constrained. Because this process alters the amount of nuclear fuel that is able to be burned, the mechanisms that govern this overshooting is an important factor in predicting the structure of stars during their life.

Through the stages of stellar evolution, the outer envelope of a star is losing mass to the stellar wind. Radiation pressure at the surface of the star exerts a force on the outermost material that is most weakly bound by gravity. The rate at which matter flows off the surface of the star varies throughout the phases of its evolution and can serve as a key factor in

the determination of stellar composition. During the RSG phase, the star is enormous in volume compared to its mass. This results in a very weak surface gravity, and thus a very high rate of mass loss due to the stellar wind. Directly modeling the stellar wind from first principles is not feasible, so stellar models rely on empirical data to prescribe a mass loss rate for stars at different stages of evolution. The models used for this mass loss rate are poorly constrained and remain an area of large uncertainty in stellar evolution codes.

1.3 Core-Collapse Supernova Theory

1.3.1 Gravitational Instability and Collapse

At the formation of iron in the core of a star, the hydrostatic balance necessary to maintain stability within the star is in jeopardy. Iron-group nuclei accumulate in the core as silicon burning continues. This iron core is mainly supported by electron degeneracy pressure with thermal pressure a small, but not negligible, contribution. At this stage, the iron core has a central density of order 10^9 g/cm^3 and temperature of 10^{10} K [23]. The electron degeneracy pressure cannot resist indefinitely the force of self-gravity of the growing mass of iron. Once the iron core reaches the Chandrasekhar limit, ~ 1.44 $M_\odot$, gravity overcomes the electron degeneracy pressure and the core undergoes a collapse, increasing the central density significantly. The increase in the density bolsters the electron capture reaction rates,

$$p^+ + e^- \rightarrow n^0 + \nu_e \tag{1.5}$$

$$n^0 + e^+ \rightarrow p^+ + \overline{\nu}_e \tag{1.6}$$

further reducing the electron degeneracy pressure in a runaway cascade called 'neutronization'. The neutrinos rob the collapsing material of energy due to their low interaction cross sections during the initial phases of collapse. This cascade is reinforced by the photodissociation of the iron nuclei in the core into alpha particles, as well as an increase in the β-decay rates of the now heavily neutronized iron-group nuclei [24, 25, 26]. The collapse of the core continues until it reaches nuclear matter densities, $\sim 10^{14}$ g/cm^3 [27], at which point nucleon-nucleon repulsion of the strong nuclear force becomes sufficient to resist further collapse. As the equation of state stiffens, the PNS decelerates rapidly, overshoots the equilibrium state, and rebounds outward into the inward falling material. An outwards moving pressure wave forms as the PNS rebounds. This pressure wave steepens

into a shock when it reaches the radius at which the speed of the infalling material exceeds the speed of sound in the medium.

As the shockwave propagates outward through the infalling core material, nuclei are photodissociated into free nucleons, a process that leads to a reduction of the thermal energy of the matter behind the shock and significantly reduces the shock's radial velocity. After the initial energy imparted by the core rebound is lost to photodissociation, a semi-stable equilibrium is reached with the shock stalled at a radius of approximately 100-200 km. The stability of the shock is sustained by the continued accretion of matter onto the PNS, known as an accretion shock. Without another source of energy, this equilibrium is is unsustainable as the mass accretion rate onto the PNS will dwindle with time. The dynamics of the matter beneath the stalled shock determine the outcome of the supernova. The energy and pressure in this matter must increase if the shock is to be revived and the star explode. Identifying and characterizing the mechanisms that drive the semi-stable equilibrium of the standing accretion shock toward shock revival and explosion, or shock retreat and collapse to a black hole, remains a central focus in supernova research.

1.3.2 Shock Revitalization Mechanisms

Given that supernovae have been observed to occur, mechanisms must exist to revive the stalled shock of core-collapse supernovae. While the means by which the energy is delivered to the shock is an active area of research, the most favored mechanism for shock reenergization is the 'delayed-neutrino heating mechanism' [28, 12, 29]. As the core undergoes neutronization during collapse (see § 1.3.1), large quantities of electron neutrinos and antineutrinos are released into the stellar material. These are supplemented by thermal processes which create additional pairs of electron neutrinos and antineutrinos, and the heavy lepton flavors. Despite the low interaction cross section with matter, the incredibly high concentration of matter, in excess of $\sim 10^{12}$ g/cm^3, results in a neutrino mean free path of only a few centimeters. Under these conditions, the $\sim 10^{53}$ neutrinos within the PNS are trapped, directing kinetic energy into heat through interactions with nucleons and electrons [10]. A small fraction of these radiated neutrinos will interact with the matter above the PNS and deposit energy into the material. However, results from 1D simulations indicate that neutrino heating mechanism alone cannot deposit sufficient energy for the shock to be revived [30].

The dynamics of a shock revival are heavily dependent on the area below the accretion shock known as the 'gain region'. This gain region is the region below the shock for which

neutrino heating per nucleon, given by

$$Q_\nu^+ \approx 5\times 10^{-39}\left(\frac{L_{\nu_e}\langle\epsilon^2_{\nu_e}\rangle}{\langle\mu\rangle_{\nu_e} r^2}Y_n + \frac{L_{\bar{\nu}_e}\langle\epsilon^2_{\bar{\nu}_e}\rangle}{\langle\mu\rangle_{\bar{\nu}_e} r^2}Y_p\right. \tag{1.7}$$

exceeds the neutrino cooling per nucleon, given by

$$Q_\nu^- \approx \left(\frac{1.146}{\text{MeV}}k_B T\right)^6. \tag{1.8}$$

Heating in this region is concentrated closer to the PNS due to the steep density gradients present in the stellar core. The contributions to the neutrino heating are dependent upon nucleon density, and density is on average decreasing radially in the gain region. Due to this inhomogeneous heating, matter at the innermost radius of the gain region is being heated more than matter further away from the core. The heating creates an inverted temperature gradient which is unstable and buoyancy begins to initiate convection within the gain region. Hot material is welled up from the core and brought up to just behind the shock, passing through the entire gain region en route. As such, the fluid properties within the gain region determine how successfully this convection cycle can deliver energy to the shock front. A plethora of physical effects could aid or hinder this delivery, and it is often the case that these effects require multidimensional models to understand fully. Should the hot material be able to spend enough time to deposit energy behind the shock, the shock is revitalized and the star will successfully explode and enrich the surrounding space with newly formed heavy elements while leaving behind a neutron star remnant. Otherwise, the shock will retreat, the supernova will fail, and a black hole will be formed instead.

The timescales required to deliver energy to the shock dictate what mechanism is responsible for shock revitalization. In general, the neutrino heating timescale is defined as the amount of time that material in the gain region would need to be exposed to the current neutrino heating rate in order that it acquire enough energy to unbind the material i.e. overcome the gravitational potential. This timescale is given by

$$\tau_\nu = \left|\frac{E_{\text{gain}}}{\dot{Q}_\nu^{\text{net}} n_b}\right|, \tag{1.9}$$

where $\dot{Q}_\nu^{\text{net}} = \frac{d}{dt}(Q_\nu^+ - Q_\nu^-)$ is the net neutrino heating rate per nucleon, n_b is the baryonic number density, $E_{\text{gain}} = E_{\text{kin}} + E_{\text{internal}} + E_B - \rho\phi$ is the sum of all sources of energy of the

gain region, E_{kin} is the kinetic energy, E_{internal} is the internal energy, E_B is the magnetic energy, ρ is the density, and ϕ is the gravitational potential. To provide a metric for the energy delivered to the shocked material by neutrinos, this quantity is compared to the amount time matter spends within the gain region, known as the advection timescale. The advection timescale is measured as

$$\tau_{\text{adv}} = \left| \frac{M_{\text{gain}}}{\dot{M}_{\text{gain}}} \right|, \tag{1.10}$$

where M_{gain} is the mass in the gain region. The ratio of these two timescales indicate if matter within the gain region spends enough time there to be heated by neutrinos to overcome the gravitational potential and become unbound. If τ_{adv} exceeds τ_{ν}, then the material in the gain region will become heated enough to allow for the shock to expand.

Considering the energy terms that contribute to the total energy in the gain region E_{gain}, a multitude of mechanisms can influence the neutrino heating timescale. Increasing any term in that equation, besides gravitational energy, will shorten the timescale as E_{gain} is negative prior to explosion. Thus, modifications to the kinetic energy, nuclear reaction rates, microphysical processes, or magnetic fields can influence the extent to which neutrinos deposit energy in the gain region.

One clear source of energy that can be fully modeled in 3D is rotation of the supernova. Rotation is a source of initial kinetic energy for the supernova and can also introduce asymmetries and instabilities into multidimensional models that foster explosion. One such fluid instability is known as the standing accretion shock instability (SASI) [31] that results in nonradial deformations of the shock front. Critically, these deformations have been seen to have rapid growth rates that can become dominant sources of kinetic energy in the gain region and drive an explosion independently of the neutrino heating [32]. A SASI can also indirectly influence the energy delivered by neutrinos to the core of the supernova, if it does not grow fast enough to drive the explosion independently. When a SASI is present, the shock front tends to expand outward as a response to the nonradial modes that are introduced into the fluid. This leads to an increase in the advection timescale as the amount of shocked mass increases significantly without major change to the mass accretion rate. At the same time, a decrease in the neutrino heating timescale will occur with the introduction of kinetic energy to the gain region from rotation. The compounding of these effects can result in a neutrino driven explosion that is promoted by the presence of a SASI [33].

Mechanisms for explosion are not solely limited to the energy and momentum deposited by neutrinos. Magnetorotational mechanisms for supernova explosion were pro-

posed early on in the history of CCSNe modeling [34, 35, 36]. Magnetic fields, coupled with rotation, provide channels through which energy can grow within the gain region and potentially drive an explosion. The most critical factor in determining if a supernova will be magnetorotationally driven is the timescale of the growth of the magnetic field [37]. If the timescale for magnetic field growth, and subsequently magnetic energy growth, is shorter than the timescales of other energy generation mechanisms, then the magnetic field energy generation can deliver the necessary energy to the shock front for revitalization.

One mechanism for magnetic field growth is the compression of accreted magnetic fields in the core. As magnetized material advects from the outer layers of the star into the core, the magnetic flux must be conserved for a given fluid element [38], as expressed in equation (1.19) below. This "flux-freezing" mechanism of magnetic field growth will occur on timescales related to the advection timescales of the infalling magnetized material. From the flux conservation equation (1.19), explained in greater detail in § 1.4.1 and Chapter 2, the timescale for such growth can be derived as

$$\tau_b = \frac{E_b}{|\vec{v} \cdot ((\nabla \times \vec{b}) \times \vec{b})|} \tag{1.11}$$

where $\vec{B} = \sqrt{4\pi}\vec{b}$ and $E_b = (\vec{b} \cdot \vec{b})/2$.

Rotation can lead to magnetic field growth via magnetic field line wrapping or dynamo effects through motion of charged particles [39, 40, 41]. In multi-dimensional simulations, rotation is not limited to bulk rotation about a coordinate axis. The potential supernova has internal convection cycles and turbulent motion which lead to magnetic field generation through small and large-scale dynamos, and thus increase the energy contribution from magnetic fields [42, 43]. Vorticity ($\vec{\omega} = \nabla \times \vec{v}$) is often used as an indicator of turbulent motion in plasma dynamics [44]. Thus, an effective measure of tracking the timescale of turbulent-related magnetic field growth can be tied to the growth rate of the vorticity, or equivalently the scalar quantity enstrophy ($\epsilon_\omega = \frac{1}{2}\vec{\omega}^2$). Derived in Chapter 2, the growth of the enstrophy can be represented by

$$\tau_\epsilon = \frac{\epsilon_\omega}{|\vec{v} \cdot ((\nabla \times \vec{\omega}) \times \vec{\omega}) + \vec{\omega} \cdot \vec{m}|} \tag{1.12}$$

where $\vec{m}$, the baroclinic vector, represents the relationship of the enstrophy to the magnetic field and will be explored in depth in later chapters.

Additionally, a moderate rotation of the star can initiate a magnetorotational instability (MRI) [45], driving the magnetic field of the PNS to grow at an exponential rate. This expo-

nential growth, if achieved, introduces a large amount of magnetic energy into supernovae on short timescales and can become a dominating source of energy in shock revitalization. The criterion for an MRI is defined as:

$$\frac{d\Omega^2}{d\ln(r)} + (\vec{k}\cdot\vec{v}_A)^2 < 0 \tag{1.13}$$

where

$$\vec{v}_A = \frac{\vec{B}}{\sqrt{4\pi\rho}} \tag{1.14}$$

is the Alfvén velocity, $\vec{k}$ is the wavenumber of an Alfvén wave, and Ω is the angular velocity [46]. In regions of high density, such as in the PNS, the the Alfvén velocity becomes negligible and the MRI condition becomes entirely dependent upon the angular velocity gradient. If this condition is met, i.e. the angular velocity gradient becomes negative in high density regions, then the magnetic field grows exponentially, with the maximum growing Fourier mode growing on a timescale of

$$\tau_{max} = 4\pi \left| \frac{d\Omega}{d\ln r} \right|^{-1}. \tag{1.15}$$

See [46, 47] for a detailed derivation. This exponential growth of the MRI outpaces the linear growth of the field due to both field line wrapping and the $\alpha-\Omega$ dynamo. With a large enough rotational gradient, the MRI growth of the field energy can outpace the energy growth of the fluid due to neutrino heating, resulting in an energy source for shock revitalization that becomes dominant relative to the neutrino heating.

It remains to be seen what conditions in CCSNe are achieved when a magnetic field is applied. While studies have been undertaken to understand these magnetohydrodynamical fluid dynamics in an isolated framework [44, 48], studying these processes in more-complete core-collapse supernova simulations is still an area of active research. Accurately capturing these behaviors is the next challenge of the field. An accurate study requires multidimensionality, high spatial resolution, and the ability to quantify these effects. Achieving this level of sophistication of supernova modeling has been a decades long enterprise and has resulted in our ability to more deeply probe the physics driving CCSNe.

1.4 Modeling CCSNe

There is a long history of modeling core-collapse supernovae under a collection of initial conditions and constraints. The complex and extreme nature of CCSNe means that modeling these events accurately demands the most powerful computational resources available. To reduce the computational expense, different approximations of the underlying physics must be implemented to provide any opportunity to evolve one of these models to completion.

CCSNe simulations were only initially achievable due to approximations of some of the more complex physics. Spherically symmetric, one dimensional (1D) models have defined the field since its inception in the 1960s [9, 49, 11] due to their computationally efficient nature. One dimensional models are still commonly pursued and we refer the reader to [23] for a comprehensive review of 1D simulations up to this point. The parameter space for the initial conditions in CCSNe modeling is vast and 1D simulations provide the opportunity to probe these parameters. 1D simulations have a strength in their efficiency and ability to explore this parameter space more fully when compared to more complex simulations. Despite their basis for the majority of the field, these simulations are not able to achieve unaided explosions observed in reality [30, 50, 51, 52, 53]. Artificial methods have been introduced to 1D simulations to allow for effective studies in the CCSN parameter space. In general, all of these artificial methods share the approach of inserting some amount of energy into the CCSN simulation to facilitate explosion. The energy has to be added in such a way that it causes the least disturbance to the properties of the supernova. Piston methods accelerate a portion of the material within the core outward at a critical juncture [54]. Other methods, known as a thermal/kinetic bomb, directly add kinetic or thermal energy into mass zones within the gain region [55, 56, 57, 58, 59]. These methods are effective at promoting the explosion of CCSNe, but they cannot account for the changes in the innermost zones during collapse and the onset of the explosion. For example, they do not account for changes in the electron fraction during these phases of the supernova. Refinements on these methods require introducing energy to the system in a way that is both more physically grounded and captures the multidimensional effects of 3D simulations. P-HOTB [60] triggers explosions by artificially increasing neutrino luminosities, a process calibrated using a 20 $M_\odot$ progenitor to match the observed explosion energy and ^{56}Ni ejecta of SN 1987A [61]. The physical motivation for this approach is to retain the sensitivity of the explosion dynamics to the progenitor's specific core structure and accretion rate. The PUSH method, detailed in more detail later in this work, also uses the energy flux

of the neutrinos to increase the heating of the matter gain region and is similarly calibrated to the observations of SN 1987A. By coupling this heating to the heavy-flavor neutrinos, PUSH acts as a proxy for the increased heating efficiency caused by multi-dimensional convection, without altering the electron fraction relevant for the nucleosynthesis. Yet another method, STIR [62], captures the effects of turbulence upon the supernova observed in multi-dimensional simulations by leveraging a mixing length approximation, condensing the complexities down to a single parameter a_λ. STIR then injects energy into 1D models through this parameter to facilitate explosions.

Advances in available computational resources have allowed for an increase in the complexity of these simulations, namely in dimensionality. The processes that dominate CCSNe evolution are 3D in nature [63, 64, 65, 66, 67] and as such it is important to model them in 3D wherever possible. 3D simulations are able to successfully explode without the incorporation of artificial energy deposition methods [26, 68, 69, 19, 70, 71, 72, 73, 74, 75]. Multidimensional models have uncovered new phenomena in the dynamics of CCSNe such as convection and turbulence. Phenomena such as the SASI and magnetorotationally driven explosions would otherwise have been missed if not for multidimensional simulations [31, 16, 19].

Despite the increased availability of computational resources, 3D simulations are still very costly in both time and resources and cannot explore to the same extent the space of initial conditions as their 1D and 2D counterparts. Concessions must still be made on some of the physics of 3D CCSN models due to the time and resource constraints. The neutrino transport is often the most computationally demanding component of simulations and the most frequent target of attempts to increase computational efficiency. Neutrino approximation schemes implemented in 3D simulations vary in complexity. Simple "leakage" schemes discard the neutrino transport equations and replace the interaction of the neutrinos with matter with a source/sink term, while more complex methods, such as ray-by-ray or moments, require a much more precise treatment of the neutrinos. The details of these approximation schemes are explored in § 1.4.2.

1.4.1 Magnetohydrodynamic Equations

The magnetohydrodynamics of the fluid in CCSNe are governed by the equations for conservation of energy, momentum, mass, and magnetic flux. Assuming no viscosity and that the electrical conductivity is infinite, the ideal magnetohydrodynamic (MHD) conserva-

tion equations can be written as

$$\frac{\partial \rho}{\partial t} + \nabla \cdot (\rho \vec{v}) = 0 \tag{1.16}$$

$$\frac{\partial (\rho \vec{v})}{\partial t} + \nabla \cdot (\rho(\vec{v} \otimes \vec{v}) - \vec{b} \otimes \vec{b} + \nabla P) = -\rho \nabla \phi \tag{1.17}$$

$$\frac{\partial E}{\partial t} + \nabla \cdot [(E+P)\vec{v} - \vec{b}(\vec{v} \cdot \vec{b})] = -\rho \vec{v} \cdot \nabla \phi \tag{1.18}$$

$$\frac{\partial \vec{b}}{\partial t} - \nabla \times (\vec{v} \times \vec{b}) = 0, \tag{1.19}$$

for the conservation of mass, momentum, energy, and magnetic flux, respectively. ρ is the density, $\vec{v}$ is the fluid velocity, and $E = \rho e_{\text{int}} + \frac{\rho}{2}\vec{v}^2 + \frac{\vec{b}^2}{2}$ is the total energy density as the sum of internal, kinetic, and magnetic energies [76]. e_{int} is the specific internal energy, which is a catchall term to represent the energy of the thermal and nuclear processes in the star. The magnetic field is given by $\vec{B} = \sqrt{4\pi}\vec{b}$ and $P = p_{\text{thermal}} + \frac{\vec{b}^2}{2}$ is the total pressure. The gravitational potential ϕ is found by solving the equation

$$\nabla^2 \phi = 4\pi G \rho. \tag{1.20}$$

Equations (1.16)- (1.19) maintain the divergence free constraint of magnetic fields,

$$\nabla \cdot \vec{b} = 0. \tag{1.21}$$

Further conservation equations can be applied to encompass the effects of nuclear reactions and neutrino heating within the supernova. Imposing these restrictions, supernovae are further governed by

$$\frac{\partial (\rho Y_e)}{\partial t} + \nabla \cdot (\rho Y_e \vec{v}) = 0 \tag{1.22}$$

$$\frac{\partial \rho X_i}{\partial t} + \nabla \cdot (\rho X_i \vec{v}) = \dot{X}_{i,\text{burn}}, \tag{1.23}$$

where Y_e is the electron fraction, X_i is the mass fraction of a nuclear species i, and $\dot{X}_{i,\text{burn}}$ accounts for the change in mass fraction due to nuclear burning.

To solve this system of partial differential equations, a closure relation is needed to couple the nuclear composition with the fluid's properties. The equation of state (EOS) relates the thermodynamic properties of stellar material (e.g., ρ, T, Y_e, P) and provides a closure to the MHD equations. In the context of CCSNe, the EOS must be able to describe matter

across several orders of magnitude of density. Since CCSNe probe regimes of physics that extend beyond nuclear saturation density ($\rho \approx 2.6 \times 10^{14}$ g/cm^3), accurately modeling the CCSN interior must account for the transition from isolated nuclei to bulk nuclear matter. The stiffness of the EOS is a parameter that represents the responsiveness of the pressure to changes in density and dictates the strength of the core bounce in CCSNe models. The choice of EOS and related parameters determines critical observable properties of observables such as the explosion energy [77, 78], making the development of accurate EOS models a primary focus of nuclear physics research.

1.4.2 Neutrino Transport

Accurate modeling of neutrino transport in supernova simulations is critically important for predicting the outcome of the simulation. In CCSNe, the neutrino transport is described by the Boltzmann equation given by

$$\begin{aligned}\frac{1}{c}\frac{\partial f_\nu}{\partial t}+4\pi\mu_0\frac{\partial(r^2\rho_0 f_\nu)}{\partial m}+\frac{1}{r}\frac{\partial[(1-\mu_0^2)f_\nu]}{\partial\mu_0}+\frac{1}{c}\left(\frac{\partial\ln\rho_0}{\partial t}+\frac{3v_0}{r}\right)\frac{\partial[\mu_0(1-m u_0^2)f_\nu]}{\partial\mu_0}\\ +\frac{1}{c}\left[\mu_0^2\left(\frac{\partial\ln\rho_0}{\partial t}+\frac{3v_0}{r}\right)-\frac{v_0}{r}\right]\frac{1}{E_0^2}\frac{\partial(E_0^3 f_\nu)}{\partial E_0}=\frac{j_\nu}{\rho_0}-\tilde{\chi}_\nu f_\nu+C_\nu,\end{aligned} \tag{1.24}$$

where f_ν is the specific neutrino distribution function F_ν/ρ_0, ρ_0 and v_0 are fluid rest-mass density and velocity, E_0 is the neutrino energy in the comoving inertial frame, and $\mu_0 = \cos\theta_0$ is the is the cosine of the neutrino direction angle relative to the radial vector in the comoving inertial frame [79]. j_ν is the neutrino emissivity and $\tilde{\chi}_\nu$ is the modified neutrino opacity, given as

$$j_\nu-\tilde{\chi}_\nu f_\nu \equiv j_\nu-(j_\nu+\chi_\nu)f_\nu=(1-f_\nu)j_\nu-\chi_\nu f_\nu. \tag{1.25}$$

The final term in (1.24), C_ν, accounts for collisions of neutrinos with electrons and nucleons. We define the neutrino luminosity L_ν, the neutrino mean energy $\langle\epsilon_\nu\rangle$, and the mean

square energy $\langle \epsilon_\nu^2 \rangle$ as

$$L_\nu(\vec{r},t) = 4\pi r^2 c \frac{2\pi}{(hc)^3} \int_0^\infty d\epsilon \int_{-1}^{+1} d\mu\, \mu\, \epsilon^3\, f_\nu(\vec{r},\mu,\epsilon,t), \tag{1.26}$$

$$\langle \epsilon_\nu \rangle(\vec{r},t) = \frac{1}{A(\vec{r},t)} \int_0^\infty d\epsilon \int_{-1}^{+1} d\mu\, \epsilon^4\, f_\nu(\vec{r},\mu,\epsilon,t), \tag{1.27}$$

$$\langle \epsilon_\nu^2 \rangle(\vec{r},t) = \frac{1}{A(\vec{r},t)} \int_0^\infty d\epsilon \int_{-1}^{+1} d\mu\, \epsilon^5\, f_\nu(\vec{r},\mu,\epsilon,t), \tag{1.28}$$

where A is the normalization, defined as

$$A(\vec{r},t) = \int_0^\infty d\epsilon_\nu \int_{-1}^{+1} d\mu\, \epsilon^2\, f_\nu(\vec{r},\mu,\epsilon,t). \tag{1.29}$$

Solving the Boltzmann equations directly is a computationally expensive task but feasible in 1D with modern computational resources. Yet, the energy from the neutrinos is still not sufficient to drive an unaided explosion, implying that multidimensional effects are necessary for accurate supernova simulations [30]. In multidimensional simulations it becomes computationally impossible at the present time to fully solve the Boltzmann transport equations coupled with the hydrodynamic equations. To handle the computational load of the neutrino transport in multi-dimensional simulations, approximation schemes are implemented to decrease the computational cost of the neutrino transport.

The approximation schemes range in complexity and are chosen based on what aspect of CCSNe is the focus of a given study. The most basic of these are leakage schemes, in which neutrino emission and absorption rates are calculated based on the neutrino opacity in each zone and an approximate diffusion timescale. In leakage schemes neutrinos are assumed to have a fixed single energy for all neutrinos. However, equations (1.26)-(1.28) make clear that the neutrino dynamics are energy dependent, so a more complete neutrino model is necessary. More complex methods introduced the ability to handle the transport of neutrinos of different energies. The multi-group flux-limited diffusion (MGFLD) proposed a relationship between the neutrino flux and the energy gradient [80]. The introduction of this energy treatment was a step in the right direction, but MGFLD was found to underestimate the solution to the 1D neutrino transport equations [81]. MGFLD, however, laid the framework for "moments"-based methods of neutrino transport. In a moments method, the distribution functions can be broken down into an infinite series of angular

moments, coupled to one another [50, 82]:

$$\{J,H,K,L,...\}(t,r,\epsilon)=\frac{1}{2}\int_{-1}^{+1}d\mu\,\mu^{\{0,1,2,3,...\}}I(t,r,\epsilon,\mu) \tag{1.30}$$

where $\mu=\cos\theta$, ϵ is the neutrino energy, and $I(t,r,\epsilon,\mu)$ is the integrand of a moments based method, in the case of neutrino transport a function which is proportional to the neutrino distribution f. Using moments introduces an infinite "tower of equations" where the evolution of each moment depends upon the next moment in the tower. In practice, one can truncate this series with a closure relation. A closure provides a physically-motivated functional form for the next term in the series that, thus making the problem computationally solvable. In the case of the Boltzmann transport, the first three moments correspond to the neutrino energy density, flux, and pressure tensor, respectively. Thus, proposing a relationship between the neutrino energy density and the energy flux, as in MGFLD, is a 0th order moment calculation (denoted M0). The most common implementations of moments calculations for neutrino transport utilize M1 transport, explicitly solving for the energy density and the neutrino flux and using the closure to provide a relationship to the pressure.

Another approach to solving the transport equations in 3D is ray-by-ray transport. This technique explicitly solves the Boltzmann equations in 1D along a large number of radial rays originating at the core of the CCSN [83]. This method operates on the assumption that each 1D ray does not communicate with one another, neglecting lateral effects. A variant of ray-by-ray, called ray-by-ray+, supplements the purely radial transport with approximate coupling terms in optically thick regions to account for the missing interactions.

The final method described here is the one used for the remainder of this work, the isotropic diffusion source approximation (IDSA). IDSA is a spectral radiative transfer code for neutrino transport that focuses on four key aspects relevant to supernova conditions: the thermodynamics of trapped neutrinos, the diffusion limit, the spectrum of transported neutrinos, and the angular focusing of the neutrino propagation directions with increasing distance from the neutrinospheres [84]. IDSA achieves this by decomposing the neutrino distribution f_ν into distributions of trapped and streaming neutrinos,

$$f_\nu=f_\nu^t+f_\nu^s, \tag{1.31}$$

and evolving each separately. Trapped neutrinos have a channel to either interact with matter, or escape and become free streaming, represented by a coupling function Σ. Sim-

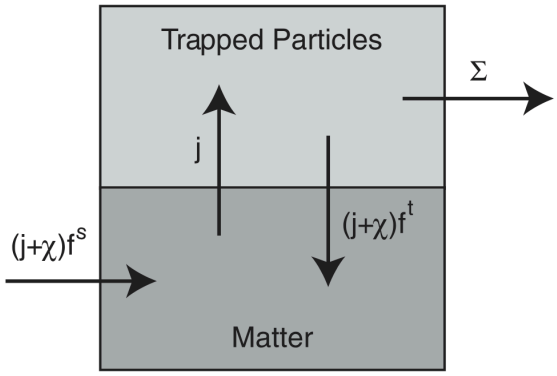

Figure 1.4: Figure taken from Liebendorfer *et.al.* [84] demonstrating the approach taken to approximate the neutrino interactions with matter. The neutrino distribution is broken up into free streaming, f^s and trapped, f^t neutrinos. Each rate shown is the rate that neutrinos may be exchanged between each state. The external source/sink represents free streaming neutrinos.

ilarly, free streaming neutrinos may interact with matter at a rate of $(j+\chi)f^s_\nu$. Figure 1.4 demonstrates the channels through which a neutrino can convert between streaming and trapped distributions. With the assumption that the distribution of trapped neutrinos is isotropic, equation (1.24) simplifies to

$$\frac{1}{c}\frac{\partial f^t_\nu}{\partial t} = j_\nu - (j_\nu + \chi_\nu) f^t_\nu - \Sigma_\nu. \tag{1.32}$$

Σ_ν is the coupling term between the trapped and free-streaming neutrinos, taken to be

$$\Sigma_\nu = \min\left\{\max\left[\alpha_\nu + \frac{1}{2}(j_\nu+\chi_\nu)\int f^s_o \, d\mu_0,\, 0\right], j_\nu\right\}, \tag{1.33}$$

with

$$\alpha_\nu = \nabla\cdot\left(\frac{-1}{3(j_\nu+\chi_\nu+\phi_\nu)}\nabla f^t_\nu\right). \tag{1.34}$$

f^s is the free-streaming neutrino distribution and ϕ_ν is the opacity for a neutrino species and accounts for isoenergetic scattering in the mean free path [80]. In practice with finite time resolution, f^s in equation (1.33) is taken to be the free-streaming neutrino distribution from the previous time step.

1.4.3 Progenitor Models

Modeling supernovae requires an accurate model of a star at the point before the core begins to collapse. These presupernova models are sensitive to the input physics and require careful modeling to make predictions about the structure of the stars at the time of collapse. The computational cost of resolving multidimensional fluid dynamics, magnetic fields, and large nuclear networks over millions of years until core collapse restricts the ability of stellar theorists to model these effects in 3D over the entire life of the star. To combat this, these stars are often modeled in 1D and implement approximation schemes for the computationally expensive physics. 3D stellar progenitors for supernova simulations have been generated [85] by evolving the cores of 1D models of stars which have been mapped to 3D for the last few minutes of their lives prior to collapse. The progenitors used in this work are 1D models produced from the KEPLER [86, 57] and MESA [87] stellar evolution codes.

KEPLER is a 1D implicit hydrodynamics solver developed to evolve supernova progenitors through the hydrostatic and explosive burning phases of stellar evolution [86]. KEPLER can evolve a collapsing stellar model through core-collapse and explosion, resulting in an all-in-one code that models a star from birth to death. KEPLER supports both piston-driven explosions and thermal bomb methods for supernova shock revival. Additionally, KEPLER includes radiative diffusion in its evolution to allow for the calculation of light curves during and after the explosion phase. KEPLER also has a large nuclear reaction network and can be used for nucleosynthesis calculations of CCSNe yields.

Modules for Experiments in Stellar Astrophysics (MESA) is a 1D open-source adaptive-mesh stellar evolution code that can be used to generate progenitors for supernova simulations [87]. While KEPLER is specifically designed and optimized for massive stars, MESA differentiates itself via its modular nature and flexibility to include a wide range of physics. MESA implements a Henyey-type mixing length theory scheme to approximate the hydrodynamic quantities in a star and is not well-equipped to handle shock evolution beyond collapse [88, 87]. MESA can be used to model candidate stars of varying ZAMS masses up to the red supergiant (RSG) phase and into core collapse, creating a 1D pre-supernova model that can be evolved separately in a chosen supernova evolution code equipped to more accurately handle the hydrodynamics of the explosion.

MESA's modularity is one of its key strengths in that it does not confine the pre-supernova models that it generates to one strict set of physics. It has been shown that evolution to the RSG phase is highly dependent on many physical and simulation parameters, including,

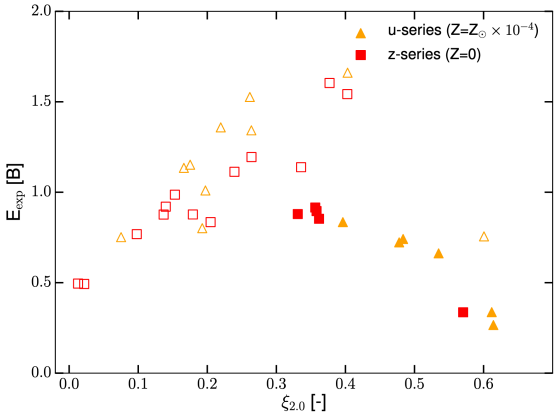

Figure 1.5: Figure from Ebinger *et. al* [92], demonstrating the effects of compactness on explosion energy for 1D supernova models. The left axis is the explosion energy of the supernova, and the bottom axis is the compactness of the supernova at bounce. Open symbols correspond to models to the left of the compactness peak of KEPLER models, while filled symbols indicate models to the right of the compactness peak.

but not limited to, resolution, dimensionality, and choice of nuclear network size [89, 90, 91]. RSGs modeled with small nuclear networks have been shown to have a different structure than those modeled with large networks [91]. For the progenitor models generated by MESA in this work, the chosen nuclear network will track 206 isotopes through stellar evolution. Specific details of our implementation can be found in Chapter 4.

As discussed previously, stellar models are highly dependent on the treatments of various processes during their evolution. The mass loss scheme for the star is an incredibly influential, yet poorly constrained, determinant of the structure of the star at the point of collapse, and thus the resulting supernova [94, 95, 96, 97]. Mass loss is the means by which a star loses mass to stellar winds over the course of its lifetime. The mass loss prescriptions used in KEPLER 2007 [57] and MESA [93] follow the prescriptions laid out in [98] and [94]. The rate of mass loss, $\dot{M}$, is described by

$$\log\frac{\dot{M}}{\eta} = \begin{cases} F(L_*, M_*, T_{\rm eff}, v_\infty/v_{\rm esc}, Z) & 12,500\ {\rm K} \leq T_{\rm eff} \leq 22,500\ {\rm K} \\ G(L_*, M_*, T_{\rm eff}, v_\infty/v_{\rm esc}, Z) & 27,500\ {\rm K} \leq T_{\rm eff} \leq 50,000\ {\rm K} \end{cases} \tag{1.35}$$

during the main-sequence hot-phase, and

$$\log\frac{\dot{M}}{\eta} = H(L_*, T_{\rm eff}) \tag{1.36}$$

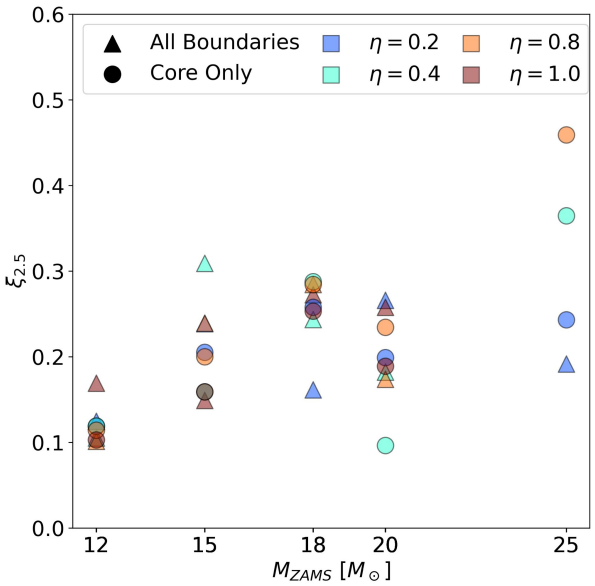

Figure 1.6: Resultant compactness of 36 MESA models with various wind efficiency parameters from Meyers *et al.*. The colors represent values of η, and the shape represent different approaches to the convective mixing scheme in `MESA` [93].

during the RSG cool-phase, where F, G and H are functions describing the relationship between the measurable quantities and the mass-loss rate $\dot{M}$ and $0 < \eta \leq 1$ is a parameter describing the efficiency of the stellar wind. For the KEPLER models used in this work [57], a value of 0.8 was used for this parameter. These progenitors will be used in the work in Chapters 2 and 3. MESA models, conversely, allow us to modify η as a free parameter. Modifications to η have been shown to impact the resultant compactness of presupernova models [99, 93].

Another adjustable parameter in MESA is the treatment of convective overshooting, the amount by which convective matter overshoots the boundary of radiative and convective interfaces [100, 101, 102, 103]. Convective overshooting has few observational constraints and it is not well understood to what depth into the radiative zone this overshooting occurs. Within the framework of MESA, the treatment of the convective overshooting is a modifiable parameter. Several treatments of convective overshooting exist, and all of them focus on the value of the diffusion coefficient $D(r)$. One such case is simple "step" overshooting, wherein the diffusion coefficient is treated as a constant throughout the region of interest, i.e.

$$D(r) = D_0. \tag{1.37}$$

A more in-depth analysis of the fluid dynamics suggest that step overshooting may not be the most accurate behavior at these boundaries. Instead, an exponential decay overshooting has been introduced,

$$D(r) = D_0 \exp\left\{\frac{-2(r-r_0)}{f_{\rm ov} H_{p,0}}\right\}, \tag{1.38}$$

where $D(r)$ is the convective mixing efficiency, D_0 is the convective mixing efficiency at the interface, r_0 is the radial position of the convective/radiative boundary, r is the radial position within the star, $H_{p,0}$ is the pressure scale height, and $f_{\rm ov}$ is a free parameter [100]. The amount by which the convection overshoots the boundary and the regions within the star in which it is implemented can impact abundances at the core of the star [102], which ultimately play a role in the structure of the star and thus the compactness.

To gain an indication of the explosion outcome of supernova progenitors, a parameter known as 'compactness' (ξ_M) has been proposed to understand correlations within CCSNe models [104]. The compactness is defined as

$$\xi_M = \frac{M/M_\odot}{R(M)/1000{\rm km}}, \tag{1.39}$$

where M is a chosen mass and $R(M)$ is the radius in km that contains M amount of mass beneath it. ξ_M is taken at an *a priori* selected mass cut M and is normally calculated at core bounce for collapsing supernova models. However, [99] have shown that the compactness calculated at bounce is nearly identical to the compactness calculated in presupernova models that have reached an infall velocity of 1000 km/s.

It has been seen that compactness correlates with many supernova properties, such as explosion energy, explosion time, and nuclear composition [105, 106, 92, 78, 107]. Figure 1.5 shows an example of one such correlation between $\xi_{2.0}$ and explosion energy from [92]. Figure 1.6 shows the compactness taken at $M = 2.5$ M$_\odot$ for an array of supernova progenitors evolved from MESA, for various treatments of the mass loss wind efficiency and the overshooting prescription. From the figure, there are clear differences in the compactness as a function of both the wind efficiency and the convective overshooting for an array of ZAMS masses. The implications of which, explored in more detail in Chapter 4, are that the wind efficiency parameter and the convective overshooting treatment can impact the outcome of CCSNe and must be a consideration when running these models.

1.5 Supernova Models

1.5.1 AGILE-IDSA with PUSH

AGILE is a 1D Lagrangian general relativistic hydrodynamics code that solves the conservation equations outlined in (1.16)- (1.18) in spherical symmetry [108]. The deleptonization scheme of [109] is applied during collapse. Given that AGILE is a 1D code, the magnetic field terms in equations (1.16)- (1.18) are set to 0, and the magnetic flux conservation condition becomes irrelevant. AGILE uses an adaptive spatial grid along with implicit time evolution to resolve the extreme gradients that occur in core-collapse supernovae. For electron neutrino and antineutrino ($\nu_e/\overline{\nu}_e$) transport, AGILE utilizes IDSA [84]. For the heavy flavor neutrinos ($\nu_x = \nu_\mu, \nu_\tau, \overline{\nu}_\mu, \overline{\nu}_\tau$) AGILE-IDSA uses the advanced spectral leakage (ASL) scheme of [110] to handle their transport.

The PUSH method is a method for triggering explosions in 1D CCSNe simulations by introducing artificial heating in a physically motivated manner [111]. The core principle is to mimic the missing energy from multi-dimensional hydrodynamics by depositing extra thermal energy in the gain region. To achieve this without disrupting the electron fraction, PUSH sources this extra heating from the heavy lepton neutrino luminosity (($\nu_x = \nu_\mu, \nu_\tau, \overline{\nu}_\mu, \overline{\nu}_\tau$). PUSH achieves this numerically by integrating a local heating term,

$$Q^+_{\rm PUSH} = 4\mathscr{G}(t)\int_0^\infty q^+_{\rm PUSH}(r,E)\,dE, \tag{1.40}$$

where

$$q^+_{\rm PUSH}(r,E) \equiv \sigma_0 \frac{1}{m_b}\left(\frac{E}{m_e c^2}\right)^2 \frac{1}{4\pi r^2}\left(\frac{dL_{\nu_x}}{dE}\right)\mathscr{F}(r,E) \tag{1.41}$$

and

$$\sigma_0 \equiv \frac{4G_F(m_e c^2)^2}{\pi(\hbar c)^4} \tag{1.42}$$

is of the order of a typical neutrino cross-section. m_e and m_b represent the electron mass and the average baryon mass, and $\mathscr{F}(r,E)$ and $\mathscr{G}(t)$ are control terms to constrain where

and when PUSH is active. $\mathscr{G}$(t) is a piecewise function that has the following prescription:

$$\mathscr{G}(t) = k_{\rm PUSH} \times \begin{cases} 0 & t \leq t_{\rm on} \\ \frac{t-t_{\rm on}}{t_{\rm rise}} & t_{\rm on} < t \leq t_{\rm on} + t_{\rm rise} \\ 1 & t_{\rm on} + t_{\rm rise} < t \leq t_{\rm off} \\ \frac{t_{\rm off}+t_{\rm rise}-t}{t_{\rm rise}} & t_{\rm off} < t \leq t_{\rm off} + t_{\rm rise} \\ 0 & t > t_{\rm off} + t_{\rm rise} \end{cases} \tag{1.43}$$

where t is the time post-bounce, and $t_{\rm on}$, $t_{\rm off}$, $t_{\rm rise}$, and $k_{\rm PUSH}$ are all free parameters controlling the strength and time of PUSH's effect. $t_{\rm on}$ is set by finding the time in multidimensional models for which the ratio of the advection timescale to the convective growth timescale satisfy $\tau_{\rm adv}/\tau_{\rm conv} > \sim 3$, signaling that convection has begun. This was found to occur in the range of $t = 0.06 - 0.08$ s. $t_{\rm off}$ is set to 1 s as the neutrino driven explosion occurs well before 1 s in CCSN simulations. By comparing the explosion energy and nucleosynthetic yields of an 18.8 $M_\odot$ supernova simulation with observations from SN1987A [112, 65], $k_{\rm PUSH}$ and $t_{\rm rise}$ have been constrained. Similarly, $\mathscr{F}(r, E)$ confines the spatial domain of PUSH to only operate in the gain region,

$$\mathscr{F}(r, E) = \begin{cases} 0 & r > R_{\rm shock} \text{ or } \dot{e}_{\nu_e, \bar{\nu}_e} < 0 \\ e^{-\tau_{\nu_e}(r,E)} & \text{otherwise} \end{cases} \tag{1.44}$$

where $R_{\rm shock}$ is the shock radius, $\dot{e}_{\nu_e, \bar{\nu}_e}$ is the electron neutrino specific energy deposition rate, and τ_{ν_e} is the optical depth for electron flavor neutrinos.

1.5.2 ELEPHANT

The **EL**egant and **E**fficient **P**arallel **H**ydrodynamics and **N**eutrino **T**ransport code (ELEPHANT) is a 3D magnetohydrodynamic code used for modeling CCSNe [113]. ELEPHANT's computational domain consists of a high-resolution fixed 3D Cartesian mesh running simultaneously with a 1D grid that extends well beyond the 3D domain. AGILE, detailed in § 1.5.1, models the spherically symmetric component of the simulation on the 1D grid, and provides information regarding the boundary conditions for the material falling into the 3D domain. ELEPHANT's 3D cartesian grid allows for a high fidelity simulation in regions that are otherwise lost to adaptive mesh approaches while also preventing singularities at

the center of the star. Based on the the work done in [114], ELEPHANT solves the hydrodynamic equations (1.16)- (1.20) and (1.22)- (**??**) in the modified Newtonian gravitational potential together with IDSA for the neutrino transport scheme. ELEPHANT does not account for nuclear burning and thus equation (1.23) is not considered in its calculations. ELEPHANT uses operator splitting between the solutions of the hydrodynamic equations and the neutrino transport equations.

In this work ELEPHANT is implemented with the Lattimer-Swesty EOS with an incompressibility parameter $K = 220$ MeV [115]. In general this can be interchanged with other choices of EOS. The gravitational potential is modified following the prescription in [116] to include general relativistic corrections to the Newtonian potential. The hydrodynamics equations (1.16)-(1.20) and (1.22)-(**??**) are solved using the second-order relaxation scheme of [117]. To enforce that the scheme is total variation diminishing, ELEPHANT implements the minmod limiter in supersonic flow regimes and the van Leer limiter in subsonic regimes [114]. For the time integration, a second-order predictor-corrector method is used.

ELEPHANT is initialized using 1D progenitor models and assumes spherical symmetry at the onset of collapse. The 3D domain of ELEPHANT is initially filled with 1D data from the progenitor model rotated symmetrically about θ, ϕ. There is no information about rotation or magnetic fields stored in the 1D progenitor. ELEPHANT thus algorithmically defines these quantities at initialization and at the boundary for any new infalling material from AGILE. The rotation profile of ELEPHANT is described by two parameters, Ω_{rot} and r_{rot}. ELEPHANT pre-calculates values for the specific angular momentum L/m for each AGILE zone i at the start of the simulation according to

$$\frac{L}{m} = \frac{2}{3}\Omega_{rot}\frac{r_i^2\, r_{rot}^2}{(r_i^2 + r_{rot}^2)}, \tag{1.45}$$

where r_i is the radius of the i'th AGILE grid zone, r_{rot} is a scaling factor to determine at what radius L/m becomes the moment of inertia of a spherical shell, and Ω_{rot} is the input parameter corresponding to the angular velocity of the spherical shell. ELEPHANT stores the specific angular momentum for the AGILE zones in a table alongside the mass coordinate of each AGILE zone. As the simulation evolves, material that is newly accreted into the 3D domain is assigned velocity components that follow from the conservation of angular momentum. To find the initial velocity of grid zone j in the 3D domain ELEPHANT performs a linear interpolation to find the value of L/m for the zone given its mass coordi-

nate, then computes the z component of the angular velocity Ω_z for that grid cell according to

$$\Omega_z = \frac{3}{2\,r_j^2}\left(\frac{L}{m}\right) \tag{1.46}$$

ELEPHANT then assigns the velocity components v_x and v_y for the cell to be $v_x = -r_y\,\Omega_z$ and $v_y = r_x\,\Omega_z$.

The magnetic field must be defined in such a way to preserve the divergence-free condition (equation (1.21)) of Maxwell's equations. ELEPHANT achieves this by first constructing the vector potential $\vec{A}$ and then computing the corresponding magnetic field as $\vec{B} = \nabla \times \vec{A}$, thus ensuring that analytically $\nabla \cdot \vec{B} = 0$. The toroidal and poloidal components of $\vec{B}$ are parameters determined at compile-time, and they are inserted into the vector potential such that

$$\vec{B} = \nabla \times \vec{A} = \langle \sqrt{2}B_{\text{toroidal}}, \sqrt{2}B_{\text{toroidal}}, B_{\text{poloidal}} \rangle, \tag{1.47}$$

where B_{toroidal} and B_{poloidal} are constant input parameters for the magnetic field strength. This algorithm results in a constant magnetic field throughout the entire core of the star, which is unphysical. The magnetic field is expected to scale with density in the core of stars. Thus we introduce an explicit scaling factor of the density in the vector potential:

$$\vec{A}_{\text{corrected}} = \vec{A}\left(\frac{\rho}{\rho_{\text{ref}}}\right)^{\frac{1}{2}} \tag{1.48}$$

where ρ_{ref} is a parameter defined at compile-time and represents the density at which the vector potential is equal to the expected value given the input magnetic field strength. This algorithm for constructing the magnetic field is applied both at simulation initialization and at the boundary of the 3D domain for material flowing onto the 3D domain from the 1D AGILE domain.

Code Modifications

As described in § 1.5.2, ELEPHANT uses a finite-differencing scheme to solve the ideal MHD equations. To perform these calculations near the edges of the 3D domain, ELEPHANT must retain a buffer of zones outside of the physical simulation domain to ensure accurate differencing at the boundaries. These zones outside of the simulation domain, denoted as boundary zones, are filled with data from the simultaneous 1D AGILE simulation that is running in tandem with ELEPHANT as described previously. The magnetic field data in these newly filled zones must be adjusted so that it is brought into agreement

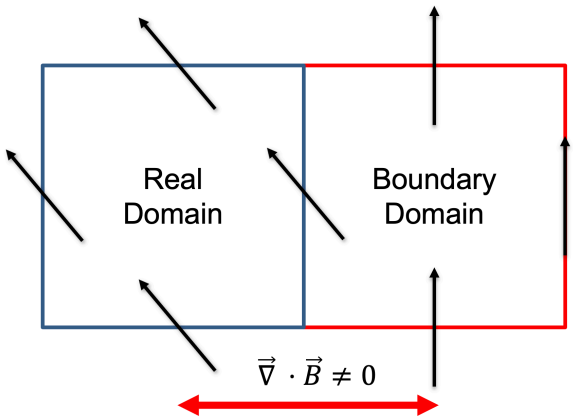

Figure 1.7: The state of the magnetic field in ELEPHANT when a new magnetic field (black arrow) is prescribed in a boundary zone (red) as compared to a zone that has undergone MHD evolution (blue).

with the evolved simulation data of the physical domain. Specifically, the constraint of equation (1.21) must be preserved throughout the simulation. Figure 1.7 gives a visual depiction of the discrepancy. ELEPHANT algorithmically corrects the data in the boundary zones, adjusting the field in such a way that the divergence between the real domain and the boundary zone is minimized. This approach is effective but results in unforeseen complications when parallelization is introduced. ELEPHANT uses MPI to parallelize the calculations within the 3D domain and this means that the computational domain is broken up into several large subdomains. In the initial version of the ELEPHANT code, an issue arose due to the lack of communication between the subdomains during the field adjustment process in the boundary zones. This manifested as discontinuities in the magnetic field advected into the 3D domain. These discontinuities propagated into the gain region of the star, resulting in what appeared as the distinct "slices" seen in Figure 1.8. In each of these slices, the magnetic field would be self-aligned and divergence free, i.e. $\nabla \cdot \vec{B} = 0$. Yet, the magnetic field in a given slice would point opposite the field in the adjacent slice, highlighted by the streamlines in the right panel of Figure 1.8. This opposition introduced an unphysical nonzero divergence of the field that persisted throughout the simulation.

To understand the source of this discontinuity, it is necessary to understand the means by which ELEPHANT parallelizes the 3D domain. The cartesian grid is partitioned into rectangular prisms such that the zones are evenly distributed across all parallel processes. This partitioning applies to the boundary zones as well. Each process handles the evolution of the MHD equations in the subdomain independently from the others. Due to this, when

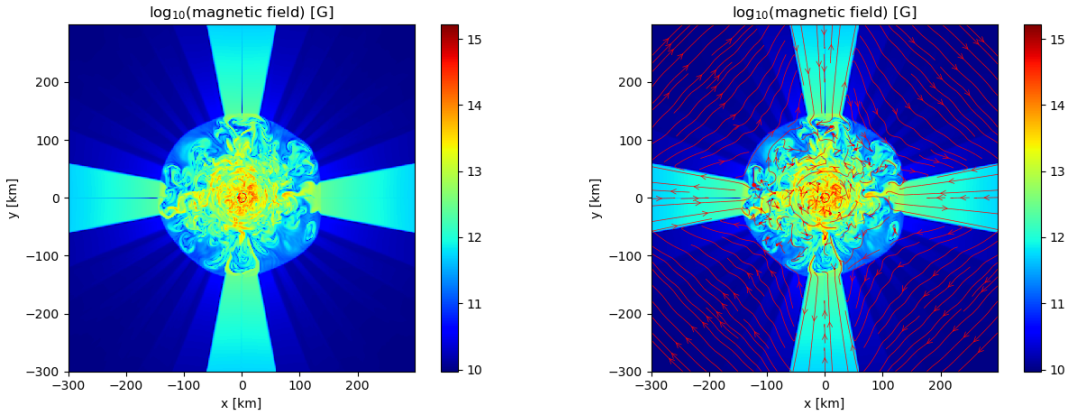

Figure 1.8: Left: An example of the magnetic field prior to code modifications. Discontinuous values of $\vec{B}$ at the interface of each subdomain are visible. The subdomain interfaces are spaced every 50 km along the boundaries. Right: the same data with streamlines overlaid. Note the alternating directions of the magnetic field on-axis.

new magnetic field is advected into a boundary zone for a particular subdomain, its divergence correction with the physical domain does not account for the adjacent subdomain. Thus, while the magnetic field on the boundary within an MPI task is divergence free, the zones adjacent to each other between MPI tasks are not divergence free. This creates a feedback loop where the magnetic field vectors continue to align themselves on the physical domain, but do not align themselves across subgrid processes in the boundary zones. Thus, clearly divergent regions appear at the interface between two boundary zones, with magnetic fields pointing in opposite directions adjacent to one another.

To address this issue, an overhaul had to be made to the means by which the boundary zones preserved the divergence-free condition. Within a subdomain, the standard process of divergence minimization through a total variation diminishing (TVD) scheme can be replicated between boundary zones. First, the TVD scheme minimizes the divergence across all spatial zones within a boundary subdomain, as is done in the original code. This method calculates a correction term for each zone to minimize the divergence. To improve upon this, we introduced an algorithm for distributing the "excess divergence" to adjacent zones. For a given subgrid, the average correction obtained from the TVD scheme is calculated for the current subgrid, as well as any subgrids that are physically adjacent. Then, the average correction of the subgrid and all adjacent subgrids is distributed such that the current subgrid has 0 correction factor, thus creating a correction flux away from the current subgrid. This process is repeated for all zones, pushing the calculated divergence out-

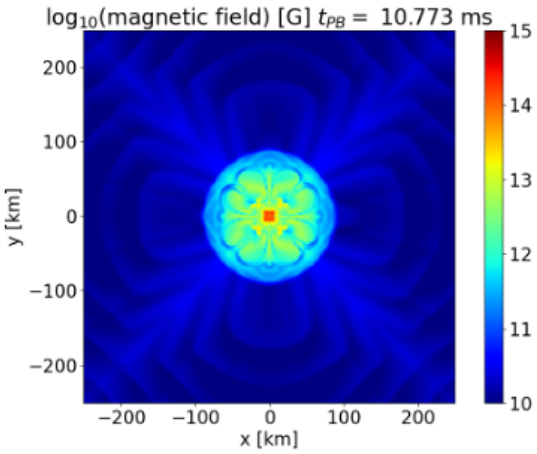

Figure 1.9: A plot of a toroidal magnetic field from the ELEPHANT code after the implementation of the divergence correction algorithm.

ward until it reaches the edge of the boundary subgrids, at which point it is removed from the simulation. In this way, there is no unphysical divergence introduced in the boundary conditions of the simulation domain and the strange behavior of the magnetic field is removed. The results of this algorithm can be seen in the magnetic field plot in Figure 1.9. Clearly the domain has become much smoother and the magnetic field is now upholding the divergence-free condition of Maxwell's equations across the entire domain.

A more nuanced problem within ELEPHANT emerged in the process of determining the appropriate magnetic field prescription on the boundary. As described, the prescription of the vector potential at the initialization of ELEPHANT has been chosen to be scaled by a factor of $\sqrt{\rho}$ to create a more physically realistic magnetic field. While ELEPHANT works on a fixed grid, AGILE has an adaptive grid structure that spaces radial grid zones at varying positions, optimized for providing the highest resolution near the shock. AGILE does not have a grid point at $r = 0$. Because of this, there are many zones within the center of the ELEPHANT domain that are not covered by an AGILE grid zone. To calculate quantities for these zones, ELEPHANT performs a linear interpolation for 3D zones that are located between AGILE radial zones. An initial density and magnetic field profile for ELEPHANT along a radial ray is shown in Figure 1.10 and immediately an issue near the core becomes clear. Without a density available at $r = 0$ km, ELEPHANT has no way to interpolate density from $r = 0$ to the first AGILE zone. As such, ELEPHANT's initial density profile is constant to nearly $r \approx 130$ km. A discontinuity is then introduced at the first AGILE grid zone. While for the evolution of the simulation this is a minor issue, our prescription for

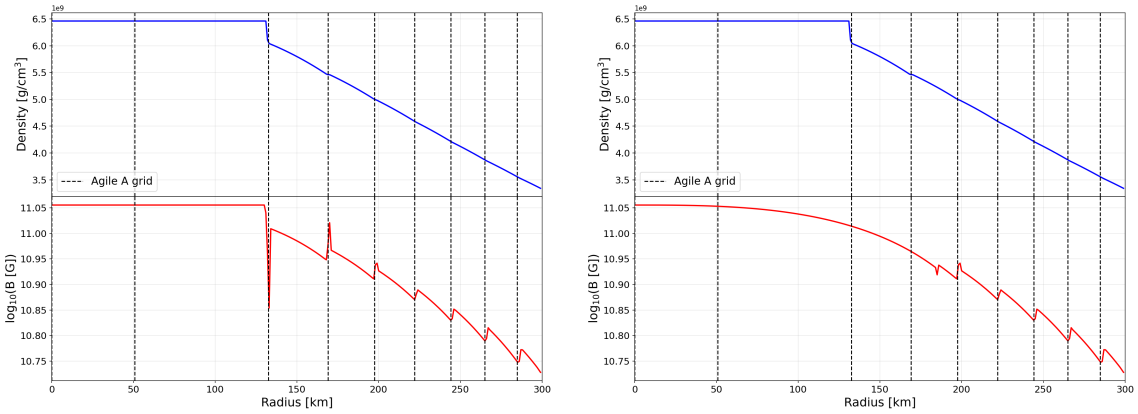

Figure 1.10: A 1D profile of density (top) and magnetic field (bottom) through the 3D ELEPHANT domain left: prior to modifications of the density interpolation and right: the same data after the introduction of power law smoothing. The black dashed lines represent the grid zones of the 1D progenitor.

the vector potential suffers greatly from a discontinuity. By introducing $\rho = \rho(x, y, z)$ into the formula for the vector potential, we now recover the formula for the magnetic field as:

$$\vec{B} = \nabla \times (\vec{A}(\frac{\rho}{\rho_{\text{ref}}})^{\frac{1}{2}}) \tag{1.49}$$

$$\vec{B} = \frac{1}{\sqrt{\rho_{\text{ref}}}}(\nabla \times \sqrt{\rho}\vec{A}) \tag{1.50}$$

$$\vec{B} = \frac{1}{\sqrt{\rho_{\text{ref}}}}(\sqrt{\rho}(\nabla \times \vec{A}) - \vec{A} \times (\nabla\sqrt{\rho})) \tag{1.51}$$

$$\vec{B} = \sqrt{\frac{\rho}{\rho_{\text{ref}}}}\vec{B}_{\text{expected}} - \frac{1}{2\sqrt{\rho}}(\vec{A} \times \nabla\rho) \tag{1.52}$$

where $\vec{B}_{\text{expected}}$ is the magnetic field expected from the input vector potential. As is evident from Equation (1.52), there is a dependence of $\vec{B}$ on the gradient of ρ. Thus, discontinuities in ρ result in discontinuities in $\vec{B}$. To remedy this, it was necessary to have a smooth density contour for the scale factor in front of $\vec{A}$. Taking care to only alter the interpolation at the core of the star and to leave the rest of the interpolation unchanged wherever possible, we modified the code to utilize a power law interpolation on ρ from $r = 0$ km to two AGILE zones beyond the discontinuity in the term preceding $\vec{A}$. This implementation removes the discontinuity in the scale factor in front of $\vec{A}$ and, when curled, results in a smooth magnetic field profile, shown in the right panel of Figure 1.10.

As CCSNe simulations in ELEPHANT evolved over time, simulations with a successful

shock revival faced the issue of expanding beyond the grid. CCSNe explosions are generally considered to be "exploding" when the shock has extended beyond 500 km after revival. Unfortunately, to simulate a full CCSNe simulation of ELEPHANT with a 1000^3 km^3 domain size would require computational resources well beyond what we can access. Further, this would be a waste of resources as the asphericity in the CCSNe do not extend beyond the shock, which does not exceed 200 km for quite some time, if at all. To maintain computational efficiency, we developed a technique to extend the 3D grid when the shock reaches the boundary of the current 3D domain. To do this we exploited the ability of ELEPHANT to fill the 3D domain from 1D data, an ability also used during the initiation process from the progenitor. To extend the grid, we use the solution computed by AGILE to fill an enlarged 3D mesh, and then insert the data from the previous, smaller, 3D domain into the center of the new, larger, 3D domain. This technique extends the boundary of the domain with model-accurate quantities and the simulation can then be continued from the extended dataset. Thus we can run the simulation until the shock reaches 500 km in a computationally efficient manner.

1.6 Motivation

A deeper understanding of the evolution of CCSNe remains one of the most challenging problems in modern astrophysics. CCSNe act both as a source of the elements and create an array of compact objects that we observe, such as magnetars, pulsars, and stellar-mass black holes [118, 119, 120, 121, 122, 123, 105]. We cannot reliably predict from the initial properties of a star the supernova outcome, or the properties of the compact object remnant. The magnetic field strengths of magnetars and pulsars can exceed 10^{14} G and can have rotation periods as short as 1.6 ms [124, 123], but the mechanism by which they attain such strong fields and rapid rotation is not conclusively answered. CCSNe with initial magnetic field configurations and rotation profiles can hold the answer to the origins of these exotic compact objects. CCSNe with magnetic fields have also been put forward as the source of Long Gamma Ray Bursts [125, 126].

Modeling of CCSNe that includes magnetic fields and rotation is necessary to answer questions about the source of these compact objects and events. The nature of capturing such physical effects demands that the simulations be three-dimensional. Magnetic fields and rotation can influence the explosion time, explosion energy, and remnant properties in CCSNe [27]. The impact of these properties is often attributed to asymmetries in the

fluid dynamics, resulting in turbulent motion within the star as it evolves [127, 128]. The current means of measuring turbulent properties of supernova simulations are not necessarily capturing the correct behavior. Exploration into the turbulence and the means by which turbulence is observed is critical for the determination of the properties of both the supernova itself and the remnant properties.

Much of a CCSN's behavior is not only tied to the dynamics in the collapse and core-bounce phase, but is also dependent on the entire history of the star itself. Stellar properties like the ZAMS mass and the metallicity are well studied and have connections to the behavior of the CCSN during explosion and to the properties of the remnant object. However, these are but two of many parameters involved in stellar modeling. Much more poorly constrained parameters like the stellar wind strength and the treatment of convective overshooting have not been well studied in their effects on CCSNe. These effects play a role in the composition [129] and the compactness [99] of presupernova models, which opens the possibility for continuing effects on the supernova explosion itself. Understanding precisely how these physical effects can alter CCSNe serves to further constrain these parameters as well as demonstrate the sensitivity of CCSNe to these particular stellar evolution effects.

In this dissertation, I aim to study the impacts of magnetic fields, rotation, and stellar properties on the evolution of CCSNe and the compact objects they produce. We conduct a thorough analysis on the effects of turbulence in the gain region of CCSNe as they relate to the likelihood of explosion of CCSNe in 3D simulations. To do this, we focus on understanding the metrics used in determining turbulence and highlight the necessity for developing an accurate tool to measure the turbulence. We investigate the amount of kinetic energy stored in turbulence in our simulations, and how that energy can vary by a significant amount based on the choices made in the turbulence metric. We also propose a new method of turbulence measurement that shows consistency with a less accepted method already existing in the literature. Building from this, we apply different magnetic fields to the same simulations to study the effects of the magnetic fields on our turbulence measurements. Further, we perform an energy analysis on the simulations with magnetic fields applied to understand the source of the growth magnetic field growth and to gain clarity on what conditions can result in magnetar-level magnetic fields in CCSNe.

Separately, we look into the effects of stellar modeling parameters on CCSNe outcomes. Knowing that modifications to the behavior of stellar winds and convection over the lifetime of a star will change the compactness of the star at collapse, we aim to understand how these effects relate to the properties of CCSNe, namely remnant mass, explosion en-

ergy, remnant mass, explosion time, and neutrino heating. Thus we seek to connect the poorly constrained models in stellar theory to real supernova observables, providing the opportunity to constrain these parameters at the advent of more observational supernova data.

In Chapter 2 we explore in depth the metrics surrounding turbulence in CCSNe and study how turbulence within the gain region can effect supernova outcomes. Chapter 3 is a study of how the introduction of magnetic fields plays a part in turbulent dynamics in the gain region of CCSNe, as well as an analysis on the source of magnetic growth in CCSNe. Chapter 4 is an investigation of the effects of two stellar modeling parameters, the wind efficiency and the convective overshooting, on presupernova models and quantifying their impact on the associated CCSNe. In Chapter 5, I summarize the results and findings within this work and highlight future research of interest based on these findings.

REFERENCES

[1] H. A. Bethe. Supernova mechanisms. *Reviews of Modern Physics*, 62(4):801–866, October 1990. Publisher: American Physical Society.

[2] David A. Green and F. Richard Stephenson. Historical Supernovae. In Kurt W. Weiler, editor, *Supernovae and Gamma-Ray Bursters*, Lecture Notes in Physics, pages 7–19. Springer, Berlin, Heidelberg, 2003.

[3] Jacco Vink. Supernova 1604, Kepler's supernova, and its remnant. pages 139–160. 2017. arXiv:1612.06905 [astro-ph].

[4] G. A. Tammann, W. Loeffler, and A. Schroeder. The Galactic Supernova Rate. *The Astrophysical Journal Supplement Series*, 92:487, June 1994. Publisher: IOP ADS Bibcode: 1994ApJS...92..487T.

[5] Enrico Cappellaro and Massimo Turatto. Supernova types and rates. volume 264, pages 199–214. 2001. arXiv:astro-ph/0012455.

[6] W. Baade and F. Zwicky. On Super-Novae. *Proceedings of the National Academy of Sciences*, 20(5):254–259, 1934. _eprint: https://www.pnas.org/doi/pdf/10.1073/pnas.20.5.254.

[7] R. Minkowski. Spectra of Supernovae. *Publications of the Astronomical Society of the Pacific*, 53:224, August 1941. ADS Bibcode: 1941PASP...53..224M.

[8] John Whelan and Icko Iben, Jr. Binaries and Supernovae of Type I. *The Astrophysical Journal*, 186:1007–1014, December 1973. ADS Bibcode: 1973ApJ...186.1007W.

[9] Stirling A. Colgate and Montgomery H. Johnson. Hydrodynamic Origin of Cosmic Rays. *Physical Review Letters*, 5:235–238, September 1960. Publisher: APS ADS Bibcode: 1960PhRvL...5..235C.

[10] Stirling A. Colgate and Richard H. White. The Hydrodynamic Behavior of Supernovae Explosions. *The Astrophysical Journal*, 143:626, March 1966. Publisher: IOP ADS Bibcode: 1966ApJ...143..626C.

[11] James R. Wilson. A Numerical Study of Gravitational Stellar Collapse. *The Astrophysical Journal*, 163:209, January 1971. Publisher: IOP ADS Bibcode: 1971ApJ...163..209W.

[12] H. A. Bethe and J. R. Wilson. Revival of a stalled supernova shock by neutrino heating. *The Astrophysical Journal*, 295:14–23, August 1985. ADS Bibcode: 1985ApJ...295...14B.

[13] David L. Tubbs and David N. Schramm. Neutrino Opacities at High Temperatures and Densities. *The Astrophysical Journal*, 201:467, October 1975.

[14] G. M. Fuller, R. W. Mayle, J. R. Wilson, and D. N. Schramm. Resonant neutrino oscillations and stellar collapse. *The Astrophysical Journal*, 322:795, November 1987.

[15] S. W. Bruenn, C. J. Dirk, A. Mezzacappa, J. C. Hayes, J. M. Blondin, W. R. Hix, and O. E. B. Messer. Modeling core collapse supernovae in 2 and 3 dimensions with spectral neutrino transport. *Journal of Physics: Conference Series*, 46:393–402, September 2006. arXiv:0709.0537 [astro-ph].

[16] Philipp Mösta, Sherwood Richers, Christian D. Ott, Roland Haas, Anthony L. Piro, Kristen Boydstun, Ernazar Abdikamalov, Christian Reisswig, and Erik Schnetter. Magnetorotational core-collapse supernovae in three dimensions. 785(2):L29, April 2014. arXiv: 1403.1230 [astro-ph.HE] Number: L29 tex.adsnote: Provided by the SAO/NASA Astrophysics Data System.

[17] A. Burrows, L. Dessart, E. Livne, C. D. Ott, and J. Murphy. Simulations of Magnetically Driven Supernova and Hypernova Explosions in the Context of Rapid Rotation. *The Astrophysical Journal*, 664(1):416, July 2007. Publisher: IOP Publishing.

[18] Christian Winteler, Roger Kaeppeli, Albino Perego, Almudena Arcones, Nicolas Vasset, Nobuya Nishimura, Matthias Liebendoerfer, and Friedrich-Karl Thielemann. Magnetorotationally driven Supernovae as the origin of early galaxy r-process elements? *The Astrophysical Journal*, 750(1):L22, May 2012. arXiv: 1203.0616.

[19] Takami Kuroda, Almudena Arcones, Tomoya Takiwaki, and Kei Kotake. Magnetorotational Explosion of A Massive Star Supported by Neutrino Heating in General Relativistic Three Dimensional Simulations. *The Astrophysical Journal*, 896(2):102, June 2020. arXiv: 2003.02004.

[20] A. S. Eddington. On the Radiative Equilibrium of the Stars. *Monthly Notices of the Royal Astronomical Society*, 77(1):16–35, November 1916.

[21] Rudolf Kippenhahn and Alfred Weigert. *Stellar Structure and Evolution*. January 1994. ADS Bibcode: 1994sse..book.....K.

[22] E. Böhm-Vitense. Theory of the hydrogen convection zone. volume 12, pages 338–345, January 1960. ADS Bibcode: 1960IAUS...12..338B.

[23] H.-Thomas Janka. Explosion Mechanisms of Core-Collapse Supernovae. *Annual Review of Nuclear and Particle Science*, 62(1):407–451, November 2012. arXiv: 1206.2503.

[24] W. R. Hix, O. E. B. Messer, A. Mezzacappa, M. Liebendörfer, J. Sampaio, K. Langanke, D. J. Dean, and G. Martínez-Pinedo. Consequences of Nuclear Electron Capture in Core Collapse Supernovae. *Physical Review Letters*, 91(20):201102, November 2003. Publisher: American Physical Society.

[25] K. Langanke, G. Martínez-Pinedo, J. M. Sampaio, D. J. Dean, W. R. Hix, O. E. Messer, A. Mezzacappa, M. Liebendörfer, H. Th. Janka, and M. Rampp. Electron Capture Rates on Nuclei and Implications for Stellar Core Collapse. *Physical Review Letters*, 90:241102, June 2003. Publisher: APS ADS Bibcode: 2003PhRvL..90x1102L.

[26] H.-Th. Janka, K. Langanke, A. Marek, G. Martínez-Pinedo, and B. Müller. Theory of core-collapse supernovae. *Physics Reports*, 442:38–74, April 2007. Publisher: Elsevier ADS Bibcode: 2007PhR...442...38J.

[27] H.-Thomas Janka, Florian Hanke, Lorenz Huedepohl, Andreas Marek, Bernhard Mueller, and Martin Obergaulinger. Core-Collapse Supernovae: Reflections and Directions. *arXiv:1211.1378 [astro-ph]*, November 2012. arXiv: 1211.1378.

[28] R. Bowers and J. R. Wilson. Collapse of iron stellar cores. *The Astrophysical Journal*, 263:366–376, December 1982. Publisher: IOP ADS Bibcode: 1982ApJ...263..366B.

[29] James R. Wilson. Supernovae and Post-Collapse Behavior. page 422, January 1985. ADS Bibcode: 1985nuas.conf..422W.

[30] Matthias Liebendörfer, Anthony Mezzacappa, Friedrich-Karl Thielemann, O. E. Bronson Messer, W. Raphael Hix, and Stephen W. Bruenn. Probing the gravitational well: No supernova explosion in spherical symmetry with general relativistic Boltzmann neutrino transport. *Physical Review D*, 63(10):103004, April 2001. Publisher: American Physical Society.

[31] John M. Blondin, Anthony Mezzacappa, and Christine DeMarino. Stability of Standing Accretion Shocks, With an Eye Toward Core Collapse Supernovae. *The Astrophysical Journal*, 584(2):971–980, February 2003. arXiv:astro-ph/0210634.

[32] L. Scheck, H.-Th Janka, T. Foglizzo, and K. Kifonidis. Multidimensional supernova simulations with approximative neutrino transport - II. Convection and the advective-acoustic cycle in the supernova core. *Astronomy & Astrophysics*, 477(3):931–952, January 2008. Publisher: EDP Sciences.

[33] A. Marek and H. Th. Janka. Delayed Neutrino-Driven Supernova Explosions Aided by the Standing Accretion-Shock Instability. *The Astrophysical Journal*, 694:664–696, March 2009. Publisher: IOP ADS Bibcode: 2009ApJ...694..664M.

[34] J. M. LeBlanc and J. R. Wilson. A Numerical Example of the Collapse of a Rotating Magnetized Star. *The Astrophysical Journal*, 161:541, August 1970. Publisher: IOP ADS Bibcode: 1970ApJ...161..541L.

[35] G. S. Bisnovatyi-Kogan, Iu. P. Popov, and A. A. Samokhin. The Magnetohydrodynamic Rotational Model of Supernova Explosion. *Astrophysics and Space Science*, 41:287–320, June 1976. Publisher: Springer ADS Bibcode: 1976Ap&SS..41..287B.

[36] D. L. Meier, R. I. Epstein, W. D. Arnett, and D. N. Schramm. Magnetohydrodynamic phenomena in collapsing stellar cores. *The Astrophysical Journal*, 204:869–878, March 1976. Publisher: IOP ADS Bibcode: 1976ApJ...204..869M.

[37] E. Mueller and W. Hillebrandt. A magnetohydrodynamical supernova model. *Astronomy and Astrophysics*, 80:147–154, December 1979. Publisher: EDP ADS Bibcode: 1979A&A....80..147M.

[38] H. Alfvén. On the Existence of Electromagnetic-Hydrodynamic Waves. *Arkiv for Matematik, Astronomi och Fysik*, 29B:1–7, January 1943. ADS Bibcode: 1943ArMAF..29B...1A.

[39] Eugene N. Parker. Hydromagnetic Dynamo Models. *The Astrophysical Journal*, 122:293, September 1955. Publisher: IOP ADS Bibcode: 1955ApJ...122..293P.

[40] Henry K. Moffatt. *Magnetic field generation in electrically conducting fluids*. Cambridge monographs on mechanics and applied mathematics. Cambridge Univ. Pr, Cambridge, 1. publ edition, 1978.

[41] J. Craig Wheeler, Insu Yi, Peter Höflich, and Lifan Wang. Asymmetric Supernovae, Pulsars, Magnetars, and Gamma-Ray Bursts. *The Astrophysical Journal*, 537:810–823, July 2000. Publisher: IOP ADS Bibcode: 2000ApJ...537..810W.

[42] Axel Brandenburg and Kandaswamy Subramanian. Astrophysical magnetic fields and nonlinear dynamo theory. *Physics Reports*, 417:1–209, October 2005. Publisher: Elsevier ADS Bibcode: 2005PhR...417....1B.

[43] Jin Matsumoto, Tomoya Takiwaki, and Kei Kotake. Neutrino-driven massive stellar explosions in 3D fostered by magnetic fields via turbulent α-effect, July 2023. arXiv:2307.03400 [astro-ph].

[44] Arkady Tsinober. *An Informal Introduction to Turbulence*, volume 63. 2004.

[45] Shizuka Akiyama, J. Craig Wheeler, David L. Meier, and Itamar Lichtenstadt. The Magnetorotational Instability in Core-Collapse Supernova Explosions. *The Astrophysical Journal*, 584:954–970, February 2003. Publisher: IOP ADS Bibcode: 2003ApJ...584..954A.

[46] Steven A Balbus and John F Hawley. A POWERFUL LOCAL SHEAR INSTABILITY IN WEAKLY MAGNETIZED DISKS. I. LINEAR ANALYSIS. *ApJ. . .*, 376.

[47] Steven A. Balbus and John F. Hawley. Instability, turbulence, and enhanced transport in accretion disks. *Reviews of Modern Physics*, 70:1–53, January 1998. Publisher: APS ADS Bibcode: 1998RvMP...70....1B.

[48] E Endeve, C Y Cardall, R D Budiardja, A Mezzacappa, and J M Blondin. Turbulence and magnetic field amplification from spiral SASI modes in core-collapse supernovae. *Physica Scripta*, 2013(T155):014022, July 2013. Publisher: IOP Publishing.

[49] W. David Arnett. Gravitational collapse and weak interactions. *Canadian Journal of Physics*, 44(11):2553–2594, November 1966. Publisher: NRC Research Press.

[50] M. Rampp and H. T. Janka. Radiation hydrodynamics with neutrinos. Variable Eddington factor method for core-collapse supernova simulations. 396:361–392, December 2002. arXiv: astro-ph/0203101 [astro-ph] tex.adsnote: Provided by the SAO/NASA Astrophysics Data System.

[51] Todd A. Thompson, Adam Burrows, and Philip A. Pinto. Shock breakout in core-collapse supernovae and its neutrino signature. 592(1):434–456, July 2003. arXiv: astro-ph/0211194 [astro-ph] tex.adsnote: Provided by the SAO/NASA Astrophysics Data System.

[52] Matthias Liebendörfer, O. E. Bronson Messer, Anthony Mezzacappa, Stephen W. Bruenn, Christian Y. Cardall, and F. K. Thielemann. A finite difference representation of neutrino radiation hydrodynamics in spherically symmetric general relativistic spacetime. 150(1):263–316, January 2004. arXiv: astro-ph/0207036 [astro-ph] tex.adsnote: Provided by the SAO/NASA Astrophysics Data System.

[53] K. Sumiyoshi, S. Yamada, H. Suzuki, H. Shen, S. Chiba, and H. Toki. Postbounce evolution of core-collapse supernovae: Long-term effects of the equation of state. 629(2):922–932, August 2005. arXiv: astro-ph/0506620 [astro-ph] tex.adsnote: Provided by the SAO/NASA Astrophysics Data System.

[54] S. E. Woosley and Thomas A. Weaver. The Evolution and Explosion of Massive Stars. II. Explosive Hydrodynamics and Nucleosynthesis. *The Astrophysical Journal Supplement Series*, 101:181, November 1995. Publisher: IOP ADS Bibcode: 1995ApJS..101..181W.

[55] Friedrich-Karl Thielemann, Ken'ichi Nomoto, and Masa-Aki Hashimoto. Core-Collapse Supernovae and Their Ejecta. *The Astrophysical Journal*, 460:408, March 1996. Publisher: IOP ADS Bibcode: 1996ApJ...460..408T.

[56] Ken'ichi Nomoto, Nozomu Tominaga, Hideyuki Umeda, Chiaki Kobayashi, and Keiichi Maeda. Nucleosynthesis yields of core-collapse supernovae and hypernovae, and galactic chemical evolution. 777:424–458, October 2006. arXiv: astro-ph/0605725 [astro-ph] tex.adsnote: Provided by the SAO/NASA Astrophysics Data System.

[57] S. E. Woosley and A. Heger. Nucleosynthesis and remnants in massive stars of solar metallicity. *Physics Reports*, 442:269–283, April 2007. ADS Bibcode: 2007PhR...442..269W.

[58] Alexander Heger and S. E. Woosley. Nucleosynthesis and Evolution of Massive Metal-free Stars. *The Astrophysical Journal*, 724:341–373, November 2010. Publisher: IOP ADS Bibcode: 2010ApJ...724..341H.

[59] Alessandro Chieffi and Marco Limongi. Pre-supernova Evolution of Rotating Solar Metallicity Stars in the Mass Range 13-120 M and their Explosive Yields. *The Astrophysical Journal*, 764:21, February 2013. Publisher: IOP ADS Bibcode: 2013ApJ...764...21C.

[60] T. Ertl, H. Th. Janka, S. E. Woosley, T. Sukhbold, and M. Ugliano. A two-parameter criterion for classifying the explodability of massive stars by the neutrino-driven mechanism. 818(2):124, February 2016. arXiv: 1503.07522 [astro-ph.SR] Number: 124 tex.adsnote: Provided by the SAO/NASA Astrophysics Data System.

[61] Tuguldur Sukhbold, T. Ertl, S. E. Woosley, Justin M. Brown, and H.-T. Janka. Core-collapse Supernovae from 9 to 120 Solar Masses Based on Neutrino-powered Explosions. *The Astrophysical Journal*, 821:38, April 2016. Publisher: IOP ADS Bibcode: 2016ApJ...821...38S.

[62] Sean M. Couch, MacKenzie L. Warren, and Evan P. O'Connor. Simulating turbulence-aided neutrino-driven core-collapse supernova explosions in one dimension. 890(2):127, February 2020. arXiv: 1902.01340 [astro-ph.HE] Number: 127 tex.adsnote: Provided by the SAO/NASA Astrophysics Data System.

[63] R. Buras, M. Rampp, H.-Th. Janka, and K. Kifonidis. Improved Models of Stellar Core Collapse and Still No Explosions: What Is Missing? *Physical Review Letters*, 90(24):241101, June 2003. Publisher: American Physical Society.

[64] Adam Burrows, Eli Livne, Luc Dessart, Christian Ott, and Jeremiah Murphy. A New Mechanism for Core-Collapse Supernova Explosions. *The Astrophysical Journal*, 640(2):878–890, April 2006. arXiv:astro-ph/0510687.

[65] S. E. Boggs, F. A. Harrison, H. Miyasaka, B. W. Grefenstette, A. Zoglauer, C. L. Fryer, S. P. Reynolds, D. M. Alexander, H. An, D. Barret, F. E. Christensen, W. W. Craig, K. Forster, P. Giommi, C. J. Hailey, A. Hornstrup, T. Kitaguchi, J. E. Koglin, K. K. Madsen, P. H. Mao, K. Mori, M. Perri, M. J. Pivovaroff, S. Puccetti, V. Rana, D. Stern, N. J. Westergaard, and W. W. Zhang. 44Ti gamma-ray emission lines from SN1987A reveal an asymmetric explosion. *Science*, 348:670–671, May 2015. ADS Bibcode: 2015Sci...348..670B.

[66] B. Müller and H.-Th Janka. Non-Radial Instabilities and Progenitor Asphericities in Core-Collapse Supernovae. *Monthly Notices of the Royal Astronomical Society*, 448(3):2141–2174, April 2015. arXiv:1409.4783 [astro-ph].

[67] Bernhard Müller, Tobias Melson, Alexander Heger, and Hans-Thomas Janka. Supernova simulations from a 3D progenitor model - Impact of perturbations and evolution of explosion properties. *Monthly Notices of the Royal Astronomical Society*, 472:491–513, November 2017. Publisher: OUP ADS Bibcode: 2017MNRAS.472..491M.

[68] Hans-Thomas Janka. Neutrino-driven explosions. In Athem W. Alsabti and Paul Murdin, editors, *Handbook of supernovae*, page 1095. 2017. tex.adsnote: Provided by the SAO/NASA Astrophysics Data System.

[69] Sean M. Couch. The mechanism(s) of core-collapse supernovae. *Philosophical Transactions of the Royal Society A: Mathematical, Physical and Engineering Sciences*, 375(2105):20160271, October 2017. Publisher: Royal Society.

[70] Robert Bollig, Naveen Yadav, Daniel Kresse, Hans-Thomas Janka, Bernhard Müller, and Alexander Heger. Self-consistent 3D supernova models from -7 minutes to +7 s: a 1-bethe explosion of a 19 M progenitor. 915(1):28, July 2021. arXiv: 2010.10506 [astro-ph.HE] Number: 28 tex.adsnote: Provided by the SAO/NASA Astrophysics Data System.

[71] Ko Nakamura, Tomoya Takiwaki, and Kei Kotake. Three-dimensional simulation of a core-collapse supernova for a binary star progenitor of SN 1987A. 514(3):3941–3952, August 2022. arXiv: 2202.06295 [astro-ph.HE] tex.adsnote: Provided by the SAO/NASA Astrophysics Data System.

[72] David Vartanyan, Matthew S B Coleman, and Adam Burrows. The collapse and three-dimensional explosion of three-dimensional massive-star supernova progenitor models. *Monthly Notices of the Royal Astronomical Society*, 510(4):4689–4705, December 2021. Publisher: Oxford University Press (OUP).

[73] Bailey Sykes and Bernhard Müller. Long-time 3D supernova simulations of non-rotating progenitors with magnetic fields, December 2024. Publication Title: arXiv e-prints ADS Bibcode: 2024arXiv241201155S.

[74] Shota Shibagaki, Takami Kuroda, Kei Kotake, Tomoya Takiwaki, and Tobias Fischer. Three-dimensional GRMHD simulations of rapidly rotating stellar core collapse. 531(3):3732–3743, July 2024. arXiv: 2309.05161 [astro-ph.HE] tex.adsnote: Provided by the SAO/NASA Astrophysics Data System.

[75] Tianshu Wang and Adam Burrows. Nucleosynthetic analysis of three-dimensional core-collapse supernova simulations. 962(1):71, February 2024. arXiv: 2311.03446 [astro-ph.HE] Number: 71 tex.adsnote: Provided by the SAO/NASA Astrophysics Data System.

[76] L.D. Landau, E.M. Lifshitz, and L.P. Pitaevskii. *Electrodynamics of Continuous Media: Volume 8*. Course of theoretical physics. Elsevier Science, 1995.

[77] A. S. Schneider, L. F. Roberts, C. D. Ott, and E. O'connor. Equation of state effects in the core collapse of a 20-$M_\odot$ star. *Physical Review C*, 100(5):055802, November 2019. arXiv:1906.02009 [astro-ph].

[78] Somdutta Ghosh, Noah Wolfe, and Carla Fröhlich. PUSHing core-collapse supernovae to explosions in spherical symmetry V: Equation of state dependency of explosion properties, nucleosynthesis yields, and compact remnants. *The Astrophysical Journal*, 929(1):43, April 2022. arXiv:2107.13016 [astro-ph].

[79] Anthony Mezzacappa and Stephen W. Bruenn. A Numerical Method for Solving the Neutrino Boltzmann Equation Coupled to Spherically Symmetric Stellar Core Collapse. *The Astrophysical Journal*, 405:669, March 1993. Publisher: IOP ADS Bibcode: 1993ApJ...405..669M.

[80] S. W. Bruenn. Stellar core collapse - Numerical model and infall epoch. *The Astrophysical Journal Supplement Series*, 58:771–841, August 1985. Publisher: IOP ADS Bibcode: 1985ApJS...58..771B.

[81] A. Mezzacappa and O. E. B. Messer. Neutrino transport in core collapse supernovae. *Journal of Computational and Applied Mathematics*, 109:281–319, September 1999. ADS Bibcode: 1999JCoAM.109..281M.

[82] Kuo-Chuan Pan, Carlos Mattes, Evan P OConnor, Sean M Couch, Albino Perego, and Almudena Arcones. The impact of different neutrino transport methods on multidimensional core-collapse supernova simulations. *Journal of Physics G: Nuclear and Particle Physics*, 46(1):014001, November 2018. Publisher: IOP Publishing.

[83] R. Buras, H.-Th Janka, M. Rampp, and K. Kifonidis. Two-Dimensional Hydrodynamic Core-Collapse Supernova Simulations with Spectral Neutrino Transport II. Models for Different Progenitor Stars. *Astronomy & Astrophysics*, 457(1):281–308, October 2006. arXiv:astro-ph/0512189.

[84] M. Liebendörfer, S. C. Whitehouse, and T. Fischer. THE ISOTROPIC DIFFUSION SOURCE APPROXIMATION FOR SUPERNOVA NEUTRINO TRANSPORT. *The Astrophysical Journal*, 698(2):1174, May 2009. Publisher: The American Astronomical Society.

[85] Adam Burrows, David Radice, David Vartanyan, Hiroki Nagakura, M. Aaron Skinner, and Joshua Dolence. The Overarching Framework of Core-Collapse Supernova Explosions as Revealed by 3D Fornax Simulations. *Monthly Notices of the Royal Astronomical Society*, 491(2):2715–2735, January 2020. arXiv:1909.04152 [astro-ph].

[86] T. A. Weaver, G. B. Zimmerman, and S. E. Woosley. Presupernova evolution of massive stars. *The Astrophysical Journal*, 225:1021–1029, November 1978. Publisher: IOP ADS Bibcode: 1978ApJ...225.1021W.

[87] Bill Paxton, Lars Bildsten, Aaron Dotter, Falk Herwig, Pierre Lesaffre, and Frank Timmes. Modules for Experiments in Stellar Astrophysics (MESA). *The Astrophysical Journal Supplement Series*, 192:3, January 2011. Publisher: IOP ADS Bibcode: 2011ApJS..192....3P.

[88] Louis Henyey, M. S. Vardya, and Peter Bodenheimer. Studies in Stellar Evolution. III. The Calculation of Model Envelopes. *The Astrophysical Journal*, 142:841, October 1965. Publisher: IOP ADS Bibcode: 1965ApJ...142..841H.

[89] R. Farmer, C. E. Fields, I. Petermann, Luc Dessart, M. Cantiello, B. Paxton, and F. X. Timmes. ON VARIATIONS OF PRE-SUPERNOVA MODEL PROPERTIES. *The Astrophysical Journal Supplement Series*, 227(2):22, December 2016. Publisher: The American Astronomical Society.

[90] C. E. Fields. The Three-dimensional Collapse of a Rapidly Rotating 16 M Star. *The Astrophysical Journal Letters*, 924(1):L15, January 2022. Publisher: The American Astronomical Society.

[91] M. Renzo, J. A. Goldberg, A. Grichener, O. Gottlieb, and M. Cantiello. Progenitor Stars Calculated with Small Reaction Networks should not be Used as Initial Conditions for Core Collapse. *Research Notes of the AAS*, 8(6):152, June 2024. Publisher: The American Astronomical Society.

[92] Kevin Ebinger, Sanjana Curtis, Somdutta Ghosh, Carla Fröhlich, Matthias Hempel, Albino Perego, Matthias Liebendörfer, and Friedrich-Karl Thielemann. PUSHing core-collapse supernovae to explosions in spherical symmetry IV: Explodability, remnant properties and nucleosynthesis yields of low metallicity stars. *The Astrophysical Journal*, 888(2):91, January 2020. arXiv:1910.08958 [astro-ph].

[93] Kenzie Myers, Claire Campbell, Kelly Patton, and James P. Kneller. The Effect of Mass Loss and Convective Overshooting on the Pre-Collapse Structure, Composition, and Neutrino Emission of Red Supergiants.

[94] C. de Jager, H. Nieuwenhuijzen, and K. A. van der Hucht. Mass loss rates in the Hertzsprung-Russell diagram. *Astronomy and Astrophysics Supplement Series*, 72:259–289, February 1988. Publisher: EDP ADS Bibcode: 1988A&AS...72..259D.

[95] H. Nieuwenhuijzen and C. de Jager. Parametrization of stellar rates of mass loss as functions of the fundamental stellar parameters M, L, and R. *Astronomy and Astrophysics*, 231:134–136, May 1990. Publisher: EDP ADS Bibcode: 1990A&A...231..134N.

[96] S. Wellstein and N. Langer. Implications of massive close binaries for black hole formation and supernovae, October 1999. ISSN: 0004-6361 Volume: 350 ADS Bibcode: 1999A&A...350..148W.

[97] Jorick S. Vink and A. de Koter. On the metallicity dependence of Wolf-Rayet winds. *Astronomy and Astrophysics*, 442:587–596, November 2005. Publisher: EDP ADS Bibcode: 2005A&A...442..587V.

[98] Jorick S. Vink, A. de Koter, and H. J. G. L. M. Lamers. Mass-loss predictions for O and B stars as a function of metallicity. *Astronomy & Astrophysics*, 369(2):574–588, April 2001. Publisher: EDP Sciences.

[99] Tuguldur Sukhbold and S. E. Woosley. THE COMPACTNESS OF PRESUPERNOVA STELLAR CORES. *The Astrophysical Journal*, 783(1):10, February 2014.

[100] B. Freytag, H.-G. Ludwig, and M. Steffen. Hydrodynamical models of stellar convection. The role of overshoot in DA white dwarfs, A-type stars, and the Sun. *Astronomy and Astrophysics*, 313:497–516, September 1996. Publisher: EDP ADS Bibcode: 1996A&A...313..497F.

[101] Klaus-Peter Schroder, Onno R. Pols, and Peter P. Eggleton. A critical test of stellar evolution and convective core 'overshooting' by means of zeta Aurigae systems. *Monthly Notices of the Royal Astronomical Society*, 285:696–710, March 1997. Publisher: OUP ADS Bibcode: 1997MNRAS.285..696S.

[102] Falk Herwig. The evolution of AGB stars with convective overshoot, July 2000. arXiv:astro-ph/0007139.

[103] D. Temaj, F. R. N. Schneider, E. Laplace, D. Wei, and Ph Podsiadlowski. Convective-core overshooting and the final fate of massive stars. *Astronomy & Astrophysics*, 682:A123, February 2024. Publisher: EDP Sciences.

[104] Evan O'Connor and Christian D. Ott. Black Hole Formation in Failing Core-Collapse Supernovae. *The Astrophysical Journal*, 730:70, April 2011. Publisher: IOP ADS Bibcode: 2011ApJ...730...70O.

[105] K. Ebinger, S. Curtis, C. Fröhlich, M. Hempel, A. Perego, M. Liebendörfer, and F.-K. Thielemann. PUSHing core-collapse supernovae to explosions in spherical symmetry. II. Explodability and remnant properties. 870:1, January 2019. arXiv: 1804.03182 [astro-ph.SR] Number: 1 tex.adsnote: Provided by the SAO/NASA Astrophysics Data System.

[106] S. Curtis, K. Ebinger, C. Fröhlich, M. Hempel, A. Perego, M. Liebendörfer, and F.-K. Thielemann. PUSHing core-collapse supernovae to explosions in spherical symmetry. III. Nucleosynthesis yields. 870:2, January 2019. arXiv: 1805.00498 [astro-ph.SR] Number: 2 tex.adsnote: Provided by the SAO/NASA Astrophysics Data System.

[107] Adam Burrows, Tianshu Wang, and David Vartanyan. Physical Correlations and Predictions Emerging from Modern Core-Collapse Supernova Theory, March 2024. arXiv:2401.06840 [astro-ph].

[108] Matthias Liebendörfer, Stephan Rosswog, and Friedrich-Karl Thielemann. An Adaptive Grid, Implicit Code for Spherically Symmetric, General Relativistic Hydrodynamics in Comoving Coordinates. *The Astrophysical Journal Supplement Series*, 141:229–246, July 2002. Publisher: IOP ADS Bibcode: 2002ApJS..141..229L.

[109] Matthias Liebendörfer. A Simple Parameterization of the Consequences of Deleptonization for Simulations of Stellar Core Collapse. *The Astrophysical Journal*, 633:1042–1051, November 2005. Publisher: IOP ADS Bibcode: 2005ApJ...633.1042L.

[110] A. Perego, R. M. Cabezón, and R. Käppeli. AN ADVANCED LEAKAGE SCHEME FOR NEUTRINO TREATMENT IN ASTROPHYSICAL SIMULATIONS. *The Astrophysical Journal Supplement Series*, 223(2):22, April 2016. Publisher: The American Astronomical Society.

[111] A. Perego, M. Hempel, C. Fröhlich, K. Ebinger, M. Eichler, J. Casanova, M. Liebendoerfer, and F.-K. Thielemann. Pushing 1D CCSNe to explosions: model and SN 1987A. *The Astrophysical Journal*, 806(2):275, June 2015. arXiv:1501.02845 [astro-ph].

[112] I. R. Seitenzahl, F. X. Timmes, and G. Magkotsios. The light curve of SN 1987A revisited: constraining production masses of radioactive nuclides. *The Astrophysical Journal*, 792(1):10, August 2014. arXiv:1408.5986 [astro-ph].

[113] Rubén M. Cabezón, Kuo-Chuan Pan, Matthias Liebendörfer, Takami Kuroda, Kevin Ebinger, Oliver Heinimann, Albino Perego, and Friedrich-Karl Thielemann. Core-collapse supernovae in the hall of mirrors. A three-dimensional code-comparison project. *åp*, 619:A118, November 2018. _eprint: 1806.09184.

[114] R. Käppeli, S. C. Whitehouse, S. Scheidegger, U.-L. Pen, and M. Liebendörfer. FISH: A THREE-DIMENSIONAL PARALLEL MAGNETOHYDRODYNAMICS CODE FOR ASTROPHYSICAL APPLICATIONS. *The Astrophysical Journal Supplement Series*, 195(2):20, August 2011.

[115] James M. Lattimer and F. Douglas Swesty. A generalized equation of state for hot, dense matter. *Nuclear Physics A*, 535(2):331–376, December 1991.

[116] A. Marek, H. Dimmelmeier, H. Th. Janka, E. Müller, and R. Buras. Exploring the relativistic regime with Newtonian hydrodynamics: an improved effective gravitational potential for supernova simulations. *Astronomy and Astrophysics*, 445:273–289, January 2006. Publisher: EDP ADS Bibcode: 2006A&A...445..273M.

[117] Shi Jin and Zhouping Xin. The relaxation schemes for systems of conservation laws in arbitrary space dimensions. *Communications on Pure and Applied Mathematics*, 48(3):235–276, 1995. _eprint: https://onlinelibrary.wiley.com/doi/pdf/10.1002/cpa.3160480303.

[118] A. Burrows and J. M. Lattimer. The birth of neutron stars. 307:178, August 1986. tex.adsnote: Provided by the SAO/NASA Astrophysics Data System.

[119] Robert C. Duncan and Christopher Thompson. Formation of very strongly magnetized neutron stars: Implications for gamma-ray bursts. 392:L9, June 1992. tex.adsnote: Provided by the SAO/NASA Astrophysics Data System.

[120] Ken'ichi Nomoto, Keiichi Maeda, Masaomi Tanaka, and Tomoharu Suzuki. Gamma-ray bursts and magnetar-forming supernovae. 336(1):129–137, November 2011. tex.adsnote: Provided by the SAO/NASA Astrophysics Data System.

[121] Sandro Mereghetti, José A. Pons, and Andrew Melatos. Magnetars: Properties, origin and evolution. 191(1-4):315–338, October 2015. arXiv: 1503.06313 [astro-ph.HE] tex.adsnote: Provided by the SAO/NASA Astrophysics Data System.

[122] L. J. Wang, H. Yu, L. D. Liu, S. Q. Wang, Y. H. Han, D. Xu, Z. G. Dai, Y. L. Qiu, and J. Y. Wei. Evidence for magnetar formation in broad-lined type ic supernovae 1998bw and 2002ap. 837(2):128, March 2017. arXiv: 1610.09061 [astro-ph.HE] Number: 128 tex.adsnote: Provided by the SAO/NASA Astrophysics Data System.

[123] Victoria M. Kaspi and Andrei M. Beloborodov. Magnetars. *Annual Review of Astronomy and Astrophysics*, 55(Volume 55, 2017):261–301, August 2017. Publisher: Annual Reviews.

[124] D. C. Backer, S. R. Kulkarni, C. Heiles, M. M. Davis, and W. M. Goss. A millisecond pulsar. *Nature*, 300:615–618, December 1982. ADS Bibcode: 1982Natur.300..615B.

[125] J. S. Bloom, S. R. Kulkarni, S. G. Djorgovski, A. C. Eichelberger, P. Côté, J. P. Blakeslee, S. C. Odewahn, F. A. Harrison, D. A. Frail, A. V. Filippenko, D. C. Leonard, A. G. Riess, H. Spinrad, D. Stern, A. Bunker, A. Dey, B. Grossan, S. Perlmutter, R. A. Knop, I. M. Hook, and M. Feroci. The unusual afterglow of the -ray burst of 26 March 1998 as evidence for a supernova connection. 401(6752):453–456, September 1999. arXiv: astro-ph/9905301 [astro-ph] tex.adsnote: Provided by the SAO/NASA Astrophysics Data System.

[126] S. E. Woosley and J. S. Bloom. The Supernova Gamma-Ray Burst Connection. *Annual Review of Astronomy and Astrophysics*, 44:507–556, September 2006. ADS Bibcode: 2006ARA&A..44..507W.

[127] Quintin A. Mabanta and Jeremiah W. Murphy. How Turbulence Enables Core-collapse Supernova Explosions. *The Astrophysical Journal*, 856(1):22, March 2018.

[128] David Radice, Ernazar Abdikamalov, Christian D. Ott, Philipp Moesta, Sean M. Couch, and Luke F. Roberts. Turbulence in Core-Collapse Supernovae. *Journal of Physics G: Nuclear and Particle Physics*, 45(5):053003, May 2018. arXiv:1710.01282 [astro-ph].

[129] M. Renzo, C. D. Ott, S. N. Shore, and S. E. de Mink. Systematic survey of the effects of wind mass loss algorithms on the evolution of single massive stars. *Astronomy and Astrophysics*, 603:A118, July 2017. Publisher: EDP ADS Bibcode: 2017A&A...603A.118R.

CHAPTER

2

TURBULENCE IN CORE-COLLAPSE SUPERNOVAE

David Calvert, Michael Redle, Bibek Gautam, Charles J. Stapleford, Carla Fröhlich, James P. Kneller, Matthias Liebendörfer

The following chapter was accepted The Astrophysical Journal DOI: 10.3847/1538-4357/ae1475

2.1 Abstract

It is understood in a general sense that turbulent fluid motion below the shock front in a core-collapse supernova stiffens the effective equation of state of the fluid and aids in the revival of the explosion. However, when one wishes to be precise and quantify the amount

of turbulence in a supernova simulation, one immediately encounters the problem that turbulence is difficult to define and measure. Using the 3D magnetohydrodynamic code ELEPHANT, we study how different definitions of turbulence change one's conclusions about the amount of turbulence in a supernova and the extent to which it helps the explosion. We find that, while all the definitions of turbulence we use lead to a qualitatively similar growth pattern over time of the turbulent kinetic energy in the gain region, the total amount of turbulent kinetic energy, and especially the ratios of turbulent to total kinetic energy, distinguish them. Some of the definitions appear to indicate turbulence is a necessary contributor to the explosion, and others indicate it is not. The different definitions also produce turbulence maps with different correlations with maps of the enstrophy, a quantity widely regarded as also indicating the presence of turbulence. We also compute the turbulent adiabatic index and observe that in regions of low enstrophy, this quantity is sensitive to the definition used. As a consequence, the effective adiabatic index depends upon the method used to measure the turbulence and thus alter one's conclusions regarding the impact of turbulence within the supernova.

2.2 Introduction

Core-collapse supernovae (CCSNe) are the explosive deaths of stars with initial masses greater than $\sim 8-10$ $M_\odot$ [1, 2, 3]. In addition to the spectacular fireworks, nuclear reactions in the ejected material will contaminate the interstellar medium of the host galaxy with freshly synthesized elements [4, 5, 6]. Stellar-mass black holes, neutron stars, pulsars, and magnetars are born out of these explosions [7, 8, 9, 10, 11, 12, 13], and observations indicate that Long Gamma-Ray Bursts are also associated with CCSNe [14, 15]. Despite the importance of CCSNe in understanding many aspects of the universe, the mechanism that drives CCSN explosions is not yet fully understood. At the present time, the prevailing theory for CCSNe is based upon the 'delayed neutrino-heating mechanism' [16, 17, 18]. In this paradigm, an initial collapse of the stellar core forms a proto-neutron star (PNS) and launches a shock-wave into the outer layers. The shock stalls 100-200 km above the PNS as its energy is consumed dissociating infalling nuclei and is then revived through energy deposition due to neutrino scattering / absorption in the material beneath the shock. However simulations of supernovae in spherical symmetry fail to explode via the delayed neutrino-heating mechanism [19, 20, 21, 22, 23]. This poses a limitation for many open questions that rely on successful explosions, e.g. predicting supernova nucleosynthe-

sis yields, unveiling the progenitor-remnant connection, and many more. One approach around this limitation is the use of so-called effective models. These are simulations in spherical symmetry where one aspect of multi-dimensional simulations is parametrized and the parameters are calibrated against observations. For example, P-HOTB [24] uses a simple approximation of increased neutrino luminosities from the proto-neutron star. The PUSH method [25, 13] instead parametrizes the effectively enhanced neutrino energy-deposition in the gain layer that is seen in multi-dimensional simulations. And finally, STIR [26] parametrizes the strength of turbulence that is observed in multi-dimensional simulations in a mixing-length type parametrization. Welcomely, modern *multi-dimensional* simulations have achieved unaided explosions [27, 28, 29, 30, 31, 32, 33, 34, 35, 36], demonstrating the viability of the delayed neutrino-heating mechanism and emphasizing the importance of multi-dimensional effects in aiding explosions. One of these multi-dimensional effects is fluid turbulence.

As a result of the violent fluid motion in the gain region of the supernova, the low viscosity, and the significant shear stress, the fluid (or some fraction of it) can become turbulent due to instabilities. High-resolution studies of turbulence in 3D simulations of CCSNe [37, 38, 39, 40, 41, 42, 43, 44, 45] are able to see the inertial range of the turbulence [44] and the 'turbulence bottleneck' – the accumulation of power in the inertial scales of the turbulence [46, 47, 48, 42]. Turbulence has the potential to serve as an aid to the shock revival by stiffening the effective adiabatic index of the fluid. However this conclusion about the effect of turbulence is inherently dependent on how the amount of turbulence present is measured, which is a notoriously difficult problem [49].

The purpose of this paper is to investigate how different measures of turbulence in a CCSNe alter the conclusions one draws about its effect upon the explosion. To explore this question, we have undertaken four simulations of core-collapse supernovae spanning initial masses from $15M_\odot$ to $27M_\odot$. The simulations were performed in three spatial dimensions using the ELEPHANT code [50, 51, 52]. This code is well suited to this study because of its good spatial resolution below the shock. We leverage this high resolution in the gain region to explore three different methods to compute turbulence. Using a variety of post-processing tests, we show that the three methods produce results that are not consistent with one another, in turn presenting the strengths and potential drawbacks of each method.

Our paper is organized as follows. The code we use, the progenitors, and general results of the simulations are described in Section 2.3. We next discuss in Section 2.4 the different methods we will use for measuring the turbulence, and then apply the measures to the

simulations in Section 2.5. Finally, in Section 2.6 we examine how turbulence alters the effective adiabatic index of the fluid and how this index evolves with time in the simulations. We summarize and present our conclusions in Section 2.7.

2.3 The Simulations

2.3.1 The ELEPHANT Code

The ELEPHANT code solves the ideal hydrodynamics equations in a modified Newtonian gravitational potential together with the Isotropic Diffusion Source Approximation (IDSA) for the neutrino transport scheme. The code uses operator splitting between the solutions of the hydrodynamic equations and the neutrino transport equations. In the hydrodynamics module, which has roots in the FISH code described in [51], the following conservation laws coupled with gravitational source terms are numerically solved in three spatial dimensions:

$$\frac{\partial \rho}{\partial t} + \boldsymbol{\nabla}\cdot(\rho\,\boldsymbol{v}) = 0, \tag{2.1}$$

$$\frac{\partial}{\partial t}(\rho\,v_i) + \frac{\partial}{\partial x_j}(\rho\,v_i\,v_j + P_{\text{thermal}}\,\delta_{ij}) = -\rho\,\tfrac{\partial \phi}{\partial x_i}, \tag{2.2}$$

$$\frac{\partial E}{\partial t} + \boldsymbol{\nabla}\cdot[(E + P_{\text{thermal}})\,\boldsymbol{v}] = -\rho\,\boldsymbol{v}\cdot\boldsymbol{\nabla}\phi, \tag{2.3}$$

$$\frac{\partial}{\partial t}(\rho\,Y_e) + \boldsymbol{\nabla}\cdot(\rho\,Y_e\,\boldsymbol{v}) = 0, \tag{2.4}$$

$$\frac{\partial}{\partial t}(\rho\,Y_\nu^t) + \boldsymbol{\nabla}\cdot(\rho\,Y_\nu^t\,\boldsymbol{v}) = 0, \tag{2.5}$$

$$\frac{\partial}{\partial t}\left[\left(\rho\,Z_\nu^t\right)^{\frac{3}{4}}\right] + \boldsymbol{\nabla}\cdot\left[(\rho\,Z_\nu^t)^{\frac{3}{4}}\boldsymbol{v}\right] = 0, \tag{2.6}$$

$$\boldsymbol{\nabla}^2\phi = 4\,\pi\,G\,\rho, \tag{2.7}$$

where the calculated unknowns with respect to space x_i and time t are the baryonic mass density ρ, velocity v_i, electron fraction Y_e, and the gravitational potential ϕ. While ELEPHANT is able to include magnetic fields, the magnetic field terms have been set to zero for this study. The temperature T is not explicitly seen in these equations, it is represented in the specific internal energy $e = e(\rho, T, Y_e)$, and the total energy $E = \rho\,e + \rho\,v^2/2$. As usual, G is the gravitational constant. We compute the thermal pressure $P_{\text{thermal}} = P_{\text{thermal}}(\rho, T, Y_e)$ using the LS220 equation of state (EOS) with an incompressibility parameter $K = 220$ MeV

[53]. Equations (2.5)–(2.6) advect the trapped neutrino fractions, Y_ν^t, and a multiple of the neutrino entropies, $\left(\rho Z_\nu^t\right)^{3/4}$ (where Z_ν is the mean neutrino specific energy) from the neutrino transport. The gravitational potential is modified following [54] to include general relativistic corrections to the Newtonian potential.

The hydrodynamics equations (2.1)–(2.7) are solved using the second-order relaxation scheme of [55]. To enforce that the scheme is total variation diminishing (a nonlinear constraint to ensure stability), ELEPHANT implements the minmod limiter in supersonic flow regimes and the van Leer limiter in subsonic regimes [51]. For the time integration, a second-order predictor-corrector method is used.

For the neutrino transport, the ELEPHANT code uses the Isotropic Diffusion Source Approximation (IDSA, [50]). The underlying idea of IDSA is that the neutrinos are separated into a trapped neutrino distribution function, f_ν^t, and a free-streaming neutrino distribution function, f_ν^s. These two components are then evolved separately. The trapped neutrino distribution functions are constructed from Y_ν^t and Z_ν^t assuming a thermal spectrum. Then, the diffusion equation, given as,

$$\frac{1}{c}\frac{\partial f_\nu^t}{\partial t} = j_\nu - (j_\nu + \chi_\nu) f_\nu^t - \Sigma_\nu, \tag{2.8}$$

where

$$\Sigma_\nu = \min\left\{\max\left[\alpha_\nu + \frac{1}{2}(j_\nu + \chi_\nu)\int f_o^s \, d\mu, \, 0\right], j_\nu\right\}, \tag{2.9}$$

with

$$\alpha_\nu = \boldsymbol{\nabla}\cdot\left(\frac{-1}{3(j_\nu + \chi_\nu + \phi_\nu)}\boldsymbol{\nabla} f_\nu^t\right), \tag{2.10}$$

is solved in three dimensions. In these equations, f_o^s denotes the use of the streaming neutrinos from the previous time step, j_ν is the spectral neutrino emissivity, χ_ν is the neutrino absorptivity, and ϕ_ν includes isoenergetic scattering in the mean free path (see [56]). The non-local value α_ν, a descriptor of the evolution of trapped neutrinos, is computed by explicit finite differencing, with all other unknowns solved locally using an implicit Euler time step in which the solution is found using the Newton-Raphson iterative solver. The numerical solution of equation (2.8) sets the net interaction rates between the matter and neutrino radiation and updates the electron fraction Y_e and the specific internal energy e so that they are consistent. The rates j_ν, χ_ν, and ϕ_ν are then used to update the trapped neutrino fraction Y_ν^t and mean energy Z_ν^t seen in equations (2.5) and (2.6). This iterative method is easily parallelizable for IDSA because the only non-local value α_ν is computed

explicitly, thus implying that zones do not need to communicate with each other within the iterative solve.

ELEPHANT uses a unique combination of 3D and 1D grids as its computational domain. The innermost computational domain consists of a 3D Cartesian cuboid, and the 1D domain extends from the center of the supernova out well beyond the 3D domain and so well into the outer layers of the progenitor star. The inner 3D grid uses a uniform fixed grid spacing, while the larger, spherically symmetric 1D domain surrounding the 3D cuboid is evolved on an adaptive grid using the Agile-IDSA solver [50]. More details of how the hydro and neutrino transport equations are solved on the 3D uniform Cartesian mesh, together with test cases, can be found in [51]. The spherically symmetric solution of the hydro and neutrino transport equations on the 1D grid is used primarily for the properties of the material falling through the boundary of the 3D mesh, but since it extends into the inner part of the Cartesian grid, it also provides a second solution of the equations that is especially useful within the PNS where it serves as a check of the entropy evolution. In addition, the combination of the two grids with the 1D solution extending well beyond the 3D, gives ELEPHANT the ability to enlarge the 3D Cartesian cuboid if necessary. With this setup of the computational domain, the ELEPHANT code has high 3D spatial fidelity in the region below the shock without the burden of a large number of grid zones where the solution is spherically symmetric. Hence, it is ideally suited for the proposed study of the post bounce phase especially for the growth of the turbulence in the shocked material. For each simulation in this study we adopt a uniform fidelity of 1 km throughout the 3D volume; initially, the 3D volume encompasses the innermost 600 km of the star (i.e., along each axis the 3D Cartesian coordinate ranges from -300 km to +300 km). A direct comparison of the resolution of the 3D volume with the resolution of the grids adopted elsewhere in the literature for studies of turbulence in supernovae, is challenging because of the wide variety of methods used: see, for example, the grids used in the studies by [57] and [45]. The most similar studies to this work are by [58, 40] which were also Cartesian and where the highest resolution simulation used a cell spacing of 1.17 km.

2.3.2 General Properties of the Simulations

For this study, we consider four solar-metallicity progenitor stars of 15, 20, 23 and 27 $M_{\odot}$ zero-age main sequence (ZAMS) mass [59]. Throughout this paper we shall refer to each simulation by reference to the progenitor model using the code 'sXX' where XX is the ZAMS mass in units of the solar mass. Two of these progenitors (s15 and s20) have been exten-

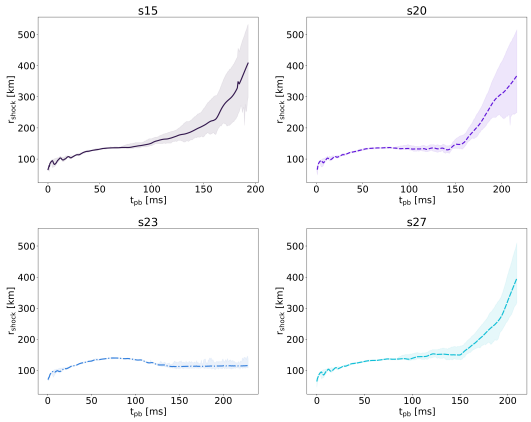

Figure 2.1: Average shock radii (lines), together with the minimum and maximum shock radii (shaded bands) as a function of the post-bounce time for all four simulations. The simulations end when the shock radius reaches the boundary of the largest (500 km) 3D domain. Note that the s23 simulation does not undergo a successful shock revival during the simulation time.

sively used in the literature. For the s20 model, explosions [60, 61] and non-explosions [62, 63] were obtained in 2D simulations. Similarly, successful and failed explosions are also reported from 3D simulations of s20, depending on the exact simulation setup and on the physics included [e.g. 64, 65, 66, 30]. The s20 model seems to be close to the threshold between successful and failed explosions, warranting further investigations. For the s15 model, the picture a slightly more consistent in the sense that most simulations find successful explosion, albeit as late as $\sim 400-500$ ms post-bounce (however, see e.g. [67] for a failed explosion in 2D). The s23 model was chosen as it is a model that often fails to explode in effective 1D simulations using the STIR or PUSH method. In a recent 3D simulation of a different 23 $M_\odot$ model, the shock evolution follows other non-exploding models for the first ~ 300 ms post-bounce, then hovers around 170 km for another ~ 300 ms, and finally expands to 500 km only at 700 ms after bounce [68]. Finally, the s27 model has been used in 3D simulations where it exhibited a similar shock evolution as the s20, with shock run-away occurring at ~ 200 ms [65]. For an earlier version of the s27 (from [1]), no shock revival was found in 3D simulations [69, 70].

As stated previously, the simultaneously computed spherically symmetric solution on the 1D grid allows ELEPHANT to expand the 3D domain if necessary. We used this feature of the code to expand the 3D domain when the maximum shock radius in the 3D solution approaches the edge of the 3D computational domain. At this point we expand the 3D

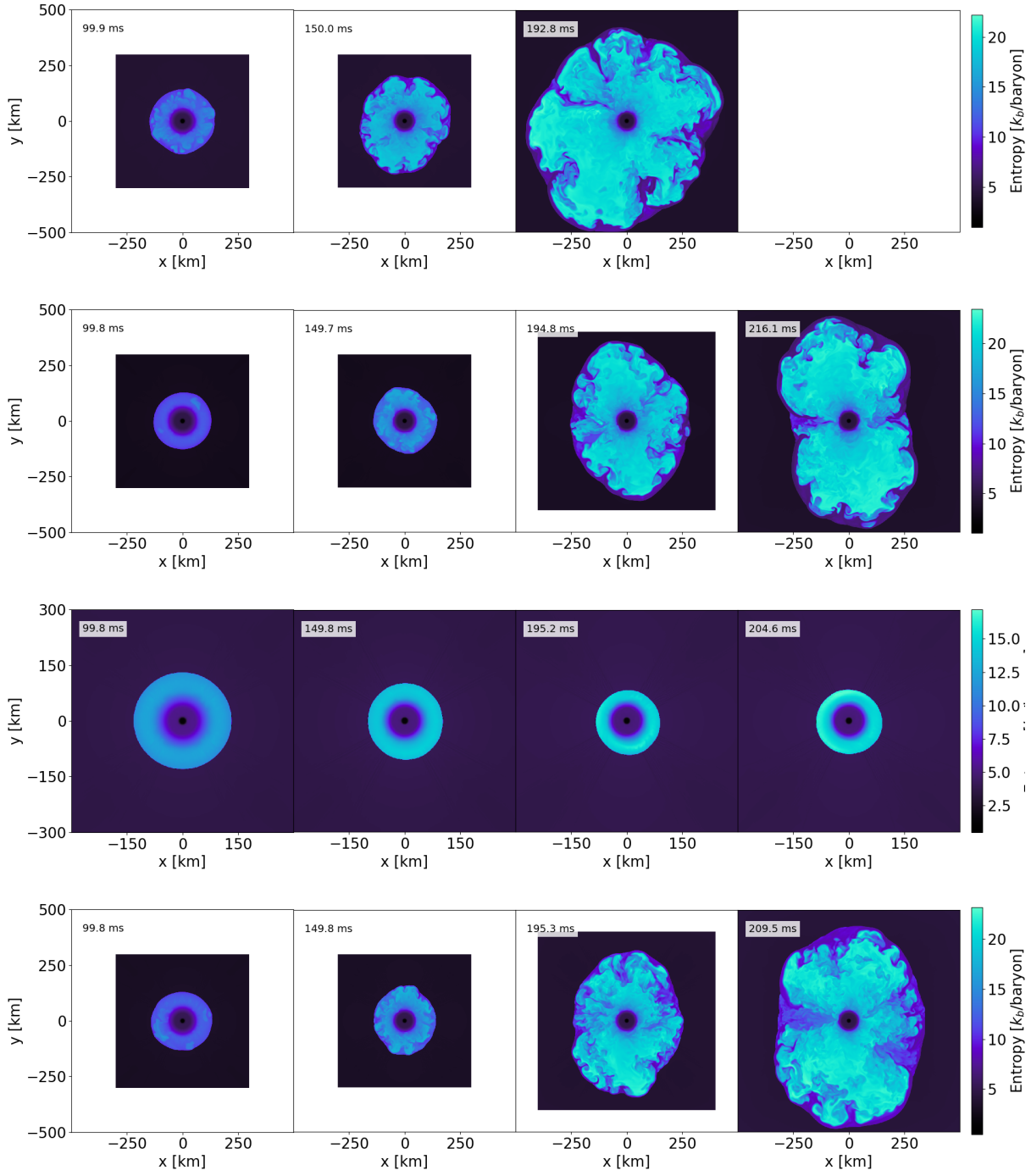

Figure 2.2: Entropy maps in the xy-plane for the s15 (top), s20 (second row), s23 (third row), and s27 (bottom row) simulations at $\sim$ 100 ms (first column), $\sim$ 150 ms (second column), $\sim$ 195 ms (third column) post bounce, and at the final simulation time (last column). Note the smaller spatial scale and entropy scale for s23.

domain by adding 100 grid zones in both the negative and positive directions along each coordinate axis. The new zones have the same, 1 km, resolution and the 1D solution is used to fill the fluid and neutrino variables of the new zones. We undertook this 3D domain expansion twice during the s15, s20 and s27 simulations and stopped when any Cartesian coordinate of the maximum shock position reached 500 km. This technique of expanding the 3D volume as the shock approaches the edge was also used by [58].

In Figure 2.1 we show the average shock radius (various line styles) for each simulation along with its minimum and maximum position (shaded bands). During the first $t_{\rm pb} \approx 70$ ms, the shock evolves similarly with post-bounce time $t_{\rm pb}$ for all simulations. In each simulation, the shock forms and propagates outward to 140 km at which point it stalls. After $t_{\rm pb} \gtrsim 70$ ms, differences in the shock evolution between the four simulations start to emerge. The s15 simulation has the earliest shock revival (at ~ 80 ms post bounce), only ~ 10 ms after the shock front starts to deform which can be seen in the figure as the increasing spread between the minimum and maximum shock radius. The s20 and s27 simulations behave similarly, albeit with shock revival and the emergence of asphericity occurring later than in the s15 simulation. Moreover, there is a longer delay of ~ 60 ms between when the shock starts to deviate from spherical symmetry and the clear shock expansion for the s20 and s27 simulations. At the end of our s15, s20 and s27 simulations, the shock appears to be irrevocably expanding outwards. Following the common definition for successful explosions found in the literature (when the shock reaches 500 km), these models could be called successfully exploding, even though it is too early for the total energy in the gain region and above to have reached positive energies by $t_{\rm pb} \sim 200$ ms. Finally, the s23 simulation does not show shock revival during the simulation time (~ 205 ms post bounce). Instead, the shock radius hovers around 100 km until the end of the simulation. This is qualitatively similar to the initial shock evolution of a different 23 $M_\odot$ model (from [71]) which follows the non-exploding models for the first 300 ms, then continues to hover around 150 km, and only starts expanding around 600 ms after bounce.

Figure 2.2 presents snapshots of the fluid entropy per baryon for all four simulations. In each snapshot, we observe low-entropy material ahead of the shock, and also in the center of the computational domain, where the proto-neutron star is forming. The higher-entropy region in-between contains the gain layer, which we define as the region interior to the shock where the entropy exceeds $5\,k_B$/baryon, the density is less than $\rho < 10^{10}$ g/cm^3, and the energy gained from electron neutrino and antineutrino absorption exceeds the energy lost by neutrino emission. We will focus our attention on this gain region in the next sections and going forward, we have truncated our time-series data to begin when

we have qualitatively determined a meaningful gain region has formed (at $t_{\rm pb} \approx 61$ ms).

In Figure 2.2 we demonstrate the evolution of the supernovae using selected snapshots from each simulation. The first three columns correspond to $t_{\rm pb}$ =100, 150, 195 ms post bounce and the last column represents the final simulation time for each simulation. In the case of s15, the shock reached 500 km before 195 ms post bounce and thus the final panel is left blank. In the s15, s20 and s27 simulations, the spherical symmetry of the simulation is visibly broken when neutrino heating initiates convection in the gain region. By 150 ms post bounce, the shocks in these three simulations are noticeably aspherical. By ∼195 ms post bounce, low-entropy downflows through the gain layer amid large convective plumes are clearly visible.

For the s23 simulation the spherical symmetry remains largely preserved for the entire duration of the simulation. Although some of the material in the gain region reaches comparable specific total energies as in the other three simulations, the energy gained by neutrino absorption is clearly not enough to revive the shock in this case. The reader may notice that the center of the quasi-circular shock front is slightly displaced from the origin of the coordinates. Indeed, from animations of the entropy as a function of post-bounce time, we observed an oscillatory motion of the shock starting at $t_{\rm pb} \sim 150$ ms characteristic of a SASI [72, 73]. This timescale is similar to the timescale of a spiral SASI in a magnetized 24 $M_\odot$ model by [74].

We can be more quantitative about the time at which convection begins in each simulation by computing the fraction of kinetic energy within the gain layer which is in the non-radial directions:

$$E_{\rm transverse} / E_{\rm kin} = \int_{V_{\rm gain}} \rho \left(v_\theta^2 + v_\phi^2 \right) dV \Big/ \int_{V_{\rm gain}} \rho \left(v_r^2 + v_\theta^2 + v_\phi^2 \right) dV, \tag{2.11}$$

where v_r, v_θ, v_ϕ are the radial, polar and azimuthal components of the velocity and $V_{\rm gain}$ is the volume of the gain region, defined above. This ratio is shown in Figure 2.3. For the s15, s20, and s27 simulations, the fraction of the kinetic energy in the transverse (i.e., non-radial) directions rises very rapidly between $t_{\rm pb} \sim 60$ ms and $t_{\rm pb} \sim 100$ ms as the shock stalls. The rise is earlier in the s15 simulation than in the s20 and s27 simulation, but by $t_{\rm pb} \sim 100$ ms they all reach the level of 30-40% with a slow growth of the ratio thereafter. Interestingly, the figure shows that the fraction of kinetic energy in the transverse directions begins to grow in the s23 simulation starting at $t_{\rm pb} \sim 120$ ms. Even though the s23 simulation is not exploding — the shock is not seen to be advancing in Figure 2.1 and we

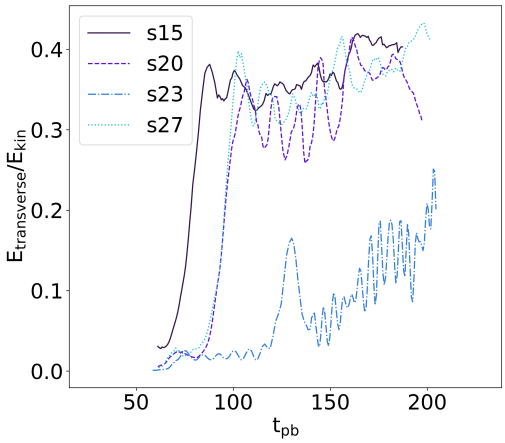

Figure 2.3: Ratio of the transverse energy to the total kinetic energy in the gain region as a function of the post-bounce time for the s15 (solid), s20 (dashed), s23 (dot-dashed), and s27 (dotted) simulations.

shall shortly show more evidence that further indicates this conclusion — the high densities and large angular motions present in this simulation due to the SASI means the ratio of the transverse and total kinetic energy in the gain region becomes comparable to the same ratio of energies in the successful explosions. While it does not reach the $\sim 40\%$ level seen in the other three simulations, it is only smaller by a factor of ~ 2 at $t_{pb} = 200$ ms.

We want to turn our analysis to the mechanism by which the shock is revived in our simulations. In a neutrino-driven explosion, the shock is revived due to neutrino-heated material in the gain region being brought up to the shock by convection and buoyancy. Shock revival occurs when the material within the gain region has sufficient time to absorb enough of this heating energy to overcome gravity. Thus the revival time can be estimated by comparing the heating timescale to the advection timescale through the gain region. For the advection timescale we adopt the definition used in [75]:

$$\tau^*_{\text{adv}}(t_1) = t_2(M) - t_1(M), \tag{2.12}$$

where $t_2(M)$ is the time at which a mass M is enclosed by the shock and $t_1(M)$ is the time at which that same mass falls beneath our gain region. The neutrino heating timescale is defined as the amount of time that material in the gain region would need to be exposed

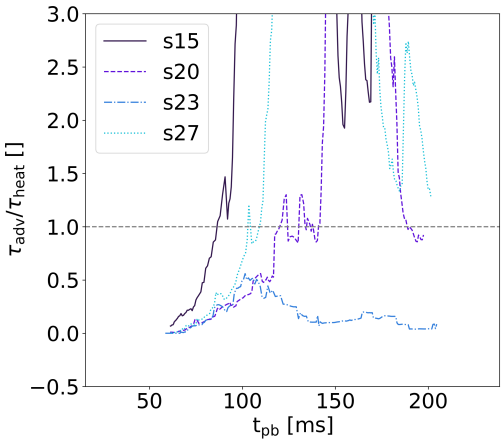

Figure 2.4: The ratio of advection timescale to heating timescale as a function of the post-bounce time for all four simulations. The gray dotted line marks where the ratio equals unity.

to the current neutrino heating rate to become gravitationally unbound, i.e.,

$$\tau_{\text{heat}} = \frac{|E_{\text{gain}}|}{\dot{Q}_{\text{heat}}}, \tag{2.13}$$

where $E_{\text{gain}} = E_{\text{kin}} + E_{\text{int}} + E_{\text{grav}}$ is the total energy in the gain region, E_{int} and E_{grav} are, respectively, the total internal and total gravitational energy of the fluid in the gain region, and $\dot{Q}_{\text{heat}}$ is the total neutrino heating rate in the gain region. It is found that when the ratio of the advection timescale to the heating timescale, $\tau_{\text{adv}}/\tau_{\text{heat}}$, exceeds unity, the stalled shock is considered revived and, on average, the shock begins to move outwards due to the increased energy of the enclosed material [76, 77, 78, 79]. Note that this does not guarantee an explosion, but simply is an indicator of an outward moving shock. Figure 2.4 shows the ratio of these two timescales for all four simulations, with the line for a ratio of 1 highlighted in gray From Figure 2.4, we see that this ratio exceeds unity in the s15, s20 and s27 simulations at times which closely match the shock revival times seen in Figure 2.1, supporting a neutrino-driven explosion mechanism for these simulations. For the s23 simulation, the ratio never exceeds unity, which is consistent with the lack of a shock revival in this simulation.

Another diagnostic invoked to investigate the phase leading up to shock revival consists of examining the mass inflow rate through the shock front ($\dot{M}_{\text{shock}}$) and the mass inflow rate onto the PNS ($\dot{M}_{\text{PNS}}$). The comparison of these rates are shown in Figure 2.5. Ini-

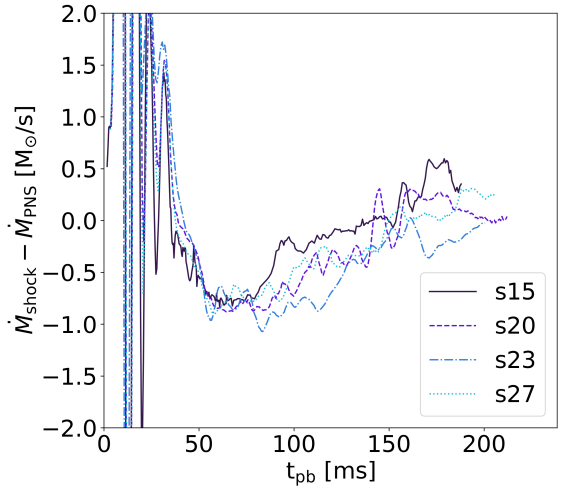

Figure 2.5: Difference between the mass accretion rate through the shock front ($\dot{M}_{\rm shock}$) and the mass accretion rate onto the PNS ($\dot{M}_{\rm PNS}$) as a function of the post-bounce time for all four simulations. The data is smoothed over a 5 ms window.

tially, $\dot{M}_{\rm shock}$ and $\dot{M}_{\rm PNS}$ are firmly related. In the first few tenths of milliseconds after bounce, $\dot{M}_{\rm shock}$ decreases more rapidly than $\dot{M}_{\rm PNS}$ and the initial shock turns into a standing accretion shock. Once non-radial fluid motion starts to develop around 60–100 ms after bounce, we observe a drop in $\dot{M}_{\rm PNS}$ (while $\dot{M}_{\rm shock}$ continues to decrease smoothly), resulting in the increase of $\dot{M}_{\rm shock} - \dot{M}_{\rm PNS}$. Once the stalled shock starts expanding again, $\dot{M}_{\rm PNS}$ is smaller than $\dot{M}_{\rm shock}$ and $\dot{M}_{\rm shock} - \dot{M}_{\rm PNS}$ reaches zero or slightly positive values. While the difference $\dot{M}_{\rm shock} - \dot{M}_{\rm PNS}$ is similar for all four simulations, the individual amount of accretion through the shock ($\dot{M}_{\rm shock} - \dot{M}$) and onto the PNS ($\dot{M}_{\rm PNS}$) are higher for the s23 model (no shock expansion) than for any of the other models (with shock expansion), by up to a factor of 2 after $\sim$ 90 ms post bounce

In summary, the results from our simulations shown in Figures 2.1 through 2.5 are broadly consistent with other 3D simulations [80, 81, 82, 83, 84, 63, 66, 85, 68, 35, 86, 87].

2.4 Measuring the turbulence

The turbulence in the gain region is conjectured to be an important ingredient in revival of the shock [43]. The prevailing theory being that the average adiabatic index of the turbulence (which we shall define later in Section 2.6) is larger than in a non-turbulent fluid

[88, 43, 89, 90, 91]. To investigate how the turbulence affects the simulations, it is first necessary to define a measure of the amount of turbulence. This is not a straight-forward task; as discussed in [92], there is no one, perfect measure of turbulence.

In some previous studies of turbulence in supernovae [93, 39, 94, 81] the reader will find the turbulent kinetic energy $E_{\rm turb}$ defined to be equivalent to the non-radial kinetic energy, i.e.,

$$E_{\rm turb} \equiv E_{\rm transverse} = \int_{V_{\rm gain}} \frac{\rho}{2} \left(v_\theta^2 + v_\phi^2 \right) dV. \tag{2.14}$$

This definition of the turbulent kinetic energy obviously does not include any contribution from flow in the radial direction which could be turbulent, but it does include a contribution from the non-radial flow which may not be turbulent; e.g., flows that are simply the lateral motion of the fluid at the top of convective plumes and/or any global rotational motion of the fluid due to a SASI. We shall not consider this definition further in this paper.

Another commonly encountered approach for measuring the amount of energy stored in turbulence is to invoke a Reynolds decomposition of the velocity field and then define the turbulent kinetic energy as

$$E_{\rm turb} = \int_{V_{\rm gain}} \frac{\rho}{2} \left| \boldsymbol{v} - \langle \boldsymbol{v} \rangle \right|^2 dV, \tag{2.15}$$

where $\langle \boldsymbol{v} \rangle$ is an expectation value for the velocity. Note that $\langle \boldsymbol{v} \rangle$ can be a function of position and time. Defining the expectation value is not straight-forward; in statistically steady-state flows, the expectation value for the velocity $\langle \boldsymbol{v} \rangle$ is the time-averaged velocity of the fluid at a given location. While it is certainly possible to time-average fluid properties in a supernova simulation, it is conceptually difficult to accept them as useful because the system is not close to a statistical steady-state (even during the period when the shock has stalled). Instead, authors usually substitute a spatial average of the the fluid velocity in place of a time average at a given location. However, spatial averages are just as conceptually fraught in situations where the fluid may have organized large-scale motions, i.e., on scales close to the dimensions of the fluid volume. In the case of a supernova, these large scale motions are due to convection and/or SASI. Since there is no clear way to define $\langle \boldsymbol{v} \rangle$, we have considered two different spatial average options.

The first method we adopt we denote as the Spherical Spatial Average (SSA) and is based on [43]. The SSA algorithm for computing $\langle \boldsymbol{v} \rangle$ is based on the observation that the general flow of the fluid in the gain region is toward the PNS. Thus, we define $\langle \boldsymbol{v} \rangle$ as $\langle v_r \rangle \hat{\mathbf{r}}$

where $\langle v_r \rangle$ is the average radial velocity for all zones at a given radius r. Since we do not use a spherical coordinate grid in our simulations, we implement this definition by finding all the Cartesian grid cells with a cell-center radius in a given 1 km thick shell. Thus, we define

$$\langle v_r \rangle = \frac{1}{M_{\text{shell}}} \int_{V_{\text{shell}}} \rho \, v_r \, dV, \tag{2.16}$$

with

$$M_{\text{shell}} = \int_{V_{\text{shell}}} \rho \, dV. \tag{2.17}$$

Note that when the shock becomes aspherical, only grid cells in the gain region are used to compute the average radial velocity, thus the shell no longer forms a complete spherical surface.

The second method we consider we call the Local Spatial Average (LSA) method. In this method, we define the expectation value of the velocity, $\langle \boldsymbol{v} \rangle$, for a particular grid cell as being the mass-weighted average of the velocity in a cube surrounding the cell:

$$\langle \boldsymbol{v} \rangle = \frac{1}{M_{\text{cube}}} \int_{V_{\text{cube}}} \rho \, \boldsymbol{v} \, dV, \tag{2.18}$$

where

$$M_{\text{cube}} = \int_{V_{\text{cube}}} \rho \, dV \tag{2.19}$$

and V_{cube} is a cubic volume of side length L centered on the grid cell under consideration. Note that when we perform the integral, the volume V_{cube} only includes those cells which are found to be in the gain region, implying that the volume is not always a complete cube. The size of the averaging volume must be chosen appropriately. In the limit where the size of the averaging volume becomes small, $\langle \boldsymbol{v} \rangle$ approaches the velocity of the grid cell under consideration, in which case the deviation of the velocity from the expectation value approaches zero, i.e., $|\boldsymbol{v} - \langle \boldsymbol{v} \rangle| \to 0$ and therefore the turbulent kinetic energy also approaches zero in this limit. We must select a suitable length scale for which the turbulent kinetic energy is captured. The turbulent kinetic energy in the gain region for a snapshot at $t_{\text{pb}} \approx 150$ ms computed using the LSA method as a function of the averaging volume scale L is shown in the left panel of Figure 2.6. As described above, when the averaging volume is small, the turbulent kinetic energy approaches zero. As the averaging volume grows we see a rise in the turbulent kinetic energy but we do not observe a plateau, implying there is

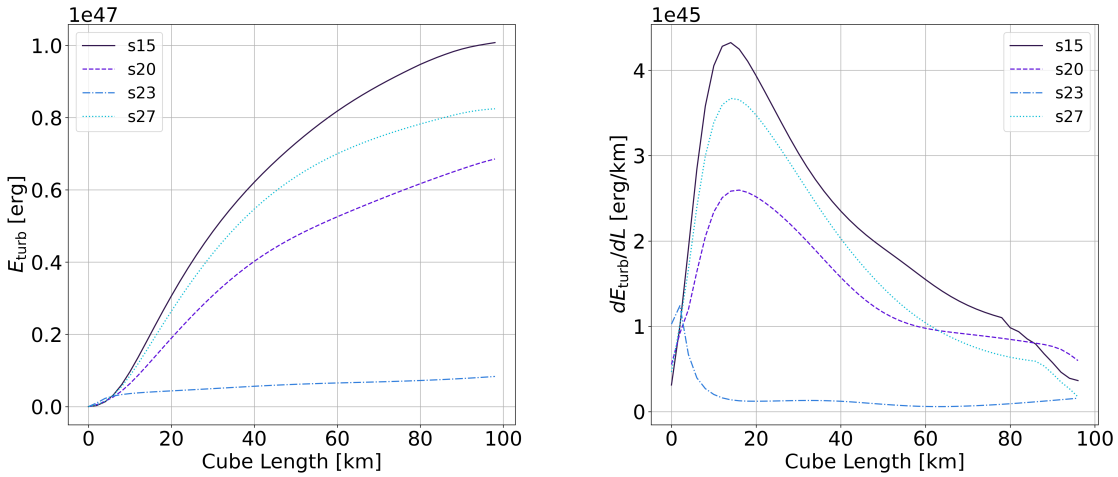

Figure 2.6: The total turbulent kinetic energy (left) and the corresponding slope of the total kinetic energy (right) as a function of the cube side length used in the LSA method at $t_{\rm pb} \approx 150$ ms for all four simulations.

no range of averaging volume sizes where the turbulent kinetic energy is independent of the size of the averaging volume. At $L \sim 20$ km we find a maximum in the derivative of $E_{\rm turb}$, seen as peak in right panel of Figure 2.6. Although there is not a clear range over which the turbulent kinetic energy is independent of the length scale, for the purposes of defining the turbulent kinetic energy using the LSA method we have adopted a cube length scale of 20 km. We shall later show that this averaging volume scale is larger than the characteristic vortex radius (see Section 2.5.2).

Finally we adopt a definition of the turbulent kinetic energy we refer to as the Spectral method based upon the approach found in [40]. A variation of this method can be found in [45]. The Spectral Method forgoes trying to define $\langle \boldsymbol{v} \rangle$ directly and instead removes the large-scale fluid motion by excluding the small wavenumbers from a Fourier transform and then integrating over the remaining range of wavenumbers. More precisely, let $\hat{\boldsymbol{f}}$ be the Fourier transform of an arbitrary vector quantity $\boldsymbol{f}$ in the gain region,

$$\hat{\boldsymbol{f}} = \frac{1}{(2\pi)^3} \int_{V_{\rm gain}} \boldsymbol{f} \, \exp(2\imath\pi \, \boldsymbol{k} \cdot \boldsymbol{x}) \, d^3x. \tag{2.20}$$

Integrating the squared magnitude of the transformed quantity over a spherical shell in

the k-space, one obtains the power spectrum

$$\hat{e}_f(k) = \frac{1}{2} \int_{\text{k-shell}} |\hat{\boldsymbol{f}}|^2 k^2 \, d\Omega_k. \tag{2.21}$$

Adopting $\boldsymbol{f} = \sqrt{\rho}\,\boldsymbol{v}$ and including only data originating from the gain layer gives the power spectrum $\hat{e}_{\sqrt{\rho}\,\boldsymbol{v}}$ of the kinetic energy in the gain region. The *turbulent* kinetic energy is defined as the integral of the power spectrum above a minimum wavenumber, i.e.

$$E_{\text{turb}} = \int_{k_{\text{min}}}^{\infty} \hat{e}_{\sqrt{\rho}\,\boldsymbol{v}} \, d\,k. \tag{2.22}$$

Here, k_{min} is the minimum wavenumber considered. As with the LSA method described above, we face the question of what to use for the minimum wavenumber k_{min}. [40] adopted $k_{\text{min}} = 0.1 \times (2\pi)\,\text{km}^{-1}$; however, we have found that for our simulations this lower bound does not sufficiently capture the onset of convection, which was not present in [40]. As such, we have followed their same method to determine a k_{min} suitable for our simulations.

If the fluid has well-developed turbulence, we expect the compensated spectral specific kinetic energy, defined to be $\hat{e}_v \, k^{5/3}$ where $\hat{e}_v$ is the spectrum of the specific kinetic energy, to be a constant for a range of wave numbers k_r. We have plotted this compensated specific kinetic energy power spectrum in Figure 2.7 for all four simulations at $t_{\text{pb}} \approx 150$ ms. This figure can be compared with the left panel of Figure 3 in [40], although we caution the reader that a) the definition of k in [40] means the wavenumbers there are $2\,\pi$ larger than those used in this paper, and b) we show a range of wavenumbers shifted to slightly higher values. Examining Figure 2.7 we do not see a horizontal section - a region of wavenumbers where the compensated spectral specific kinetic energy is constant - in any of the curves in our plot, but in the three successful explosions we find: a minimum in the spectrum at $k_r = 0.1 - 0.2$ km (corresponding to a physical scale of 5 - 10 km), and a maximum at $k_r \sim 0.04$; km (corresponding to a physical scale of 25 km). For the purposes of defining the turbulent kinetic energy using the Spectral method we set the lower bound of integration k_{min} to be $k_{\text{min}} = 0.025\,\text{km}^{-1}$, equivalent to a physical scale of 40 km.

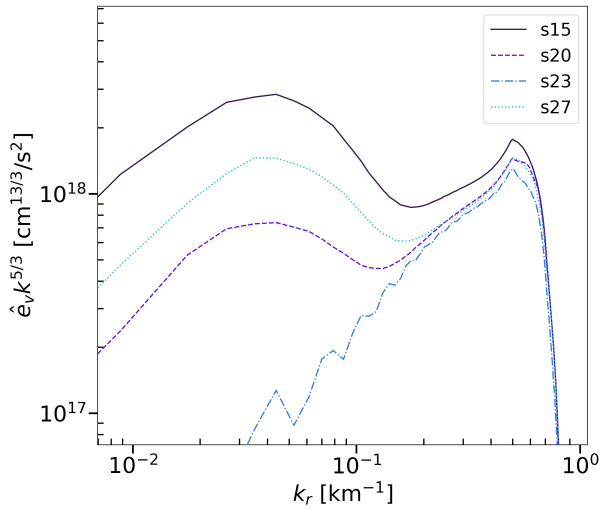

Figure 2.7: The compensated specific kinetic energy power spectrum at $t_{\rm pb} = 150$ ms for all four simulations.

2.5 Application to Simulations

2.5.1 Turbulent Kinetic Energy

We compute the total turbulent kinetic energy in the gain region using the three methods described above. The results are shown in the top row of Figure 2.8. No matter the method used, for a successful explosion, there is a rapid increase in the amount of turbulent kinetic energy in the gain region when convection begins (80–100 ms after bounce). Thereafter, the increase is more gradual in the interval 100 ms $\lesssim t_{\rm pb} \lesssim$ 200 ms. While the general trend of the results is the same across all methods, we note that the LSA and Spectral methods give values consistently smaller than the SSA method with the consequence that the growth in the turbulent kinetic energy during the interval 100 ms $\lesssim t_{\rm pb} \lesssim$ 200 ms using the LSA and Spectral methods is only by a factor ~ 2 compared to a factor closer to ~ 8 over the same period when using the SSA method.

The s23 simulation is clearly distinct from the successful explosions across all three methods. The amount of turbulent kinetic energy is smaller for s23 by approximately an order of magnitude (or more) compared to s15, s20 and s27. Moreover, there is little (if any) growth of the turbulent kinetic energy over the period 100 ms $\lesssim t_{\rm pb} \lesssim$ 200 ms for the s23 simulation.

The difference between the amount of turbulent kinetic energy computed in the s23 simulation compared to the s15, s20, and s27 simulations is largely due to the difference in

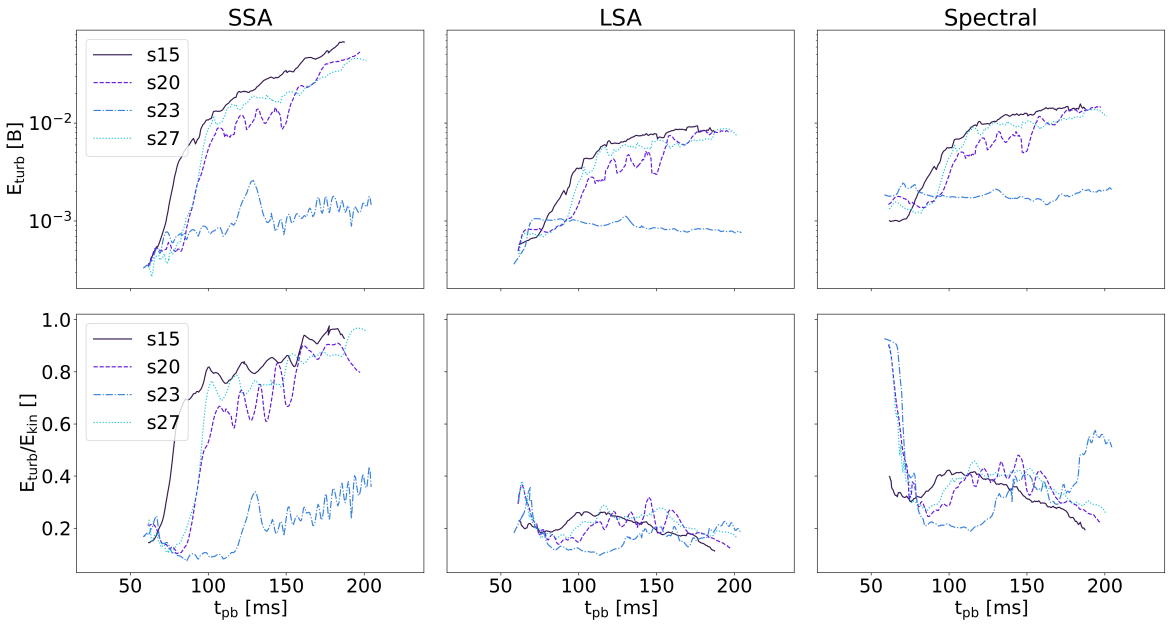

Figure 2.8: Top: The turbulent kinetic energy in the gain region as a function of the post-bounce time for all four simulations. Bottom: Ratio of the total turbulent kinetic energy to the total kinetic energy in the gain region as a function of the post-bounce time for all four simulations. Each column represents a different method for computing the turbulent kinetic energy. Left: Spherical Spatial Average (SSA) method; Middle: Local Spatial Average (LSA) method; Right: Spectral Method.

size / mass in the gain regions of the simulations. To eliminate this dependence, we show, in the bottom row of Figure 2.8, the evolution of the ratio of the turbulent kinetic energy to the total kinetic energy within the gain region, using each of the three methods. These panels reveal there are fundamental differences between the methods already hinted at by the previously noted differences in the growth rates of the turbulent kinetic energy in the top panels. Using the SSA method there is still a clear distinction between a successful and a failing supernova in the energy ratio, but this distinction disappears in the ratios computed using the LSA and Spectral methods. Note that the ratio of turbulent kinetic energy to total kinetic energy using the SSA method has strong resemblance to Figure 2.3. When the SSA method is used, the ratio of turbulent kinetic energy to total kinetic energy is of order $\sim 60\%$ in successful explosions at the onset of the explosion and later rises to $\sim 80\%$ by the end of the simulation. The s23 stands apart from the other runs. Although the ratio of kinetic energies in s23 using the SSA method does not reach the same level as the successful explosions, there is still an overall growth of the ratio after $t_{\rm pb} \sim 120$ ms to $\sim 40\%$ by the end of the simulation. In contrast, the ratio of turbulent to total kinetic energy computed using the LSA or Spectral method are very similar for all *four* simulations. There is no substantial distinction between successful and failing simulations. Aside from some temporary fluctuations, the ratio of energies lies between $\sim 20\%$ and $\sim 40\%$ for all four simulations after $t_{\rm pb} \sim 80$ ms, with no apparent change during shock revival of the s15, s20 and s27 simulations. One feature of note is that at approximately 195 ms post bounce, there is an uptick in the percentage of turbulent energy calculated by the spectral method for s23. We posit that this uptick is related to the SASI that occurs in the s23 at late times. As the large scale angular motion of the shock increases, these SASI modes begin to be detected by the Fourier Transform.

The different methods for computing the turbulent kinetic energy clearly do not capture the same physics, and the differences would lead to different conclusions about the relative importance of turbulence for successful explosions. To further probe this, we turn our attention to other fluid quantities which are also associated with turbulence. For this, we focus on the 3 simulations that have a substantial amount of turbulence in the gain region; the s15, s20, and s27 simulations.

2.5.2 Enstrophy Comparison

Fluid vorticity, $\boldsymbol{\omega} = \boldsymbol{\nabla} \times \boldsymbol{v}$, or alternatively enstrophy $\epsilon = |\boldsymbol{\omega}|^2/2$, are also regarded as intrinsic aspects of turbulence [49] and thus a good, but not sufficient, measure of its presence.

Therefore, one might expect a map of the enstrophy should resemble a map of the specific turbulent kinetic energy $e_{\rm turb}$. We present the spatial maps of the specific turbulent kinetic energy at the snapshot time of $t_{\rm pb} = 150$ ms in Figure 2.9. These spatial plots are masked to show only the values in the gain region. For the Spectral method we generate the map by Fourier transforming the velocity $\boldsymbol{v}$, setting the amplitude of all Fourier modes to zero for all wavenumbers $k \leq k_{\rm min}$, then transforming back to real space to produce the velocity field $\boldsymbol{u}$. Using $\boldsymbol{u}$, the specific turbulent kinetic energy for the Spectral method is defined as $e_{\rm turb} = |\boldsymbol{u}|^2/2$. Finally, the map of the enstrophy is also shown in the same figure in the bottom row for direct comparison.

Comparing these figures, we observe that, using either the LSA or Spectral methods, the areas of greatest specific turbulent energy are coincident with the areas of greatest enstrophy. And similarly, areas where we find the lowest amounts of specific turbulent kinetic energy are also areas with low enstrophy. In contrast, the SSA method yields maps where we observe regions with large amounts of specific turbulent kinetic energy but where the enstrophy is low. These are regions where the fluid is moving outwards, such as in convective plumes. At the other end of the scale, in places where the SSA finds only a small amount of specific turbulent kinetic energy, there is also a small amount of enstrophy. Thus the amount of correlation between the maps of specific turbulent kinetic energy and enstrophy is larger when using the LSA or Spectral methods than when using the SSA.

That the specific turbulent kinetic energy using the SSA is dominated by the convective plumes can be explained by examining how the expectation value for the velocity is defined for this method. In the SSA method, the average radial velocity $\langle v_r \rangle$ is computed from all the fluid on a spherical shell. Given that the general flow of the fluid in the gain region is toward the PNS, $\langle v_r \rangle$ will be negative. The specific turbulent kinetic energy for the SSA method is $e_{\rm turb} = |\boldsymbol{v} - \langle v_r \rangle \hat{\mathbf{r}}|^2/2$. For a fluid element which is moving outwards, i.e., $\boldsymbol{v} \approx |\boldsymbol{v}|\hat{\mathbf{r}}$, the contribution to the specific turbulent kinetic energy is $e_{\rm turb} = (|\boldsymbol{v} - \langle v_r \rangle \hat{\mathbf{r}}|)^2/2 \approx (|\boldsymbol{v}|^2 + \langle v_r \rangle^2 + 2|\boldsymbol{v}||\langle v_r \rangle|)/2$. For a fluid element with an inward velocity, i.e., $\boldsymbol{v} \approx -|\boldsymbol{v}|\hat{\mathbf{r}}$, the contribution to the specific turbulent kinetic energy is approximately $e_{\rm turb} = (|\boldsymbol{v}|^2 + \langle v_r \rangle^2 - 2|\boldsymbol{v}||\langle v_r \rangle|)/2$. Thus, outflows dominate the specific turbulent kinetic energy in the SSA method. In comparison, in the LSA method the expectation value for the velocity is computed from the local surrounding fluid. In a convective plume the expectation value will point in approximately the same direction as the velocity of the fluid element under consideration, and so the deviation of the fluid velocity in the outflow will be smaller, thus leading to a much smaller contribution to the specific turbulent kinetic energy from a convective plume.

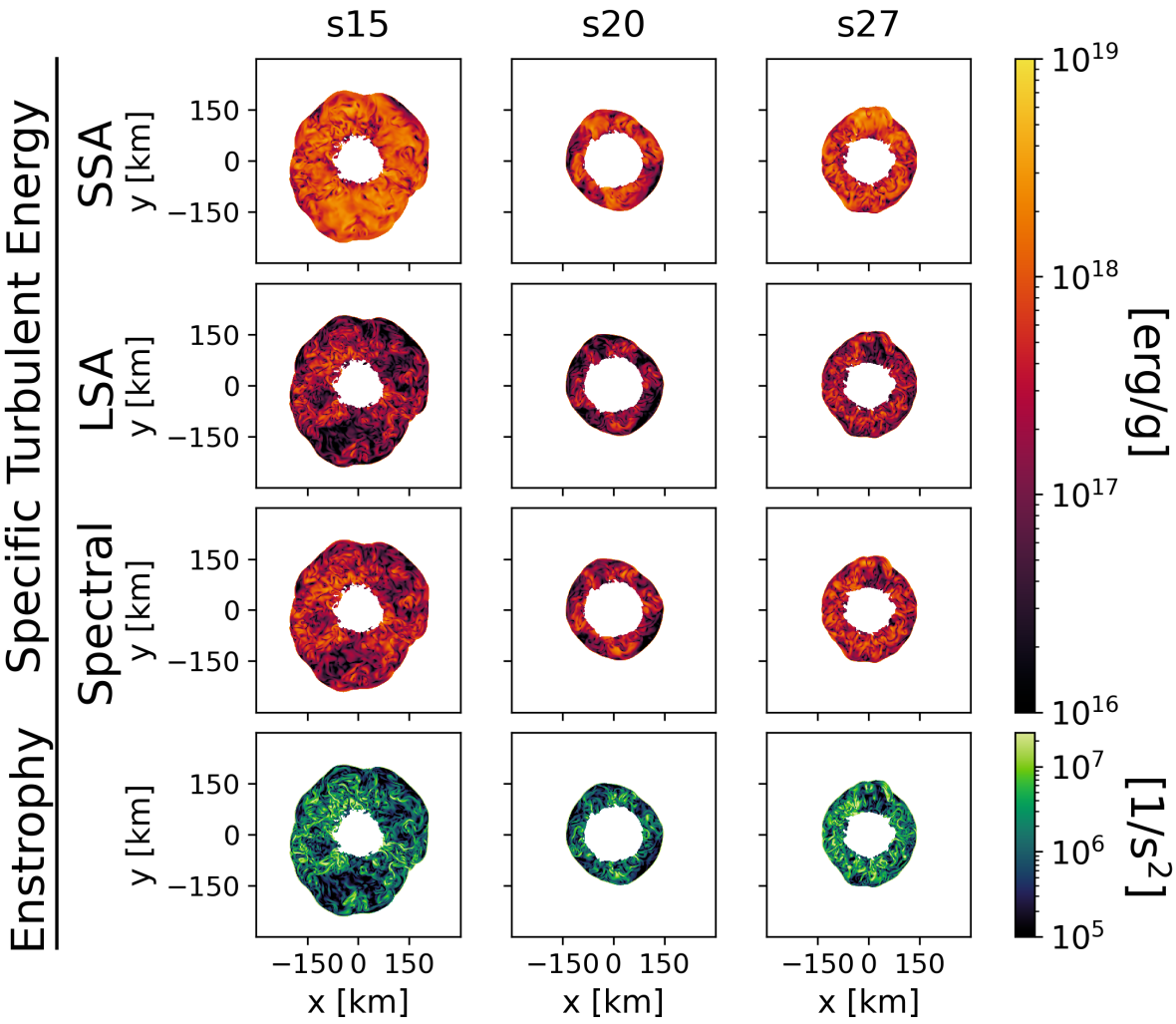

Figure 2.9: Spatial maps of the specific turbulent energy in the xy-plane computed using all three methods (First row: SSA; Second row: LSA; Third row: Spectral Method) for the exploding simulations. Bottom: Spatial maps of the enstrophy in the xy-plane for the same simulations. All panels are at 150 ms post bounce.

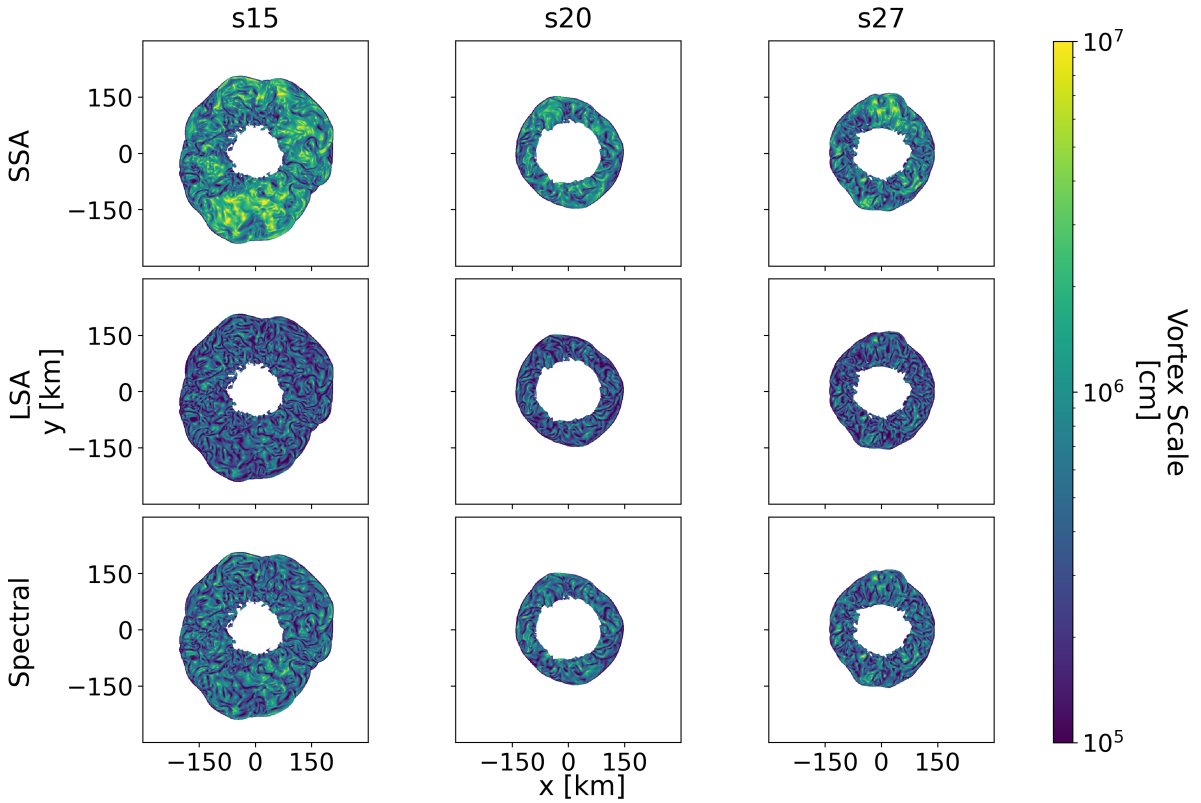

Figure 2.10: The vortex radius scale using the SSA (top row), LSA (middle row), and spectral method (bottom row) for the s15, s20, and s27 simulations (from left to right). All panels are at 150 ms post bounce.

The calculation of the enstrophy also allows us to determine the characteristic scale for the turbulent vortices. Knowing this scale allows us to validate the choice of LSA averaging volume and the k_{min} chosen for the Spectral method. We follow the method outlined in [95] and define the characteristic vortex scale as

$$\ell = \sqrt{e_{\text{turb}}/\epsilon}, \tag{2.23}$$

where ϵ is the enstrophy. Note that [95] and [58] call this same quantity the 'flow Taylor microscale'. In Figure 2.10 we plot 2D slices of the characteristic vortex scale using all the definitions of turbulence for the same snapshots as those shown in Figure 2.9. We find that the characteristic vortex scale using the LSA or Spectral definitions of the turbulent kinetic energy is of a few kilometers over the entire gain region. This characteristic vortex scale is both smaller than the size of the averaging cube used ($L = 20$ km) in the LSA method and $1/k_{\text{min}}$ used in the Spectral method ($1/k_{\text{min}} = 40$ km). [58] use this same quantity to also justify their choice of k_{min}. This is an indicator that the LSA and Spectral methods are sufficiently capturing the turbulence. In contrast, using the SSA to compute the specific turbulent kinetic energy we obtain a characteristic vortex scale which is generally larger than when using the LSA or Spectral method. From Figure 2.10 we see that when using the SSA method, the characteristic vortex scale can be as large as $\ell \sim 100$ km. A vortex of this size more closely resembles the size of the convective Bénard cells which extend across the gain region rather than local turbulence.

In summary, we find that different definitions of the turbulent kinetic energy lead to similar, but distinct, measurements of this quantity relative to the total kinetic energy in the simulations. Using the SSA method we observe a growing amount of turbulent kinetic energy relative to the total kinetic energy from the onset of convection, whereas the LSA and Spectral methods find a somewhat constant (and perhaps even diminishing) amount of turbulence over the same period. The SSA method clearly distinguishes between successful and failing supernovae, whereas the LSA and Spectral method do not show a distinction. Further, maps of the specific turbulent kinetic energy using the SSA method are seen to be dominated by the convective plumes, whereas maps made using the LSA method more closely match the enstrophy, another metric of turbulence.

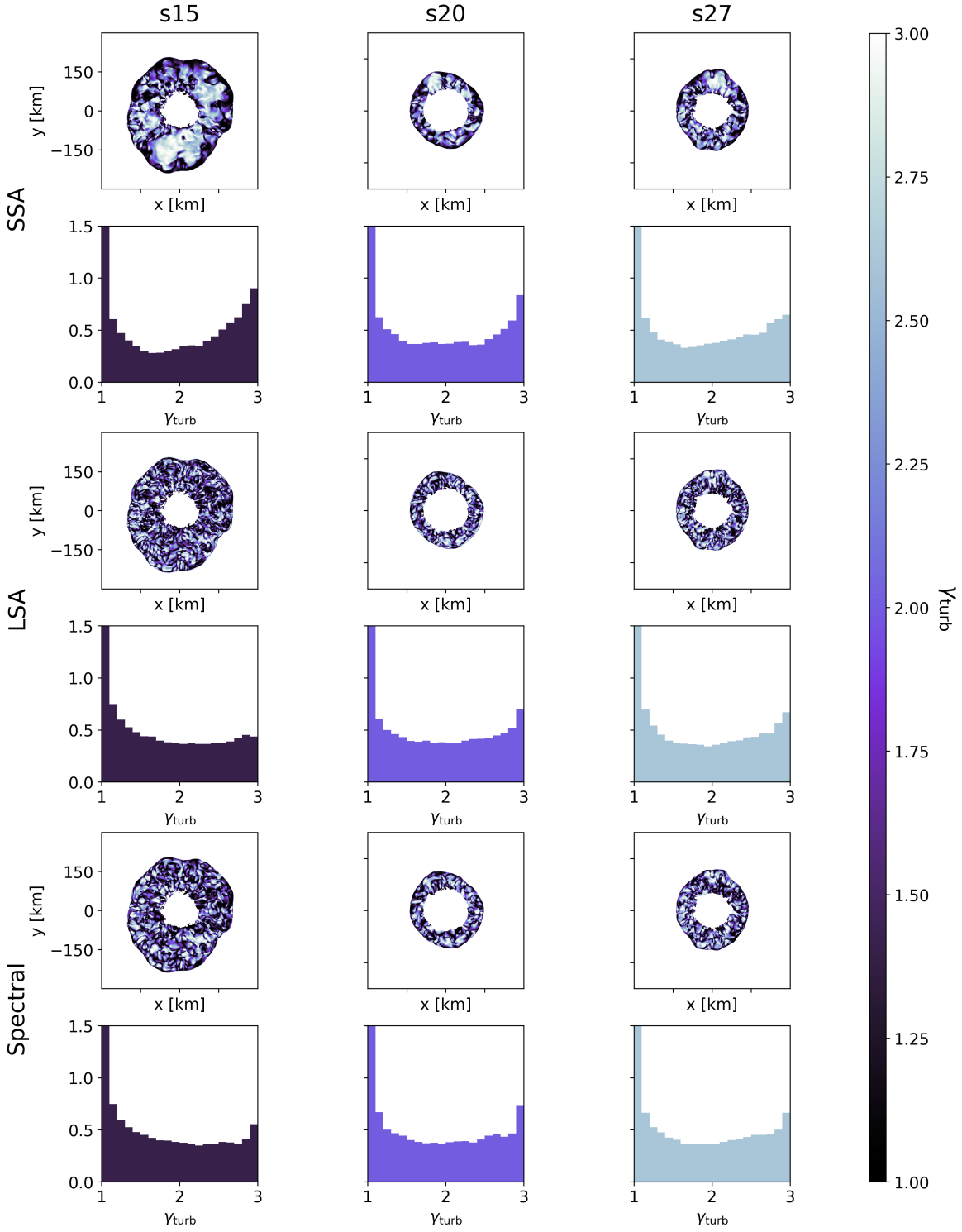

Figure 2.11: Top: Maps in the xy-plane and histograms of the turbulent adiabatic index $\gamma_{\rm turb}$ in the gain region for the s15, s20, and s27 simulations using SSA (top), LSA (middle), and the Spectral method (bottom row).

Table 2.1: Average thermal, turbulent, and effective adiabatic indices, and difference (Δ) of $\overline{\gamma}_{\rm eff}$ relative to $\overline{\gamma}_{\rm thermal}$.

Simulation	$\overline{\gamma}_{\rm thermal}$	$\overline{\gamma}_{\rm turb}$			$\overline{\gamma}_{\rm eff}$			Δ		
		SSA	LSA	Spectral	SSA	LSA	Spectral	SSA	LSA	Spectral
s15	1.4271	1.9985	1.8171	1.8203	1.4961	1.4481	1.4522	0.0483	0.0147	0.0176
s20	1.4364	1.9334	1.9084	1.8986	1.4777	1.4635	1.4616	0.0288	0.0189	0.0175
s27	1.4326	1.9362	1.9044	1.8998	1.4933	1.4630	1.4623	0.0424	0.0212	0.0207

$\Delta = (\overline{\gamma}_{\rm thermal} - \overline{\gamma}_{\rm eff,X})/\overline{\gamma}_{\rm thermal}$, *where X represents SSA, LSA, or Spectral, respectively.*

2.6 The Turbulent and Effective Adiabatic Index

We can now address the question of how the turbulence alters the fluid properties, and how one's conclusions about the effect of turbulence depends upon the definition. The quantities we focus upon are the adiabatic indices: the turbulent adiabatic index and the effective adiabatic index. The turbulent adiabatic tensor is defined as

$$(\gamma_{\rm turb})_{ij} = 1 + \frac{R_{ij}}{\rho\, e_{\rm turb}}, \tag{2.24}$$

where R_{ij} the ij^{th} element of the Reynolds stress tensor. For the LSA and SSA we define R_{ij} by $R_{ij} = \rho\,(v_i - \langle \boldsymbol{v} \rangle_i)\left(v_j - \langle \boldsymbol{v} \rangle_j\right)$, where, again, $\langle \boldsymbol{v} \rangle$ is the expectation value of the fluid velocity, and $\rho\, e_{\rm turb}$ is the turbulent kinetic energy density. As discussed in §2.5.2, we can recover the turbulent velocity field, and thus the Reynolds stress tensor, for the Spectral method as follows. We compute R_{ij} by Fourier transforming the velocity $\boldsymbol{v}$, setting the amplitude of all Fourier modes to zero for all wavenumbers $k \leq k_{\rm min}$, then transforming back to real space to produce the velocity field $\boldsymbol{u}$. We then define R_{ij} as $R_{ij} = \rho\, u_i\, u_j$. Due to its effect upon the shock radius, the most important component of the tensor is the $ij = rr$ element; therefore we will refer to $(\gamma_{\rm turb})_{rr}$ as the turbulent adiabatic index $\gamma_{\rm turb}$.

For well-developed isotropic turbulence, one expects each diagonal element (such as rr) of the tensor $(\gamma_{\rm turb})_{ij}$ to have a triangular distribution. If the turbulence is anisotropic such that the distribution of $(\gamma_{\rm turb})_{rr}$ is the same as the distribution of the sum $(\gamma_{\rm turb})_{\theta\theta} + (\gamma_{\rm turb})_{\phi\phi}$ — as has been found in the simulations reported in [39] — we would expect $\gamma_{\rm turb}$ to have a uniform distribution (see Appendix 2.9 for a detailed derivation of these expectations). For the case of non-turbulent, bulk flow in the radial direction (either inward or outward), $\gamma_{\rm turb}$ should have a distribution that peaks toward $\gamma_{\rm turb} = 3$ when using the SSA method. This last expectation arises because, for a location in the bulk flow, $\boldsymbol{v}$ will point approximately radially inwards (for a downflow) or outwards (for a convective plume). The

combination of flows in both directions has the consequence that the average radial velocity $\langle v_r \rangle$ will point inwards (mass is still accreting onto the PNS even if convection is occurring) but $\langle v_r \rangle$ will be smaller than the velocity of the fluid in the downflows. This has the effect that the Reynolds tensor element R_{rr} will typically be larger than the elements $R_{\theta\theta}$ and $R_{\phi\phi}$. Given a larger R_{rr}, we anticipate that, in the SSA method, our values of $\gamma_{\rm turb}$ will be pushed upwards toward 3. In contrast, for the LSA method, the velocity of a given fluid element relative to the local average velocity would be closer to random than for the SSA, regardless of the relative size of the average fluid velocity $\langle \boldsymbol{v} \rangle$ and the deviation from the average $\boldsymbol{v} - \langle \boldsymbol{v} \rangle$. Thus we expect the value of $\gamma_{\rm turb}$ for fluid elements in a bulk flow will not have the same bias toward $\gamma_{\rm turb} = 3$ when using the LSA method. Similarly, when using the Spectral method to compute $\gamma_{\rm turb}$, we should also find values for $\gamma_{\rm turb}$ in fluid with bulk flow which are also not biased toward $\gamma_{\rm turb} = 3$ because this method removes the large scale bulk flow component and retains only the small scale fluid motion.

In Figure 2.11 we show a 2D slice of the turbulent adiabatic index $\gamma_{\rm turb}$ we obtain in each grid zone, and their histograms at the $t_{\rm pb} = 150$ ms, using the SSA method (top panels), the LSA method (middle panels), and the Spectral method (bottom panels) for the s15, s20, and s27 simulations. The number of bins in every histogram is determined by Sturges's rule [96] Again, the different methods for defining the turbulence lead to distinct spatial maps. In the spatial distribution of the LSA and Spectral methods, the structures are of smaller scale, whereas when we use the SSA method, we observe large regions where the adiabatic index has a value $\gamma_{\rm turb} \geq 2$. The histograms of the adiabatic index for the fluid in the gain region are seen to be very similar when using either the LSA or Spectral methods, while the SSA is different. In particular, the distributions for the SSA method have a more pronounced peak toward $\gamma_{\rm turb} = 3$ compared with the LSA and Spectral Methods. The histograms of $\gamma_{\rm turb}$ are consistent with the idea that the fluid in the gain region can be divided into three components: the fluid that has well-developed, isotropic turbulence, the fluid that has anisotropic turbulence, and the fluid that is only moderately turbulent and has a bulk flow. Each of these components of the fluid in the gain region result in different pieces of the distribution of $\gamma_{\rm turb}$ in the gain region; e.g. a triangular distribution for $\gamma_{\rm turb}$ in the case of isotropic turbulence or a uniform distribution for $\gamma_{\rm turb}$ for anisotropic turbulence. For the moderately turbulent component the distribution for $\gamma_{\rm turb}$ is peaked toward $\gamma_{\rm turb} = 3$ when using the SSA; for the LSA or Spectral methods the distribution of $\gamma_{\rm turb}$ will be more similar to the distribution of the other two fluid components.

The different components of the fluid can be seen more clearly if we select small patches of the gain region. We select two 50 km square patches in each simulation, one with high

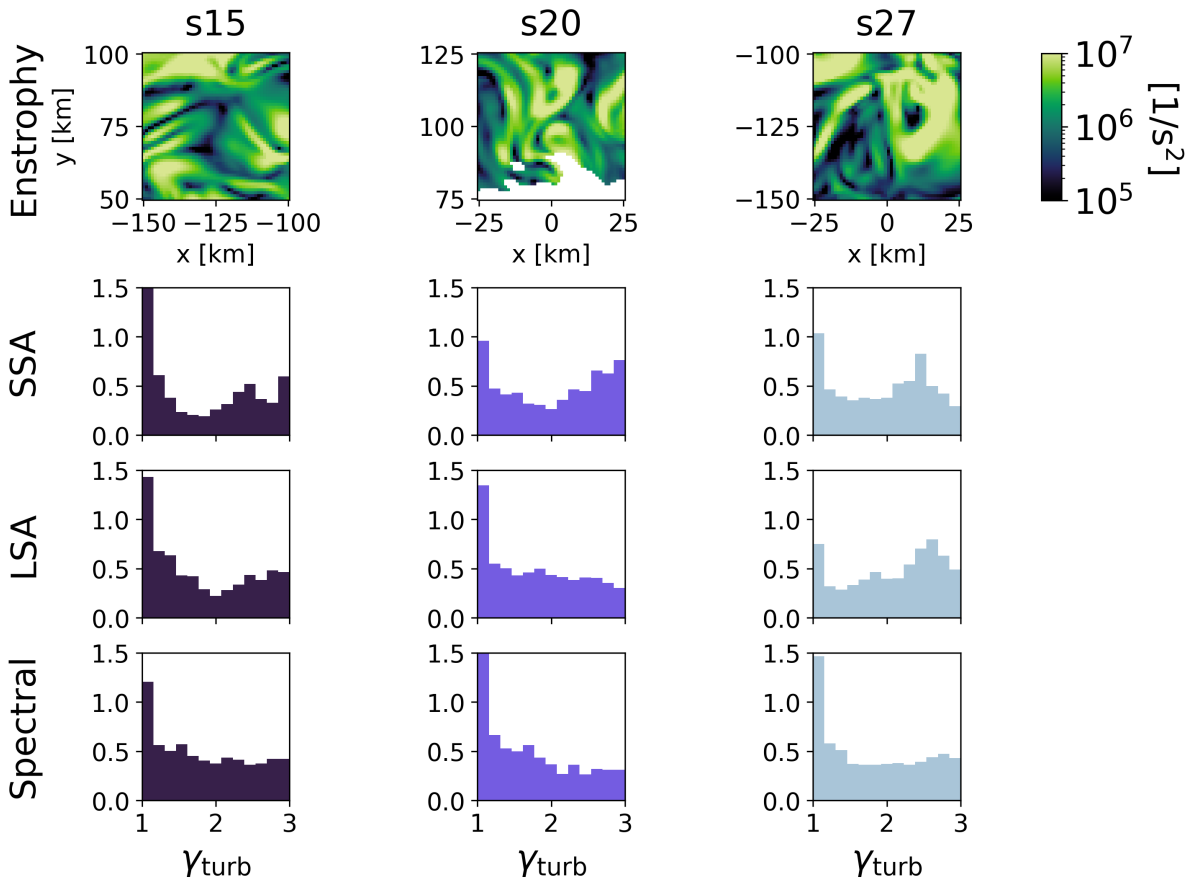

Figure 2.12: Enstrophy map in the xy-plane (top row) and distribution of γ_{turb} for a high-enstrophy patch in the gain region. The γ_{turb} are computed using the SSA method (second row), the LSA method (third row), and the Spectral method (bottom row).

enstrophy and the other with low enstrophy. The patches we select and the histograms of γ_{turb} for these patches are shown in Figures 2.12 and 2.13. First, the high enstrophy regions in Figure 2.12 demonstrate that all the methods for measuring the turbulence give similar distributions of γ_{turb} in regions of high enstrophy albeit with a tendency toward larger γ_{turb} from the SSA method. Conversely, Figure 2.13 demonstrates that in regions of low enstrophy, the different methods yield very different distributions of γ_{turb}.

The effect of turbulence upon the fluid and explosion, if any, needs to be compared with other sources of energy and pressure in the fluid. For this purpose, we can define an effective adiabatic index to be:

$$\gamma_{\text{eff}} = 1 + \frac{R_{rr} + P_{\text{thermal}}}{E_{\text{turb}} + E_{\text{thermal}}} = \left(\frac{\alpha}{1+\alpha}\right)\gamma_{\text{turb}} + \left(\frac{1}{1+\alpha}\right)\gamma_{\text{thermal}}, \tag{2.25}$$

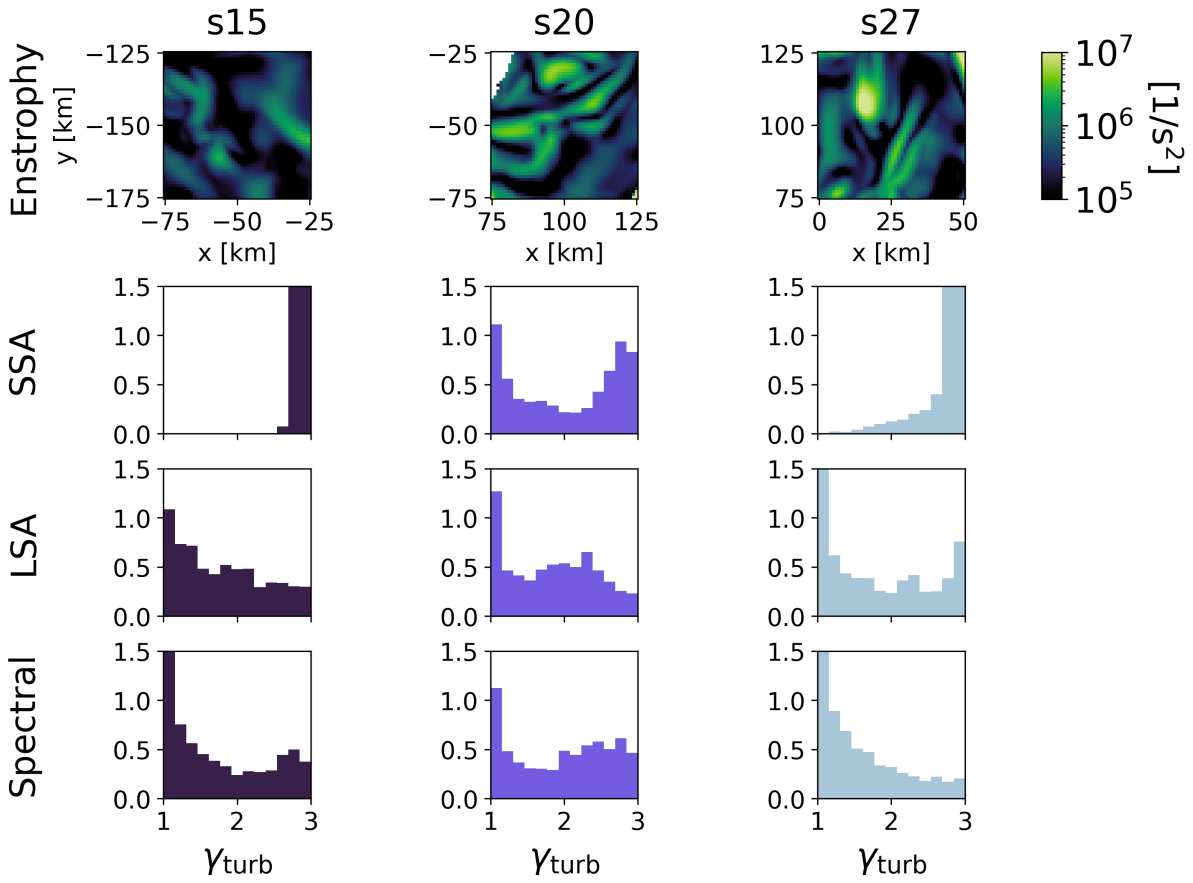

Figure 2.13: Enstrophy map in the xy-plane (top row) and distribution of γ_{turb} for a low-enstrophy patch in the gain region. The γ_{turb} are computed using the SSA method (second row), the LSA method (third row), and the Spectral method (bottom row).

where $E_{\rm thermal} = \rho\, e_{\rm thermal}$ and $P_{\rm thermal}$ represent the specific thermal energy and pressure, $\gamma_{\rm thermal} = 1 + P_{\rm thermal}/(\rho\, e_{\rm thermal})$, and $\alpha = e_{\rm turb}/e_{\rm thermal}$. In Figure 2.14 we show histograms of $\gamma_{\rm thermal}$ and $\gamma_{\rm eff}$ for the gain region from the same snapshots at 150 ms post bounce of the exploding simulations using the three different turbulence calculation methods. The thermal adiabatic index is approximately $\gamma_{\rm thermal} = 1.43$ for all fluid within the gain region at this time. When we add the contribution from turbulence and compute $\gamma_{\rm eff}$, the peak at 1.43 is retained but its width increases. When we use the LSA or Spectral methods, the broadening is smaller than when we use the SSA method. The addition of the turbulence shifts the average value of $\gamma_{\rm eff}$ upwards, and the average $\gamma_{\rm eff}$ for these snapshots are shown in Table 2.1. Whatever method we use to define the turbulence, the shift of $\gamma_{\rm eff}$ from $\gamma_{\rm thermal}$ is not large; for the successful explosions, $\gamma_{\rm eff}$ is larger than $\gamma_{\rm thermal}$ by, at most, 5%, as seen in Table 2.1. Notably the largest shifts come from the SSA method, while similar but smaller shifts come from the LSA and Spectral methods. This further confirms the notion that the methods can suggest different amounts of importance of turbulence relative to other physics.

Finally, in Figures 2.15 and 2.16 we show the evolution of the average thermal and effective adiabatic indices for the entire gain region as a function of the post-bounce time. As the fluid in the gain region is heated, its thermal adiabatic index gradually decreases due to a greater proportion of relativistic material to non-relativistic material. The decrease is not large; only 3% over the 100 ms period shown. The evolution of $\gamma_{\rm eff}$ over this same period, on the other hand, depends upon the method used to define turbulence, as shown in Figure 2.15. In all three successful explosions, the SSA method yields an average $\gamma_{\rm eff}$ which is larger than for the other two definitions of turbulence, and remains consistently between 1.48 and 1.5. This behavior is just as we saw at the single time point above, but we can now generalize to more of the simulation as a function of post-bounce time. In contrast, the LSA and Spectral methods for computing the turbulence yield average $\gamma_{\rm eff}$ which gradually decrease with time, although by only $\sim 4\%$.

2.7 Summary, Conclusions and Discussion

In this paper, we have investigated the question of how different definitions of the turbulence alters one's conclusions about the effect of turbulence in supernova simulations. We have undertaken four simulations using four progenitors and used three different methods for computing the turbulence. We find that how the turbulence is defined alters the amount of measured turbulent kinetic energy in the gain region. The Spherical Spatial Av-

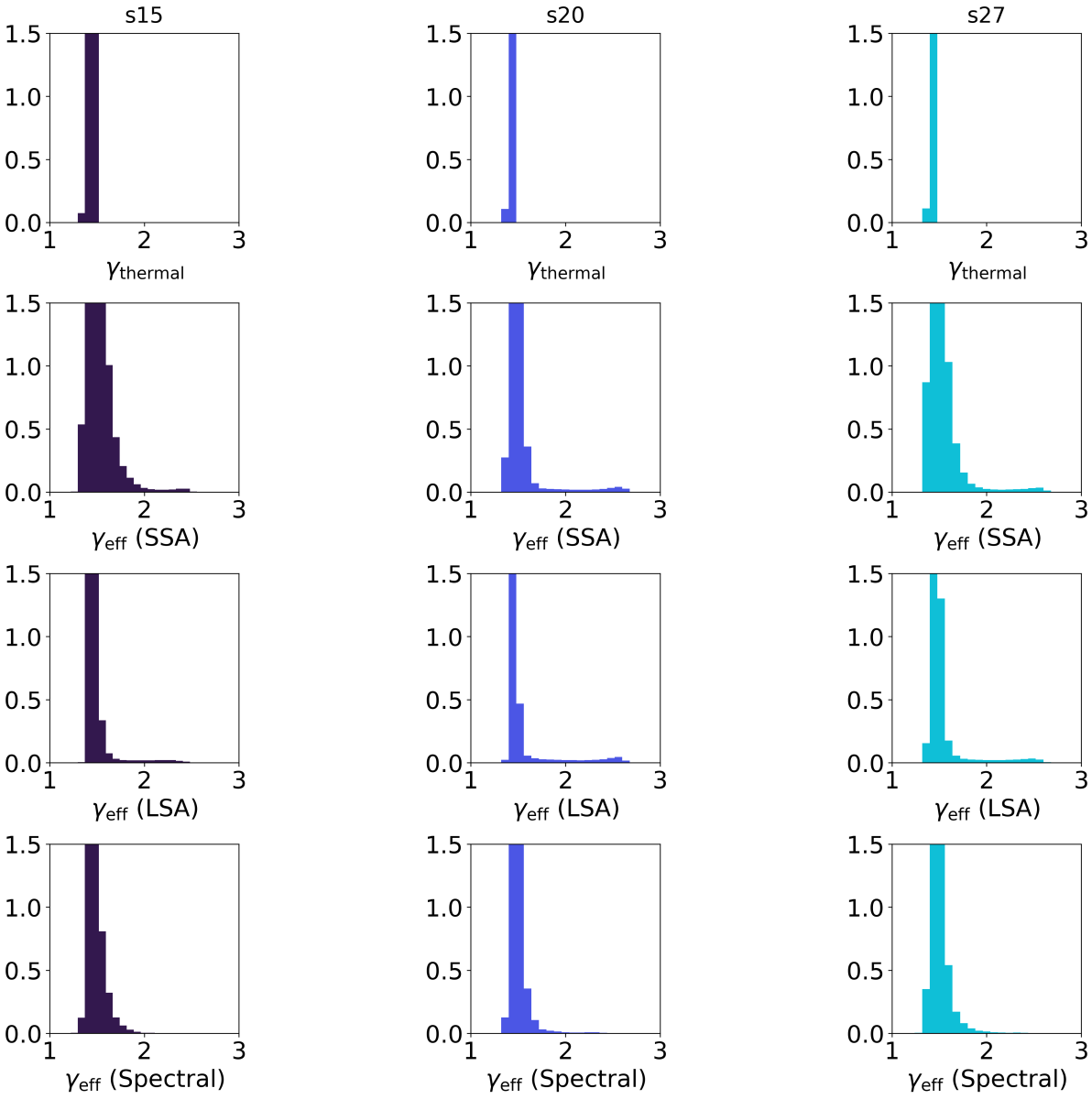

Figure 2.14: Distribution of the thermal adiabatic index $\gamma_{\rm thermal}$ (top) and the effective adiabatic index $\gamma_{\rm eff}$ using the SSA (2nd row), LSA (3rd row), and Spectral method (bottom).

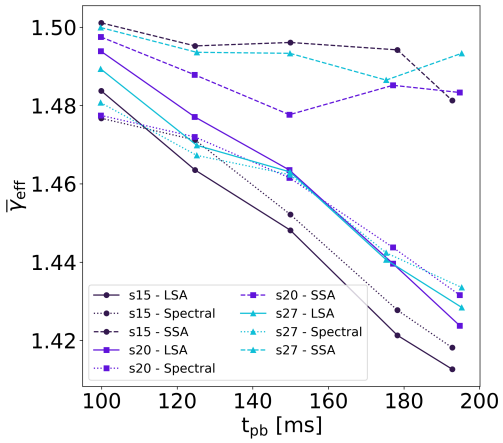

Figure 2.15: Average effective adiabatic index $\overline{\gamma}_{\rm eff}$ in the gain region as a function of post-bounce time using the LSA (solid line), SSA (dashed line), and Spectral method (dotted line) for the s15, s20, and s27 simulations.

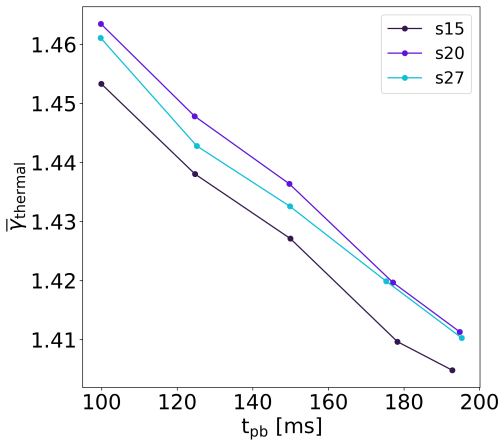

Figure 2.16: Average thermal adaibatic index $\overline{\gamma}_{\rm thermal}$ in the gain region as a function of post-bounce time for the s15, s20, s27 simulations.

erage method consistently yields values for the turbulent kinetic energy which are larger than the values obtained with the Local Spatial Average and Spectral Methods. The differences are only partly explained away by the choices one has to make for the averaging volume scale in the LSA method and the minimum wavenumber in the Spectral Method. The remaining difference is indicative of the fundamental differences of the definitions. These fundamental differences are seen most clearly in Figure 2.8, which shows how the ratio of the turbulent kinetic energy to total kinetic energy in the gain region evolves with time. The SSA method finds a consistently larger ratio of the energies for successful explosions and the ratio tends to grow as a function of post-bounce time. Using the SSA one would conclude that the presence of turbulence correlates with the success of the explosion. In contrast, the ratio of energies calculated using the LSA and Spectral methods are similar for both successful *and* unsuccessful explosions. Using these methods one would conclude that the presence of turbulence does not correlate with the success of the supernova. This divergence of conclusions indicates that the different methods of measuring the turbulence are actually not measuring the same thing.

To determine which method, if any, is a better measure of the turbulence we compared maps of the specific turbulent kinetic energy with maps for the enstrophy, a quantity that is often associated with the presence of turbulence. The comparison revealed that the LSA and Spectral methods produce maps which are more similar to the enstrophy than the SSA method.

Finally, we examined the effect of turbulence upon the fluid by computing the turbulent and effective adiabatic indices. Maps of the turbulent adiabatic index calculated using the SSA show larger coherent regions with $\gamma_{\text{turb}} > 2$ compared to those produced by the LSA and Spectral methods. These large regions of high γ_{turb} alter the distributions of this adiabatic index, producing a peak in the distribution toward the maximum value $\gamma_{\text{turb}} = 3$. The net effect is to shift the average turbulent adiabatic index in the gain region upward by a larger amount when using the SSA definition compared to the shift when using either of the other two definitions.

The contribution of turbulence to the explosion can be measured by computing the effective adiabatic index γ_{eff}. All definitions of turbulence shift the average γ_{eff} upwards. However, the shift is more pronounced when we use the SSA method compared to the LSA and Spectral definitions. Furthermore, the average γ_{eff} in the gain region remains approximately constant when we use the SSA. In contrast, when we use the LSA or Spectral definitions, the average γ_{eff} decreases with time. These findings once again demonstrate that the method selected for defining the turbulence changes the interpretation of the impact

of turbulence as a function of post-bounce time.

When assessing the impact of turbulence on the evolution of CCSNe, it is necessary to understand the strengths and limitations of the method used to measure it. We conclude from our study that the SSA method for defining the turbulence is not as accurate of a measure of this quantity as the LSA and Spectral methods. The LSA and Spectral methods are more consistent with each other *and* with the distribution of enstrophy in the simulations. The SSA yields a turbulent kinetic energy which is dominated by the upflowing convective plumes, not actual turbulence. However, the LSA and Spectral definition are not free of systematic problems. For example, using the LSA for the fluid in the vicinity of counterflows means there is a great deal of cancellation of momentum within the averaging volume which tends to yield low average velocities, and thus larger contributions to the turbulent kinetic energy. Further, both methods require one to define an additional parameter, and we have found that the measure of the turbulent kinetic energy is not independent of this choice. Thus the LSA and Spectral Methods suffer from an element of subjectivity that the SSA does not share. Nevertheless, the systematic issues of the LSA and Spectral definitions appear to not have as great an effect upon turbulent kinetic energy as convection has upon the SSA.

While the LSA and Spectral methods correlate more closely to the often-used turbulence tool of enstrophy, the quantity measured by the SSA method is clearly useful because it correlates with the success of the explosion. Since the turbulent kinetic energy computed using the SSA is dominated by convective plumes, the correlation suggests that the transition to explosion is because the kinetic energy in the gain region is increasingly directed toward countering the ram pressure of the infalling material. Since the turbulent kinetic energy computed using the SSA is dominated by convective plumes, the correlation suggests that the SSA is more likely tracking convection than turbulence. While there are a multitude of mechanisms, such as neutrino heating and deleptonization, contributing to the convection, the connection between SSA and explosion can be more accurately attributed to the necessity for convection for a supernova to explode

2.8 Acknowledgments

The work at NC State was supported by United States Department of Energy, Office of Science, Office of Nuclear Physics (award number DE-FG02-02ER41216). The work of Michael Redle was partially funded by German Research Foundation (DFG) Research Unit FOR5409

“Structure-Preserving Numerical Methods for Bulk- and Interface-Coupling of Heterogeneous Models (SNuBIC)" (grant #463312734). This work used Bridges-2 at Pittsburgh Supercomputing Center through allocation PHY200074 from the Advanced Cyberinfrastructure Coordination Ecosystem: Services & Support (ACCESS) program, which is supported by National Science Foundation grants #2138259, #2138286, #2138307, #2137603, and #2138296. This work also used the Extreme Science and Engineering Discovery Environment (XSEDE), which is supported by National Science Foundation grant number ACI-1548562. Specifically, it used the Bridges-2 system, which is supported by NSF award number ACI-1928147, at the Pittsburgh Supercomputing Center (PSC). The authors also acknowledge the Texas Advanced Computing Center (TACC) at The University of Texas at Austin for providing computational resources that have contributed to the research results reported within this paper. URL: http://www.tacc.utexas.edu

Software: *ELEPHANT [50, 51], astropy [97, 98, 99], Matplotlib [100], NumPy [101]*

2.9 Appendix: The Distribution of the Turbulent Adiabatic Index in Well-Developed Turbulence

The elements of the adiabatic index tensor for turbulence are defined to be

$$(\gamma_{\text{turb}})_{ij} = 1 + \frac{R_{ij}}{E_{\text{turb}}} \tag{2.26}$$

with R_{ij} the ij'th element of the Reynolds stress tensor given by $R_{ij} = \rho\,(v_i - \langle\vec{v}\rangle_i)\left(v_j - \langle\vec{v}\rangle_j\right)$, $\langle\vec{v}\rangle$ is the expectation value of the fluid velocity, and E_{turb} is the turbulent kinetic energy $E_{\text{turb}} = \rho\,|\vec{v} - \langle\vec{v}\rangle|^2/2$. For our derivation of the distribution of the adiabatic index in well-developed turbulence, it does not matter how $\langle\vec{v}\rangle$ is defined. The diagonal elements of the Reynolds stress tensor are non-negative, and from the definition of the Reynolds stress tensor, we see that

$$2\,E_{\text{turb}} = \sum_i R_{ii}. \tag{2.27}$$

Thus the three diagonal components of the Reynold's stress tensor are not independent, they are constrained, and the constraint defines a simplex in the space of R_{rr}, $R_{\theta\theta}$ and $R_{\phi\phi}$ (using spherical coordinate labels for the diagonal elements of R_{ij}).

2.9.1 Isotropic Turbulence

In isotropic turbulence the values for the diagonal elements of the Reynold's stress tensor at a given location in the fluid may be regarded as random and equally likely i.e. each diagonal element of the stress tensor has the same probability distribution. This means that, for a fixed total energy E_{turb}, the infinitesimal probability $dP(R_{rr}, R_{\theta\theta}, R_{\phi\phi})$ of finding the diagonal elements of the stress tensor in the ranges R_{rr} to $R_{rr} + dR_{rr}$, $R_{\theta\theta}$ to $R_{\theta\theta} + dR_{\theta\theta}$, and $R_{\phi\phi}$ to $R_{\phi\phi} + dR_{\phi\phi}$, is uniform across the surface of the simplex and so proportional to the surface element $dA = \delta(2\,E_{\text{turb}} - R_{rr} - R_{\theta\theta} - R_{\phi\phi})\,dR_{rr}\,dR_{\theta\theta}\,dR_{\phi\phi}$ of the simplex. Thus we can write the probability of a given set of diagonal elements as

$$dP(R_{rr}, R_{\theta\theta}, R_{\phi\phi}) \propto \delta(2\,E_{\text{turb}} - R_{rr} - R_{\theta\theta} - R_{\phi\phi})\,dR_{rr}\,dR_{\theta\theta}\,dR_{\phi\phi}. \tag{2.28}$$

To find the distribution of any one diagonal element, e.g. R_{rr}, we integrate this probability distribution over the other two diagonal elements i.e.

$$\frac{dP(R_{rr})}{dR_{rr}} = C\int_0^{2E_{\text{turb}}}\int_0^{2E_{\text{turb}}} \delta(2E_{\text{turb}} - R_{rr} - R_{\theta\theta} - R_{\phi\phi})\, dR_{\theta\theta}\, dR_{\phi\phi}. \tag{2.29}$$

where C is a normalization constant. To evaluate the integral we first insert two Heaviside step functions so that we can change the limits of the integration for one variable, e.g. $R_{\phi\phi}$, and write

$$\frac{dP(R_{rr})}{dR_{rr}} = C\int_0^{2E_{\text{turb}}}\int_{-\infty}^{\infty} \delta(2E_{\text{turb}} - R_{rr} - R_{\theta\theta} - R_{\phi\phi})\Theta(2E_{\text{turb}} - R_{\phi\phi})\Theta(R_{\phi\phi})\, dR_{\theta\theta}\, dR_{\phi\phi}. \tag{2.30}$$

From the integral over $R_{\phi\phi}$ we obtain

$$\frac{dP(R_{rr})}{dR_{rr}} = C\int_0^{2E_{\text{turb}}} \Theta(2E_{\text{turb}} - R_{rr} - R_{\theta\theta})\Theta(R_{rr} + R_{\theta\theta})\, dR_{\theta\theta} \tag{2.31}$$

and now we can remove the step functions by changing the limits of the remaining integral over $R_{\theta\theta}$ to give

$$\frac{dP(R_{rr})}{dR_{rr}} = C\int_0^{2E_{\text{turb}}-R_{rr}} dR_{\theta\theta} \tag{2.32}$$

The integral is now trivial and after normalizing we find

$$\frac{dP(R_{rr})}{dR_{rr}} = \frac{1}{E_{\text{turb}}}\left(1 - \frac{R_{rr}}{2E_{\text{turb}}}\right) \tag{2.33}$$

This is a triangular distribution for R_{rr}. Now we know the distribution of R_{rr} we see the distribution for γ_{rr} (or any other diagonal element of the tensor) is also a triangular distribution

$$\frac{dP(\gamma_{rr})}{d\gamma_{rr}} = \frac{(3-\gamma_{rr})}{2} \tag{2.34}$$

with a range $1 \le \gamma_{rr} \le 3$. The average adiabatic index is $\langle\gamma_{rr}\rangle = 5/3$ which matches the well known result of the adiabatic index of isotropic turbulence [102].

2.9.2 Anisotropic Turbulence

For anisotropic turbulence, one of the diagonal components of the Reynold's stress has a distribution different from the other two. In many models of anisotropic turbulence e.g.

[103], the distribution of the biased component is equal to the distribution of the sum of the other two components. Defining $R_{tt} = R_{\theta\theta} + R_{\phi\phi}$, the probability $dP(R_{rr}, R_{tt})$ of finding the elements of the stress tensor in the ranges R_{rr} to $R_{rr} + dR_{rr}$ and R_{tt} to $R_{tt} + dR_{tt}$, is uniform across the line $2E_{\text{turb}} = R_{rr} + R_{tt}$ and so proportional to the line element $d\ell = \delta(2E_{\text{turb}} - R_{rr} - R_{tt})\, dR_{rr}\, dR_{tt}$. We can proceed exactly as before to integrate over R_{tt} to determine the distribution of R_{rr}. We find

$$\frac{dP(R_{rr})}{dR_{rr}} = \frac{1}{2E_{\text{turb}}}\Theta(R_{rr})\Theta(2E_{\text{turb}} - R_{rr}) \tag{2.35}$$

which is a uniform distribution. Thus $\gamma_{rr} = 1 + R_{rr}/E_{\text{turb}}$ is also uniform and equal to

$$\frac{dP(\gamma_{rr})}{d\gamma_{rr}} = \frac{1}{2}\Theta(\gamma_{rr} - 1)\Theta(3 - \gamma_{rr}). \tag{2.36}$$

From this result we recover the result that for anisotropic turbulence, the average adiabatic index is $\langle\gamma_{rr}\rangle = 2$ [102].

REFERENCES

[1] S. E. Woosley, A. Heger, and T. A. Weaver. The evolution and explosion of massive stars. *Rev. Mod. Phys.*, 74:1015–1071, Nov 2002.

[2] S. J. Smartt, J. J. Eldridge, R. M. Crockett, and J. R. Maund. The death of massive stars - I. Observational constraints on the progenitors of Type II-P supernovae. *MNRAS*, 395(3):1409–1437, May 2009.

[3] S. E. Woosley and Alexander Heger. The Remarkable Deaths of 9-11 Solar Mass Stars. *ApJ*, 810(1):34, September 2015.

[4] Ken'ichi Nomoto, Nozomu Tominaga, Hideyuki Umeda, Chiaki Kobayashi, and Keiichi Maeda. Nucleosynthesis yields of core-collapse supernovae and hypernovae, and galactic chemical evolution. *Nucl. Phys. A*, 777:424–458, October 2006.

[5] S. Curtis, K. Ebinger, C. Fröhlich, M. Hempel, A. Perego, M. Liebendörfer, and F.-K. Thielemann. PUSHing Core-collapse Supernovae to Explosions in Spherical Symmetry. III. Nucleosynthesis Yields. *ApJ*, 870:2, January 2019.

[6] Luca Boccioli and Lorenzo Roberti. The Physics of Core-Collapse Supernovae: Explosion Mechanism and Explosive Nucleosynthesis. *Universe*, 10(3):148, March 2024.

[7] A. Burrows and J. M. Lattimer. The Birth of Neutron Stars. *ApJ*, 307:178, August 1986.

[8] Robert C. Duncan and Christopher Thompson. Formation of Very Strongly Magnetized Neutron Stars: Implications for Gamma-Ray Bursts. *ApJL*, 392:L9, June 1992.

[9] Ken'ichi Nomoto, Keiichi Maeda, Masaomi Tanaka, and Tomoharu Suzuki. Gamma-Ray Bursts and magnetar-forming Supernovae. *Ap&SS*, 336(1):129–137, November 2011.

[10] Sandro Mereghetti, José A. Pons, and Andrew Melatos. Magnetars: Properties, Origin and Evolution. *Space Sci. Rev.*, 191(1-4):315–338, October 2015.

[11] L. J. Wang, H. Yu, L. D. Liu, S. Q. Wang, Y. H. Han, D. Xu, Z. G. Dai, Y. L. Qiu, and J. Y. Wei. Evidence for Magnetar Formation in Broad-lined Type Ic Supernovae 1998bw and 2002ap. *ApJ*, 837(2):128, March 2017.

[12] Victoria M. Kaspi and Andrei M. Beloborodov. Magnetars. *ARA&A*, 55(1):261–301, August 2017.

[13] K. Ebinger, S. Curtis, C. Fröhlich, M. Hempel, A. Perego, M. Liebendörfer, and F.-K. Thielemann. PUSHing Core-collapse Supernovae to Explosions in Spherical Symmetry. II. Explodability and Remnant Properties. *ApJ*, 870:1, January 2019.

[14] J. S. Bloom, S. R. Kulkarni, S. G. Djorgovski, A. C. Eichelberger, P. Côté, J. P. Blakeslee, S. C. Odewahn, F. A. Harrison, D. A. Frail, A. V. Filippenko, D. C. Leonard, A. G. Riess, H. Spinrad, D. Stern, A. Bunker, A. Dey, B. Grossan, S. Perlmutter, R. A. Knop, I. M. Hook, and M. Feroci. The unusual afterglow of the γ-ray burst of 26 March 1998 as evidence for a supernova connection. *Nature*, 401(6752):453–456, September 1999.

[15] S. E. Woosley and J. S. Bloom. The Supernova Gamma-Ray Burst Connection. *ARA&A*, 44(1):507–556, September 2006.

[16] H. A. Bethe and J. R. Wilson. Revival of a stalled supernova shock by neutrino heating. *ApJ*, 295:14–23, August 1985.

[17] Adam Burrows, John Hayes, and Bruce A. Fryxell. On the Nature of Core-Collapse Supernova Explosions. *ApJ*, 450:830, September 1995.

[18] H. Thomas Janka. Long-Term Multidimensional Models of Core-Collapse Supernovae: Progress and Challenges. *arXiv e-prints*, page arXiv:2502.14836, February 2025.

[19] Anthony Mezzacappa, Matthias Liebendörfer, O. E. Messer, W. Raphael Hix, Friedrich-Karl Thielemann, and Stephen W. Bruenn. Simulation of the Spherically Symmetric Stellar Core Collapse, Bounce, and Postbounce Evolution of a Star of 13 Solar Masses with Boltzmann Neutrino Transport, and Its Implications for the Supernova Mechanism. *Phys. Rev. Lett.*, 86(10):1935–1938, March 2001.

[20] M. Rampp and H. T. Janka. Radiation hydrodynamics with neutrinos. Variable Eddington factor method for core-collapse supernova simulations. *A&A*, 396:361–392, December 2002.

[21] Todd A. Thompson, Adam Burrows, and Philip A. Pinto. Shock Breakout in Core-Collapse Supernovae and Its Neutrino Signature. *ApJ*, 592(1):434–456, July 2003.

[22] Matthias Liebendörfer, O. E. Bronson Messer, Anthony Mezzacappa, Stephen W. Bruenn, Christian Y. Cardall, and F. K. Thielemann. A Finite Difference Representation of Neutrino Radiation Hydrodynamics in Spherically Symmetric General Relativistic Spacetime. *ApJS*, 150(1):263–316, January 2004.

[23] K. Sumiyoshi, S. Yamada, H. Suzuki, H. Shen, S. Chiba, and H. Toki. Postbounce Evolution of Core-Collapse Supernovae: Long-Term Effects of the Equation of State. *ApJ*, 629(2):922–932, August 2005.

[24] T. Ertl, H. Th. Janka, S. E. Woosley, T. Sukhbold, and M. Ugliano. A Two-parameter Criterion for Classifying the Explodability of Massive Stars by the Neutrino-driven Mechanism. *ApJ*, 818(2):124, February 2016.

[25] A. Perego, M. Hempel, C. Fröhlich, K. Ebinger, M. Eichler, J. Casanova, M. Liebendörfer, and F.-K. Thielemann. PUSHing Core-collapse Supernovae to Explosions in Spherical Symmetry I: the Model and the Case of SN 1987A. *Astrophys. J.*, 806:275, June 2015.

[26] Sean M. Couch, MacKenzie L. Warren, and Evan P. O'Connor. Simulating Turbulence-aided Neutrino-driven Core-collapse Supernova Explosions in One Dimension. *ApJ*, 890(2):127, February 2020.

[27] H. Th. Janka, K. Langanke, A. Marek, G. Martínez-Pinedo, and B. Müller. Theory of core-collapse supernovae. *Phys. Rep.*, 442(1-6):38–74, April 2007.

[28] Hans-Thomas Janka. *Neutrino-Driven Explosions*, page 1095. 2017.

[29] Sean M. Couch. The mechanism(s) of core-collapse supernovae. *Philosophical Transactions of the Royal Society of London Series A*, 375(2105):20160271, September 2017.

[30] Takami Kuroda, Almudena Arcones, Tomoya Takiwaki, and Kei Kotake. Magnetorotational explosion of a massive star supported by neutrino heating in general relativistic three-dimensional simulations. *The Astrophysical Journal*, 896(2):102, Jun 2020.

[31] Robert Bollig, Naveen Yadav, Daniel Kresse, Hans-Thomas Janka, Bernhard Müller, and Alexander Heger. Self-consistent 3D Supernova Models From -7 Minutes to +7 s: A 1-bethe Explosion of a 19 $M_\odot$ Progenitor. *ApJ*, 915(1):28, July 2021.

[32] Ko Nakamura, Tomoya Takiwaki, and Kei Kotake. Three-dimensional simulation of a core-collapse supernova for a binary star progenitor of SN 1987A. *MNRAS*, 514(3):3941–3952, August 2022.

[33] David Vartanyan, Matthew S. B. Coleman, and Adam Burrows. The collapse and three-dimensional explosion of three-dimensional massive-star supernova progenitor models. *MNRAS*, 510(4):4689–4705, March 2022.

[34] Bailey Sykes and Bernhard Müller. Long-time 3D supernova simulations of non-rotating progenitors with magnetic fields, December 2024. arXiv:2412.01155 [astro-ph].

[35] Shota Shibagaki, Takami Kuroda, Kei Kotake, Tomoya Takiwaki, and Tobias Fischer. Three-dimensional GRMHD simulations of rapidly rotating stellar core collapse. *MNRAS*, 531(3):3732–3743, July 2024.

[36] Tianshu Wang and Adam Burrows. Nucleosynthetic Analysis of Three-dimensional Core-collapse Supernova Simulations. *ApJ*, 962(1):71, February 2024.

[37] J. W. Murphy and C. Meakin. A Global Turbulence Model for Neutrino-driven Convection in Core-collapse Supernovae. *ApJ.*, 742:74, December 2011.

[38] R. Fernández. Hydrodynamics of Core-collapse Supernovae at the Transition to Explosion. I. Spherical Symmetry. *Astrophys. J.*, 749:142, April 2012.

[39] J. C. Dolence, A. Burrows, J. W. Murphy, and J. Nordhaus. Dimensional Dependence of the Hydrodynamics of Core-collapse Supernovae. *Astrophys. J.*, 765:110, March 2013.

[40] E. Endeve, C. Y. Cardall, R. D. Budiardja, A. Mezzacappa, and J. M. Blondin. Turbulence and magnetic field amplification from spiral SASI modes in core-collapse supernovae. *Physica Scripta Volume T*, 155(1):014022, July 2013.

[41] T. Handy, T. Plewa, and A. Odrzywołek. Toward Connecting Core-collapse Supernova Theory with Observations. I. Shock Revival in a 15 M Blue Supergiant Progenitor with SN 1987A Energetics. *Astrophys. J.*, 783:125, March 2014.

[42] E. Abdikamalov, C. D. Ott, D. Radice, L. F. Roberts, R. Haas, C. Reisswig, P. Mösta, H. Klion, and E. Schnetter. Neutrino-driven Turbulent Convection and Standing Accretion Shock Instability in Three-dimensional Core-collapse Supernovae. *Astrophys. J.*, 808:70, July 2015.

[43] S. M. Couch and C. D. Ott. The Role of Turbulence in Neutrino-driven Core-collapse Supernova Explosions. *Astrophys. J.*, 799:5, January 2015.

[44] D. Radice, C. D. Ott, E. Abdikamalov, S. M. Couch, R. Haas, and E. Schnetter. Neutrino-driven Convection in Core-collapse Supernovae: High-resolution Simulations. *Astrophys. J.*, 820:76, March 2016.

[45] Jordi Casanova, Eirik Endeve, Eric J. Lentz, O. E. Bronson Messer, W. Raphael Hix, J. Austin Harris, and Stephen W. Bruenn. On the character of turbulent-like flows in self-consistent models of core-collapse supernovae. *Phys. Scr.*, 95(6):064005, June 2020.

[46] G. Falkovich. Bottleneck phenomenon in developed turbulence. *Physics of Fluids*, 6:1411–1414, April 1994.

[47] W. Dobler, N. E. Haugen, T. A. Yousef, and A. Brandenburg. Bottleneck effect in three-dimensional turbulence simulations. *Phys. Rev.*, 68(2):026304, August 2003.

[48] G. G. Katul, C. Manes, A. Porporato, E. Bou-Zeid, and M. Chamecki. Bottlenecks in turbulent kinetic energy spectra predicted from structure function inflections using the Von Kármán-Howarth equation. *Phys. Rev. E*, 92(3):033009, September 2015.

[49] Arkady Tsinober. *An Informal Introduction to Turbulence*, volume 63. 2004.

[50] M. Liebendörfer, S. C. Whitehouse, and T. Fischer. The Isotropic Diffusion Source Approximation for Supernova Neutrino Transport. *ApJ*, 698:1174–1190, June 2009.

[51] Roger Käppeli, Stuart C Whitehouse, Simon Scheidegger, U-L Pen, and Matthias Liebendörfer. Fish: a three-dimensional parallel magnetohydrodynamics code for astrophysical applications. *The Astrophysical Journal Supplement Series*, 195(2):20, 2011.

[52] Rubén M. Cabezón, Kuo-Chuan Pan, Matthias Liebendörfer, Takami Kuroda, Kevin Ebinger, Oliver Heinimann, Albino Perego, and Friedrich-Karl Thielemann. Core-collapse supernovae in the hall of mirrors. A three-dimensional code-comparison project. *A&A*, 619:A118, November 2018.

[53] James M Lattimer and F Douglas Swesty. A generalized equation of state for hot, dense matter. *Nuclear Physics A*, 535(2):331–376, 1991.

[54] A Marek, Harold Dimmelmeier, H-Th Janka, E Müller, and R Buras. Exploring the relativistic regime with newtonian hydrodynamics: an improved effective gravitational potential for supernova simulations. *Astronomy & Astrophysics*, 445(1):273–289, 2006.

[55] Shi Jin and Zhouping Xin. The relaxation schemes for systems of conservation laws in arbitrary space dimensions. *Communications on pure and applied mathematics*, 48(3):235–276, 1995.

[56] Stephen W Bruenn. Stellar core collapse-numerical model and infall epoch. *The Astrophysical Journal Supplement Series*, 58:771–841, 1985.

[57] Hiroki Nagakura, Adam Burrows, David Radice, and David Vartanyan. Towards an understanding of the resolution dependence of core-collapse supernova simulations. *Monthly Notices of the Royal Astronomical Society*, 490(4):4622–4637, 10 2019.

[58] Eirik Endeve, Christian Y. Cardall, Reuben D. Budiardja, Samuel W. Beck, Alborz Bejnood, Ross J. Toedte, Anthony Mezzacappa, and John M. Blondin. Turbulent magnetic field amplification from spiral sasi modes: Implications for core-collapse supernovae and proto-neutron star magnetization. *The Astrophysical Journal*, 751(1):26, may 2012.

[59] Stanford E Woosley and Alexander Heger. Nucleosynthesis and remnants in massive stars of solar metallicity. *Physics Reports*, 442(1-6):269–283, 2007.

[60] Stephen W. Bruenn, Eric J. Lentz, W. Raphael Hix, Anthony Mezzacappa, J. Austin Harris, O. E. Bronson Messer, Eirik Endeve, John M. Blondin, Merek Austin Chertkow, Eric J. Lingerfelt, Pedro Marronetti, and Konstantin N. Yakunin. The Development of Explosions in Axisymmetric Ab Initio Core-collapse Supernova Simulations of 12-25 M Stars. *ApJ*, 818(2):123, February 2016.

[61] Alexander Summa, Florian Hanke, Hans-Thomas Janka, Tobias Melson, Andreas Marek, and Bernhard Müller. Progenitor-dependent Explosion Dynamics in Self-consistent, Axisymmetric Simulations of Neutrino-driven Core-collapse Supernovae. *ApJ*, 825(1):6, July 2016.

[62] M. Aaron Skinner, Adam Burrows, and Joshua C. Dolence. Should One Use the Ray-by-Ray Approximation in Core-collapse Supernova Simulations? *ApJ*, 831(1):81, November 2016.

[63] David Vartanyan, Adam Burrows, David Radice, M. Aaron Skinner, and Joshua Dolence. Revival of the fittest: exploding core-collapse supernovae from 12 to 25 $M_{\odot}$. *MNRAS*, 477(3):3091–3108, July 2018.

[64] Tobias Melson, Hans-Thomas Janka, Robert Bollig, Florian Hanke, Andreas Marek, and Bernhard Müller. Neutrino-driven Explosion of a 20 Solar-mass Star in Three Dimensions Enabled by Strange-quark Contributions to Neutrino-Nucleon Scattering. *ApJL*, 808(2):L42, August 2015.

[65] Christian D. Ott, Luke F. Roberts, André da Silva Schneider, Joseph M. Fedrow, Roland Haas, and Erik Schnetter. The Progenitor Dependence of Core-collapse Supernovae from Three-dimensional Simulations with Progenitor Models of 12-40 $M_{\odot}$. *ApJL*, 855(1):L3, March 2018.

[66] Robert Glas, Oliver Just, H. Thomas Janka, and Martin Obergaulinger. Three-dimensional Core-collapse Supernova Simulations with Multidimensional Neutrino Transport Compared to the Ray-by-ray-plus Approximation. *ApJ*, 873(1):45, March 2019.

[67] Yudai Suwa, Shoichi Yamada, Tomoya Takiwaki, and Kei Kotake. The Criterion of Supernova Explosion Revisited: The Mass Accretion History. *ApJ*, 816(1):43, January 2016.

[68] David Vartanyan, Adam Burrows, Tianshu Wang, Matthew S. B. Coleman, and Christopher J. White. Gravitational-wave signature of core-collapse supernovae. *Phys. Rev. D*, 107(10):103015, May 2023.

[69] Florian Hanke, Bernhard Müller, Annop Wongwathanarat, Andreas Marek, and Hans-Thomas Janka. SASI Activity in Three-dimensional Neutrino-hydrodynamics Simulations of Supernova Cores. *ApJ*, 770(1):66, June 2013.

[70] Tomoya Takiwaki, Kei Kotake, and Thierry Foglizzo. Insights into non-axisymmetric instabilities in three-dimensional rotating supernova models with neutrino and gravitational-wave signatures. *MNRAS*, 508(1):966–985, November 2021.

[71] Tuguldur Sukhbold, S. E. Woosley, and Alexander Heger. A High-resolution Study of Presupernova Core Structure. *ApJ*, 860(2):93, June 2018.

[72] John M. Blondin, Anthony Mezzacappa, and Christine DeMarino. Stability of Standing Accretion Shocks, with an Eye toward Core-Collapse Supernovae. *ApJ*, 584(2):971–980, February 2003.

[73] John M. Blondin and Anthony Mezzacappa. Pulsar spins from an instability in the accretion shock of supernovae. *Nature*, 445(7123):58–60, January 2007.

[74] Ko Nakamura, Tomoya Takiwaki, Jin Matsumoto, and Kei Kotake. Three-dimensional magnetohydrodynamic simulations of core-collapse supernovae - I. Hydrodynamic evolution and protoneutron star properties. *MNRAS*, 536(1):280–294, January 2025.

[75] R. Buras, H. Th. Janka, M. Rampp, and K. Kifonidis. Two-dimensional hydrodynamic core-collapse supernova simulations with spectral neutrino transport. II. Models for different progenitor stars. *A&A*, 457(1):281–308, October 2006.

[76] H. Th. Janka and W. Keil. Perspectives of Core-Collapse Supernovae beyond SN 1987A. In Lukas Labhardt, Bruno Binggeli, and Roland Buser, editors, *Supernovae and cosmology*, page 7, January 1998.

[77] H. Th. Janka. Conditions for shock revival by neutrino heating in core-collapse supernovae. *A&A*, 368:527–560, March 2001.

[78] Todd A. Thompson, Eliot Quataert, and Adam Burrows. Viscosity and Rotation in Core-Collapse Supernovae. *ApJ*, 620(2):861–877, February 2005.

[79] Jeremiah W. Murphy and Adam Burrows. Criteria for Core-Collapse Supernova Explosions by the Neutrino Mechanism. *ApJ*, 688(2):1159–1175, December 2008.

[80] Sean M. Couch and Christian D. Ott. Revival of the Stalled Core-collapse Supernova Shock Triggered by Precollapse Asphericity in the Progenitor Star. *ApJL*, 778(1):L7, November 2013.

[81] Sean M. Couch and Evan P. O'Connor. High-resolution Three-dimensional Simulations of Core-collapse Supernovae in Multiple Progenitors. *ApJ*, 785(2):123, April 2014.

[82] Irene Tamborra, Georg Raffelt, Florian Hanke, Hans-Thomas Janka, and Bernhard Müller. Neutrino emission characteristics and detection opportunities based on three-dimensional supernova simulations. *Phys. Rev. D*, 90(4):045032, August 2014.

[83] Anthony Mezzacappa, Eric J. Lentz, Stephen W. Bruenn, W. Raphael Hix, O. E. Bronson Messer, Eirik Endeve, John M. Blondin, J. Austin Harris, Pedro Marronetti, Konstantin N. Yakunin, and Eric J. Lingerfelt. A Neutrino-Driven Core Collapse Supernova Explosion of a 15 M Star. *arXiv e-prints*, page arXiv:1507.05680, July 2015.

[84] H. Andresen, B. Müller, E. Müller, and H. Th. Janka. Gravitational wave signals from 3D neutrino hydrodynamics simulations of core-collapse supernovae. *MNRAS*, 468(2):2032–2051, June 2017.

[85] Bernhard Müller and Vishnu Varma. A 3D simulation of a neutrino-driven supernova explosion aided by convection and magnetic fields. *MNRAS*, 498(1):L109–L113, November 2020.

[86] Jade Powell and Bernhard Müller. The gravitational-wave emission from the explosion of a 15 solar mass star with rotation and magnetic fields. *MNRAS*, 532(4):4326–4339, August 2024.

[87] Swapnil Shankar, Philipp Mösta, Roland Haas, and Erik Schnetter. 3D full-GR simulations of magnetorotational core-collapse supernovae on GPUs: A systematic study of rotation rates and magnetic fields. *arXiv e-prints*, page arXiv:2504.11537, April 2025.

[88] Tobias Melson, Hans-Thomas Janka, and Andreas Marek. Neutrino-driven Supernova of a Low-mass Iron-core Progenitor Boosted by Three-dimensional Turbulent Convection. *ApJL*, 801(2):L24, March 2015.

[89] David Radice, Ernazar Abdikamalov, Christian D. Ott, Philipp Moesta, Sean M. Couch, and Luke F. Roberts. Turbulence in Core-Collapse Supernovae. *Journal of Physics G: Nuclear and Particle Physics*, 45(5):053003, May 2018. arXiv:1710.01282 [astro-ph].

[90] A. Burrows and D. Vartanyan. Core-collapse supernova explosion theory. *Nature*, 589(7840):29–39, January 2021.

[91] Jin Matsumoto, Tomoya Takiwaki, and Kei Kotake. Neutrino-driven massive stellar explosions in 3D fostered by magnetic fields via turbulent α-effect. *MNRAS*, 528(1):L96–L101, February 2024.

[92] R. J. Adrian, K. T. Christensen, and Z. C. Liu. Analysis and interpretation of instantaneous turbulent velocity fields. *Experiments in Fluids*, 29(3):275–290, September 2000.

[93] Florian Hanke, Andreas Marek, Bernhard Müller, and Hans-Thomas Janka. Is Strong SASI Activity the Key to Successful Neutrino-driven Supernova Explosions? *ApJ*, 755(2):138, August 2012.

[94] Rodrigo Fernández, Bernhard Müller, Thierry Foglizzo, and Hans-Thomas Janka. Characterizing SASI- and convection-dominated core-collapse supernova explosions in two dimensions. *MNRAS*, 440(3):2763–2780, May 2014.

[95] Dongsu Ryu, T. W. Jones, and Adam Frank. The Magnetohydrodynamic Kelvin-Helmholtz Instability: A Three-dimensional Study of Nonlinear Evolution. *ApJ*, 545(1):475–493, December 2000.

[96] Herbert A. Sturges. The choice of a class interval. *Journal of the American Statistical Association*, 21(153):65–66, 1926.

[97] Astropy Collaboration, Thomas P. Robitaille, Erik J. Tollerud, Perry Greenfield, Michael Droettboom, Erik Bray, Tom Aldcroft, Matt Davis, Adam Ginsburg, Adrian M. Price-Whelan, Wolfgang E. Kerzendorf, Alexander Conley, Neil Crighton, Kyle Barbary, Demitri Muna, Henry Ferguson, Frédéric Grollier, Madhura M. Parikh, Prasanth H. Nair, Hans M. Unther, Christoph Deil, Julien Woillez, Simon Conseil, Roban Kramer, James E. H. Turner, Leo Singer, Ryan Fox, Benjamin A. Weaver, Victor Zabalza, Zachary I. Edwards, K. Azalee Bostroem, D. J. Burke, Andrew R. Casey, Steven M. Crawford, Nadia Dencheva, Justin Ely, Tim Jenness, Kathleen Labrie, Pey Lian Lim, Francesco Pierfederici, Andrew Pontzen, Andy Ptak, Brian Refsdal, Mathieu Servillat, and Ole Streicher. Astropy: A community Python package for astronomy. *A&A*, 558:A33, Oct 2013.

[98] Astropy Collaboration, A. M. Price-Whelan, B. M. Sipőcz, H. M. Günther, P. L. Lim, S. M. Crawford, S. Conseil, D. L. Shupe, M. W. Craig, N. Dencheva, A. Ginsburg, J. T. VanderPlas, L. D. Bradley, D. Pérez-Suárez, M. de Val-Borro, T. L. Aldcroft, K. L. Cruz, T. P. Robitaille, E. J. Tollerud, C. Ardelean, T. Babej, Y. P. Bach, M. Bachetti, A. V. Bakanov, S. P. Bamford, G. Barentsen, P. Barmby, A. Baumbach, K. L. Berry, F. Biscani, M. Boquien, K. A. Bostroem, L. G. Bouma, G. B. Brammer, E. M. Bray, H. Breytenbach, H. Buddelmeijer, D. J. Burke, G. Calderone, J. L. Cano Rodríguez, M. Cara, J. V. M. Cardoso, S. Cheedella, Y. Copin, L. Corrales, D. Crichton, D. D'Avella, C. Deil, É. Depagne, J. P. Dietrich, A. Donath, M. Droettboom, N. Earl, T. Erben, S. Fabbro, L. A. Ferreira, T. Finethy, R. T. Fox, L. H. Garrison, S. L. J. Gibbons, D. A. Goldstein, R. Gommers, J. P. Greco, P. Greenfield, A. M. Groener, F. Grollier, A. Hagen, P. Hirst, D. Homeier, A. J. Horton, G. Hosseinzadeh, L. Hu, J. S. Hunkeler, Ž. Ivezić, A. Jain, T. Jenness, G. Kanarek, S. Kendrew, N. S. Kern, W. E. Kerzendorf, A. Khvalko, J. King, D. Kirkby, A. M. Kulkarni, A. Kumar, A. Lee, D. Lenz, S. P. Littlefair, Z. Ma, D. M. Macleod, M. Mastropietro, C. McCully, S. Montagnac, B. M. Morris, M. Mueller, S. J. Mumford, D. Muna, N. A. Murphy, S. Nelson, G. H. Nguyen, J. P. Ninan, M. Nöthe, S. Ogaz, S. Oh, J. K. Parejko, N. Parley, S. Pascual, R. Patil, A. A. Patil, A. L. Plunkett, J. X. Prochaska, T. Rastogi, V. Reddy Janga, J. Sabater, P. Sakurikar, M. Seifert, L. E. Sherbert, H. Sherwood-Taylor, A. Y. Shih, J. Sick, M. T. Silbiger, S. Singanamalla, L. P. Singer, P. H. Sladen, K. A. Sooley, S. Sornarajah, O. Streicher, P. Teuben, S. W. Thomas, G. R. Tremblay, J. E. H. Turner, V. Terrón, M. H. van Kerkwijk, A. de la Vega, L. L. Watkins, B. A. Weaver, J. B. Whitmore, J. Woillez, V. Zabalza, and Astropy Contributors. The Astropy Project: Building an Open-science Project and Status of the v2.0 Core Package. *AJ*, 156(3):123, September 2018.

[99] Astropy Collaboration, Adrian M. Price-Whelan, Pey Lian Lim, Nicholas Earl, Nathaniel Starkman, Larry Bradley, David L. Shupe, Aarya A. Patil, Lia Corrales, C. E. Brasseur, Maximilian Nöthe, Axel Donath, Erik Tollerud, Brett M. Morris, Adam Ginsburg, Eero Vaher, Benjamin A. Weaver, James Tocknell, William Jamieson, Marten H. van Kerkwijk, Thomas P. Robitaille, Bruce Merry, Matteo Bachetti, H. Moritz Günther, Thomas L. Aldcroft, Jaime A. Alvarado-Montes, Anne M. Archibald, Attila Bódi, Shreyas Bapat, Geert Barentsen, Juanjo Bazán, Manish Biswas, Médéric Boquien, D. J. Burke, Daria Cara, Mihai Cara, Kyle E. Conroy, Simon Conseil, Matthew W. Craig, Robert M. Cross, Kelle L. Cruz, Francesco D'Eugenio, Nadia Dencheva, Hadrien A. R. Devillepoix, Jörg P. Dietrich, Arthur Davis Eigenbrot, Thomas Erben, Leonardo Ferreira, Daniel Foreman-Mackey, Ryan Fox, Nabil Freij, Suyog Garg, Robel Geda, Lauren Glattly, Yash Gondhalekar, Karl D. Gordon, David Grant, Perry Greenfield, Austen M. Groener, Steve Guest, Sebastian Gurovich, Rasmus Handberg, Akeem Hart, Zac Hatfield-Dodds, Derek Homeier, Griffin Hosseinzadeh, Tim Jenness, Craig K. Jones, Prajwel Joseph, J. Bryce Kalmbach, Emir Karamehmetoglu, Mikołaj Kałuszyński, Michael S. P. Kelley, Nicholas Kern, Wolfgang E. Kerzendorf, Eric W. Koch, Shankar Kulumani, Antony Lee, Chun Ly, Zhiyuan Ma, Conor MacBride, Jakob M. Maljaars, Demitri Muna, N. A. Murphy, Henrik Norman, Richard O'Steen, Kyle A. Oman, Camilla Pacifici, Sergio Pascual, J. Pascual-Granado, Rohit R. Patil, Gabriel I. Perren, Timothy E. Pickering, Tanuj Rastogi, Benjamin R. Roulston, Daniel F. Ryan, Eli S. Rykoff, Jose Sabater, Parikshit Sakurikar, Jesús Salgado, Aniket Sanghi, Nicholas Saunders, Volodymyr Savchenko, Ludwig Schwardt, Michael Seifert-Eckert, Albert Y. Shih, Anany Shrey Jain, Gyanendra Shukla, Jonathan Sick, Chris Simpson, Sudheesh Singanamalla, Leo P. Singer, Jaladh Singhal, Manodeep Sinha, Brigitta M. Sipőcz, Lee R. Spitler, David Stansby, Ole Streicher, Jani Šumak, John D. Swinbank, Dan S. Taranu, Nikita Tewary, Grant R. Tremblay, Miguel de Val-Borro, Samuel J. Van Kooten, Zlatan Vasović, Shresth Verma, José Vinícius de Miranda Cardoso, Peter K. G. Williams, Tom J. Wilson, Benjamin Winkel, W. M. Wood-Vasey, Rui Xue, Peter Yoachim, Chen Zhang, Andrea Zonca, and Astropy Project Contributors. The Astropy Project: Sustaining and Growing a Community-oriented Open-source Project and the Latest Major Release (v5.0) of the Core Package. *ApJ*, 935(2):167, August 2022.

[100] J. D. Hunter. Matplotlib: A 2d graphics environment. *Computing in Science & Engineering*, 9(3):90–95, 2007.

[101] Charles R. Harris, K. Jarrod Millman, Stéfan J. van der Walt, Ralf Gommers, Pauli Virtanen, David Cournapeau, Eric Wieser, Julian Taylor, Sebastian Berg, Nathaniel J. Smith, Robert Kern, Matti Picus, Stephan Hoyer, Marten H. van Kerkwijk, Matthew Brett, Allan Haldane, Jaime Fernández del Río, Mark Wiebe, Pearu Peterson, Pierre Gérard-Marchant, Kevin Sheppard, Tyler Reddy, Warren Weckesser, Hameer Abbasi, Christoph Gohlke, and Travis E. Oliphant. Array programming with NumPy. *Nature*, 585(7825):357–362, September 2020.

[102] David Radice, Ernazar Abdikamalov, Christian D. Ott, Philipp Mösta, Sean M. Couch, and Luke F. Roberts. Turbulence in core-collapse supernovae. *Journal of Physics G Nuclear Physics*, 45(5):053003, May 2018.

[103] Jeremiah W. Murphy, Joshua C. Dolence, and Adam Burrows. The Dominance of Neutrino-driven Convection in Core-collapse Supernovae. *ApJ*, 771(1):52, July 2013.

CHAPTER

3

THE INTERPLAY OF MAGNETIC FIELDS, TURBULENCE AND VORTICITY IN CORE-COLLAPSE SUPERNOVAE

David Calvert, Michael Redle, Bibek Gautam, Charles J. Stapleford, Carla Fröhlich, James P. Kneller, Matthias Liebendörfer

The following chapter will be submitted the the Astrophysical Journal

3.1 Abstract

The turbulent, vortical motion of the fluid below the shock in a core-collapse supernova amplifies the magnetic field present in the progenitor. The energy contained in the field is due to the work done by the fluid on the field which comes at the expense of the fluid's kinetic and internal energy. In addition to the energy exchange with the fluid, the magnetic field has an additional back-reaction upon the fluid vorticity via the baroclinic vector. In this paper we explore the interplay of the magnetic field, turbulence and vorticity in core-collapse supernovae using the ELEPHANT code. We find the magnetic field in the gain region never becomes so large (except in small localized patches) that it affects the global dynamics above the 10% level. The structure of the field quickly becomes a tangled mass of flux ropes. Energy exchange between the fluid and field occurs predominantly around the inner boundary of the gain region as long, narrow ribbons of adjacent loss and gain, so that it is difficult to identify where exactly the net energy of the field is generated. The energy exchange does not predominantly occur in the vicinity of the turbulence as identified using the Local-Spatial Average method. The highly-tangled field structure leads to a large contribution to the baroclinic vector that dominates over the hydrodynamic contribution to the vector. Whereas in the field-free simulations the baroclinic vector is largest around the base of the downflows that thread the gain region from the shock to the proto-neutron star, in the simulations with a magnetic field the baroclinic vector is large over a much greater volume of the gain region. Although governed by very similar transport/evolution equations to the magnetic field, the vorticity/enstrophy is closely associated with the turbulent kinetic energy and concentrates around the downflows. The fluid vorticity and magnetic field are always close to being randomly aligned.

3.2 Introduction

At the present time a general consensus has been reached that the mechanism by which most massive stars explode as core-collapse supernovae (CCSNe) is due to the 'neutrino heating mechanism' [1, 2, 3]: the stalled shock is revived due to energy deposition by neutrinos into material located in a 'gain region' below the shock. While simulations of CCSNe in spherical symmetry consistently fail to explode - except for the lightest progenitors [4, 5] – via the neutrino heating mechanism [6, 7, 8, 9, 10], multi-dimensional simulations have achieved unaided explosions [11, 12, 13, 14, 15, 16, 17, 18, 19, 20]. This difference indicates that, in addition to the heating by the neutrinos, multi-dimensional effects somehow aid

the explosions. Among these multi-dimensional effects are magnetic fields.

Many 3D simulations of CCSNe do not regularly include magnetic fields even though the formation of pulsars and magnetars in CCSNe would require them. Long-duration GRBs are associated with CCSNe [21, 22] and the relativistic jets that pierce the outer layers of the star are expected to possess strong magnetic fields. Magnetorotationally-driven supernovae are often proposed as alternatives to the neutrino heating mechanism for fast spinning, highly magnetized stars [23, 24, 14]. To date the few simulations that have included magnetic fields have reported a mixture of results. [25] showed that explosion energies can vary by over an order of magnitude depending upon the strength and morphology of the initial magnetic field. In some cases, they also found the supernova explosion to be caused primarily by the pressure from the magnetic fields rather than the neutrino heating. The inclusion of magnetic fields and rotation in simulations of a 20 $M_{\odot}$ star was found to be the difference between achieving an explosion or not by [14]. More recently [26] found that if the magnetic field reached magnetar-level strength at an early enough time in their simulations [27, 28], the shocks were revived sooner and with much more energy when they included magnetic fields when compared to the unmagnetized simulations. However in a set of simulations where the initial field of the progenitor was not as strong, [18] found that the field had little effect upon the dynamics.

The magnetic field in a CCSN is the twisted and amplified field of the progenitor star. The magnetic fields of progenitors are expected to be large due to the action of a small-scale turbulent dynamo that operates during the late burning stages (e.g. oxygen burning) [29]. Field strengths of 10^{10} G are readily achieved in models. Once the star begins to collapse, the magnetic field will amplify due to compression and stretching even before the fluid passes through the shock. Once inside the shock, the evolution is more dynamic and complicated. The growth of the field energy inside the shock has been attributed to instabilities such as the magnetorotational instability (MRI) [30] by field stretching due to turbulence [31], a Standing Accretion Shock Instability (SASI)[32, 33, 34], or small-scale turbulent dynamos from the onset of neutrino driven convection [26]. However it grows, if the field becomes large enough, it affects the fluid through well-known effects such as magnetic buoyancy [35] and the field's contribution to the baroclinic vector. The baroclinic vector generates vorticity, a metric often taken to be the defining characteristic of turbulence [36, 37].

The purpose of our paper is to investigate the interplay of the magnetic field, turbulence and vorticity in CCSNe. Our study is a continuation of [38]. We explore the interplay of magnetic field, turbulence and vorticity by simulating six core-collapse supernovae in

three spatial dimensions using the ELEPHANT code [39, 40, 41]. This code is ideal for this study because of its good spatial resolution throughout the simulation volume. Our paper is organized as follows. The code, the progenitors, the initial magnetic field and the initial rotation profiles are described in section §3.3.1. We then present our results in section §3.3.3, where we dig into the global properties of the simulations before looking more closely at the magnetic field structure, the energy exchanged between the field and fluid, the turbulent kinetic energy, and the vorticty/enstrophy. We summarize and present our conclusions in section §3.7

3.3 The Simulations

3.3.1 The ELEPHANT code

The ELEPHANT code, described in detail in [41, 40, 39], solves the equations of ideal MHD as a function of position $\vec{x}$ and time t in a modified Newtonian gravitational potential, and uses the Isotropic Diffusion Source Approximation (IDSA) for the neutrino transport scheme [41]. The equations are solved using operator splitting into the magnetohydrodynamic equations and the neutrino transport equations. The magnetohydrodynamic equations that are solved are:

$$\frac{\partial \rho}{\partial t} + \nabla \cdot (\rho\, \vec{v}) = 0, \tag{3.1}$$

$$\frac{\partial}{\partial t}(\rho\, v_i) + \frac{\partial}{\partial x_j}(\rho\, v_i\, v_j - b_i\, b_j + P\, \delta_{ij}) = -\rho\, \frac{\partial \phi}{\partial x_i}, \tag{3.2}$$

$$\frac{\partial E}{\partial t} + \nabla \cdot \left[(E+P)\, \vec{v} - (\vec{v}\cdot\vec{b})\, \vec{b}\right] = -\rho\, \vec{v} \cdot \nabla \phi, \tag{3.3}$$

$$\frac{\partial}{\partial t}(\rho\, Y_e) + \nabla \cdot (\rho\, Y_e\, \vec{v}) = 0, \tag{3.4}$$

$$\nabla^2 \phi = 4\pi\, G\, \rho, \tag{3.5}$$

$$\frac{\partial \vec{b}}{\partial t} - \nabla \times \left(\vec{v} \times \vec{b}\right) = \vec{0}, \tag{3.6}$$

$$\vec{\nabla} \cdot \vec{b} = 0, \tag{3.7}$$

where ρ is the baryonic mass density, $\vec{v}$ the fluid velocity, the electron fraction is represented by Y_e, and the gravitational potential by ϕ. As usual, G is the gravitational constant. The vector $\vec{b}$ is the reduced magnetic field, related to the true magnetic field $\vec{B}$ in

Gaussian units by $\vec{B} = \sqrt{4\pi}\,\vec{b}$. The temperature T is not explicitly part of the state vector but found from the specific internal energy $e = e(\rho, T, Y_e)$, and the total energy density $E = \rho\, e + \rho\, v^2/2 + (\vec{b}\cdot\vec{b})/2$. We compute the thermal pressure $P_{\rm th} = P_{\rm th}(\rho, T, Y_e)$ using the [42] equation of state (EOS) with an incompressibility parameter $K = 220$ MeV, and the magnetic pressure is $P_{\rm mag} = (\vec{b}\cdot\vec{b})/2$. The total pressure P is $P = P_{\rm th} + P_{\rm mag}$. The gravitational potential is modified following [43] to include general relativistic corrections. In addition, the staggered constrained transport method (CT) proposed by [44] is applied to ensure that the constraint $\nabla\cdot\vec{b} = 0$ in (3.7) is fulfilled (within numerical error) for all time: see [40]. The MHD equations (3.1)-(3.6) are solved using the second-order relaxation scheme of [45]. To enforce that the scheme is total variation diminishing (a nonlinear constraint to ensure stability), ELEPHANT implements the min-mod limiter in supersonic flow regimes and the van Leer limiter in subsonic regimes [40]. For the time integration, a second-order predictor corrector method is used.

The underlying idea of IDSA is that for each neutrino flavor, the population can be separated into a trapped neutrino fraction with a distribution function $f_\nu^{(t)}$, and a free-streaming neutrino population with a distribution function $f_\nu^{(s)}$. These two populations evolve separately connected by a "diffusion source" Σ_ν which converts trapped neutrino into free-streaming ones, and vice versa. First, for the trapped neutrinos we define the trapped neutrino fraction $Y_\nu^{(t)}$ and the the mean neutrino specific energy Z_ν for flavor ν as

$$Y_\nu^{(t)} = \frac{m_b}{\rho}\frac{4\pi}{(hc)^3}\int f_\nu^{(t)} E^2\, dE\, d\mu \tag{3.8}$$

$$Z_\nu^{(t)} = \frac{m_b}{\rho}\frac{4\pi}{(hc)^3}\int f_\nu^{(t)} E^3\, dE\, d\mu \tag{3.9}$$

with m_b the baryon mass. The trapped neutrino fraction $Y_\nu^{(t)}$ and the the mean neutrino specific energy $Z_\nu^{(t)}$ for flavor ν evolve according to the equations

$$\frac{\partial}{\partial t}\left(\rho\, Y_\nu^{(t)}\right) + \nabla\cdot\left(\rho\, Y_\nu^{(t)}\,\vec{v}\right) = 0, \tag{3.10}$$

$$\frac{\partial}{\partial t}\left[\left(\rho\, Z_\nu^{(t)}\right)^{\frac{3}{4}}\right] + \nabla\cdot\left[\left(\rho\, Z_\nu^{(t)}\right)^{\frac{3}{4}}\vec{v}\right] = 0. \tag{3.11}$$

These two equations are solved simultaneously with the MHD equations (3.1) through (3.7). In the IDSA step, the trapped neutrino distribution functions are reconstructed from $Y_\nu^{(t)}$ and $Z_\nu^{(t)}$ assuming a thermal spectrum. With $f_\nu^{(t)}$ in hand, ELEPHANT then solves the diffu-

sion equation given by

$$\frac{1}{c}\frac{\partial f_\nu^{(t)}}{\partial t} = j_\nu - (j_\nu + \chi_\nu) f_\nu^{(t)} - \Sigma_\nu. \tag{3.12}$$

with j_ν the spectral neutrino emissivity, χ_ν the neutrino absorptivity, and ϕ_ν includes isoenergetic scattering (see [46]). The "diffusion source" term Σ_ν for flavor ν is taken to be

$$\Sigma_\nu = \min\left\{\max\left[\alpha_\nu + \frac{1}{2}(j_\nu + \chi_\nu)\int f_{\nu,0}^{(s)}\, d\mu,\, 0\right], j_\nu\right\}, \tag{3.13}$$

with

$$\alpha_\nu = \nabla\cdot\left(\frac{-1}{3(j_\nu + \chi_\nu + \phi_\nu)}\nabla f_\nu^{(t)}\right). \tag{3.14}$$

Here $f_{\nu,0}^{(s)}$ denotes the distribution function of the free-streaming neutrinos from the previous time step. The non-local diffusion term α_ν is computed by explicit finite differencing; all other unknowns in the IDSA step are solved using an implicit Euler time step using the Newton-Raphson iterative solver. That is, the numerical solution of equation (3.12) sets the net interaction rates s_ν between the matter and neutrino flavor ν which is then used to updates the electron fraction Y_e and the specific internal energy e of the fluid so that they are consistent. The net interaction rates are given by

$$s_\nu = \frac{1}{c}\frac{\partial f_\ell}{\partial t} + \Sigma_\nu - \frac{(j_\nu + \chi_\nu)}{2}\int f_\nu^{(s)} d\mu \tag{3.15}$$

and the electron fraction Y_e and the specific internal energy e of the fluid are updated according to

$$\frac{\partial Y_e}{\partial t} = -\frac{4\pi}{h^3 c}\frac{m_b}{\rho}\int (s_{\nu_e} - s_{\bar{\nu}_e}) E^2 dE \tag{3.16}$$

$$\frac{\partial e}{\partial t} = -\frac{4\pi}{h^3 c}\frac{m_b}{\rho}\int (s_{\nu_e} - s_{\bar{\nu}_e}) E^3 dE. \tag{3.17}$$

The rates j_ν, χ_ν, and ϕ_ν are then adjusted according to the new values of the electron fraction and specific internal energy which then update the trapped neutrino fraction $Y_\nu^{(t)}$ and mean energy $Z_\nu^{(t)}$ seen in equations (3.10) and (3.11). This iterative scheme is repeated until convergence is achieved. The IDSA transport scheme is easily parallelizable because the only non-local quantity is α_ν and the grid zones do not need to communicate much with each other within the iterative solve. At the end of the IDSA step the fluid velocity is

updated via

$$\frac{\partial \vec{v}}{\partial t} = -\frac{1}{\rho}\nabla\left(\frac{\rho Z_{\nu}^{(t)}}{3m_b}\right) \tag{3.18}$$

The computational domain of ELEPHANT consists of a 3D Cartesian cuboid for the innermost region of the supernova surrounded by a 1D spherically symmetric domain for the outer layers of the progenitor star. More details on the implementation of the hydro equations in ELEPHANT on a 3D uniform Cartesian mesh, together with test cases, can be found in [40]. The larger, spherically symmetric domain surrounding the 3D cuboid is evolved on an adaptive grid using the AGILE-IDSA solver [41]. The spherically symmetric solution is used primarily for the properties of the material falling through the boundary of the 3D mesh, but since it extends into the inner part of the Cartesian grid, it also provides a second solution of the equations that is particularly useful within the PNS where it serves as a check of the entropy evolution. The 1D solution also gives us the ability to enlarge the 3D Cartesian cuboid when the shock expands and reaches the boundary of the 3D cuboid. With this setup of the computational domain, the ELEPHANT code has high 3D spatial fidelity in the region below the shock without the burden of a large number of grid zones where the solution is spherically symmetric. Hence, it is ideally suited for the proposed study of the post-bounce phase especially for the growth of the turbulence in the shocked material.

3.3.2 The Progenitor Model

For our study we adopt two solar-metallicity progenitor stars of 15 and 20 $M_{\odot}$ zero-age main sequence (ZAMS) mass of [47] used in our previous study [38]. In this paper, we will refer to the simulations by a codename composed of the progenitor mass and magnetic field, sXX-TYY, where 'XX' is the mass of the progenitor model and 'YY' is the log base ten of the field strength parameter B_0 in Gauss, i.e. $B_0 = 10^{\mathrm{YY}}$ Gauss. For the magnetic field-free cases, the name of the run will instead use the word "Control" for the magnetic field. The nomenclature is outlined in Table 3.1. The progenitors do not have any rotation nor magnetic field included, and thus we must impose both of these properties onto the progenitor.

The magnetic field we insert is a very simple toroidal field. Our initial field configuration is deliberately simple so that the amount of field growth during the collapse phase before the fluid passes through the shock is minimized. This allows us to focus on the processes that cause the field to grow inside the gain region as opposed to accretion through

the shock. In other studies of magnetic fields in supernovae, authors have adopted split-monopole fields [32, 33, 34] or pure poloidal fields [48, 49, 28, 26]. Mixed toroidal/poloidal field configurations were used in Sykes & Müller [18].

We start from the vector potential $\vec{A}_T$ given by

$$\vec{A}_T = B_0\, r\, \sin\theta\, \hat{\mathbf{k}}, \tag{3.19}$$

where B_0 is a parameter that sets the magnetic field strength. Similar to [50], this vector potential is then scaled by the square root of the initial mass density profile so as to avoid the magnetic pressure overwhelming the thermal pressure. Thus our initial magnetic field has the form

$$\vec{B} = \nabla \times \left(\sqrt{\frac{\rho}{\rho_0}} \vec{A}_T \right), \tag{3.20}$$

which implies the initial field has two components,

$$\vec{B} = \sqrt{\frac{\rho}{\rho_0}} \left(\nabla \times \vec{A}_T \right) + \frac{\left(\nabla \sqrt{\rho} \right) \times \vec{A}_T}{\sqrt{\rho_0}}. \tag{3.21}$$

Here, ρ_0 is a reference density set to $\rho_0 = 10^{10}$ g/cm^3. Both terms on the right hand side of equation (3.20) are toroidal in the sense that the field lines are circles in the xy-plane. The first term is the density-scaled toroidal field as desired; the second is also a toroidal field but (i) it winds in the opposite direction because the density decreases with r; and (ii) it has a strength that is proportional to $\sin\theta$, i.e., it is strongest in the xy-plane. On a discrete level, the initial magnetic field is implemented as follows. For the magnetic field values inside the cuboid, the curl in (3.20) is computed on the cell interfaces using the central differences for each directional derivative. These derivatives are calculated using the cell center values of $\sqrt{\rho}\,\vec{A}_T$, resulting in an initial magnetic field on a staggered mesh which is guaranteed to be divergence-free.

As we said, `ELEPHANT` uses an inner cuboid embedded in a larger, 1D spherically symmetric domain. The solution in the spherical domain provides the hydrodynamical quantities advecting into the cuboid, however it does *not* provide information on the configuration of the magnetic field. Our solution for the advected magnetic field is to construct a field in the boundary cells using the same algorithm used to build the initial field within the Cartesian grid, and then correct the field so that the divergence of the accreting field vanishes.

We also add a small amount of rotation into the progenitor. The rotation profile we

Table 3.1: Initial Parameters of Simulations

Run Name	Progenitor	B_0 (G)	Ω_{rot} (rad/s)	$r_{\rm rot}$ (km)
s15 Control	s15	0	0	250
s15 T10	s15	10^{10}	0.3	250
s15 T12	s15	10^{12}	0.3	250
s20 Control	s20	0	0	250
s20 T10	s20	10^{10}	0.3	250
s20 T12	s20	10^{12}	0.3	250

adopt is described by two parameters, Ω_{rot} and r_{rot}. The first step is to calculate values for the specific angular momentum L/m for each AGILE zone i according to

$$\frac{L}{m} = \frac{2}{3}\Omega_{rot}\,\frac{r_i^2\,r_{rot}^2}{(r_i^2+r_{rot}^2)}, \tag{3.22}$$

where r_i is the radius of the i'th AGILE grid zone, r_{rot} is a scaling factor to determine at what radius L/m becomes the moment of inertia of a spherical shell, and Ω_{rot} is the input parameter corresponding to the angular velocity of the spherical shell. ELEPHANT records the specific angular momentum for the AGILE zones in a table alongside the mass coordinate of each AGILE zone. To find the initial velocity of grid zone j in the 3D domain ELEPHANT performs a linear interpolation to find the L/m for the zone given its mass coordinate, then computes the z component of the angular velocity Ω_z for that grid cell according to

$$\Omega_z = \frac{3}{2\,r_j^2}\left(\frac{L}{m}\right) \tag{3.23}$$

ELEPHANT then assigns the velocity components v_x and v_y for the cell to be $v_x = -r_y\,\Omega_z$ and $v_y = r_x\,\Omega_z$. As the simulation evolves, material that is newly accreted into the 3D domain is assigned velocity components that follow from the conservation of angular momentum. Note that while the accretion of material into the 3D domain means the angular momentum inside the 3D domain is not conserved, the MHD equations in 3.3.1 are evolved with a momentum and angular momentum preserving scheme so the angular momentum growth in the 3D domain is solely due to accretion. For the simulations in this work, we have selected $r_{rot} = 250$ km for all simulations and use $\Omega_{rot} = 0.3$ rad/s for those that include rotation. The six simulations are summarized in Table 3.1.

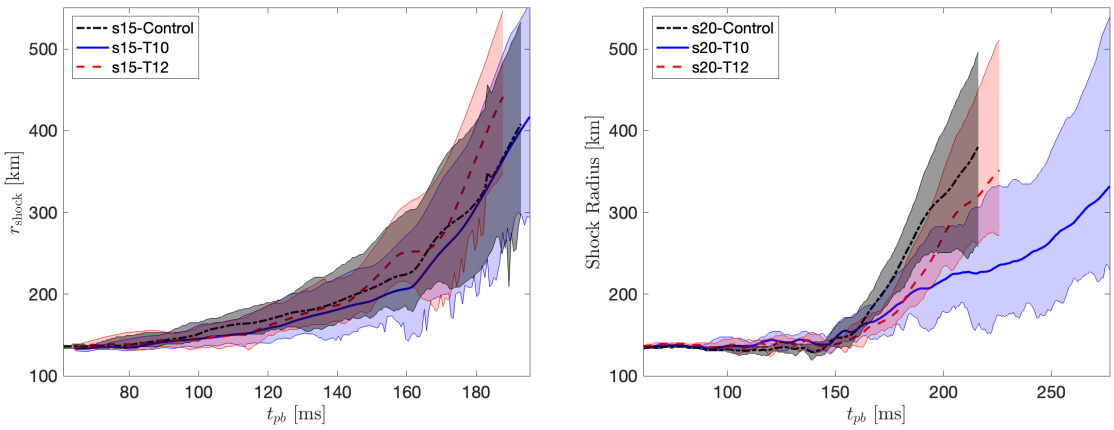

Figure 3.1: Average, minimum and maximum shock radii as a function of the post-bounce time for the s15 (left) and s20 (right) simulations.

3.3.3 General Properties of the Simulations

We begin the presentation of our results by discussing some general properties of our simulations: the evolution of the shock radius, entropy, and the mass accretion. For each simulation we adopt a uniform fidelity of 1 km throughout the 3D volume; initially, the 3D volume encompasses the innermost 600 km of the star (i.e., along each axis the 3D volume ranges from -300 km to +300 km). When the shock reaches the edge of the 3D computational domain, we expand the 3D domain by adding 100 km in both the negative and positive directions along each coordinate axis. We expand the 3D volume twice and stop the simulation when the shock reaches 500 km in any direction.

We show in the panels of Figure 3.1 the average shock radius (various line styles) for each simulation along with its minimum and maximum position (shaded bands). The left panel of Figure 3.1 is the data for the simulations using the s15 progenitor, while the right panel is the data for the simulations using the s20 progenitor. For the s15 progenitor cases, the T10 simulation lags the Control and T12 by a few tens of kilometers after $t_{\rm pb} \sim 150$ ms. For the s20 progenitor, the shock revival is delayed relative to the s15 until $t_{\rm pb} \sim 150$ ms. After $t_{\rm pb} \sim 150$ ms, T10 falls behind the shock radius in the Control and T12 simulations. We find no evidence for a standing accretion shock instability (SASI) [51, 52] in any of our simulations - we refer the reader to [32, 33, 34] for studies of the growth of the magnetic field in simulations where the SASI does appear.

In Figure 3.3 we plot 2D slices of the entropy for the three s20 simulations. The low-entropy, pre-shocked material and the low-entropy proto-neutron star form the innermost

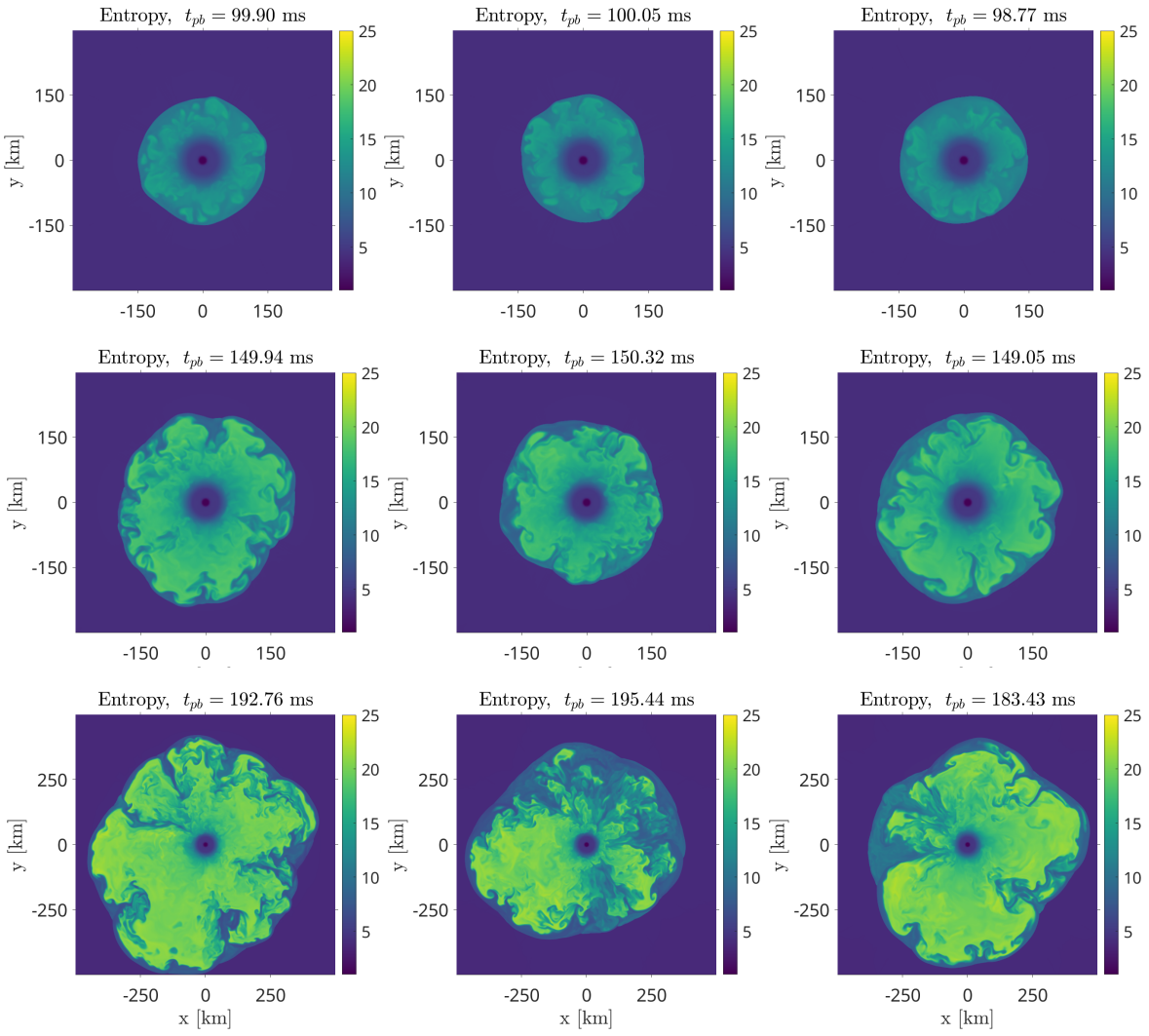

Figure 3.2: The entropy for the s15-Control (left), s15-T10 (middle), and s15-T12 (right) simulations at the post-bounce times of ~ 100 ms (first row), ~ 150 ms (second row), and at final time for each simulation (third row).

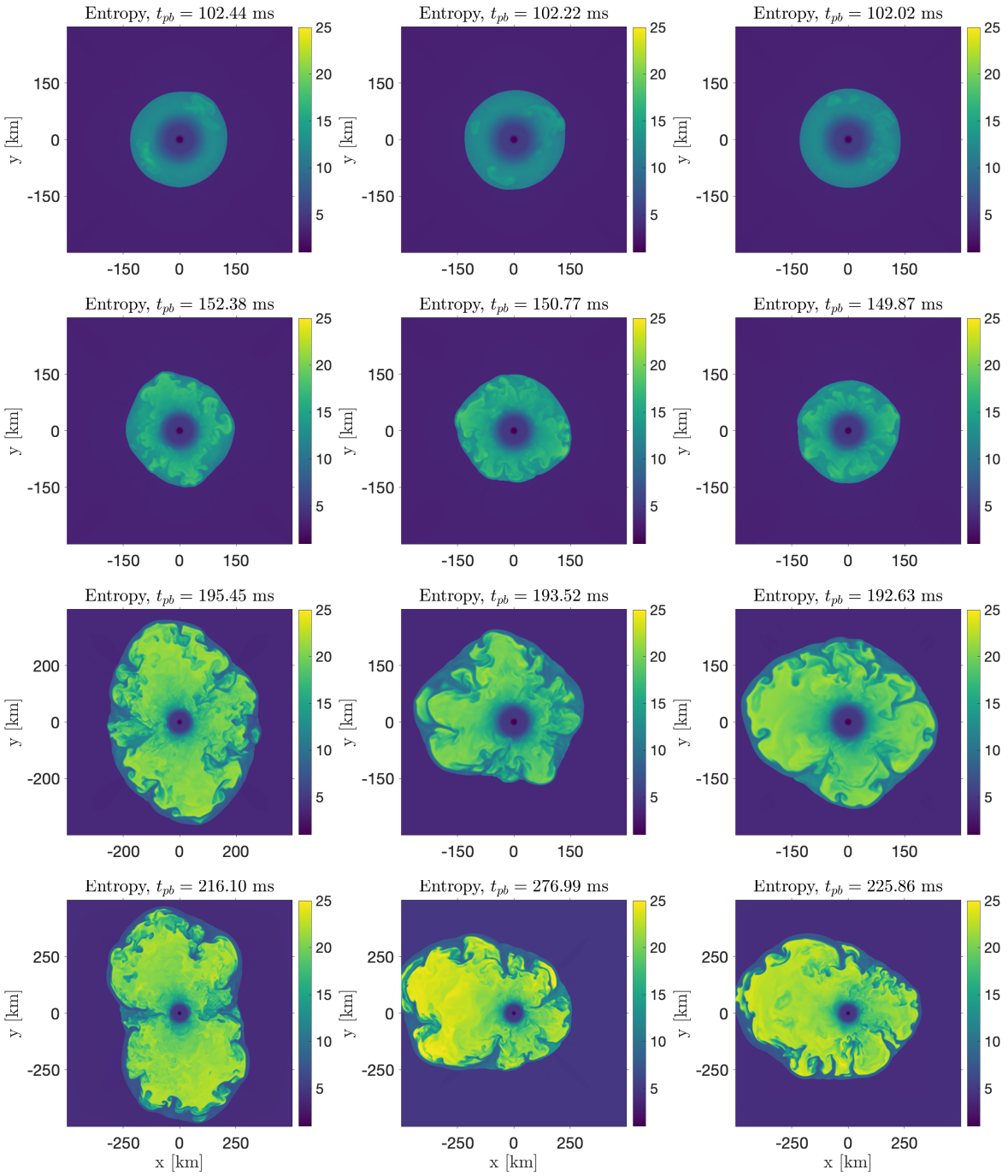

Figure 3.3: The entropy for the s20-Control (left), s20-T10 (middle), and s20-T12 (right) simulations at the post-bounce times of ∼ 102 ms (first row), ∼ 150 ms (second row), ∼ 193 ms (third row), and at final time (last row).

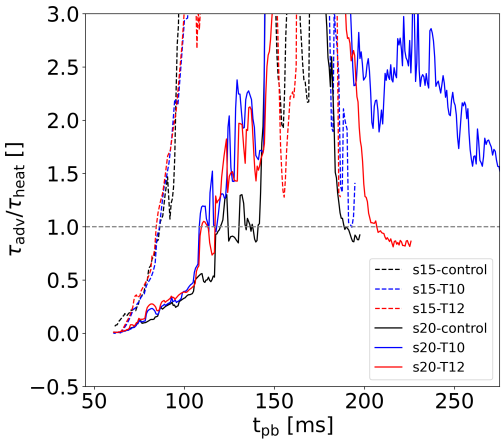

Figure 3.4: The ratio of advection timescale to heating timescale as a function of the post-bounce time.

and outermost layers. Between them is the gain region, which we define as the interior region of the shock where the entropy exceeds $S > 5\,k_B$/baryon, the density is less than $\rho < 10^{10}$ g/cm^3, and the neutrino heating is positive. The spherical symmetry of the initial collapse, proto neutron star formation, shock formation and expansion is broken by neutrino heating at approximately 100 ms postbounce in all three simulations. By 150 ms postbounce the shock is noticeably aspherical, and by 195 ms postbounce the presence of low entropy downflows piercing through large convective plumes are seen. Note that 195 ms postbounce is after the shock was seen to be revived in Figure 3.1. By the end of the simulation the shock front has expanded preferentially into one hemisphere. The evolution of the entropy is similar to that seen previously in multi-D simulations, such as [2, 53, 54] to name a few.

The shock is revived due to the neutrino heating of the material in the gain region. There are two relevant timescales that we need to consider: the heating timescale which is the time it would take for the neutrinos to deposit enough energy to unbind the material, and the advection timescale which is the time that matter spends in the gain region. For shock revival, the heating timescale must become shorter than the advection timescale. To define the two timescales precisely, we adopt the definitions used in [55] which were also used in [38].

Figure 3.4 shows the ratio of the advection timescale to the heating timescale as a function of the post-bounce time for all six simulations. In the simulations suing the s15 progenitor the ratio exceeds unity as early as $t_{pb} \approx 80$ ms, whereas the ratio exceeds unity in

the simulations using the s20 progenitor only at $t_{\rm pb} \approx 120$ ms. The magnetic field we inserted into the progenitors appears to have little effect on the ratio of the two timescales, except in the case of s20-T10 after $t_{\rm pb} \approx 200$ ms. The delay of $\tau_{adv}/\tau_{heat} = 1$ in the s20 simulations relative to s15, and the insensitivity to the imposed field except for the s20-T10 at late times, are consistent with the interpretation of Figure 3.1.

In summary, the results shown in this section from our simulations are broadly consistent with other 3D simulations using the same progenitors [56, 57, 58, 59, 60, 61, 62, 63, 64, 19, 65, 66]. We now proceed to more closely examine the magnetic field, the turbulence, and the vorticity/enstrophy in the simulations.

3.4 The Magnetic Field

The magnetic field at a given point and time within the supernova will evolve due to processes which are typically divided into the three categories of 'advection', 'stretching', and 'compression' [67, 68]. The field passing through a fluid element begins its evolution due to compression and stretching even before the element reaches the shock. For radial infall, the solid angle subtended by a spherical wedge-shaped mass element does not change as it falls inwards. Since the fluid is taken to be a perfect conductor and thus the magnetic field is frozen in the fluid, the magnetic flux through the faces of the mass element are conserved. This means the components of the field grow as

$$b_r(r) = b_r(r_0)\left(\frac{r_0}{r}\right)^2, \tag{3.24}$$

$$b_{\theta,\phi}(r) = b_{\theta,\phi}(r_0)\left(\frac{r_0}{r}\frac{dr_0}{dr}\right), \tag{3.25}$$

where r_0 is the initial location of the mass element. The ratio dr/dr_0 is the radial stretch factor. For the case of pure freefall, the stretch factor is given by an analytic, albeit complicated, expression; see Appendix §3.9. As the mass element falls towards the core and r_0/r increases, both the radial and non-radial (transverse) components the field grow due to compression. For the radial component, this is the only contributing factor to the growth. For the non-radial components there is a dependence upon the stretch factor dr/dr_0. For material that is initially well outside the core, the radial stretching of a mass element is initially small, resulting in $dr/dr_0 \approx 1$. Thus, if there is a non-zero transverse component of the field at the initial location of the fluid element, this component grows as $1/r$ during the initial phase of collapse compared to the $1/r^2$ growth of the radial component. As

the mass element falls further, the stretch factor dr/dr_0 begins to increase from unity and eventually will scale as $1/\sqrt{r}$ when the mass elements are in freefall, indicating that the growth of the transverse components of the magnetic field slows to $1/\sqrt{r}$. In contrast, if there is a non-zero radial component of the magnetic field through a mass element at its initial location equation (3.24) indicates that this component grows as $1/r^2$ through the collapse. Therefore, if the initial magnetic field passing through a mass element has both transverse and radial components, the field will become increasingly dominated by the radial field as the fluid collapses. This leads to field configurations which resemble the split monopole as seen in [49, 26] and used by [32, 33, 34] as the initial magnetic field in their simulations. Rotation of the star will modify these expectations (a mass element gets squeezed in the transverse direction because the orbital planes defining the faces of the mass element must intersect at some point) but the squeezing is only important if the mass element completes a substantial fraction of an orbit.

As the fluid element falls, the magnetic field energy of the element grows due to the compression no matter its orientation. However the rate of growth of the field energy density *relative* to the kinetic energy density of the element does depend upon the orientation. The density of the fluid element increases as $\rho(r) \propto (1/r^2)(dr_0/dr)$ and the fluid velocity grows as $v(r) \propto 1/\sqrt{r}$ for pure freefall in the weak field limit. Pulling these together, the fluid kinetic energy density thus scales as $E_{kin} \propto (1/r^3)(dr_0/dr)$. For an initial mass density profile that falls off rapidly with r_0 and for $r \ll r_0$, $dr_0/dr \propto \sqrt{r}$ and so $E_{kin} \propto 1/r^{5/2}$.

If the field is purely transverse, the magnetic field energy density, $E_b = |\vec{b}|^2/2$, scales as $E_b \propto (1/r^2)(dr_0/dr)^2$. Therefore the ratio of magnetic to kinetic energy density is seen to scale as $E_b/E_{kin} \propto r(dr_0/dr)$, indicating the ratio decreases as the element falls radially inward. For the case of a pure radial field, $E_b \propto (1/r^4)$ and the ratio E_b/E_{kin} is seen to scale as $E_b/E_{kin} \propto 1/(r\,dr_0/dr)$, meaning the ratio increases as the element falls. It is this scaling during the collapse that motivates our decision to focus upon initially pure toroidal magnetic fields because it allows us to better observe the processes which generate the magnetic field within the shock rather than advecting a lot of field energy.

The evolution of the magnetic field becomes much more complicated once the fluid passes through the shock, as seen in [26]. The standard paradigm for the growth of the magnetic field is the amplification of the field lines due to streamline stretching [67]. This picture emerges by combining the evolution of the magnetic field, given by equation (3.6),

with the mass continuity equation (3.1), to produce

$$\frac{\partial}{\partial t}\left(\frac{\vec{b}}{\rho}\right)+(\vec{v}\cdot\nabla)\left(\frac{\vec{b}}{\rho}\right)-\left(\frac{\vec{b}}{\rho}\cdot\nabla\right)\vec{v}=0. \tag{3.26}$$

This combination of time and spatial derivatives is often known as the fluid derivative. The interpretation of this equation emerges from considering the vector $\Delta\vec{x}$ which connects two fluid elements. This vector evolves (to linear order in $\Delta\vec{x}$) according to the similar equation

$$\frac{\partial}{\partial t}(\Delta\vec{x})+(\vec{v}\cdot\nabla)(\Delta\vec{x})-(\Delta\vec{x}\cdot\nabla)\ \vec{v}=0. \tag{3.27}$$

Thus if we consider two fluid elements along a field line, i.e. they satisfy $\vec{b}/\rho\propto\Delta\vec{x}$, then as the distance between the fluid elements grows, the magnetic field must also grow, assuming the fluid is incompressible. The growth of the field continues until the magnetic field has become sufficiently large to induce a back-reaction upon the fluid.

If the magnetic field grows, the energy in the field increases. From equation (3.6) one can derive that the magnetic field energy density $E_{\rm mag}=(\vec{b}\cdot\vec{b})/2$ grows as

$$\begin{aligned}\frac{\partial E_{\rm mag}}{\partial t}+\nabla\cdot\vec{S}_{\rm mag} &= -\vec{v}\cdot\left[(\nabla\times\vec{b})\times\vec{b}\right], &(3.28)\\ &= \vec{v}\cdot\nabla E_{mag}-\vec{v}\cdot(\vec{b}\cdot\nabla)\vec{b} &(3.29)\end{aligned}$$

where $\vec{S}_{\rm mag}=\vec{v}(\vec{b}\cdot\vec{b})-\vec{b}(\vec{v}\cdot\vec{b})$ is the Poynting vector. Note that if the velocity and magnetic field are aligned/anti-aligned, the Poynting vector is zero. The term on the right hand side of equation (3.28) is the rate at which magnetic field energy is exchanged with the fluid. Note that if the velocity and magnetic field are aligned/anti-aligned then this term goes to zero. Thus, the fluid can only do work on the magnetic field if the fluid velocity is not parallel/anti-parallel with the magnetic field. The right hand side of equation (3.29) shows that the energy exchanged between the field and the fluid can be split into the energy exchanged due to the magnetic pressure gradient, and the field curvature.

3.4.1 The Total Magnetic Field Energy in the Gain Region

The left panel of Figure 3.5 shows the integrated magnetic energy within the gain region for all four simulations with magnetic fields that we undertook, and the total kinetic energy in the gain region of all simulations as a reference. We observe that for all the simulations with magnetic fields, the total magnetic field energy in the gain region is smaller than the

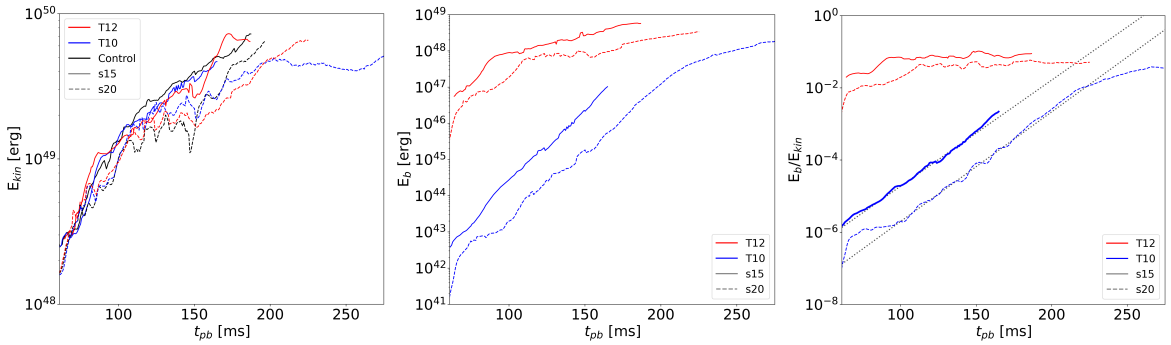

Figure 3.5: Kinetic energy (left) and magnetic field energy (middle) in the gain region as a function of the post-bounce time for the s20 (dashed) and s15 (solid) simulations. Right: Ratio of magnetic to kinetic energy. Two fits of the form $y = 10^{0.03x}$ are shown in black.

kinetic energy in the gain region by at least an order of magnitude. The s15 models have a larger amount of magnetic field energy - by a factor of approximately 3-10 - than the two s20 simulations. The growth of the magnetic field energy in the gain region is due to an increasing volume of the gain region, the net accumulation of field energy through the shock minus that lost through the inner boundary, and the conversion of fluid energy into field energy inside the gain region. Before convection begins, the magnetic field energy in the gain region grows only due to accretion of the field through the shock and compression. After convection is initiated at $t_{\rm pb} \approx 80-100$ ms, there is a temporary and rapid increase in the growth rate of the magnetic field energy which lasts for ~ 20 ms in the two T12 simulations. This feature is similar to the one seen in [26], in which they attribute this growth to the operation of a small-scale dynamo formed once the neutrino-driven convection is initiated. A small-scale dynamo mechanism converts fluid kinetic energy at scales below the turbulence forcing scale into magnetic field energy (although the ultimate source of the fluid energy may be different e.g. gravitational potential energy). After $t_{\rm pb} \approx 120$ ms the field energy in the two T12 simulations grows at a rate similar to the kinetic energy while the field energy in the two T10 simulations continues to grow exponentially. Note that the amount of magnetic field energy in the gain region shown in Fig. 3.5 is slightly larger (by a factor of a few) than the energies seen in [18], who found values for their simulations that were in the range $10^{47}-10^{48}$ erg.

The similarity of the growth rates of the field energy and kinetic energy in the T12 simulations after $t_{\rm pb} \sim 120$ ms suggests that the ratio of the two may be almost constant. This is verified in the right panel of Figure 3.5 where we plot the ratio of magnetic to kinetic energy for the four simulations that include the field. In the two T12 simulations we still

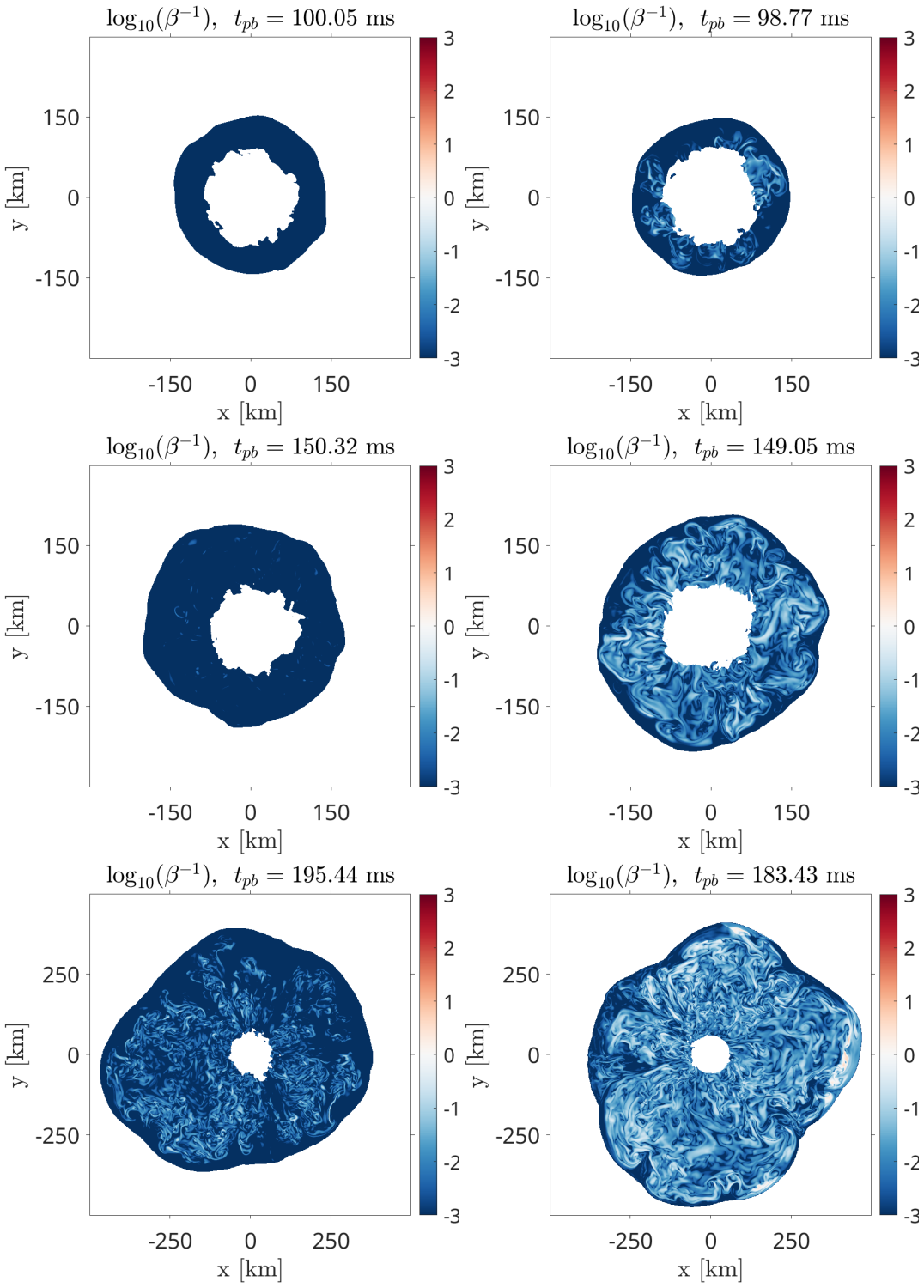

Figure 3.6: Inverse of plasma beta, scaled logarithmically, for the s15-T10 run (left column) and s15-T12 run(right column) at the post-bounce times of $\sim$ 100 ms (top row), $\sim$ 150 ms (middle row), and at the final simulation time for each simulation (bottom row). Note the change of domain size in the last row as the shock expands.

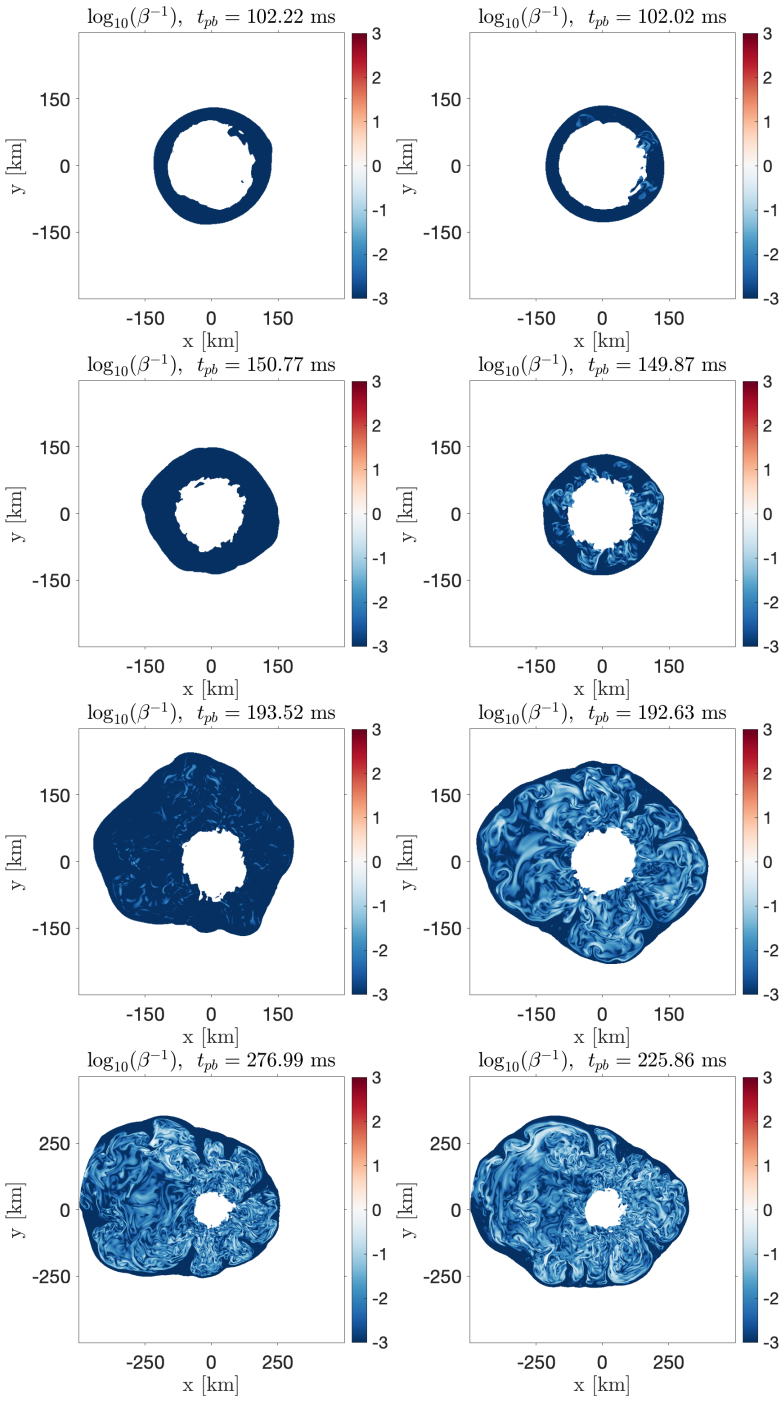

Figure 3.7: Inverse of plasma beta, scaled logarithmically, for the s20-T10 run (left column) and s20-T12 run(right column) at the post-bounce times of $\sim$ 150 ms (top row), $\sim$ 193 ms (middle row), and at the final simulation time for each simulation (bottom row). Note the change of domain size in the last row as the shock expands.

see the rapid rise in the magnetic field energy around $t_{\rm pb} \approx 80-100$ ms and thereafter the ratio of the two energies is almost constant at $E_b/E_{\rm kin} \approx 5\%$ for the simulation using the s20 progenitor, and 8% for the simulation using the s15 progenitor. We note that this plateau in the ratio is reached before the shock is revived at $t_{\rm pb} \sim 150$ ms. In contrast, the ratio of the field energy to kinetic energy in the gain region in the two T10 simulations grows approximately exponentially until the magnetic field energy is a few percent of the kinetic energy. Thereafter the ratio appears to approach the same, approximately constant, ratio of $E_b/E_{\rm kin} \approx 5\%-8\%$. We caution that this ratio of magnetic to kinetic energy is likely to be influenced by the spatial resolution of the simulations - see, for example, [32], who showed how the spatial resolution affected the saturation level of the field in their simulations.

For the T10 simulations this plateau stage does not occur until well after the shock has been revived. During the the exponential growth phase between ~ 120 ms and ~ 200 ms, the growth rates in the two T10 simulations are 71.5 /s equivalent to a growth timescale of 14 ms. This is longer than the 3 ms timescale found in [26] but smaller than the timescale of 60 ms found by [33] for the growth of the magnetic field energy in their simulations (although the reader should be aware that two the setups are different and may not be directly comparable), as well as the 43 ms timescale for the growth of the field found by [18] in their simulations using a different set of progenitors. We have not attempted to determine the timescale for the field growth during the short, 20 ms, period around $t_{\rm pb} \approx 80-100$ ms in the two T12 simulations.

3.4.2 The Spatial Structure of the Magnetic Field

While Figure 3.5 shows that the total magnetic field energy in the gain region is always significantly less than the total kinetic energy in the gain region, locally we find pockets of material where the magnetic field energy density is similar to the local kinetic energy density, or similarly where the magnetic field pressure is similar to the thermal pressure. Such local enhancements of the field pressure were also seen in [33]. Adopting the parameter 'plasma beta', defined to be $1/\beta = P_{\rm mag}/P_{\rm th}$, to quantify the strength of the magnetic pressure relative to the thermal pressure, we show in Figures 3.6 and 3.7 2D slices of $1/\beta$ at fixed times for the two s15 simulations, and the two s20 simulations respectively. The figures indicate that at $t_{\rm pb} \approx 100$ ms, the two T10 simulations have a negligible contribution from the field pressure to the total pressure, and even by $t_{\rm pb} \approx 150$ ms, there are faint hints that $1/\beta$ is not zero in small regions of the gain region in the s15-T10 simulation. In the s20-T10 simulation the growth of the field pressure appears to be delayed relative to

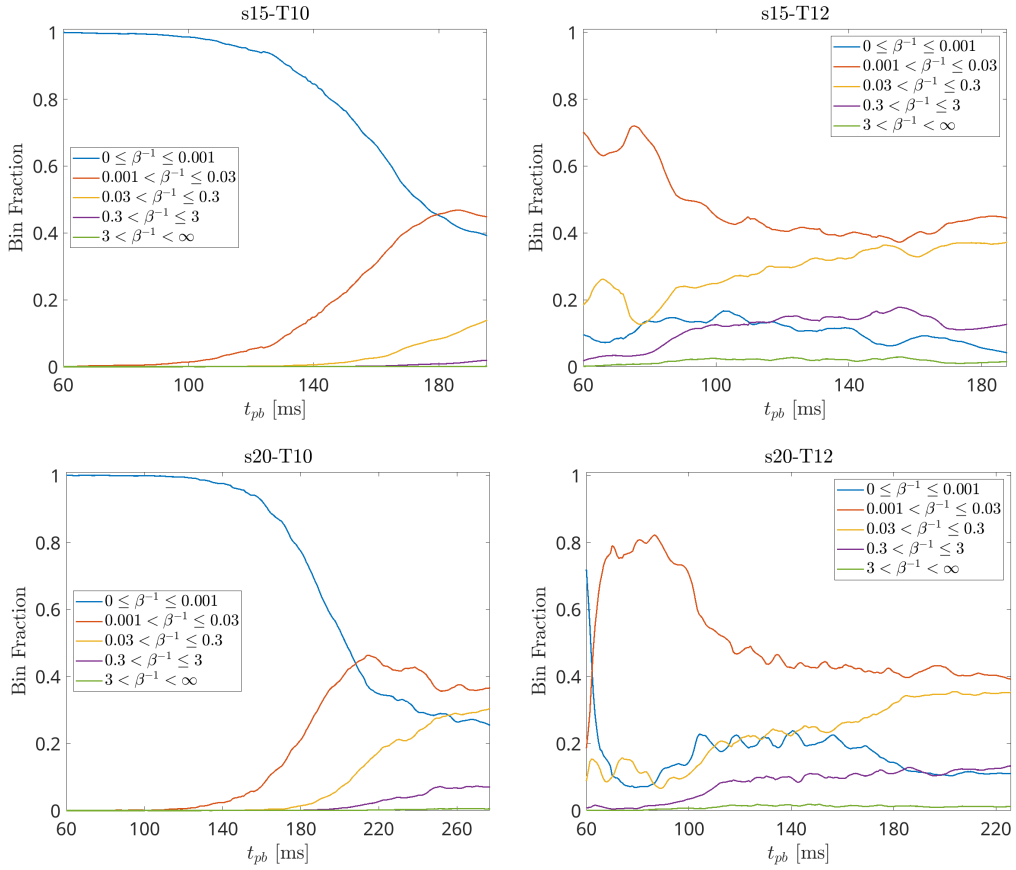

Figure 3.8: The fraction of the gain region volume with $1/\beta$ in given ranges as a function of time for s15-T10 (top left), s15-T12 (top right), s20-T10 (bottom left) and s20-T12 (bottom right).

the s15-T10 because we do not observe that $1/\beta$ is of order $\mathcal{O}(0.1)$ until $t_{\rm pb} \approx 200$ ms. At the time when the s20-T10 simulation was terminated, the field pressure grew to be as large (or even larger) than the thermal pressure in some places. In the two T12 simulations the contribution to the total pressure is apparent even at $t_{\rm pb} \approx 100$ ms in the s15-T12 simulation and by $t_{\rm pb} \approx 150$ ms one can find places where $1/\beta$ is $\mathcal{O}(1)$ through the gain region. Like the two T10 simulations, the growth of the field in the s20-T12 simulation appears to be somewhat delayed relative to the s15-T12.

Comparing with Figures 3.2 and 3.3, we see that, generally, $1/\beta$ is smallest immediately below the shock and in the low-entropy accretion downflows which thread the gain region, though the correspondence is not exact. Within the high-entropy heated fluid there is a great deal of intermittency of $1/\beta$ with large variations over small distances i.e. over scales much smaller than the size of the gain region. This suggests that the field is generated at the base of the convective plumes and then the tangled field is transported towards the shock.

We can analyze the maps of $1/\beta$ in the gain region and determine the fraction of the gain region volume where the parameter $1/\beta$ falls within particular ranges. The results are shown in Figure 3.8 and make the impressions from figures (3.6) and (3.7) more quantitative. At $t_{\rm pb} = 60$ ms the magnetic pressure everywhere in the gain region is very small in both the s15-T10 and s20-T10 simulations. It is not until $t_{\rm pb} \sim 140$ ms in the s15-T10 simulation and $t_{\rm pb} \sim 160$ ms in the s20-T10 simulation that the magnetic pressure reaches the level of $\sim$1 % of the thermal pressure in $\sim$ 10% of the gain region volume, and it takes until $t_{\rm pb} \sim 190$ ms in the s15-T10 simulation before the field pressure reaches $\sim$10% of the thermal pressure in $\sim$ 10% of the volume, and $t_{\rm pb} \sim 200$ ms in the s20-T10 simulation. By $t_{\rm pb} \sim 190$ ms the shock in the s15-T10 simulation has reached 500 km and the simulation has been terminated, but the shock progresses more slowly in the s20 models and so we are able to observe that after $t_{\rm pb} \sim 200$ ms the fraction of the gain region volume which has a value of $1/\beta$ in the respective ranges appears to plateau suggesting a steady-state has been approached.

In contrast, the magnetic pressure in the s15-T12 and s20-T12 simulations is already $\sim$1 % of the thermal pressure in more than half of the gain region as soon as convection begins at $t_{\rm pb} = 80-100$ ms, and 10% of the gain region volume has a value of $1/\beta \sim 10\%$ at the same time. By $t_{\rm pb} \sim 120$ ms both simulations show that about 10% of the gain region volume has approximately equal amounts of thermal and magnetic pressure, or in other words, a $1/\beta \approx 1$. We even see there is a small but non-zero fraction of the gain region volume which has $1/\beta \gtrsim 10$. Our results are similar to those of [32] but it appears that our

simulations have a greater fraction of the gain region filled with zones where $1/\beta > 0.1$.

To explore whether the field has any large scale structure we decompose the magnetic field into a mean field and a turbulent field. Our approach is similar to the Local-Spatial Average method used in [38]. The field $\vec{b}$ is decomposed into $\vec{b} = \langle \vec{b} \rangle + \vec{b}'$ where $\langle \vec{b} \rangle$ is the mean field and the turbulent component is $\vec{b}'$. The mean field for a particular grid cell in the simulation is defined to be average of the field in a cube surrounding the cell, that is:

$$\langle \vec{b} \rangle = \frac{1}{V_{\rm cube}} \int_{V_{\rm cube}} \vec{b}\, dV, \tag{3.30}$$

where $V_{\rm cube}$ is the volume of the cube of side length L centered on the grid cell under consideration. Note that the volume $V_{\rm cube}$ only includes those cells which are found to be inside the gain region so that the averaging volume is not always a full cube. Once $\langle \vec{b} \rangle$ is found, the turbulent component for the grid cell, $\vec{b}'$, is simply $\vec{b}' = \vec{b} - \langle \vec{b} \rangle$. Other methods for obtaining the mean field can be found in the literature e.g. [69, 26].

In Figure 3.9 we show the decomposition of the field for the s15-T10 simulation at $t_{\rm pb} = 98.7$ ms. The figure shows that the mean field is approximately an order of magnitude smaller than the turbulent field at this time. This dominance of the turbulent field over the mean field was also seen in [26].

3.5 The Fluid Kinetic Energy and Turbulence

Next we turn to the fluid kinetic energy. The total kinetic energy in the gain region is shown in the left panel of Figure 3.5 for all four simulations with magnetic fields. The kinetic energy grows over time from an initial value of order 10^{48} erg at $t_{\rm pb} = 60$ ms up to 10^{49}–10^{50} erg by $t_{\rm pb} = 200$ ms. This growth is due to net accretion of kinetic energy through the shock minus that lost through the inner boundary of the gain region, as well as work done on the fluid inside the gain region. There is not a distinctive change in the growth of the total kinetic energy at $\approx 80-100$ ms postbounce when convection begins. We note that the s15 models have a larger amount of kinetic energy in the gain region than the s20 models after $t_{\rm pb} \approx 120$ ms because the shock region is larger in those simulations.

The right-hand side of equation (3.28) is the rate of energy exchange between the magnetic field and the fluid. Of course, this same energy exchange term appears with the opposite sign in the equation for the evolution of the fluid energy. Starting from equation (3.3) we can derive the transport equation for the sum of the kinetic and internal energy of the

fluid to be:

$$\frac{\partial}{\partial t}(E_{\rm kin}+E_{\rm int})+\nabla\cdot[(E_{\rm kin}+E_{\rm int})\,\vec{v}]=-\rho\,\vec{v}\cdot\nabla\phi-\nabla\cdot(P_{\rm th}\,\vec{v})+\vec{v}\cdot\left(\left(\nabla\times\vec{b}\right)\times\vec{b}\right) \tag{3.31}$$

Note that this equation does not include the energy gained by the fluid due to interactions with the neutrinos: that is handled in ELEPHANT in a separate step, and would be positive over the entire gain region by definition. The three terms on the right hand side of equation (3.31) are the rates at which work is done on the fluid by gravity, the surrounding fluid, and the magnetic field. If the work done on the fluid by gravity and pressure forces is negligible, the magnetic field energy grows at the expense of the fluid's kinetic and internal energy, but if the work done on the fluid by gravity and pressure forces is large then the fluid kinetic plus internal energy *and* the magnetic field energy can grow together. Indeed, this simultaneous growth of fluid kinetic+internal energy and the magnetic field energy occurs outside the shock as the fluid collapses.

In Figures 3.10 through 3.13 we show 2D slices of the three terms from the right hand side of equation (3.31) for the four simulations with magnetic fields. The first column of each figure clearly indicates the convection in the gain region. At early times, $t_{\rm pb}\approx 100$ ms, the volume fraction of the gain region where the fluid is ascending is a small fraction of the total and the size of these regions is ~ 50 km at most. As time progresses, the volume fraction of the uprising fluid grows and also the size of these regions grow. At $t_{\rm pb}\approx 150$ ms the convective plumes are of 100 km in size, and by $t_{\rm pb}\approx 200$ ms they are of 200 km in size (or larger) and occupy the majority of the gain region volume.

The rate of work done on the fluid by the surrounding fluid is shown in the third column of the figures. At $t_{\rm pb}\approx 100$ ms the majority of the fluid in the gain region is losing energy as flows towards the PNS, with only small regions, coincident with the uprising fluid, where the fluid is gaining energy from the surrounding fluid. The scale of these regions is again ~ 50 km. As time progresses more of the fluid starts to gain energy but we note that the size of the structures remains small, i.e. ~ 50 km and does not grow as large in scale as the convective plumes. Indeed, even deep within the convective plumes, the fluid can be either gaining or losing energy. We also notice what look like partial spherical shells of energy gain and loss that might indicate the presence of standing acoustic / magnetoacoustic waves [70].

The work done on the fluid by the magnetic field is shown in the second column of the figures, and we immediately notice that the geometry and scale of the regions where the fluid is gaining or losing energy to the field are different than for the other two en-

ergy exchange mechanisms. These figures are very similar to those shown in [32]. The energy exchange between the fluid and field is strongest around the inner boundary of the gain region and we do not observe any feature coincident with the downflows seen in the gravitational rate of work panels. Close inspection reveals that the energy exchange is not preferentially from fluid to field. Instead we observe long ribbons where the fluid is losing energy to the field adjacent to ribbons where the fluid is gaining. So even though the field is gaining energy relative to the kinetic energy over time when integrated over the entire gain region, the gain is highly intermittent. The rate of work done by field upon the fluid can be split into two parts since $\vec{v}\cdot\left((\nabla\times\vec{b})\times\vec{b}\right)=\vec{v}\cdot(\vec{b}\cdot\nabla)\vec{b}-\vec{v}\cdot\nabla E_{mag}$. The term $\vec{v}\cdot(\vec{b}\cdot\nabla)\vec{b}$ is the rate of work done by the rotational part of the Lorentz force, and the term $-\vec{v}\cdot\nabla E_{mag}$ is the rate of work from the irrotational component.

As we mentioned previously, the energy exchanged by the fluid and field depends upon the relative orientation of the fluid velocity and the field. When the field and fluid velocity align, no energy is exchanged. In figure (3.14) we show a histogram of the alignment of the fluid velocity and magnetic field within the gain region for the s15-T12 simulation at three snapshots in time. Also shown is the expectation if the two vectors are random and have no correlation. At $t_{\rm pb}\approx 100$ ms the two vectors are preferentially orthogonal - recall that that the initial field we adopt is toroidal while the velocity will be almost radial at such times. But very quickly i.e. by $t_{\rm pb}\approx 133;$ms, the two vectors become randomly aligned in the s15-T12 simulation. This time matches the time at which the ratio of magnetic field energy to fluid kinetic energy reaches the plateau stage in the right panel of figure (3.5).

3.5.1 The Turbulence

The kinetic energy of the fluid may be decomposed into two parts: the turbulent kinetic energy density (TKE), E_{TKE}, and (for lack of a better term) the non-turbulent kinetic energy[1] density (NTKE) . By non-turbulent kinetic energy we mean the kinetic energy density associated with fluid flow on the largest scales, in our case, on the scale of the gain region; by turbulent kinetic energy we mean the energy associated with the fluid motion on much smaller scales i.e. the scale of the turbulent eddies. These two quantities need to be suitably defined, a task which is not trivial in the case of core-collapse supernovae. As in [38], we undertake a Reynolds decomposition of the fluid velocity so $\vec{v}=\langle\vec{v}\rangle+\vec{v}\,'$ where $\langle\vec{v}\rangle$ is an expectation value and $\vec{v}\,'$ is the deviation (fluctuation) from $\langle\vec{v}\rangle$. In a fluid which has

[1]We avoid using the term 'laminar kinetic energy' since this is often used in the literature with a different meaning than we require here.

reached a statistical steady state the expectation value of the velocity is the time-average of $\vec{v}$. In situations where the fluid is not in a statistical steady state, the expectation value is often computed as a spatial (volume) average. Of the two methods of this type considered in [38], we shall consider only the Local Spatial Average (LSA) method which was seen to yield maps of TKE which were a better match to other indicators of the turbulence. In the LSA method we define the expectation value of the velocity, $\langle \vec{v} \rangle$, for a particular grid cell to be the mass-weighted volume average (MWVA) of the velocity in a cube surrounding the cell, that is:

$$\langle \vec{v} \rangle = \frac{1}{M_{\text{cube}}} \int_{V_{\text{cube}}} \rho \, \vec{v} \, dV, \tag{3.32}$$

where

$$M_{\text{cube}} = \int_{V_{\text{cube}}} \rho \, dV \tag{3.33}$$

and V_{cube} is a cubic volume of side length L centered on the grid cell under consideration. Note that, in practice, the volume V_{cube} only includes those cells which are found to be inside the gain region so that the averaging volume is not always a full cube. We also note that this method for computing $\langle \vec{v} \rangle$ guarantees that the Reynolds Rules are satisfied within the averaging volume. The size of the averaging volume must be chosen appropriately and we adopt the same scale of $L = 20$ km used in [38] (because they are the same simulations). Once computed, the local turbulent kinetic energy density is thus $E_{TKE} = \rho \, |\vec{v}\,'|^2/2$.

In Figures 3.15 and 3.16 we plot a 2D slice of the specific TKE using the LSA method in the xy plane at a set of snapshot times for the six simulations. Comparing with the maps of the entropy in Figures 3.2 and 3.3, and the energy gained/lost by the fluid due to gravity in Figures 3.10 through 3.13, we see the specific turbulence is concentrated around the downflows with the convective plumes visible as the areas relatively free of turbulence. These maps can be compared with the maps of $1/\beta$ in Figures 3.6 and 3.7 which do not show structures that resemble the convective upflows.

The TKE relative to the total kinetic energy in the gain region at several points in time for three simulations with magnetic fields is shown in Figure 3.17, plus the same ratio computed for the two control simulations. At least for the s15-T10 simulation, there is no apparent difference in the amount of turbulent kinetic energy. In contrast the s15-T12 simulation appears to show a somewhat smaller ratio of turbulent to total kinetic energy starting at $t_{\text{pb}} \approx 80$ ms when convection begins, and similarly the s20-T12 also hints at a small reduction of the turbulent kinetic energy. In both simulations, the decrease is small and approximately $5-10\%$, i.e. similar to the ratio of magnetic to total kinetic energy seen in

Figure (3.5). However, we caution the reader that the turbulent kinetic energy is a difficult quantity to measure and the LSA method we use in this paper is known to yield values which depend upon the size of the averaging volume - see [38]. Therefore the $5-10\%$ reduction shown in figure (3.17) must be regarded as being somewhat qualitative.

3.6 The Vorticity

The presence of vorticity is often regarded as indicating the presence of turbulence in a fluid. Like the magnetic field, the vorticity, $\vec{\omega} = \nabla \times \vec{v}$, is divergence free, i.e. $\nabla \cdot \vec{\omega} = 0$. From equations (3.1) and (3.2) we find the vorticity evolves according to

$$\frac{\partial \vec{\omega}}{\partial t} = \nabla \times (\vec{v} \times \vec{\omega}) + \vec{m}, \tag{3.34}$$

where $\vec{m}$ is the baroclinic vector. The combination $\vec{\omega} \times \vec{v}$ is known as the Lamb vector or force. Using a vector calculus identity and that $\nabla \cdot \omega = 0$, equation (3.34) can be written as

$$\frac{\partial \vec{\omega}}{\partial t} + (\vec{v} \cdot \nabla)\vec{\omega} = (\vec{\omega} \cdot \nabla)\vec{v} - \vec{\omega}(\nabla \cdot \vec{v}) + \vec{m} \tag{3.35}$$

The left-hand of this equation is seen to be the convective derivative, and the first two terms on the right-hand side describe the effect of stretching and compression respectively, and depend only on the gradients of the fluid velocity, not the gradients of the vorticity. The stretching term $(\vec{\omega} \cdot \nabla)\vec{v}$ is often re-written as $S_{ij}\,\omega_j$ (using the Einstein summation convention) where S_{ij} is the strain-rate tensor

$$S_{ij} = \frac{1}{2}\left(\frac{\partial v_i}{\partial x_j} + \frac{\partial v_j}{\partial x_i}\right). \tag{3.36}$$

Including the magnetic field contribution, the expression for the baroclinic vector $\vec{m}$ is given by

$$\vec{m} = \frac{1}{\rho^2}\left(\nabla\rho \times \nabla\left(P_{\text{th}} + P_{\text{mag}}\right)\right) + \frac{1}{\rho}\nabla \times \left(\frac{(\vec{b} \cdot \nabla)\vec{b}}{\rho}\right). \tag{3.37}$$

The presence of the magnetic field in the baroclinic vector indicates that the magnetic field affects the vorticity, and we note that the baroclinic vector depends upon the *derivative* of the magnetic field. Thus the greater the amount of structure in the magnetic field the greater its contribution to the baroclinic vector. We do not require that the magnetic field dominate the pressure: it is possible that even in places where $1/\beta$ is small, the con-

tribution of the magnetic field to the baroclinic vector could be significant if the gradients of the field are large.

As with the magnetic field, one can derive from equation (3.34) and equation (3.1) that the ratio $\vec{\omega}/\rho$ evolves according to

$$\frac{\partial}{\partial t}\left(\frac{\vec{\omega}}{\rho}\right)+(\vec{v}\cdot\nabla)\left(\frac{\vec{\omega}}{\rho}\right)-\left(\frac{\vec{\omega}}{\rho}\cdot\nabla\right)\vec{v}=\frac{\vec{m}}{\rho}. \tag{3.38}$$

Again, the left hand side of this equation defines the fluid derivative of $\vec{\omega}/\rho$, the interpretation of which is the same as that of the combination $\vec{b}/\rho$. In the absence of a magnetic field and when the fluid is barotropic, the baroclinic vector vanishes and $\vec{\omega}/\rho$ remains fixed between any two fluid elements connected along a vortex line. However, in the presence of a magnetic field, it is possible for the right-hand side to be non-zero even if the fluid is barotropic.

In Figures 3.18 and 3.19 we show maps of the baroclinic vector at various snapshots through the three s15 and three s20 simulations respectively, which the reader should compare with the maps of the entropy in Figures 3.2 and 3.3, the maps of $1/\beta$ in Figures 3.6 and 3.7, and the rate of work maps in figures 3.10 through 3.13. At $t_{\rm pb}\sim 100$ ms there is little difference between the Control and T10 simulations, but the gain region of the T12 simulations at these times has a noticeably stronger baroclinic vector. As time progresses the baroclinic vector in the Control and T10 simulations is largest around the downflows This similarity begins to disappear after $t_{\rm pb}\gtrsim 150$ ms where the baroclinic vector in the s20-T12 simulation is now noticeably larger than in the other two simulations over much of the gain region. By $t_{\rm pb}\gtrsim 190$ ms the s20-T10 is now noticeably different from the s20-Control; the baroclinic vector is largest near the shock and at the inner edge of the gain region. At the end of the simulations greater than 50% of the area of the gain region shown in the slices of the s20-T10 and s20-T12 simulations is seen to be filled with a large baroclinic vector.

It has previously been suggested that the similarity of the equations (3.26) and (3.38) for the magnetic field and vorticity might indicate they evolve similarly. In the simulations by [33] the authors found the distribution of the angle between the vorticity and the magnetic field had two peaks at zero and π supporting this conjecture - see also [31]. In Figure 3.20 we show the results from our investigation of whether the magnetic field and vorticity align in our simulations in the gain region as a function of post-bounce time. The black horizontal line in the figure is the uniform distribution that one would expect if the two vectors were random and uncorrelated. The results indicate there is only a slight preference for alignment and anti-alignment of the vorticity and magnetic fields when considered

Table 3.2: The correlation coefficient r between the specific TKE and the enstrophy at various snapshot times.

s15-Control		s15-T10		s15-T12		s20-Control		s20-T10		s20-T12	
$t_{\rm pb}$ (ms)	r (-)	$t_{\rm pb}$ (ms)	r (-)	$t_{\rm pb}$ (ms)	r (-)	$t_{\rm pb}$ (ms)	r (-)	$t_{\rm pb}$ (ms)	r (-)	$t_{\rm pb}$ (ms)	r (-)
99.9	0.382	100.0	0.441	98.7	0.395	152.4	0.404	150.8	0.329	148.0	0.185
149.9	0.429	150.3	0.352	149.0	0.434	195.4	0.556	193.5	0.425	190.8	0.551
192.8	0.558	195.4	0.512	183.4	0.602	216.1	0.595	277.0	0.593	224.0	0.566

over the entire gain region in all our simulations. That the vorticity and magnetic field are not correlated for the T12 simulations after $t_{\rm pb} \approx 125$ ms is perhaps not surprising given that the field reaches some sort of equilibrium with the fluid, as seen in Figure 3.5. That there is also no strong alignment at $t_{\rm pb} \approx 100$ ms in the T12 simulations, and at any time in the T10 simulations, is more informative that the vorticity and magnetic field do not grow together. We suspect the neutrino heating and convection - something not present in [33] - breaks the connection.

3.6.1 The Enstrophy

Related to the vorticity is the enstrophy ϵ_ω, defined to be $\epsilon_\omega = (\vec{\omega}\cdot\vec{\omega})/2$. In Figures 3.21 and 3.22 we show 2D slices of the enstrophy at various snapshot times for the three s15 simulations and three s20 simulations respectively. The reader will observe that these maps closely resemble the maps of the specific TKE shown in Figures 3.15 and 3.16 with regions of little enstrophy corresponding to the upflows. Indeed, in [38] we used the good visual agreement between the specific TKE and enstrophy to argue that the LSA method for computing the TKE was a good one. Note that the distribution of the enstrophy in the gain region of our simulations is quite different than the distribution of vorticity seen in the simulations of [32], although the reader should be aware that those simulations did not include neutrino heating and that a SASI was present.

We can go beyond a visual comparison and compute the correlation between the enstrophy and specific TKE. The correlation coefficient between the specific TKE and enstrophy in the gain regions at various snapshot times for all simulations is shown in table (3.2). The table shows that the correlation grows over time with and can become as strong as 0.6 at late times and thus enstrophy is a good, but not perfect, proxy for the turbulence.

If so, we should expect that the growth of the magnetic field energy should also lead

to a decrease in the integrated enstrophy over the gain region. In Figure 3.23 we show the ratio of the integral of $\rho\,\epsilon_\omega$ over the gain region to the integrated kinetic energy of the gain region for all six simulations. We include the additional factor of the density in the enstrophy integral in order to compensate for the smaller size of the region close to the inner boundary of the gain region. The figure shows that for both the s15 and s20 progenitors, the Control and T10 simulations have ratios which are very similar until $t_{\rm pb} \approx 200$ ms. In contrast the T12 simulations have a ratio which is smaller by $\sim 30\%$ relative to the other two simulations with the same progenitor. Thus the magnetic field appears to have the effect of reducing the net enstrophy in the gain region.

In addition to the energy exchange, the field has a back-reaction upon the vorticity/enstrophy of the fluid via the presence of the magnetic field in the baroclinic vector. We can derive that enstrophy is transported according to the equation

$$\begin{aligned} \frac{\partial \epsilon_\omega}{\partial t} + \nabla \cdot \vec{S}_\omega &= -\vec{v} \cdot [(\nabla \times \vec{\omega}) \times \vec{\omega}] + \vec{\omega} \cdot \vec{m} && (3.39) \\ &= \vec{v} \cdot \nabla \epsilon_\omega - \vec{v} \cdot (\vec{\omega} \cdot \nabla)\,\vec{\omega} + \vec{\omega} \cdot \vec{m} && (3.40) \end{aligned}$$

where $\vec{S}_\omega = \vec{v}\,(\vec{\omega} \cdot \vec{\omega}) - \vec{\omega}\,(\vec{v} \cdot \vec{\omega})$ plays the same role as $\vec{S}_{\rm mag}$, i.e. it is the enstrophy flux. The two terms on the right hand side of equation (3.39) are the sources/sinks of enstrophy. As with the magnetic field, if the vorticity is parallel or anti-parallel to the velocity then the first term, $\vec{v} \cdot ((\nabla \times \vec{\omega}) \times \vec{\omega})$, is zero. The second term, $\vec{\omega} \cdot \vec{m}$, is unaffected by the relative orientation of the velocity and vorticity. Equation (3.40) uses a vector identity to separate the rate of enstrophy change due to the fluid motion into two parts which can be interpreted, as with equation (3.29) for the transport of magnetic field energy density, as being the rate of enstrophy change due to the rotational and irrotaional components of the vorticity. In Figures 3.24 through 3.27 we show snapshots of the two enstrophy source terms and the sum for the four simulations with magnetic field. Comparing with the maps of $1/\beta$ in Figures 3.6 and 3.7, we see that the enstrophy is predominantly created/destroyed where $1/\beta$ is largest, which is around the edges of the downflows. What is also seen in the sets of figures is that the maps of the source term $-\vec{v} \cdot ((\nabla \times \vec{\omega}) \times \vec{\omega})$ possess parallel ribbons where the source on one side of the ribbon is positive, i.e. it generates enstrophy, and the adjacent side destroys it. These features are similar to those seen in the magnetic field - fluid energy exchange maps in Figures 3.10 through 3.13.

Looking more closely at the two T10 cases, the reader will observe there is the significant difference in the size of the two source terms at $t_{pb} \approx 100$ ms: the $-\vec{v} \cdot ((\nabla \times \vec{\omega}) \times \vec{\omega})$ dwarfs $\vec{\omega} \cdot \vec{m}$ Of the two source of enstrophy, the contribution from the baroclinic vector

is much smaller than the contribution from the fluid stretching and compression. As time progresses, the growth of the magnetic field means the baroclinic vector grows rapidly - as seen in Figures 3.18 and 3.19 - but, at $t_{pb} \approx 150$ ms, it is still the case that fluid stretching and compression dominates. Only by $t_{pb} \approx 200$ ms are the two contributions to the enstrophy within an order of magnitude of each other. The picture changes for the two T12 simulation as shown in Figure 3.25 and 3.27 where the two enstrophy sources are similar in size at every snapshot shown.

3.7 Conclusions and Discussion

The magnetic field, the turbulence and the vorticity/enstrophy in a core-collapse supernova are interlinked, as demonstrated in equations (3.28), (3.31), and (3.34) - (3.40). To explore the connection between these quantities we have undertaken six 3D magnetohydrodynamic simulations using two progenitors and three different initial magnetic field strengths. Our main findings are the following.

- The results of our simulations indicate the magnetic field energy relative to the fluid kinetic energy in the gain region grows exponentially over time until it reaches a quasi-stationary value in the range of $5-10\%$. For the two T12 simulations this equilibrium is reached well before the shock is revived, in the two T10 simulations the equilibrium is reached well after the shock revival. The field energy does not appear to greatly affect the dynamics of the supernova or the shock revival time.

- The structure of the field quickly becomes a tangled mass of flux ropes. We find isolated pockets of fluid where the field pressure equals, and even exceeds, the thermal pressure. The field does not have an large mean field but is, instead, dominated by its turbulent component.

- The energy exchanged between the fluid and field occurs predominantly around the inner boundary of the gain region in long, narrow ribbons of adjacent loss and gain. The constant energy exchange between field and fluid makes it challenging to identify where exactly the net energy flow into the field occurs. We note that the energy exchange does not occur only in the vicinity of the turbulence as identified using the Local-Spatial Average method.

- The highly-tangled field structure means the field is the dominant contribution to the baroclinic vector, the source of fluid vorticity. In the simulations with a magnetic

field, the baroclinic vector is large over a much greater volume of the gain region compared to the simulations without a field. The vorticity/enstrophy in the fluid is concentrated around the downflows that thread the gain region. We confirm that the enstrophy and turbulent kinetic energy show good, but not perfect, correlation over the gain region allowing enstrophy to be used as a proxy for the turbulence.

- Although governed by very similar transport/evolution equations to the magnetic field, the fluid vorticity and magnetic field are always close to being randomly aligned.
- We find that the integral of the fluid density times the enstrophy over the gain region decreases relative to the total kinetic energy in the gain region in simulations with magnetic fields.

Our findings are similar to previous studies. [18] also saw that the magnetic field energy density was only a few percent of kinetic equipartition in their simulations and did not greatly affect the shock revival time. Our results can also be compared with [33] and [34], although these are not of a supernova because their simulations did not include neutrino heating and thus do not explode. Nevertheless, [33] also find the magnetic field does not noticeably change the dynamics of the simulations. We also similarly find that in the gain region the turbulent kinetic energy is only $\sim 25\%$ of the total kinetic energy (although this value is dependent upon the non-physical parameter choices made in the methods used to calculate the TKE), and also find the magnetic field is highly structured with localized pockets of high magnetic field energy. However we do not find that the magnetic field and vorticity are preferentially aligned or anti-aligned indicating that something in our simulations - presumably the neutrino heating / convection - breaks the connection.

In summary, the magnetic field, turbulence and vorticity/enstrophy exhibit a dynamic interaction in the gain region of a core-collapse supernova. Exactly how the field is amplified is unclear, although ultimately the energy in the field comes at the expense of the fluid's kinetic plus internal energy. As net field energy in the gain region is growing, locally there is a constant energy exchange back-and-forth that we expect is due to a combination of Alfven, magneto-acoustic, and gravity waves, which we plan to explore in future work.

3.8 Acknowledgments

The work at NC State was supported by United States Department of Energy, Office of Science, Office of Nuclear Physics (award number DE-FG02-02ER41216). The work of Michael

Redle was partially funded by German Research Foundation (DFG) Research Unit FOR5409 “Structure-Preserving Numerical Methods for Bulk- and Interface-Coupling of Heterogeneous Models (SNuBIC)" (grant #463312734). This study used Bridges-2 at Pittsburgh Supercomputing Center through allocation PHY200074 from the Advanced Cyberinfrastructure Coordination Ecosystem: Services & Support (ACCESS) program, which is supported by National Science Foundation grants #2138259, #2138286, #2138307, #2137603, and #2138296. This study also used the Extreme Science and Engineering Discovery Environment (XSEDE), which is supported by National Science Foundation grant number ACI-1548562. Specifically, it used the Bridges-2 system, which is supported by NSF award number ACI-1928147, at the Pittsburgh Supercomputing Center (PSC). Finally, the authors also acknowledge the Texas Advanced Computing Center (TACC) at The University of Texas at Austin for providing computational resources that have contributed to the research results reported within this paper. URL: http://www.tacc.utexas.edu

3.9 Appendix: The Growth of the Magnetic Field During Collapse

A magnetic field inserted into a mass distribution is distorted as the distribution collapses due to gravity. In the case of pure freefall of a spherically symmetric density profile (i.e. without rotation), we can analytically solve for the evolution of the field in the weak field limit.

Consider a test point mass initially at radius r_0 within a mass distribution given by the function $\rho(r)$. The mass enclosed within r_0 is M_0 and as the mass distribution collapses, the mass enclosed within the sphere given by the radial position r of the test mass remains a constant.

If the test mass is initially at rest, we find from the conservation of energy that the velocity of the point mass when it is at a radius r is

$$v = \frac{dr}{dt} = -\sqrt{\frac{2GM_0}{r_0}}\sqrt{\frac{r_0 - r}{r}}. \tag{3.41}$$

Integrating the equation gives the amount of time taken for the point mass to fall from r_0 to r as

$$t = \sqrt{\frac{r_0^3}{2GM_0}}\left[\sqrt{\frac{r}{r_0}\left(1-\frac{r}{r_0}\right)} + \cos^{-1}\left(\sqrt{\frac{r}{r_0}}\right)\right] \tag{3.42}$$

This well-known result is commonly used to obtain $r(t)$ for a given r_0, but it can also be interpreted as the equation which gives $r(r_0)$ at a given t.

Now we consider a cubic segment of the mass distribution - a mass element - defined by the eight vertices which form the corners of the element. The inner four vertices lie on a sphere of radius r_0 and the outer four a radius $r_0 + dr_0$. The outer vertices are aligned radially with one of the inner vertices. The volume of the mass distribution enclosed by the vertices is $dV = r_0^2\, dr_0\, d\Omega_0$ and the density within it is ρ_0. As the element falls inward the solid angle $d\Omega_0$ does not change. By differentiating equation (3.42) with respect to r_0 (not forgetting that M_0 is a function of r_0) we find that at a given time t, the radial separation between the inner vertices and the outer vertices of the mass element changes as

$$\frac{dr}{dr_0} = \frac{r}{r_0} - \frac{3vt}{2r_0}\left[1 - \frac{4\pi\rho_0 r_0^3}{3M_0}\right] \tag{3.43}$$

with v given by equation (3.41) and t given by equation (3.42). The second term in the

square brackets on the right hand side of equation (3.43) is seen to be the ratio of the mass within a sphere of radius r_0 with constant density ρ_0, and the actual mass within the sphere M_0 that caused the element to fall. If the initial mass distribution were indeed uniform with a value of ρ_0, this ratio would be unity and so $dr/dr_0 = r/r_0$ i.e. the mass element is compressed as it falls. However if the ratio is less than unity, the second ($v\,t$) term on the right hand side of equation (3.43) is positive (the velocity is negative) which alters the evolution of dr/dr_0. Indeed, in a 'typical' supernova progenitor profile ρ falls rapidly with the radius r allowing us to neglect the mass ratio term in equation (3.43). In this limit we find that once the mass element has fallen so that $r \ll r_0$, the ratio dr/dr_0 approaches $dr/dr_0 \propto \sqrt{r_0/r}$. This is not a compression but rather a stretch: $dr/dr_0 > 1$.

In figure (3.28) we show the evolution of r and stretch factor dr/dr_0 as a function of time for mass elements with an initial density profile given by

$$\rho = \rho_\star \left(\frac{r_\star}{r + r_\star} \right)^3 \tag{3.44}$$

with $\rho_\star = 10^{12}$ g/cm^3 and $r_\star = 100$ km. Figure (3.28) indicates that the compression is only noticeable for the innermost mass elements because the density profile approaches a constant at small r which causes the $v\,t$ term in equation (3.43) to become small. Outside the core region, $dr/dr_0 \approx 1$ for a mass element initially but eventually dr/dr_0 grows as expected.

Now that we know how the dimensions of the mass element change with time, we can determine the evolution of the magnetic field. From the conservation of flux through the faces of a mass element, we find, the radial component of the magnetic field b_r and the transverse components, $b_{\theta,\phi}$, evolve as

$$b_r(r) = b_r(r_0) \left(\frac{r_0}{r} \right)^2 \tag{3.45}$$

$$b_{\theta,\phi}(r) = b_{\theta,\phi}(r_0) \left(\frac{r_0}{r} \frac{dr_0}{dr} \right) \tag{3.46}$$

These equations show the radial component grows as $b_r \propto 1/r^2$ as the element falls. The transverse components also grow: for elements in the core region they also grow initially as as $1/r^2$ when $dr/dr_0 \approx r/r_0$, but for mass elements that were outside the core region the growth is initially only as $1/r$ because dr/dr_0 is approximately constant. As they pick up speed $dr/dr_0 \propto 1/\sqrt{r}$ so the transverse components of the field through elements that start outside the core grow more slowly as $b_{\theta,\phi} \propto 1/\sqrt{r}$. Thus, if the initial field through

the outer mass elements has both radial and transverse components, the field through the element will become increasingly dominated by the radial field as it falls.

We show this evolution in figure (3.29). We set up a spherical grid of mass elements inside the density profile given by equation (3.44). On each face of the elements we set a component of the magnetic field normal to the face. The component is the projection onto the normal of a vector with fixed magnitude but random direction. We then allow the mass distribution to collapse and evolve the component of the magnetic field on each face of the elements so as to conserve the flux. At every snapshot in time we reconstruct the field at the center of the mass element as the average of the components on the six faces. The left panel of figure (3.29) shows the components of the unit vector of this reconstructed field in the xy plane at $t = 0$; the right panel shows the same at $t = 50$ ms. As the reader will observe, initially the field points in random directions and elements towards the top-right remain somewhat randomly oriented at $t = 50$ ms because they have not fallen far, but elements which started closer to the center have fallen farther (i.e. they are now towards the bottom-left) and they are clearly preferentially radially aligned.

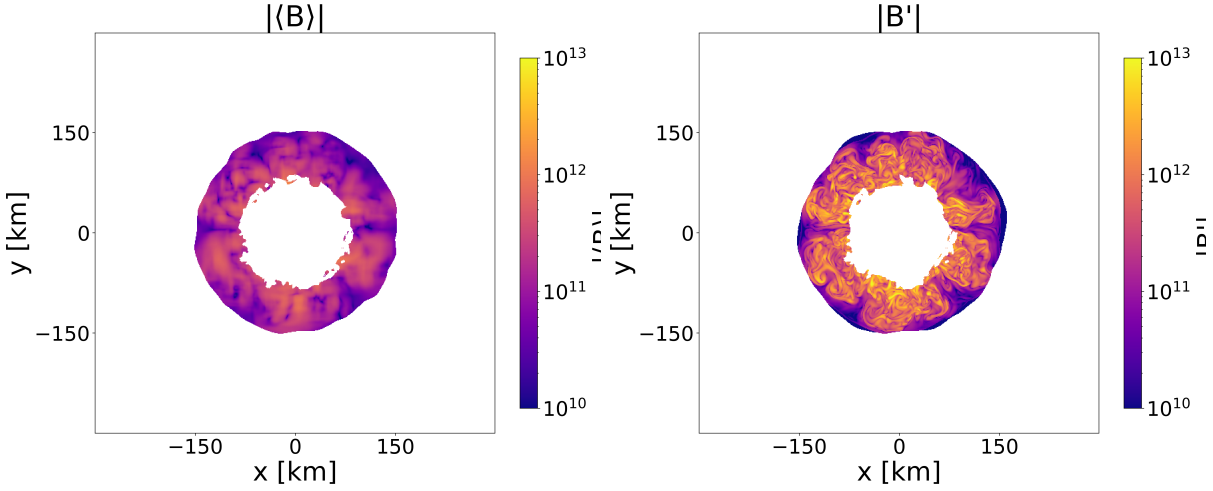

Figure 3.9: The mean field (left) and turbulent field (right) for the s15-T10 simulation at $t_{\rm pb} = 98.7$ ms.

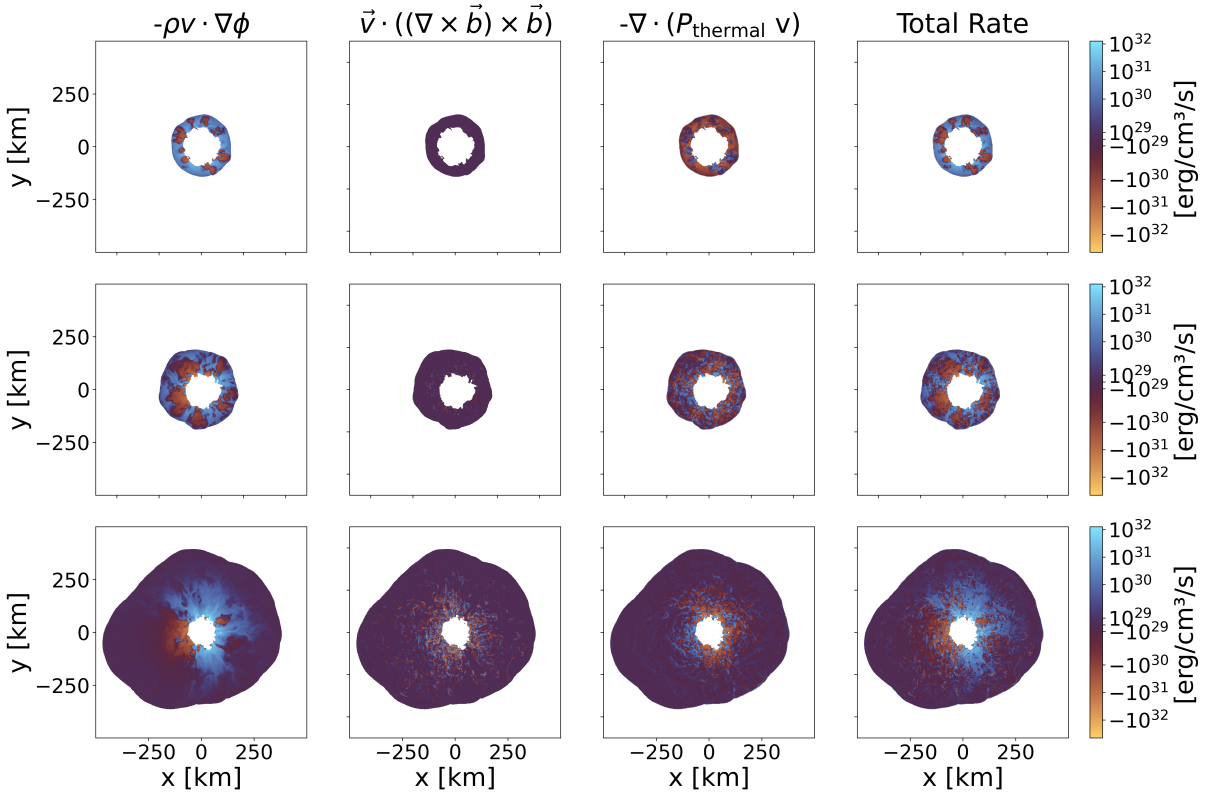

Figure 3.10: The rate of work done on the fluid due to gravity (left column), fluid pressure (second column), the magnetic field (third column) and the sum (fourth column) for the s15-T10 simulation at the post-bounce times of ∼ 100 ms (first row), ∼ 150 ms (second row), and ∼ 195 ms (third row).

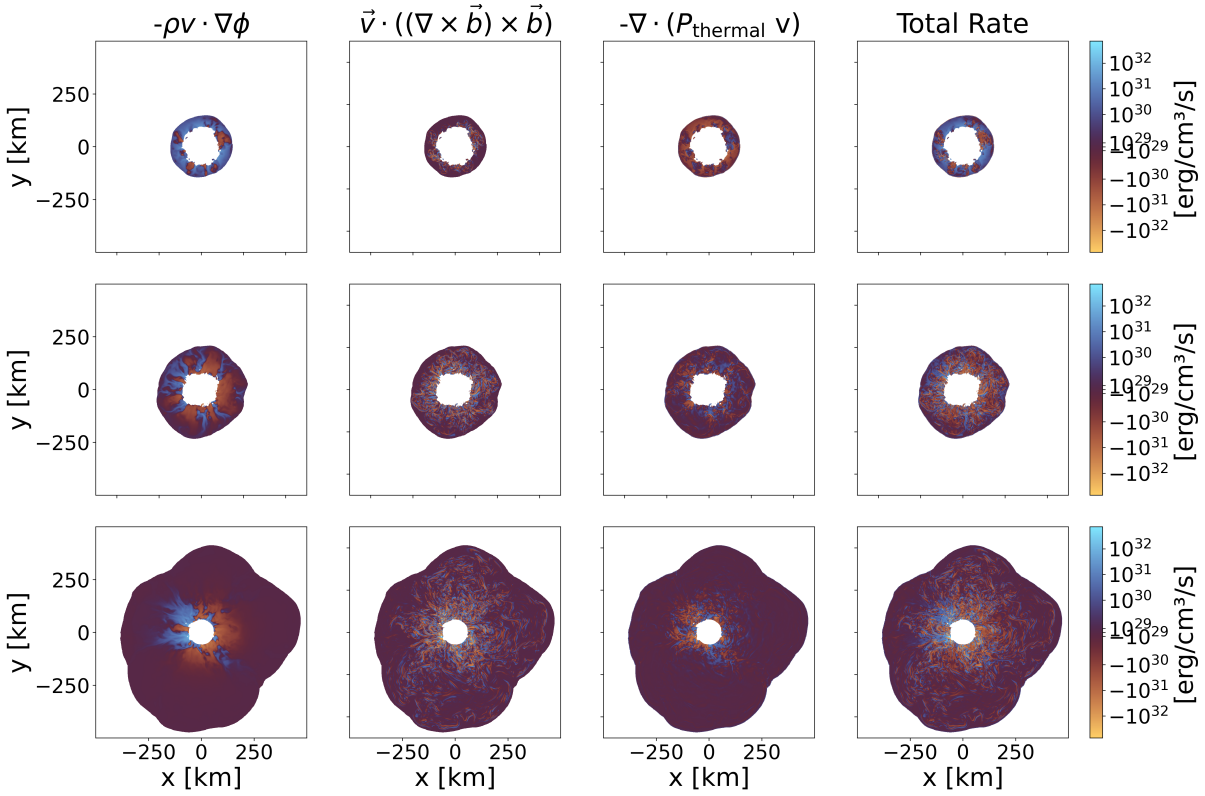

Figure 3.11: The rate of work done on the fluid due to gravity (left column), fluid pressure (second column), the magnetic field (third column) and the sum (fourth column) for the s15-T12 simulation at the post-bounce times of $\sim$ 100 ms (first row), $\sim$ 150 ms (second row), and $\sim$ 195 ms (third row).

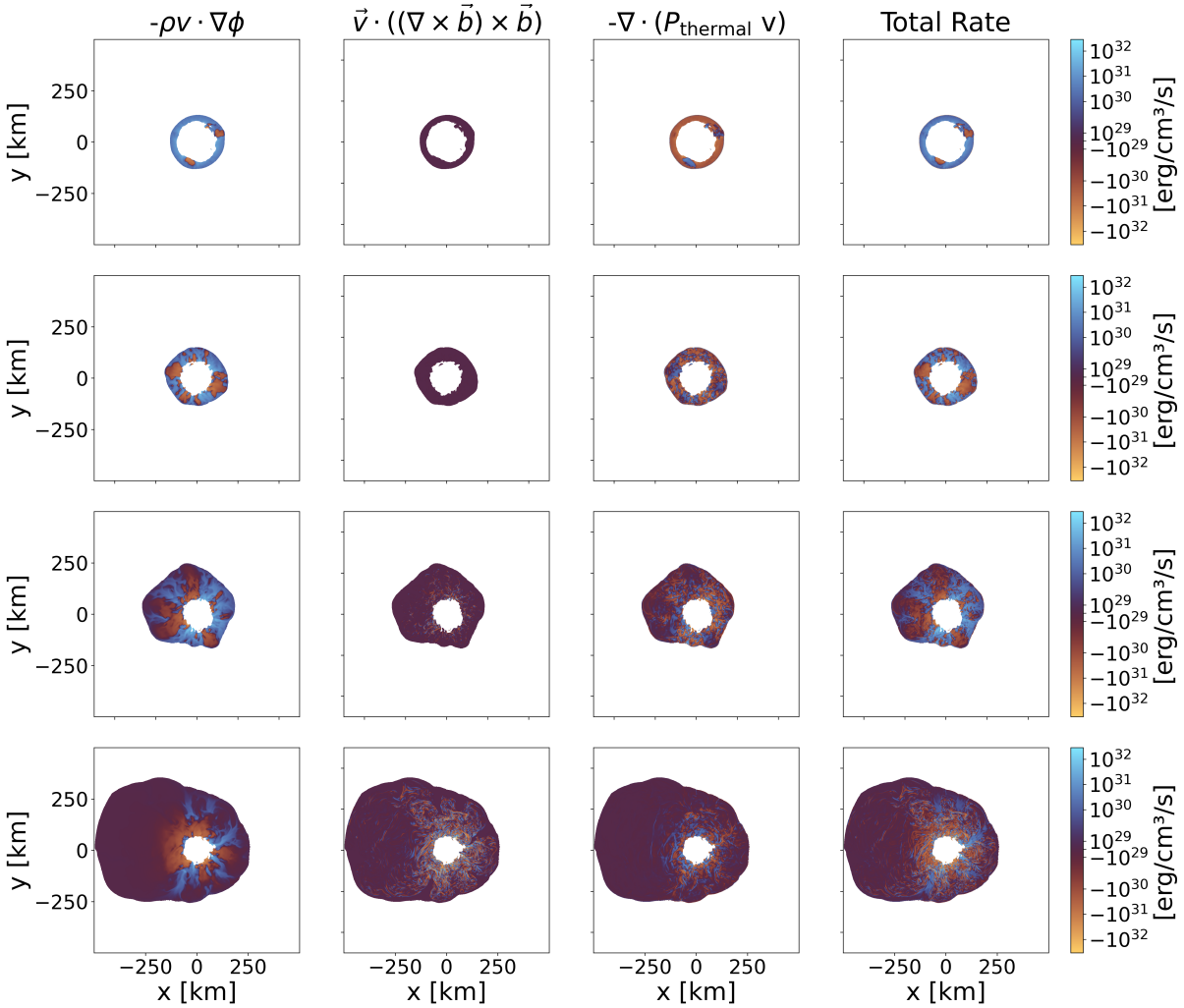

Figure 3.12: The rate of work done on the fluid due to gravity (left column), fluid pressure (second column), the magnetic field (third column) and the sum (fourth column) for the s20-T10 simulation at the post-bounce times of ∼ 100 ms (first row), ∼ 150 ms (second row), and ∼ 195 ms (third row)., and at the final time (fourth row)

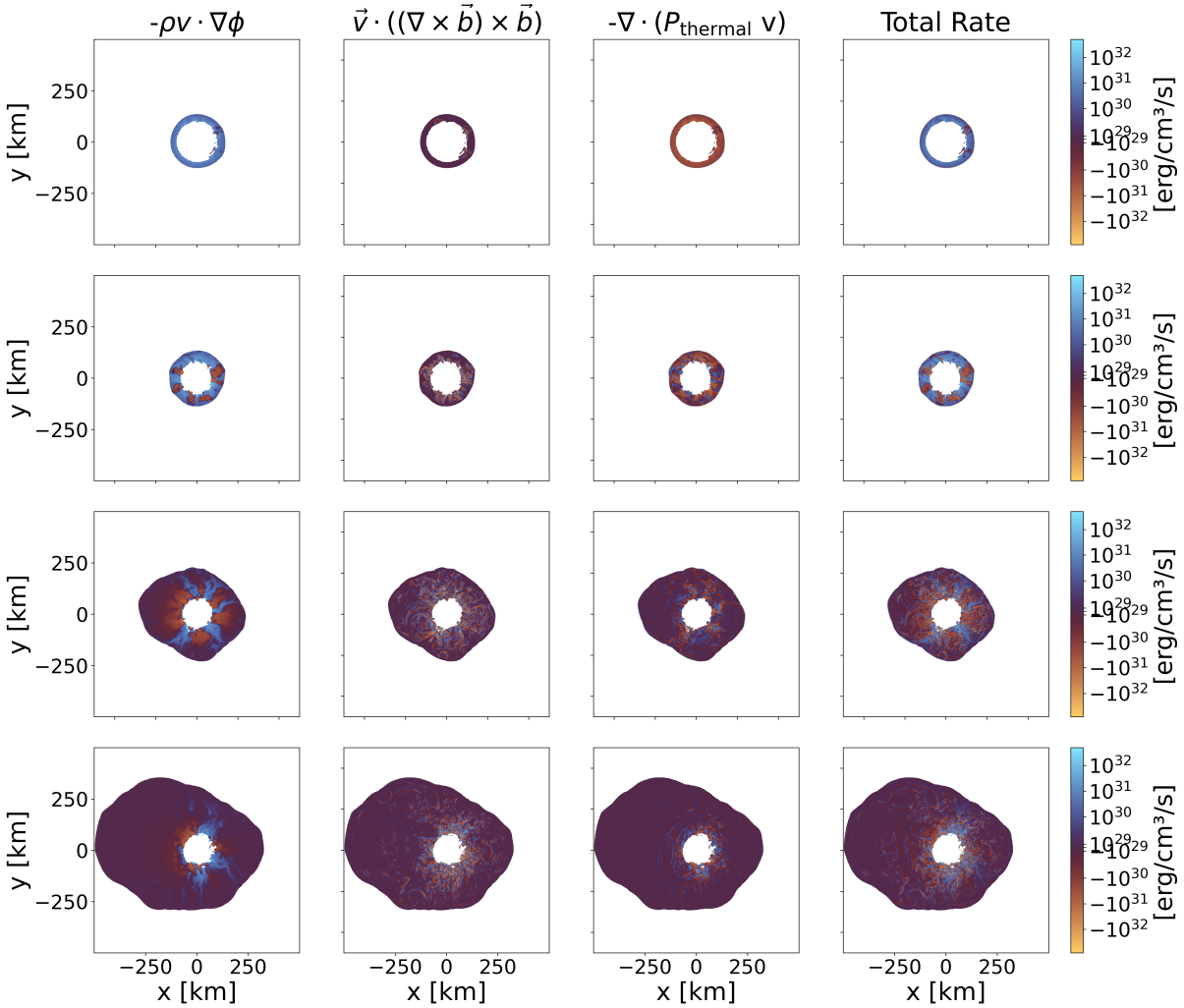

Figure 3.13: The rate of work done on the fluid due to gravity (left column), fluid pressure (second column), the magnetic field (third column) and the sum (fourth column) for the s20-T12 simulation at the post-bounce times of $\sim$ 100 ms (first row), $\sim$ 150 ms (second row), and $\sim$ 195 ms (third row)., and at the final time (fourth row)

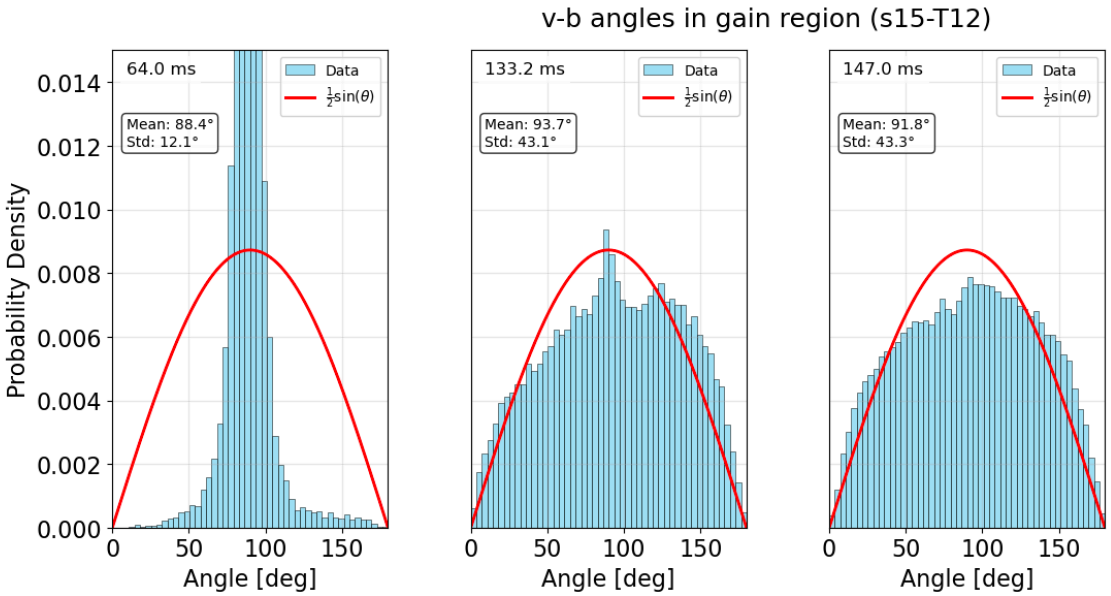

Figure 3.14: The angle between the fluid velocity and magnetic field within the gain region at the sanpshot times for the s15-T12 simulation

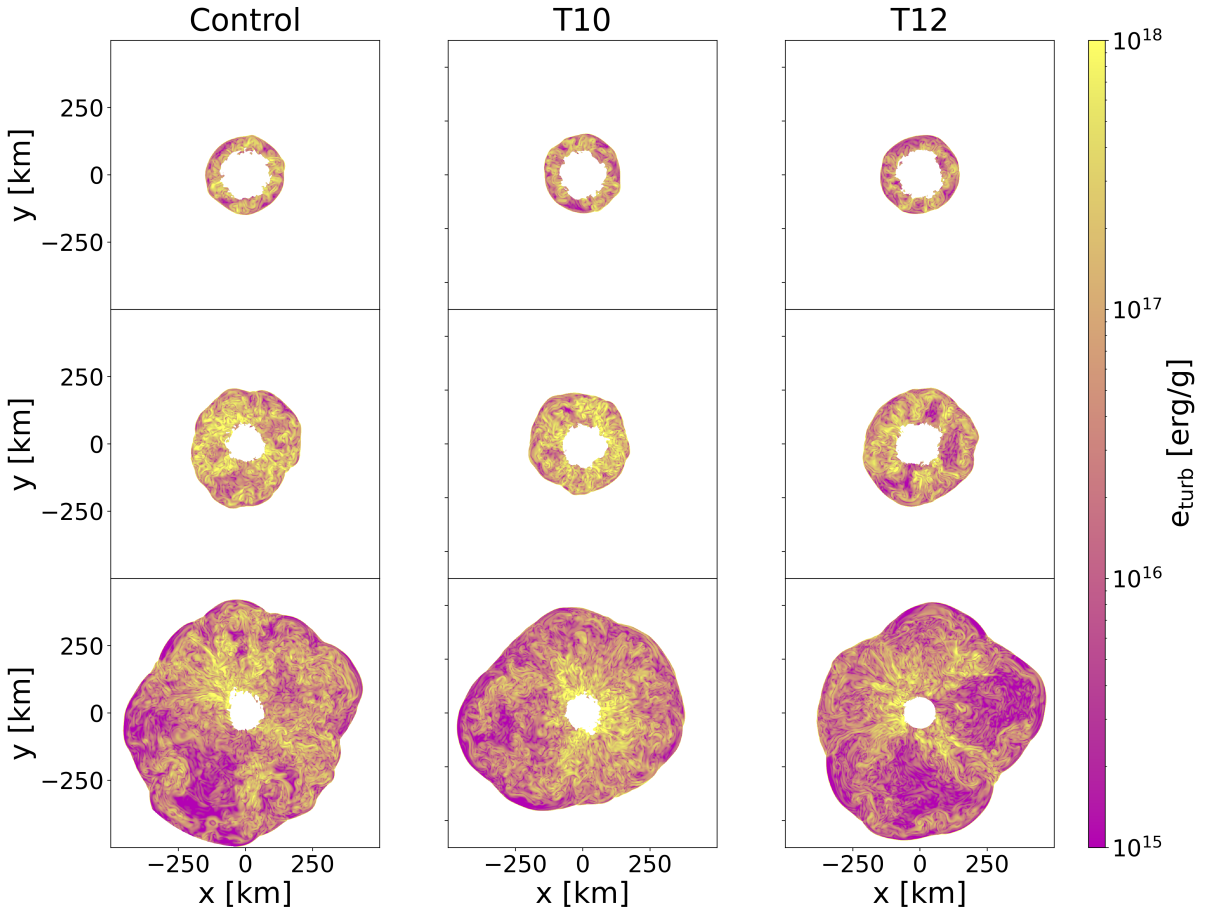

Figure 3.15: The specific TKE for the s15-Control (left), s15-T10 (middle), and s15-T12 (right) simulations at the post-bounce times of $\sim$ 100 ms (first row), $\sim$ 150 ms (second row), and at final time for each simulation (third row).

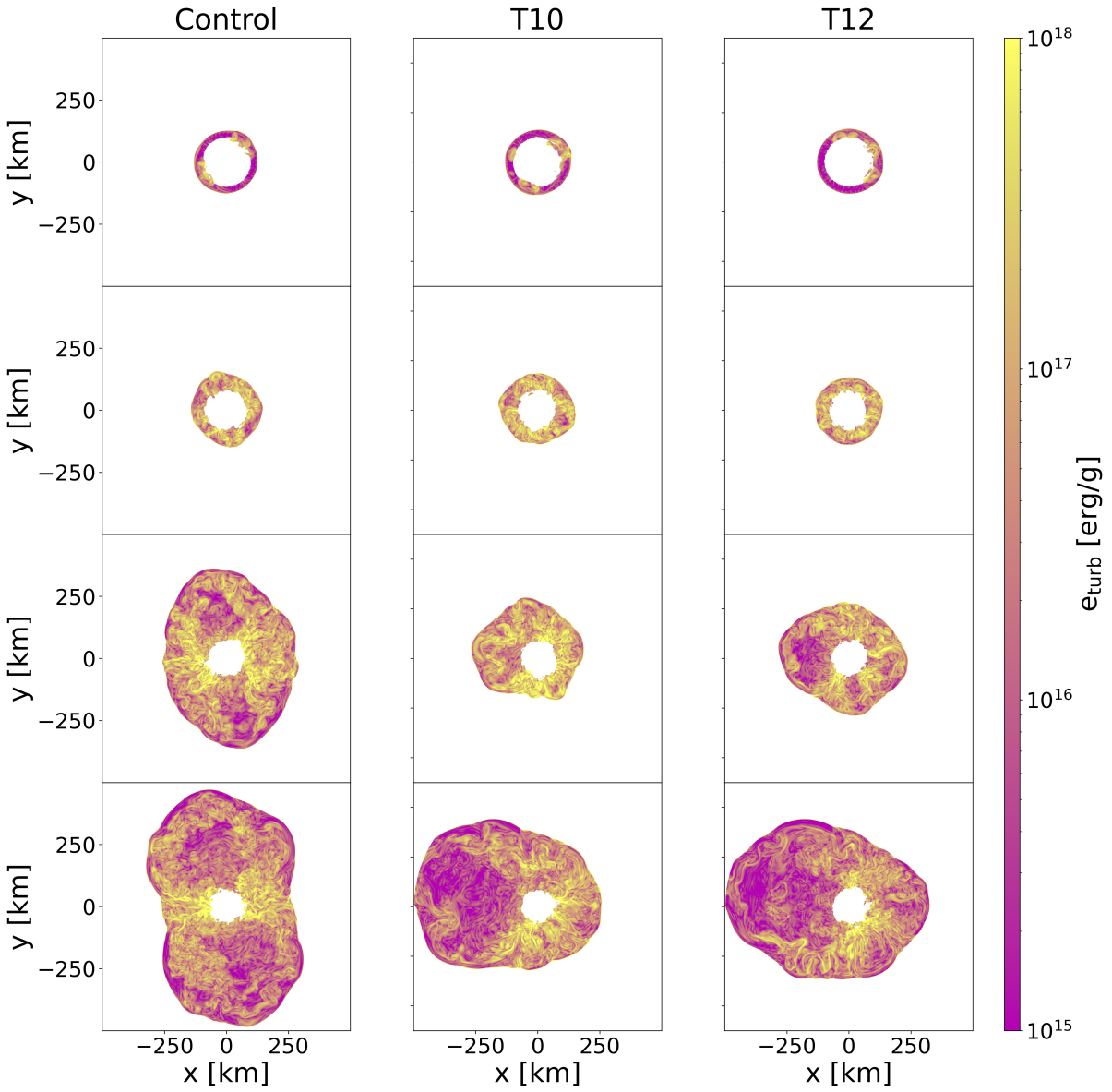

Figure 3.16: The specific TKE for the s20-Control (left), s20-T10 (middle), and s20-T12 (right) simulations at the post-bounce times of ∼ 102 ms (first row), ∼ 150 ms (second row), ∼ 193 ms (third row), and at final time for each simulation (last row).

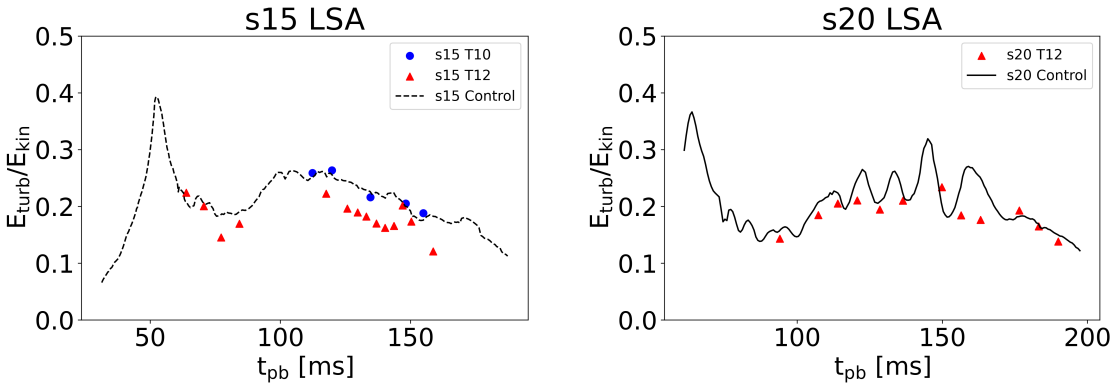

Figure 3.17: The ratio of integrated turbulent kinetic energy to kinetic energy in the gain region for all simulations.

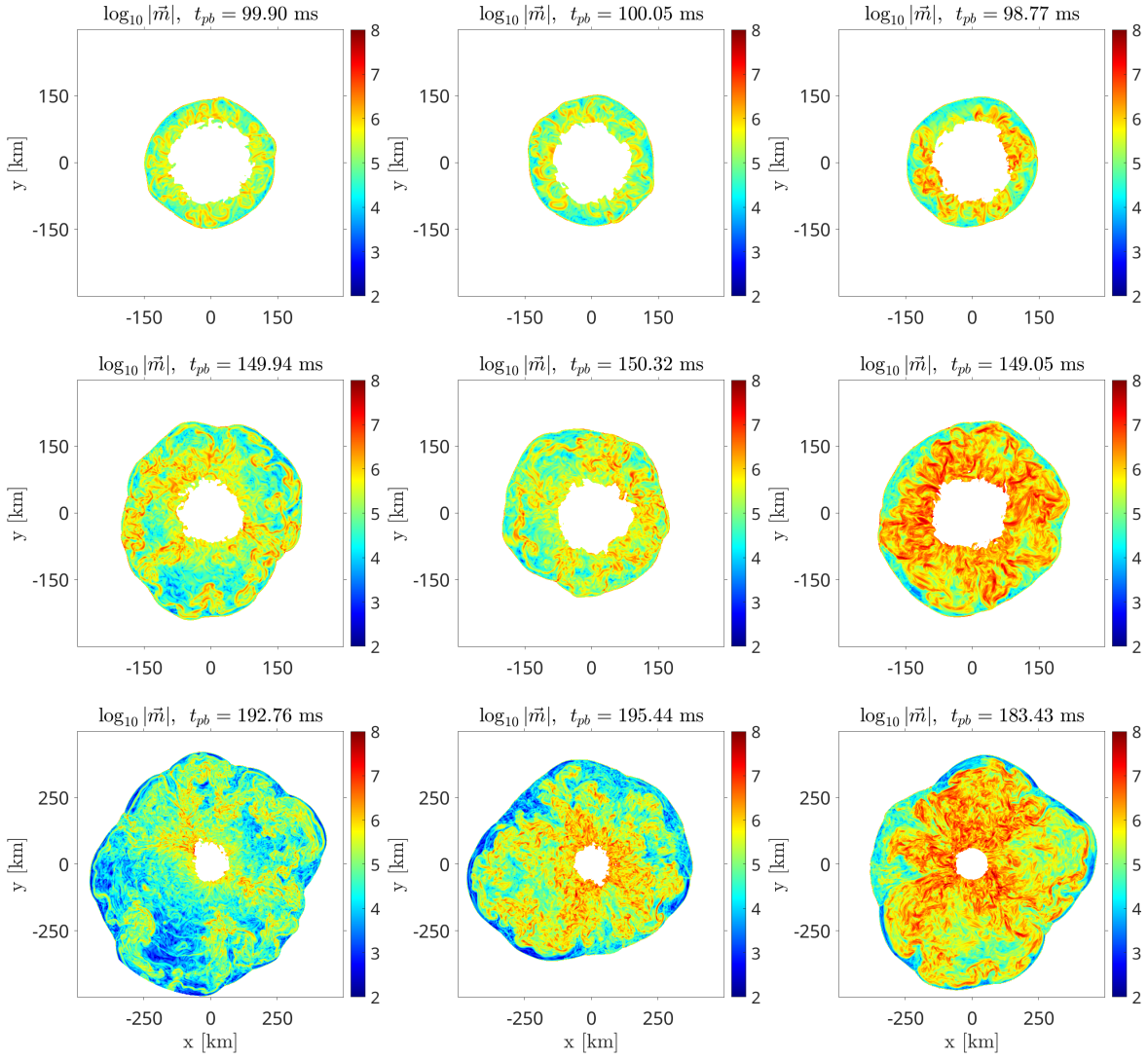

Figure 3.18: The magnitude of the baroclinic vector $[1/s^2]$ at different post-bounce times for the s15-Control (left), s15-T10 (middle), and s15-T12 (right) simulations.

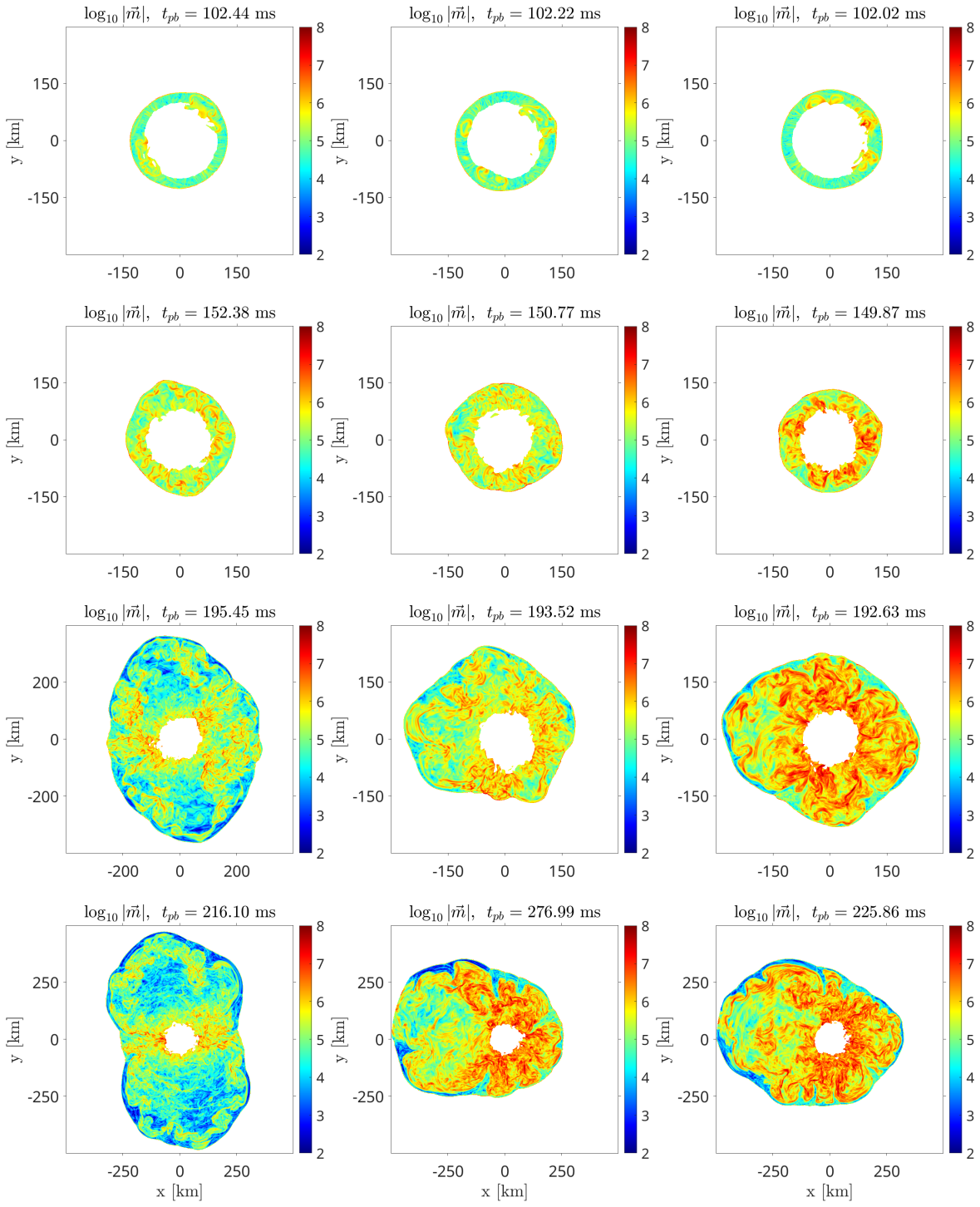

Figure 3.19: The magnitude of the baroclinic vector $[1/s^2]$ at different post-bounce times for the s20-Control (left), s20-T10 (middle), and s20-T12 (right) simulations.

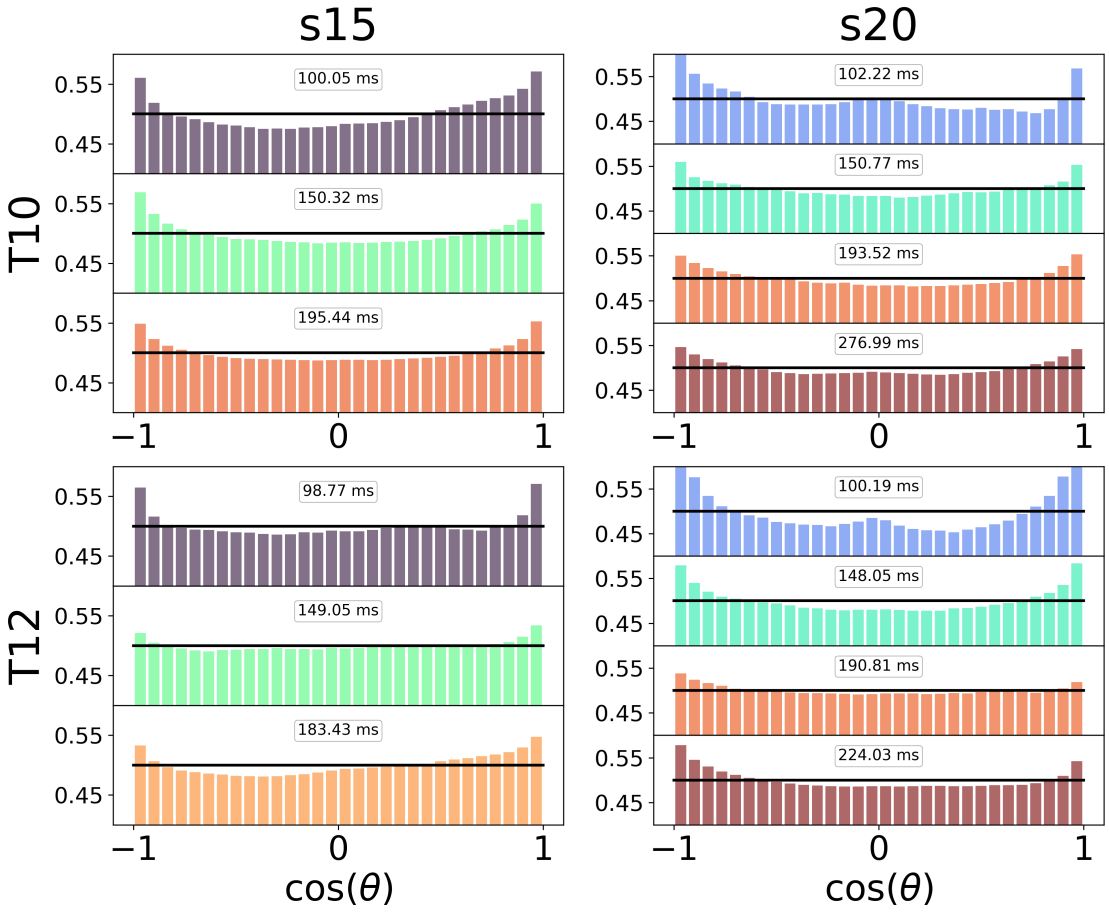

Figure 3.20: Distribution of $\cos\theta$ between $\vec{B}$ and $\vec{\omega}$ for the post bounce times shown in the other figures. Blue data represent earlier t_{pb} and red data represent later t_{pb}. The black horizontal line represents a uniform distribution.

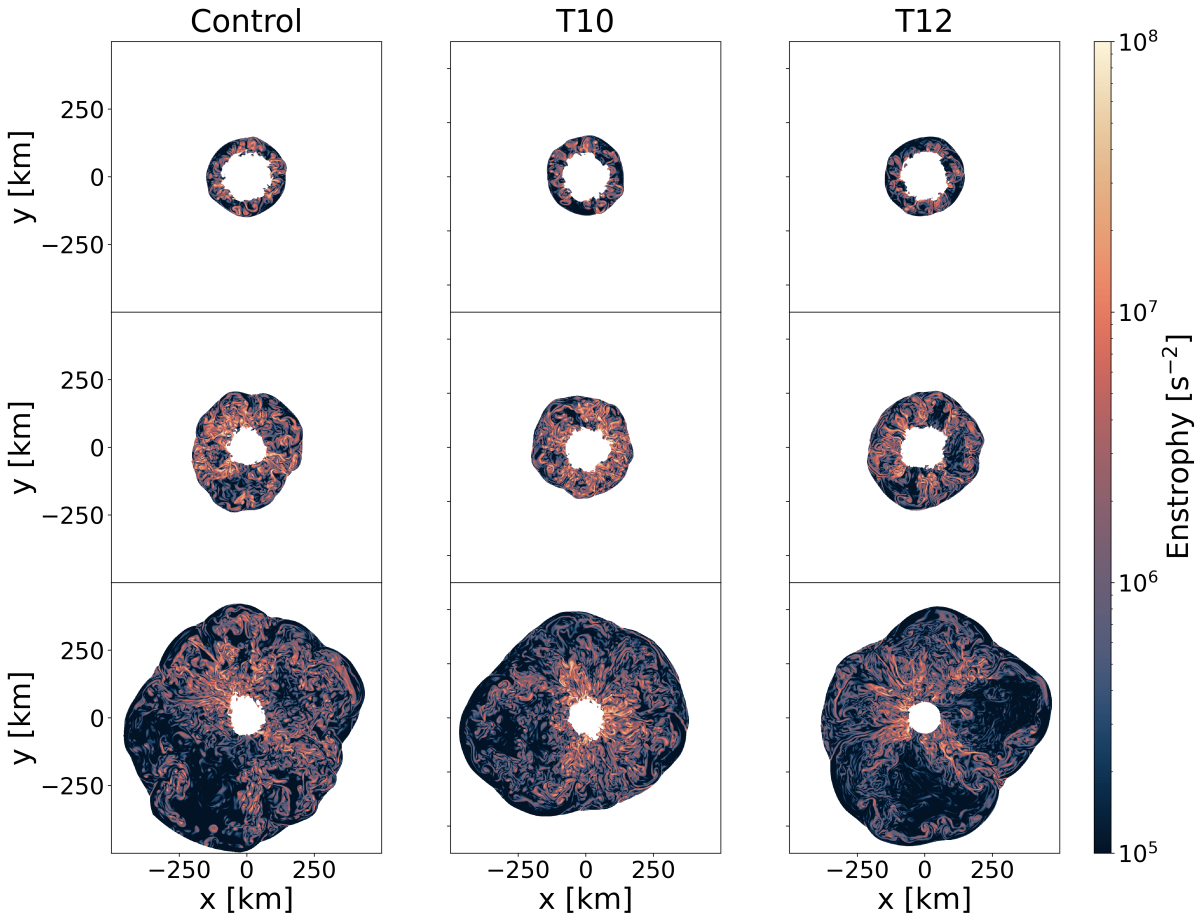

Figure 3.21: The enstrophy for the s15-Control (left), s15-T10 (middle), and s15-T12 (right) simulations at the post-bounce times of $\sim$ 100 ms (first row), $\sim$ 150 ms (second row), and at final time for each simulation (third row).

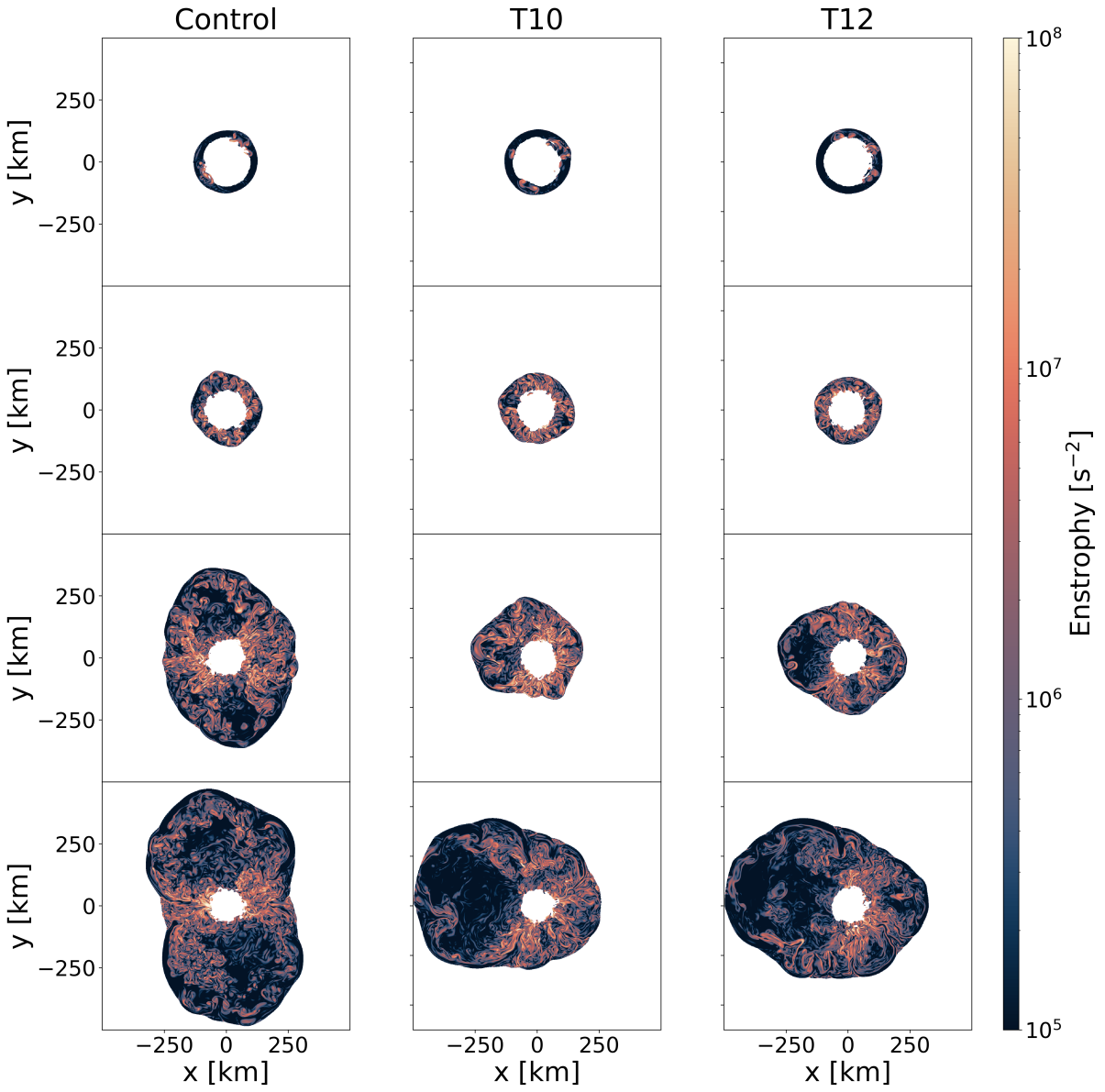

Figure 3.22: The enstrophy for the s20-Control (left), s20-T10 (middle), and s20-T12 (right) simulations at the post-bounce times of $\sim$ 102 ms (first row), $\sim$ 150 ms (second row), $\sim$ 193 ms (third row), and at final time for each simulation (last row).

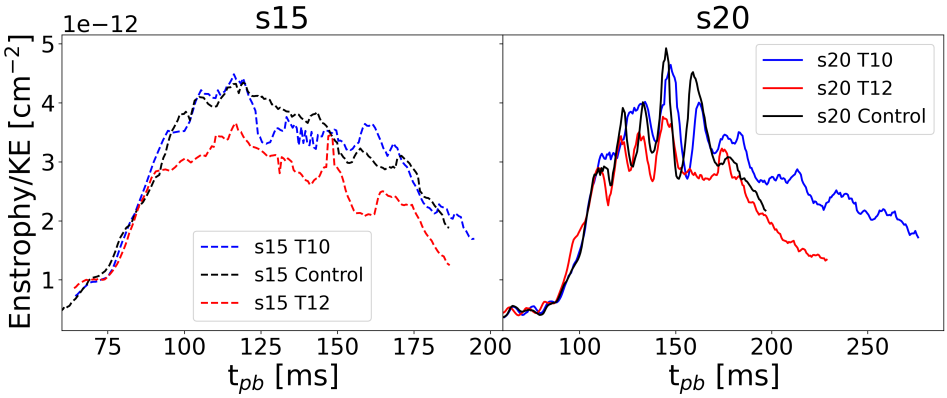

Figure 3.23: The ratio of the enstrophy to the kinetic energy, integrated over the gain region

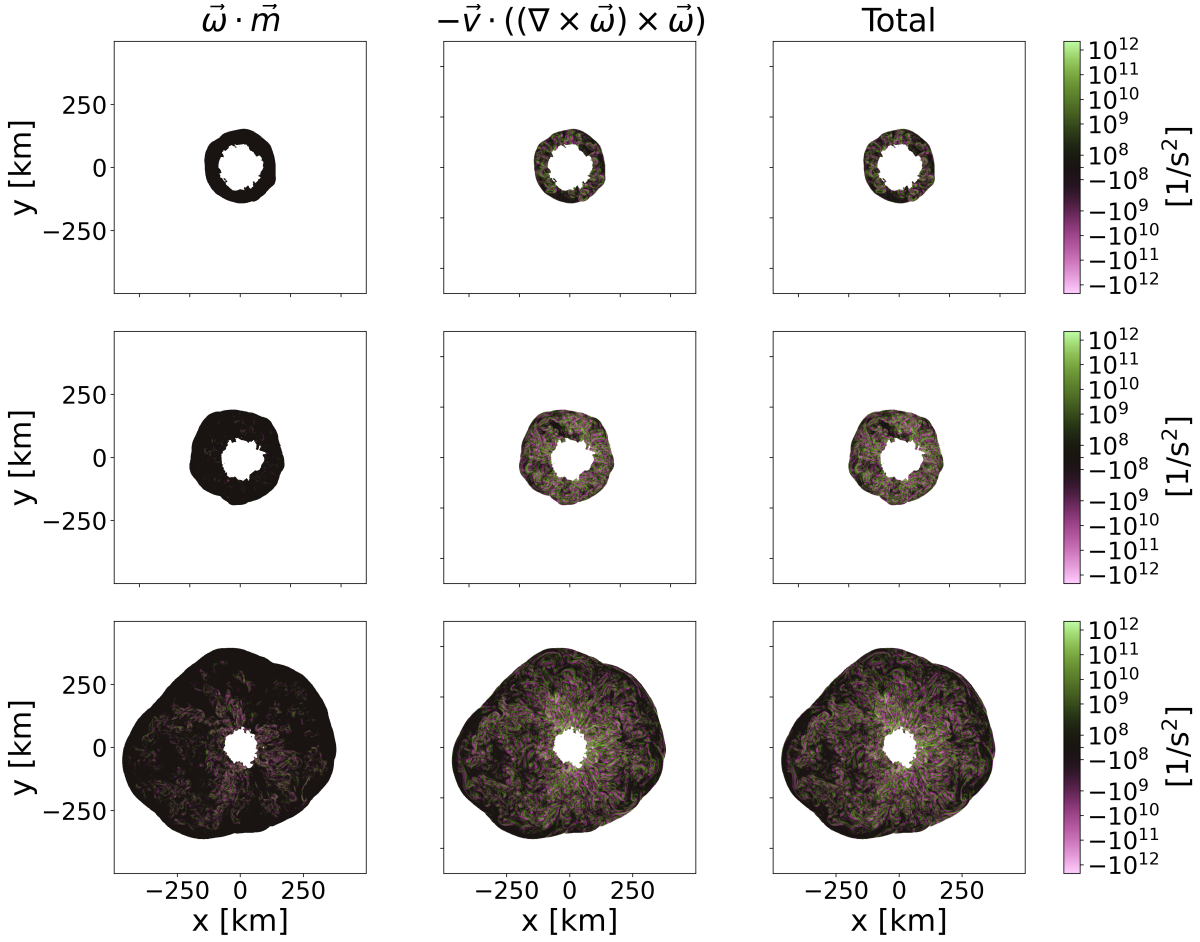

Figure 3.24: The enstrophy source terms from the right hand side of equation (3.39) for the s15-T10 simulation at the post-bounce times of ∼ 100 ms (first row), ∼ 150 ms (second row), and at ∼ 200 ms for each simulation (third row).

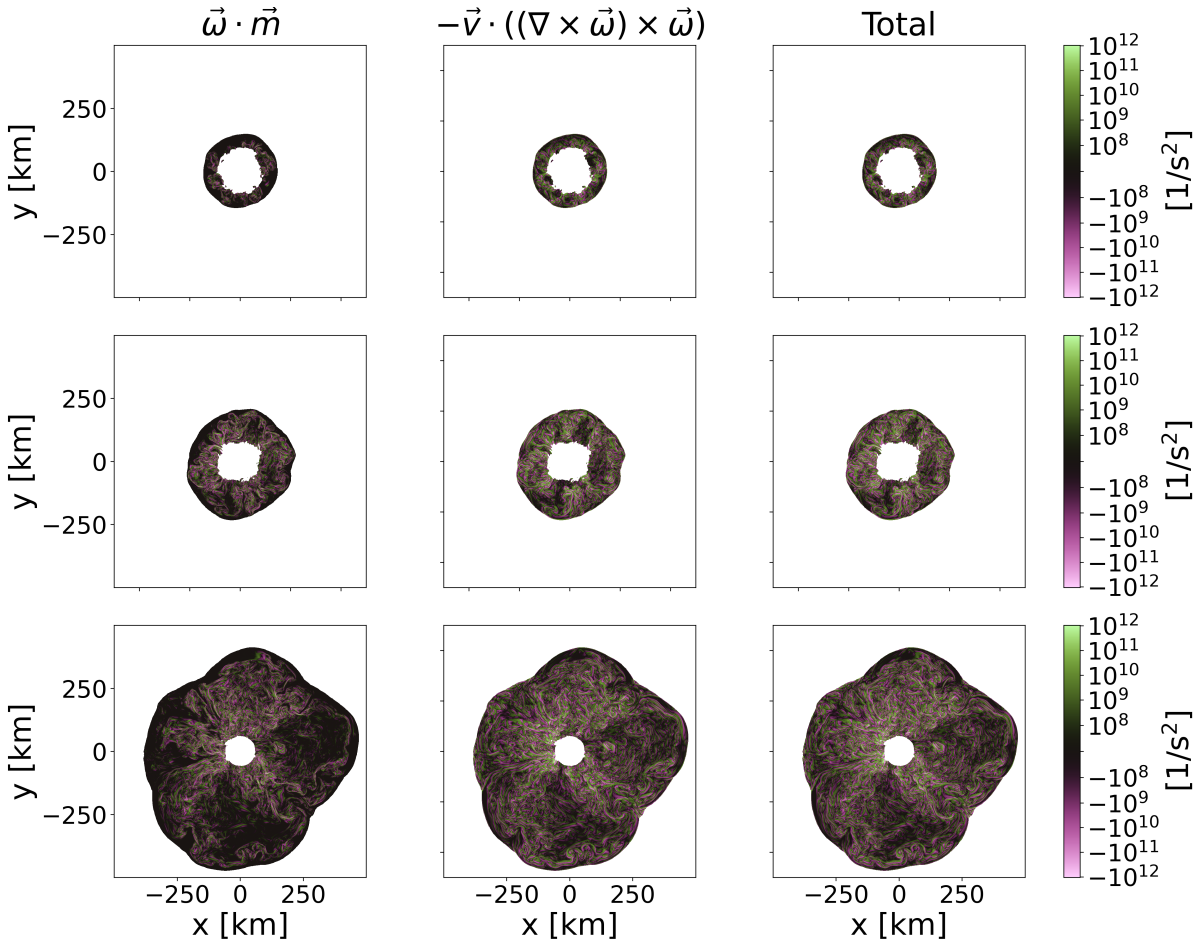

Figure 3.25: The enstrophy source terms from the right hand side of equation (3.39) for the s15-T12 simulation at the post-bounce times of ∼ 100 ms (first row), ∼ 150 ms (second row), and at ∼ 200 ms for each simulation (third row).

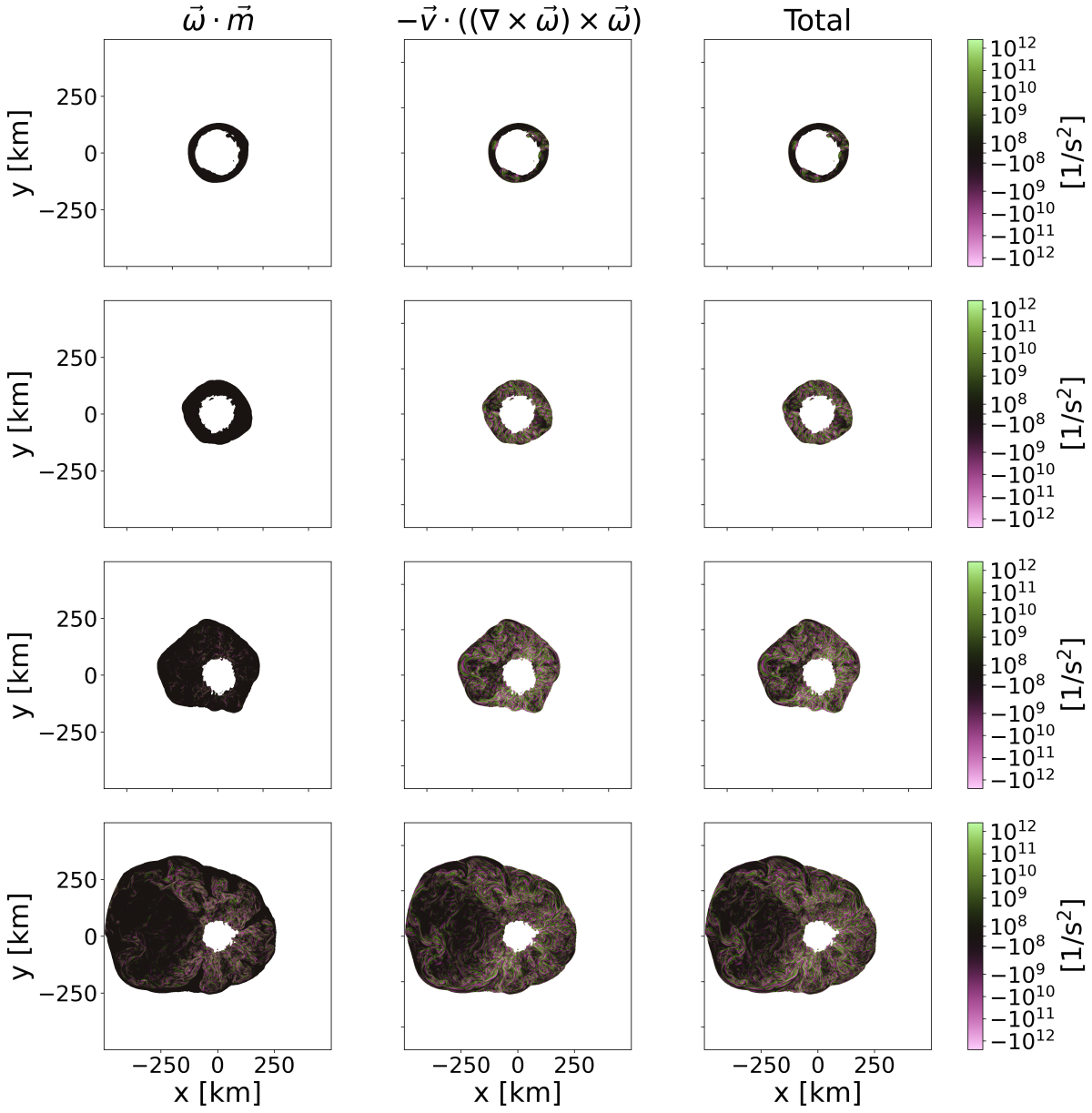

Figure 3.26: The enstrophy source terms from the right hand side of equation (3.39) for the s20-T10 simulation at the post-bounce times of ∼ 100 ms (first row), ∼ 150 ms (second row), and at ∼ 200 ms for each simulation (third row).

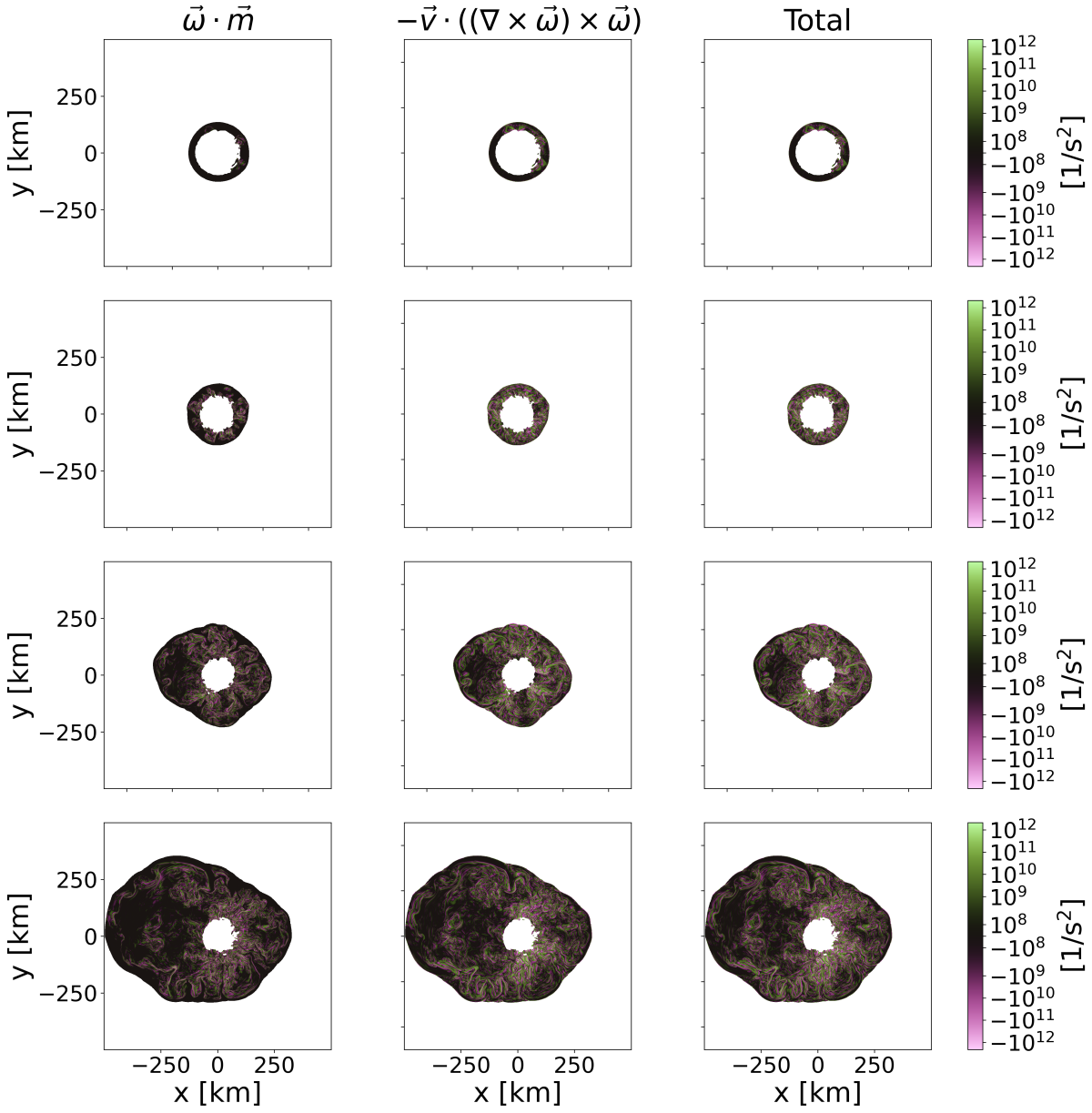

Figure 3.27: The enstrophy source terms from the right hand side of equation (3.39) for the s20-T12 simulation at the post-bounce times of ∼ 100 ms (first row), ∼ 150 ms (second row), and at ∼ 200 ms for each simulation (third row).

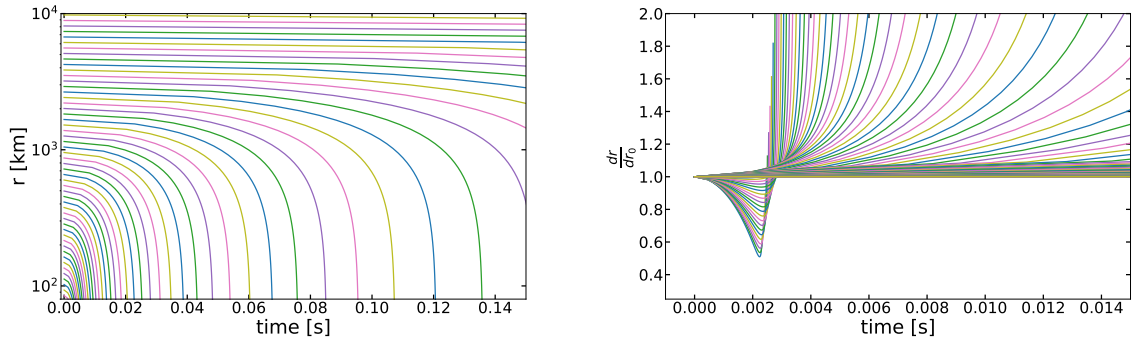

Figure 3.28: The radial coordinate r of mass elements (left panel) and stretch factor dr/dr_0 (right panel) as a function of time t given the density profile in equation (3.44).

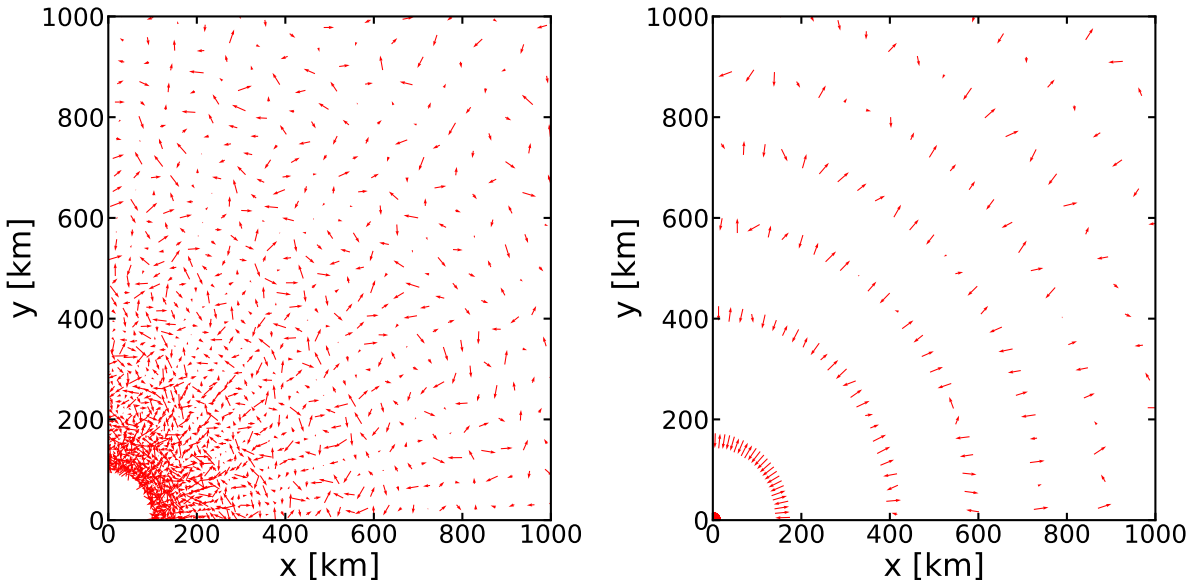

Figure 3.29: The 'xy' component of the magnetic field unit vectors for a grid of collapsing mass elements. The left panel shows the unit vectors at $t = 0$, the right panel at $t = 50$ ms.

REFERENCES

[1] H. A. Bethe and J. R. Wilson. Revival of a stalled supernova shock by neutrino heating. *ApJ*, 295:14–23, August 1985.

[2] Adam Burrows, John Hayes, and Bruce A. Fryxell. On the Nature of Core-Collapse Supernova Explosions. *ApJ*, 450:830, September 1995.

[3] H. Thomas Janka. Long-Term Multidimensional Models of Core-Collapse Supernovae: Progress and Challenges. *arXiv e-prints*, page arXiv:2502.14836, February 2025.

[4] T. Fischer, S. C. Whitehouse, A. Mezzacappa, F.-K. Thielemann, and M. Liebendörfer. Protoneutron star evolution and the neutrino-driven wind in general relativistic neutrino radiation hydrodynamics simulations. *Astronomy and Astrophysics*, 517:A80, July 2010.

[5] L. Hüdepohl, B. Müller, H. T. Janka, A. Marek, and G. G. Raffelt. Neutrino Signal of Electron-Capture Supernovae from Core Collapse to Cooling. *Phys. Rev. Lett.*, 104(25):251101, June 2010.

[6] Anthony Mezzacappa, Matthias Liebendörfer, O. E. Messer, W. Raphael Hix, Friedrich-Karl Thielemann, and Stephen W. Bruenn. Simulation of the Spherically Symmetric Stellar Core Collapse, Bounce, and Postbounce Evolution of a Star of 13 Solar Masses with Boltzmann Neutrino Transport, and Its Implications for the Supernova Mechanism. *Phys. Rev. Lett.*, 86(10):1935–1938, March 2001.

[7] M. Rampp and H. T. Janka. Radiation hydrodynamics with neutrinos. Variable Eddington factor method for core-collapse supernova simulations. *A&A*, 396:361–392, December 2002.

[8] Todd A. Thompson, Adam Burrows, and Philip A. Pinto. Shock Breakout in Core-Collapse Supernovae and Its Neutrino Signature. *ApJ*, 592(1):434–456, July 2003.

[9] Matthias Liebendörfer, O. E. Bronson Messer, Anthony Mezzacappa, Stephen W. Bruenn, Christian Y. Cardall, and F. K. Thielemann. A Finite Difference Representation of Neutrino Radiation Hydrodynamics in Spherically Symmetric General Relativistic Spacetime. *ApJS*, 150(1):263–316, January 2004.

[10] K. Sumiyoshi, S. Yamada, H. Suzuki, H. Shen, S. Chiba, and H. Toki. Postbounce Evolution of Core-Collapse Supernovae: Long-Term Effects of the Equation of State. *ApJ*, 629(2):922–932, August 2005.

[11] H. Th. Janka, K. Langanke, A. Marek, G. Martínez-Pinedo, and B. Müller. Theory of core-collapse supernovae. *Phys. Rep.*, 442(1-6):38–74, April 2007.

[12] Hans-Thomas Janka. *Neutrino-Driven Explosions*, page 1095. 2017.

[13] Sean M. Couch. The mechanism(s) of core-collapse supernovae. *Philosophical Transactions of the Royal Society of London Series A*, 375(2105):20160271, September 2017.

[14] Takami Kuroda, Almudena Arcones, Tomoya Takiwaki, and Kei Kotake. Magnetorotational explosion of a massive star supported by neutrino heating in general relativistic three-dimensional simulations. *The Astrophysical Journal*, 896(2):102, Jun 2020.

[15] Robert Bollig, Naveen Yadav, Daniel Kresse, Hans-Thomas Janka, Bernhard Müller, and Alexander Heger. Self-consistent 3D Supernova Models From -7 Minutes to +7 s: A 1-bethe Explosion of a 19 $M_\odot$ Progenitor. *ApJ*, 915(1):28, July 2021.

[16] Ko Nakamura, Tomoya Takiwaki, and Kei Kotake. Three-dimensional simulation of a core-collapse supernova for a binary star progenitor of SN 1987A. *MNRAS*, 514(3):3941–3952, August 2022.

[17] David Vartanyan, Matthew S. B. Coleman, and Adam Burrows. The collapse and three-dimensional explosion of three-dimensional massive-star supernova progenitor models. *MNRAS*, 510(4):4689–4705, March 2022.

[18] Bailey Sykes and Bernhard Müller. Long-time 3D supernova simulations of non-rotating progenitors with magnetic fields, December 2024. arXiv:2412.01155 [astro-ph].

[19] Shota Shibagaki, Takami Kuroda, Kei Kotake, Tomoya Takiwaki, and Tobias Fischer. Three-dimensional GRMHD simulations of rapidly rotating stellar core collapse. *MNRAS*, 531(3):3732–3743, July 2024.

[20] Tianshu Wang and Adam Burrows. Nucleosynthetic Analysis of Three-dimensional Core-collapse Supernova Simulations. *ApJ*, 962(1):71, February 2024.

[21] J. S. Bloom, S. R. Kulkarni, S. G. Djorgovski, A. C. Eichelberger, P. Côté, J. P. Blakeslee, S. C. Odewahn, F. A. Harrison, D. A. Frail, A. V. Filippenko, D. C. Leonard, A. G. Riess, H. Spinrad, D. Stern, A. Bunker, A. Dey, B. Grossan, S. Perlmutter, R. A. Knop, I. M. Hook, and M. Feroci. The unusual afterglow of the γ-ray burst of 26 March 1998 as evidence for a supernova connection. *Nature*, 401(6752):453–456, September 1999.

[22] S. E. Woosley and J. S. Bloom. The Supernova Gamma-Ray Burst Connection. *ARA&A*, 44(1):507–556, September 2006.

[23] A. Burrows, L. Dessart, E. Livne, C. D. Ott, and J. Murphy. Simulations of magnetically driven supernova and hypernova explosions in the context of rapid rotation. *The Astrophysical Journal*, 664(1):416434, Jul 2007.

[24] C. Winteler, R. Käppeli, A. Perego, A. Arcones, N. Vasset, N. Nishimura, M. Liebendörfer, and F.-K. Thielemann. MAGNETOROTATIONALLY DRIVEN SUPERNOVAE AS THE ORIGIN OF EARLY GALAXY r -PROCESS ELEMENTS? *The Astrophysical Journal*, 750(1):L22, apr 2012.

[25] M. Obergaulinger and M. Á. Aloy. Magnetorotational core collapse of possible GRB progenitors - III. Three-dimensional models. *MNRAS*, 503(4):4942–4963, May 2021.

[26] Jin Matsumoto, Tomoya Takiwaki, and Kei Kotake. Neutrino-driven massive stellar explosions in 3D fostered by magnetic fields via turbulent α-effect. *MNRAS*, 528(1):L96–L101, February 2024.

[27] Ko Nakamura, Tomoya Takiwaki, Jin Matsumoto, and Kei Kotake. Three-dimensional magnetohydrodynamic simulations of core-collapse supernovae - I. Hydrodynamic evolution and protoneutron star properties. *MNRAS*, 536(1):280–294, January 2025.

[28] J. Matsumoto, Y. Asahina, T. Takiwaki, K. Kotake, and H. R. Takahashi. Magnetic support for neutrino-driven explosion of 3D non-rotating core-collapse supernova models. *MNRAS*, 516(2):1752–1767, October 2022.

[29] G. Leidi, R. Andrassy, J. Higl, P. V. F. Edelmann, and F. K. Röpke. Turbulent dynamo action and its effects on the mixing at the convective boundary of an idealized oxygen-burning shell. *A&A*, 679:A132, November 2023.

[30] Shizuka Akiyama, J. Craig Wheeler, David L. Meier, and Itamar Lichtenstadt. The Magnetorotational Instability in Core-Collapse Supernova Explosions. *ApJ*, 584(2):954–970, February 2003.

[31] A. Brandenburg, R. L. Jennings, Å. Nordlund, M. Rieutord, R. F. Stein, and I. Tuominen. Magnetic structures in a dynamo simulation. *Journal of Fluid Mechanics*, 306:325–352, January 1996.

[32] Eirik Endeve, Christian Y. Cardall, Reuben D. Budiardja, and Anthony Mezzacappa. Generation of Magnetic Fields By the Stationary Accretion Shock Instability. *ApJ*, 713(2):1219–1243, April 2010.

[33] Eirik Endeve, Christian Y. Cardall, Reuben D. Budiardja, Samuel W. Beck, Alborz Bejnood, Ross J. Toedte, Anthony Mezzacappa, and John M. Blondin. Turbulent magnetic field amplification from spiral sasi modes: Implications for core-collapse supernovae and proto-neutron star magnetization. *The Astrophysical Journal*, 751(1):26, may 2012.

[34] E. Endeve, C. Y. Cardall, R. D. Budiardja, A. Mezzacappa, and J. M. Blondin. Turbulence and magnetic field amplification from spiral SASI modes in core-collapse supernovae. *Physica Scripta Volume T*, 155(1):014022, July 2013.

[35] E. N. Parker. The Dynamical State of the Interstellar Gas and Field. *ApJ*, 145:811, September 1966.

[36] P. Bradshaw. *An Introduction to Turbulence and Its Measurement*. Pergamon Press, 1971.

[37] Arkady Tsinober. *An Informal Introduction to Turbulence*, volume 63. 2004.

[38] David Calvert, Michael Redle, Bibek Gautam, Charles J. Stapleford, Carla Fröhlich, James P. Kneller, and Matthias Liebendorfer. Turbulence in Core-Collapse Supernovae. *arXiv e-prints*, page arXiv:2511.16755, November 2025.

[39] Rubén M. Cabezón, Kuo-Chuan Pan, Matthias Liebendörfer, Takami Kuroda, Kevin Ebinger, Oliver Heinimann, Albino Perego, and Friedrich-Karl Thielemann. Core-collapse supernovae in the hall of mirrors. A three-dimensional code-comparison project. *A&A*, 619:A118, November 2018.

[40] Roger Käppeli, Stuart C Whitehouse, Simon Scheidegger, U-L Pen, and Matthias Liebendörfer. Fish: a three-dimensional parallel magnetohydrodynamics code for astrophysical applications. *The Astrophysical Journal Supplement Series*, 195(2):20, 2011.

[41] M. Liebendörfer, S. C. Whitehouse, and T. Fischer. The Isotropic Diffusion Source Approximation for Supernova Neutrino Transport. *ApJ*, 698:1174–1190, June 2009.

[42] James M Lattimer and F Douglas Swesty. A generalized equation of state for hot, dense matter. *Nuclear Physics A*, 535(2):331–376, 1991.

[43] A Marek, Harold Dimmelmeier, H-Th Janka, E Müller, and R Buras. Exploring the relativistic regime with newtonian hydrodynamics: an improved effective gravitational potential for supernova simulations. *Astronomy & Astrophysics*, 445(1):273–289, 2006.

[44] Ue-Li Pen, Phil Arras, and ShingKwong Wong. A free, fast, simple, and efficient total variation diminishing magnetohydrodynamic code. *The Astrophysical Journal Supplement Series*, 149(2):447, 2003.

[45] Shi Jin and Zhouping Xin. The relaxation schemes for systems of conservation laws in arbitrary space dimensions. *Communications on pure and applied mathematics*, 48(3):235–276, 1995.

[46] Stephen W Bruenn. Stellar core collapse-numerical model and infall epoch. *The Astrophysical Journal Supplement Series*, 58:771–841, 1985.

[47] Stanford E Woosley and Alexander Heger. Nucleosynthesis and remnants in massive stars of solar metallicity. *Physics Reports*, 442(1-6):269–283, 2007.

[48] M. Obergaulinger, H.-Th. Janka, and M. A. Aloy. Magnetic field amplification and magnetically supported explosions of collapsing, non-rotating stellar cores. *Monthly Notices of the Royal Astronomical Society*, 445(3):3169–3199, 10 2014.

[49] J Matsumoto, T Takiwaki, K Kotake, Y Asahina, and H R Takahashi. 2d numerical study for magnetic field dependence of neutrino-driven core-collapse supernova models. *Monthly Notices of the Royal Astronomical Society*, 499(3):4174–4194, 10 2020.

[50] Martin Obergaulinger and Hans-Thomas Janka. Magnetic field amplification in collapsing, non-rotating stellar cores. *arXiv e-prints*, page arXiv:1101.1198, January 2011.

[51] John M. Blondin, Anthony Mezzacappa, and Christine DeMarino. Stability of Standing Accretion Shocks, with an Eye toward Core-Collapse Supernovae. *ApJ*, 584(2):971–980, February 2003.

[52] John M. Blondin and Anthony Mezzacappa. Pulsar spins from an instability in the accretion shock of supernovae. *Nature*, 445(7123):58–60, January 2007.

[53] A. Mezzacappa, A. C. Calder, S. W. Bruenn, J. M. Blondin, M. W. Guidry, M. R. Strayer, and A. S. Umar. An Investigation of Neutrino-driven Convection and the Core Collapse Supernova Mechanism Using Multigroup Neutrino Transport. *ApJ*, 495(2):911–926, March 1998.

[54] H. Thomas Janka and Ewald Mueller. The First Second of a Type II Supernova: Convection, Accretion, and Shock Propagation. *ApJL*, 448:L109, August 1995.

[55] R. Buras, H. Th. Janka, M. Rampp, and K. Kifonidis. Two-dimensional hydrodynamic core-collapse supernova simulations with spectral neutrino transport. II. Models for different progenitor stars. *A&A*, 457(1):281–308, October 2006.

[56] Sean M. Couch and Christian D. Ott. Revival of the Stalled Core-collapse Supernova Shock Triggered by Precollapse Asphericity in the Progenitor Star. *ApJL*, 778(1):L7, November 2013.

[57] Sean M. Couch and Evan P. O'Connor. High-resolution Three-dimensional Simulations of Core-collapse Supernovae in Multiple Progenitors. *ApJ*, 785(2):123, April 2014.

[58] Irene Tamborra, Georg Raffelt, Florian Hanke, Hans-Thomas Janka, and Bernhard Müller. Neutrino emission characteristics and detection opportunities based on three-dimensional supernova simulations. *Phys. Rev. D*, 90(4):045032, August 2014.

[59] Anthony Mezzacappa, Eric J. Lentz, Stephen W. Bruenn, W. Raphael Hix, O. E. Bronson Messer, Eirik Endeve, John M. Blondin, J. Austin Harris, Pedro Marronetti, Konstantin N. Yakunin, and Eric J. Lingerfelt. A Neutrino-Driven Core Collapse Supernova Explosion of a 15 M Star. *arXiv e-prints*, page arXiv:1507.05680, July 2015.

[60] H. Andresen, B. Müller, E. Müller, and H. Th. Janka. Gravitational wave signals from 3D neutrino hydrodynamics simulations of core-collapse supernovae. *MNRAS*, 468(2):2032–2051, June 2017.

[61] David Vartanyan, Adam Burrows, David Radice, M. Aaron Skinner, and Joshua Dolence. Revival of the fittest: exploding core-collapse supernovae from 12 to 25 $M_{\odot}$. *MNRAS*, 477(3):3091–3108, July 2018.

[62] Robert Glas, Oliver Just, H. Thomas Janka, and Martin Obergaulinger. Three-dimensional Core-collapse Supernova Simulations with Multidimensional Neutrino Transport Compared to the Ray-by-ray-plus Approximation. *ApJ*, 873(1):45, March 2019.

[63] Bernhard Müller and Vishnu Varma. A 3D simulation of a neutrino-driven supernova explosion aided by convection and magnetic fields. *MNRAS*, 498(1):L109–L113, November 2020.

[64] David Vartanyan, Adam Burrows, Tianshu Wang, Matthew S. B. Coleman, and Christopher J. White. Gravitational-wave signature of core-collapse supernovae. *Phys. Rev. D*, 107(10):103015, May 2023.

[65] Jade Powell and Bernhard Müller. The gravitational-wave emission from the explosion of a 15 solar mass star with rotation and magnetic fields. *MNRAS*, 532(4):4326–4339, August 2024.

[66] Swapnil Shankar, Philipp Mösta, Roland Haas, and Erik Schnetter. 3D full-GR simulations of magnetorotational core-collapse supernovae on GPUs: A systematic study of rotation rates and magnetic fields. *arXiv e-prints*, page arXiv:2504.11537, April 2025.

[67] L.D. Landau, J.S. Bell, M.J. Kearsley, L.P. Pitaevskii, E.M. Lifshitz, and J.B. Sykes. *Electrodynamics of Continuous Media*. COURSE OF THEORETICAL PHYSICS. Elsevier Science, 2013.

[68] Axel Brandenburg and Kandaswamy Subramanian. Astrophysical magnetic fields and nonlinear dynamo theory. *Physics Reports*, 417(1):1–209, 2005.

[69] James F. Hollins, Graeme R. Sarson, Cetin Can Evirgen, Anvar Shukurov, Andrew Fletcher, and Frederick A. Gent. Mean fields and fluctuations in compressible magnetohydrodynamic flows. *Geophysical and Astrophysical Fluid Dynamics*, 116(4):261–289, July 2022.

[70] Ernazar Abdikamalov and Thierry Foglizzo. Acoustic wave generation in collapsing massive stars with convective shells. *MNRAS*, 493(3):3496–3512, April 2020.

CHAPTER

4

MASS-LOSS AND CONVECTIVE OVERSHOOTING TREATMENTS AS INDICATORS OF CORE-COLLAPSE SUPERNOVAE OUTCOMES

David Calvert, Kenzie Myers, Claire B. Campbell, James P. Kneller, Carla Fröhlich

The following chapter will be submitted to the Astrophysical Journal

4.1 Abstract

While core-collapse supernovae (CCSNe) are highly dynamical and complex events, the greatest influence upon the outcome is the structure of the star at the point where it begins to collapse. In stellar evolution, however, there are many uncertain quantities that dictate the properties of a star beginning the process of core-collapse. The mass loss treatment and the convective overshooting of stars during their lifetime affect the thermal and chemical properties of star's core when the collapse begins. Different mass loss and overshooting treatments will change the carbon/oxygen core mass and compactness parameter ξ_M, which are frequently used as measures for the properties of the subsequent supernova. In this paper we explore the impacts of changing the mass loss and overshooting treatments upon the stellar structure of the star and explore how they affect the outcome of the simulations. We use MESA to evolve a set of stars through to the end of their lives and then AGILE-IDSA with PUSH to simulate the explosion. We find that an increased wind efficiency correlates moderately negatively with the ejecta mass due to a reduced hydrogen envelope mass at the start of core-collapse. Further, we also find that applying the convective overshooting treatments at more radiative/convective boundaries within the star can result in a greater iron core mass through extension of the burning phases, which ultimately results in a greater neutrino luminosity.

4.2 Introduction

Stars whose zero-age main sequence (ZAMS) masses are in excess of $\sim 8-10$ $M_\odot$ will undergo core-collapse in the final stage of their evolution [1, 2, 3]. This collapse has the potential to result in one of the most energetic events in the universe, a core-collapse supernova (CCSN). These events provide us the opportunity to understand physics at temperatures and pressures unlike anything on Earth and can hold the answer to questions about nucleosynthesis, compact object formation, and neutrino properties. A portion of these events are unsuccessful in explosion and instead collapse to form a black hole.

The structure of a star at pre-supernova stages depends on the entire lifetime of that star [4]. The specifics of what features of the star determines its likelihood to explode is an area of active research and remains to be fully answered. One widely adopted measure of

the progenitor is the compactness [5], defined to be:

$$\xi_M = \frac{M/M_\odot}{R/1000\,\mathrm{km}}. \tag{4.1}$$

Compactness is useful because it has been shown to correlate with supernova success [6, 7, 5, 8] and relate to the explosion energy and remnant mass of supernovae [9, 10, 11]. Several studies have now demonstrated that the compactness of a star at collapse is sensitive to different treatments of physics within stellar evolution models [12, 13]. [12] points out that due to the complicated and ill-constrained nature of stellar modeling, different groups will "universally" obtain different results for pre-supernova models of the same ZAMS mass. While there are many aspects of stellar evolution that we can focus upon, the two that interest us most in this paper are the mass loss and the convective overshooting. Mass loss due to stellar winds is poorly understood [14, 15]. Various prescriptions have been put forward to describe the effects of mass-loss in stellar models [16, 17, 18, 19]. The most pertinent of these studies is that by [15] who showed that the choice of algorithm for the the mass loss rate can greatly impact the value of $\xi_{2.5}$ at collapse for an array of stellar models.

Similarly, how to best treat convective overshooting in stellar evolution codes is another area of uncertainty. In the mixing length theory used to model convection in stars, buoyant bubbles that are unstable to convection travel upward through the convective zone and stop at radiative boundaries [20]. As it approaches the interface between a convective and radiative zone, the bubble is traveling with nonzero momentum. The bubble will penetrate some distance into the radiative zone and thus overshoots the boundary. This phenomenon is named convective overshooting. Since there are no observational constraints on the process, it is not well understood to what degree overshooting occurs and how best to describe it. The prevailing model for the treatment of convective overshooting is known as "step" overshooting where the code will use a constant diffusion coefficient for the mixing across the radiative/convective boundary. Convective overshooting has been studied in the context of stars on the main sequence [21, 22], but few works outside [23] have systematically studied the effects of the convective overshooting treatment on CCSNe, and none have yet to explore how varying the treatment beyond step overshooting affects CCSNe. [24] have developed a different, exponentially diffusive overshoot model for the diffusion coefficient. This model contains a free parameter f_{ov} which is not strongly constrained by observation. However it is treated, the amount by which the convection overshoots the boundary of convective stability impacts the nuclear burning throughout the star's life and thus the size of various layers of the CCSN progenitor and

their chemical composition [25, 23]. [12] have found that the compactness $\xi_{2.5}$ is dependent on the mass of the CO core.

These previous studies demonstrate that the stellar evolution plays a critical role in the determination of compactness. This present paper aims to build on these investigations and to further understand the supernova parameter space. In this work we use 29 pre-supernova models from [26] to investigate how the effects of convective overshooting and mass-loss rates impact supernova explosions in the PUSH framework [27].

The remainder of the paper is organized as follows. In section §4.3 we describe the progenitor models, the treatment of mass-loss rates and convective overshooting, and the details of the supernova code. Section §4.4 presents the results of the supernova simulations and highlights the relationships between the stellar modeling and the resultant supernovae. Section §4.5 summarizes our findings.

4.3 Progenitor Models and Simulation Setup

4.3.1 Progenitor models

In this work, we model a suite of collapsing red supergiant progenitors of ZAMS masses {12,15,18,20,25} $M_\odot$ constructed by [26] through core-collapse and explosion. These models have been evolved using the Modules for Experiments in Stellar Astrophysics (MESA) [28], an open-source 1D stellar evolution code, until the infall velocity reaches ∼1000 km/s. Since studies by [29] and [30] have shown that the size of the nuclear network used in the stellar evolution codes can also lead to change sin the structure of the star, all of these models are evolved using a 206-isotope nuclear network. The models all have solar metallicity and are non-rotating. The models are varied across two axes; the stellar wind efficiency parameter η in the mass loss scheme, and the treatment of the convective overshooting, labeled either “all-bounds” or “core-only”.

The mass loss efficiency is controlled by a dimensionless parameter η [17, 31]. The exact equations are detailed and so we do not reproduce them here; the essence of them is that as η increases, the star loses mass more efficiently.

The overshooting prescription we adopt in MESA uses either a step or an exponential function for the diffusion coefficient $D(r)$ that is used to model the mixing at the boundary. The step case has a constant mixing efficiency D_0 applied over a distance of the pressure

scale height across the boundary, while the exponential mixing is of the form

$$D(r) = D_0 \exp\left\{\frac{-2(r-r_0)}{f_{\rm ov} H_{p,0}}\right\}, \tag{4.2}$$

where D_0 is the convective mixing efficiency at the radiative/convective interface, r_0 is the radial position of the convective/radiative boundary, r is the radial position within the star, $H_{p,0}$ is the pressure scale height, and $f_{\rm ov}$ is a free parameter. The names "All-bounds" and "Core-only" that we adopt to describe the models refer to the placement and interfaces where we apply the convective overshooting treatment. For both, the convective/radiative boundaries within the hydrogen layer are handled with a step function. For the "core-only" models, the exponential mixing efficiency in equation (4.2) is only applied at the convective/radiative boundaries within the helium layer, while all other boundaries are treated as the basic step function. In "all-bounds" models, the exponential mixing efficiency prescription is applied to all convective/radiative boundaries throughout the star, save for those in the hydrogen layer and at the boundary of the He/CO layers. The specifics of these treatments and the selected parameters in this implementation of MESA are laid out in detail in [26].

The variation of these parameters has resulted in a grid of 12 progenitors for use in this work. The differences in the treatments of mass loss and convective overshooting have resulted in significant differences in the properties of the pre-supernova models. Figure 4.1 shows the density profiles of the progenitors for each initial ZAMS mass using each value of η and treatment of convective overshooting, color coded by the compactness at 2.0 $M_\odot$ measured at the time of collapse. While the inner cores of the stars, up to $M \lesssim 1$ $M_\odot$ do not show much difference as we vary the overshooting and mass loss efficiency, the density profiles exhibit much more sensitivity in the crucial 1 $M_\odot \lesssim M \lesssim 2.5$ $M_\odot$ range. This is the material which falls through the shock a few hundred milliseconds after core bounce i.e. during the stalled shock phase.

It is not solely the density profile of the star that is different between models. Figure 4.2 summarizes the size of the various layers of the star at the point of collapse. To make this figure, we define the Fe-core mass as being the mass enclosed by the innermost point where the mass fraction of silicon satisfies $X_{\rm Si} < 0.3$; the carbon/oxygen core mass is defined as the mass enclosed beneath $X_{\rm He} \leq 0.2$; the helium core mass is defined as the enclosed mass beneath $X_{\rm H} \leq 0.2$ and above the CO-core, and the hydrogen envelope is defined as all zones above the helium boundary. Additionally, the bottom panel highlights the silicon/oxygen

interface, defined as the point at which $X_{Si} = X_O$. From Figure 4.2 it is clear that for a larger wind efficiency parameter η, unsurprisingly more of the hydrogen envelope is lost during stellar evolution. More interestingly, the wind efficiency parameter has an impact on the composition at the core of the star. For models above 12 $M_\odot$, the data in Figure 4.2 show that the iron core mass, as well as the location of the silicon/oxygen interface, is affected by changes to η.

Further, the convective overshooting treatment appears to be moderately impactful on the core composition. While there appears to be differences in the iron core masses of order ~ 0.1 $M_\odot$ for all other models, the 25 $M_\odot$ models have a larger difference in the size of both the CO core and the He shell masses across convective overshooting treatments. Additionally the silicon/oxygen interface has a dependence on the treatment of the convective overshooting, except in the case of the 18 $M_\odot$ models with $\eta = 0.8$.

Figure 4.3 shows the compactness $\xi_{2.0}$ of the progenitors in this work calculated at collapse alongside the compactness of the progenitors modeled with the KEPLER code by [1] (red) and [32] (green). This figure highlights that the compactness of the MESA progenitors generally seem to have a slightly higher compactness than the KEPLER models, yet there are not enough MESA models to conclusively claim whether the compactness peak has shifted compared to KEPLER models. Figure 4.3, coupled with the color scale of Figure 4.1, confirm the idea that the compactness of these models responds to modifications to the input parameters. In the suite of progenitors, the compactness at 2 $M_\odot$ ranges from 0.14 to 0.71. For a single ZAMS mass this compactness can have a large variance, made particularly clear in the case of the 15 $M_\odot$ model.

Convective overshooting and the mass-loss rates have very clearly affected the properties of the progenitor models in this work. The data showcase the unpredictable nature of the effects of parameter variation in stellar modeling. Density, core composition, and compactness are three such quantities that have the potential to impact supernova evolution and have been shown to be sensitive to the treatment of η and the convective overshooting within the MESA models. Thus the properties of the progenitors suggest that our supernova simulations could see effects from the mass loss rates and the convective overshooting treatments. The remnant mass is calculated by calculating the energy of each zone outward from the core at the time of explosion. At the threshold where the total energy of a zone becomes positive, the matter is unbound gravitationally and will be ejected. Any mass below this point is gravitationally bound and will ultimately become the remnant neutron star.

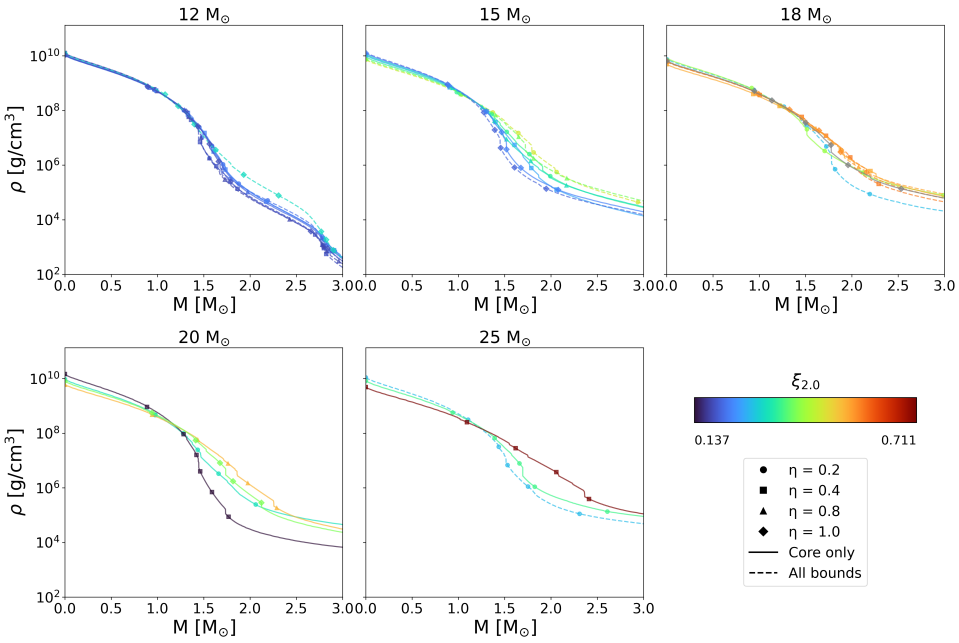

Figure 4.1: The density profile of the progenitor models, color-coded by compactness $\xi_{2.0}$.

4.3.2 Hydrodynamic Simulations

In this work we implement the AGILE [33] 1D Lagrangian general relativistic hydrodynamics code alongside the Isotropic Diffusion Source Approximation (IDSA) [34] for neutrino transport and the PUSH method [27, 9] for driving the explosion. This code has been used extensively in other works [27, 9, 35, 10], so only the relevant details are discussed here.

AGILE solves the general relativistic hydrodynamics equations in spherical symmetry. It implements an adaptive spatial grid mesh, along with implicit time evolution, to resolve the extreme gradients of CCSNe. The deleptonization scheme of [36] is applied during collapse. For ν_e transport we use IDSA [34] and for ν_x transport we use the ASL scheme of [37]. For material in NSE, we use the HS(DD2) EOS [38, 39]. AGILE reads in the progenitor model from the core up to whichever of these criteria is achieved first: density < 10 g/cm^3, radius $> 10^{10}$ cm, or M $>$ 10 M$_\odot$. The simulations in this work have been run to 10 seconds post-bounce, or when the forward shock reaches the outermost zones, whichever occurs first. In this work we will study the dynamics up to 1 second post-bounce, as all of our simulations reach explosion prior to this time.

The PUSH method is used in this work to promote the explosion of the 1D models. The PUSH method artificially introduces a physically-motivated heating term to emulate the

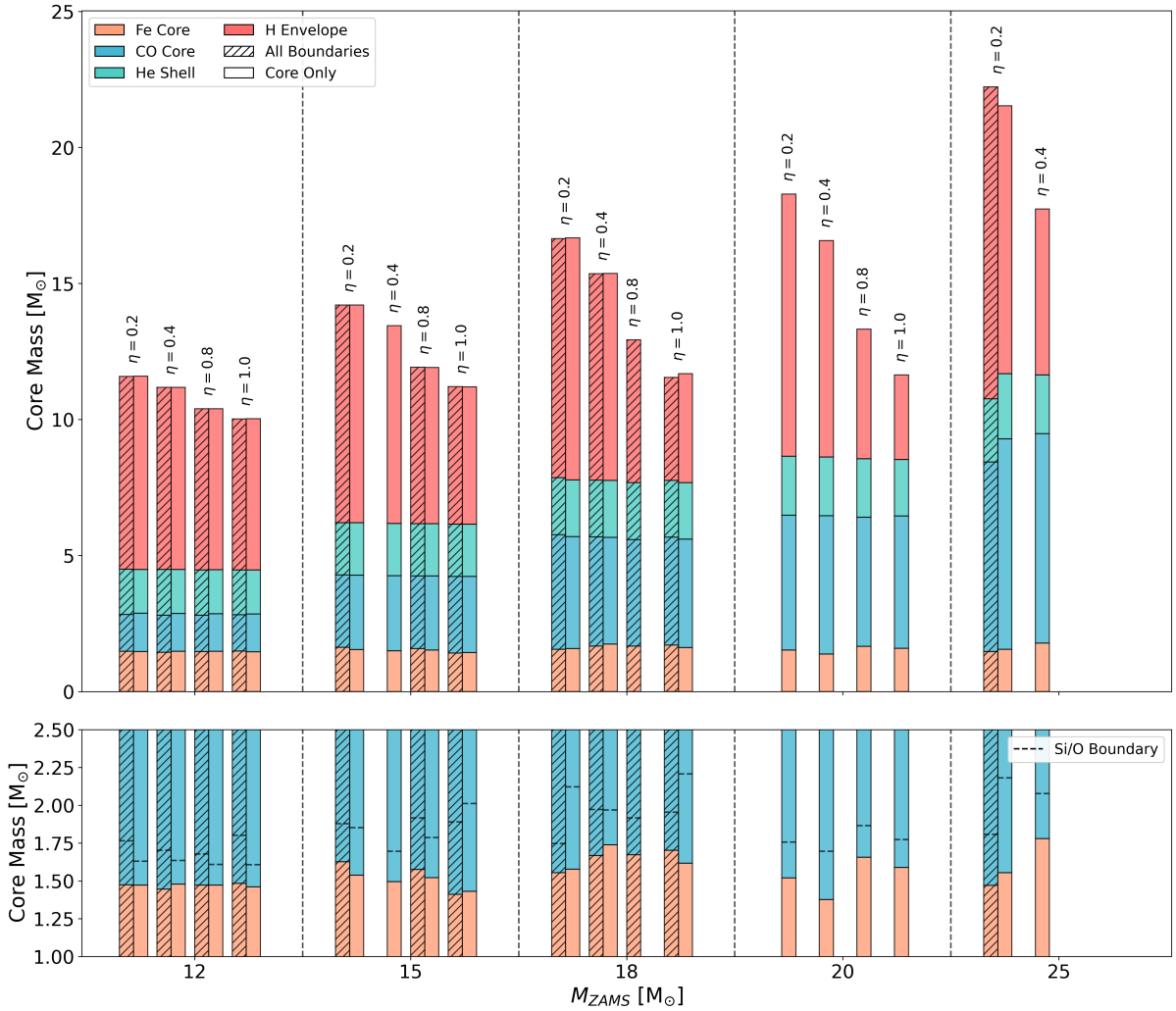

Figure 4.2: Upper panel: the composition for each of the progenitor models. Yellow represents the iron core, blue the carbon-oxygen shell, green the helium layer, and red the outer hydrogen envelope. Lower panel: a zoomed in plot of the composition from 1-2.5 $M_{\odot}$. The black dashed line represents the Silicon/Oxygen interface.

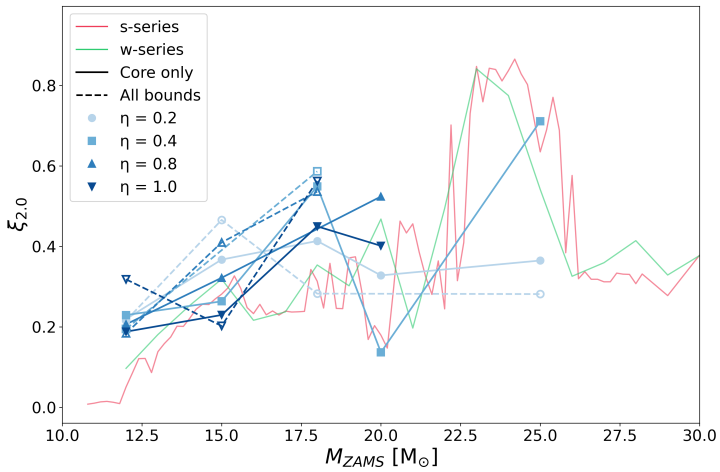

Figure 4.3: The compactness of the progenitor models, grouped by values of η and the convective overshooting treatment. The red and green lines are the compactness of the solar metallicity models of [1] (s) and [32] (w).

convection and heating effects present in multi-dimensional simulations. PUSH converts some of the heavy flavor ($\nu_x = \nu_\mu, \nu_\tau, \overline{\nu}_\mu, \overline{\nu}_\tau$) neutrino luminosity within the PNS into an energy source term in the gain region. PUSH is dependent on two free parameters, the amount of time it takes for PUSH to reach its maximum strength $t_{\rm rise}$ and the maximum strength of the PUSH effect $k_{\rm push}$. All other parameters are fixed and calibrated in [27] In this work, we set $t_{\rm rise} = 0.4$ s and $k_{\rm push}$ follows the parabolic dependence on the compactness $\xi_{2.0}$ calculated at bounce outlined in [9].

4.3.3 Mapping Procedure

Prior to initiating the hydrodynamic code, the stellar structure data from MESA must be mapped onto AGILEs computational grid. AGILE is configured with 180 zones and employs a dynamically adaptive mesh to maintain high spatial resolution in regions of physical interest. Because the MESA profiles contain $\mathcal{O}(10^3)$ grid points, the data must be downsampled to AGILEs more compact grid.

During initialization, AGILE reads the progenitor profile and determines the placement of its 180 zones using an implicit finite-difference scheme designed to concentrate grid points in regions far from hydrostatic equilibrium. One of the criteria used for determining grid spacing is the logarithmic derivative of the density, $\frac{d\ln\rho}{d\ln r}$. Although the MESA profile is generally smooth in its hydrodynamic quantities, the data have large spikes in

$\frac{d\ln\rho}{d\ln r}$. These huge gradients prevent AGILE from converging on an acceptable grid distribution, causing the adaptive mesh to concentrate points on spikes in $\frac{d\ln\rho}{d\ln r}$.

To address this issue, we implemented a grid-smoothing procedure to ensure that $\frac{d\ln\rho}{d\ln r}$ does not exceed a specified threshold. The threshold was chosen by computing the maximum value of $\frac{d\ln\rho}{d\ln r}$ in a well-behaved KEPLER progenitor. Because the MESA profile is much more finely resolved than AGILE, the smoothing algorithm selectively merges zones that violate this threshold. For each grid point, $\frac{d\ln\rho}{d\ln r}$ is calculated; if a zone exceeds the predetermined threshold, it and the next outward zone are removed. Their mass and hydrodynamic quantities are then incorporated into the next outward zone through mass-weighted interpolation. This procedure is applied across the full radial domain of the progenitor. The algorithm is then iterated on the updated grid until no zone exceeds the threshold value of $\frac{d\ln\rho}{d\ln r}$. The resulting smoothed profile is then provided to AGILE for its standard grid-allocation routines. We have confirmed that the application of this algorithm preserves the total mass of the progenitor models up to 0.03%.

4.4 Results

4.4.1 Explosion properties

Due to difficulties with mapping some of the progenitor models to the initial AGILE grid only 12 of the 29 progenitors provided have been simulated. For the rest of this work all results will consider only these models.

Figure 4.4 shows the shock radius of our simulations from core bounce out to 1 second post bounce. For all models we see successful shock revival with a high variance in revival times. Notably, the 20 $M_\odot$ model with $\eta = 0.8$ and a core-only treatment has the longest time to shock revival, taking nearly 400 ms to begin expanding outward. Further, for identical mass models, variations in values of η impact the shock radius evolution. For the core-only convective overshooting treatment, the 15 $M_\odot$ models have a wide dispersion in shock radii for different values of η. When $\eta = 1.0$, the 15 $M_\odot$ model has the earliest shock revivals, yet when η is reduced to 0.8 for this model the shock radius has one of the latest revivals. The convective overshooting treatment shows a similar impact on the shock evolution. Looking again to the 15 $M_\odot$ model with $\eta = 1.0$, the all-bounds treatment has a smaller shock radius when compared to the core-only treatment. These changes appear to be less drastic than the changes in the shock evolution that result from varying η. The red star markers in this figure represent the point in time at which the Si/O interface,

shown in Figure 4.2, crosses the shock, an event often correlated with shock revival due to the decrease in density [40, 41, 42, 43, 13]. While the majority of our models have an Si/O interface crossing corresponding to the shock revival, 3 of these models do not see this interface crossing the shock front until well beyond the shock revitalization. Indeed, for both of the $M_{\rm ZAMS} = 15{\rm M}_\odot$ models with $\eta = 1.0$, the Si/O interface does not cross the shock for the entirety of the simulation. Instead it appears the shock expansion is driven by another drop in the density that occurs at a smaller mass coordinate. From closer inspection of the progenitor models, we have identified this feature as being the extent of the core convective region that formed during silicon core burning. Figure 4.5 shows one such example of this in the case of the $M_{\rm ZAMS} = 15\ {\rm M}_\odot$, $\eta = 1.0$, core-only model. This figure shows, from top to bottom, the entropy, density, and mass fractions of the star as functions of the mass coordinate. The vertical green line represents the Si/O interface and the red vertical line represents the upper end of the iron core. There exist two nominal density drops near $M = 1.5\ {\rm M}_\odot$, as seen in the middle panel. These density drops correspond to the $s = 4$ k_B/baryon criterion used to detect the sharp density gradients of the Si/O layer [41], as can be seen in the top panel of this figure. The bottom panel shows the extended layer of silicon and oxygen where they seem to be in a semi-stable ratio. These density drops fall into the shock prior to the Si/O interface, and thus provide the shock enough of a reduction in ram pressure to expand outward before the Si/O interface has a chance to contribute.

Another quantity impacted by the stellar modeling is the neutrino luminosity. Figure 4.6 highlights the wide variance in this quantity as a result of changing the stellar evolution modeling parameters. The change can be large, as in the case of the 20 $\rm M_\odot$ models, where the ν_e luminosity varies as much as 30 B/s (where 1 B = 1 Bethe = 10^{51} erg) for different values of η. Models with the all-bounds core overshooting prescription tend to have higher peak luminosities in all neutrino flavors when compared to their core-only counterparts. This can be attributed to an increase in the mass of the iron core in the progenitor. The increased mixing within the star via the all-bounds treatment effectively increases the size of the convective cores of the progenitor models, which in turn extends the burning phases during stellar evolution. In addition to the increased burning time, the extended convection dredges up heavy iron-group nuclei away from the core, allowing for more iron-group nuclei to be generated prior to core collapse. The combination of these two effects can result in a larger iron core mass, which in turn produces more neutrinos during collapse and explosion [42]. This agrees with [23] who find heavier iron core masses as they increase the strength of their convective overshooting prescription for progenitors in the same ZAMS mass range as the progenitors in our work.

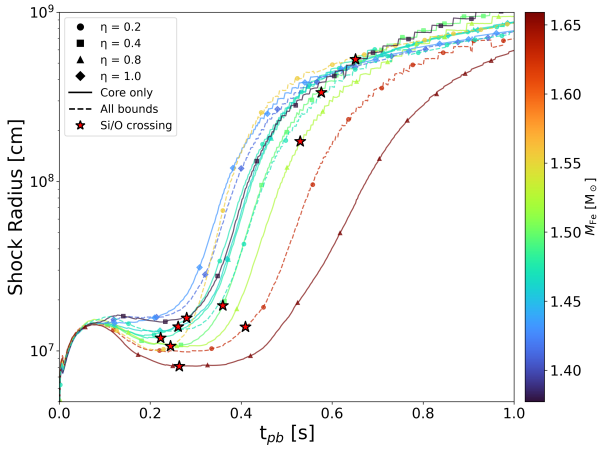

Figure 4.4: Shock radius over time for the 12 simulations. The red stars represent the time the Si/O interface falls beneath the shock. Filled markers represent the core-only treatment of convective overshooting, while empty markers represent the all-bounds treatment.

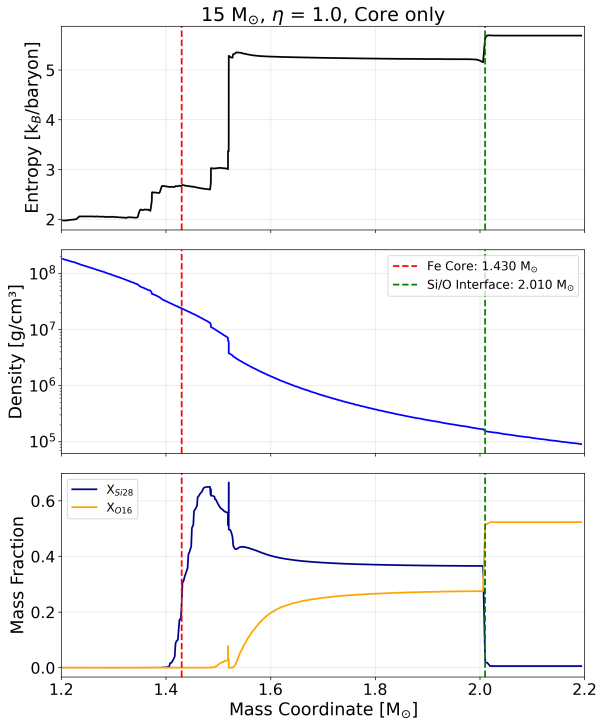

Figure 4.5: Selected data shown from the $M_{\mathrm{ZAMS}} = 15\ \mathrm{M}_{\odot}$, $\eta = 1.0$, core only model as a function of mass coordinate. The red vertical line is the iron core mass, and the green vertical line is the Si/O interface. Top: entropy, middle: density, bottom: mass fractions.

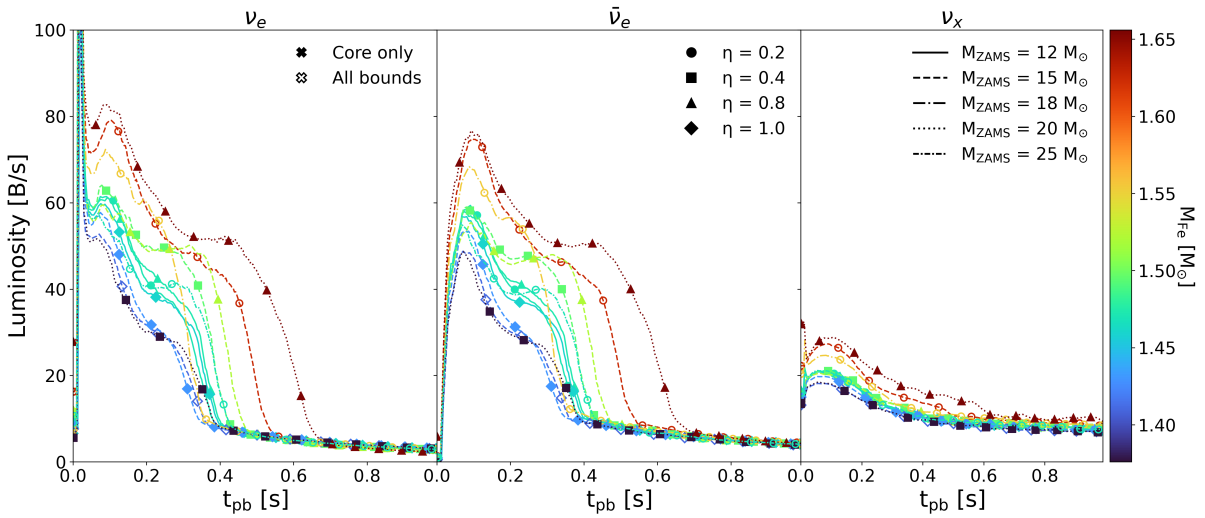

Figure 4.6: Neutrino luminosity, smoothed over a 15 ms window. Colored by progenitor iron core masses. Filled markers represent the core-only treatment of convective overshooting, while empty markers represent the all-bounds treatment.

4.4.2 Correlations

Figure 4.7 shows correlation plots of our stellar evolution parameters with our predicted supernova properties. For this plot and all plots in this section, the r-value shown is the Pearson correlation coefficient. From top to bottom the plots show the explosion energy, remnant mass, ejecta mass, explosion time, and compactness at bounce against the ZAMS mass, wind efficiency parameter η, and compactness $\xi_{2.0}$ at bounce.

The first column plots the correlation of M_{ZAMS} of our progenitor models with our supernova properties. We achieve explosion energies in the range of 0.69 B - 1.46 B across all of our models. There is a moderate negative correlation between M_{ZAMS} and the final explosion energy of the supernova. This finding is consistent with trends seen in the s and w series models [9, 10, 11] in this range of ZAMS masses. The ejecta mass is also weakly correlated with the ZAMS mass in these models. The trend in the data suggests that it may be more strongly correlated if not for what appears to be an outlier at $M_{ZAMS} = 25\ M_\odot$. The positive correlation can be explained purely from a mass conservation standpoint. Stars with a larger ZAMS mass generally start their collapse phase with a larger starting mass, as Figure 4.2 shows. The ejecta mass is only dependent upon the initial mass of the collapsing progenitor and the remnant mass. Because the remnant mass is not correlated with the ZAMS mass (seen in the second row of this figure) then we can conclude that the moderate correlation of ZAMS mass to ejecta mass is tied to the relationship between a star's mass at

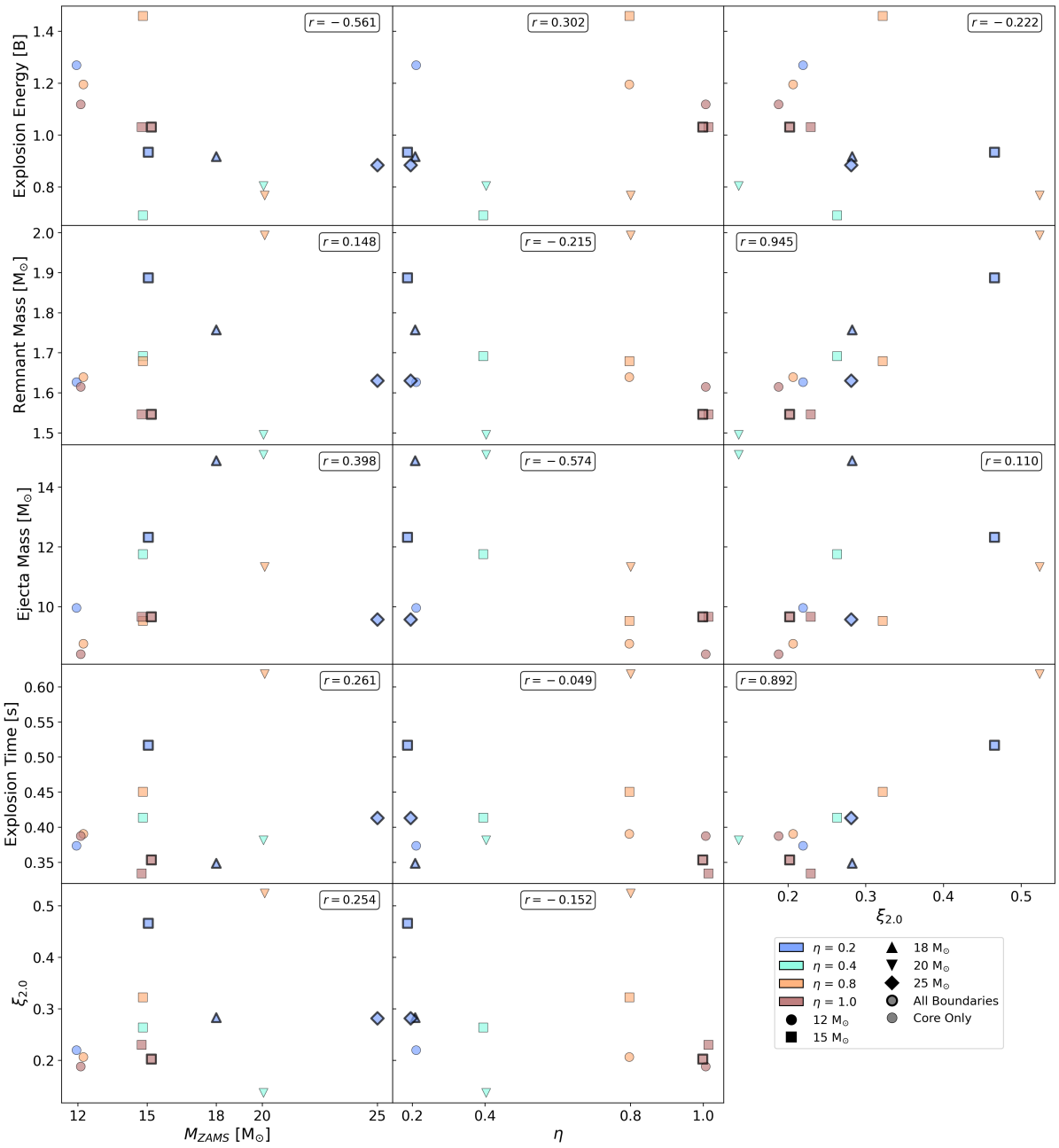

Figure 4.7: Left column: versus ZAMS mass. Middle column: versus η. Right column: versus compactness. Top: explosion energy. Second: remnant mass. Third: ejecta mass. Fourth: Explosion time. Bottom: Compactness. Note: some offsets have been introduced to the values of M_{ZAMS} and η in the left and central columns to make all data points visible. These offsets are not reflected in the r-values.

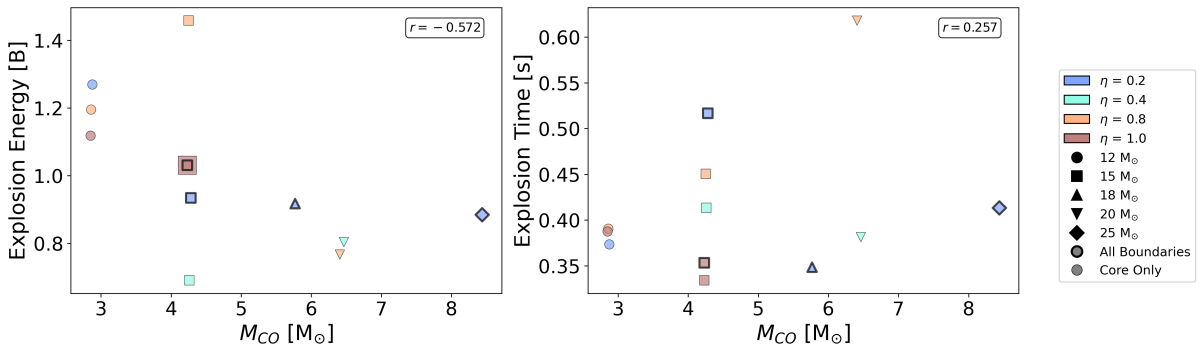

Figure 4.8: Correlations of the CO core mass with the explosion energy (left) and explosion time (right). Note that for both treatments of the convective overshooting in the 15M $\eta = 1.0$ models, they have nearly identical CO core masses and explosion energies. This is denoted by the enlarged point on the left panel of this plot.

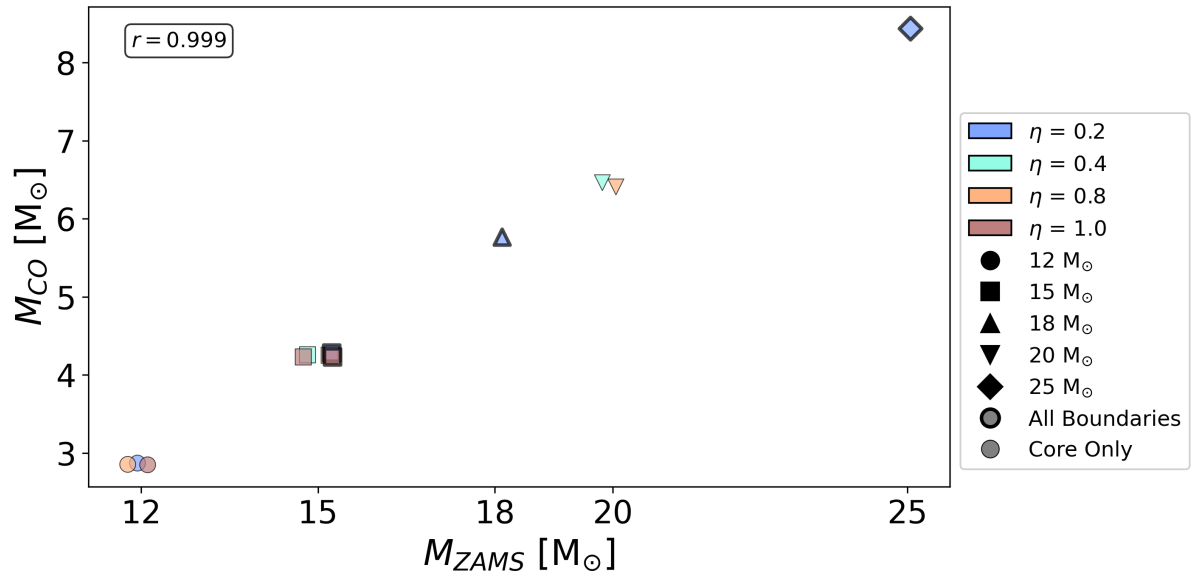

Figure 4.9: Correlations of the CO core mass with the ZAMS mass. Note: small offsets have been introduced to the values of M_{ZAMS} to make all data points visible. These offsets are not reflected in the r-value.

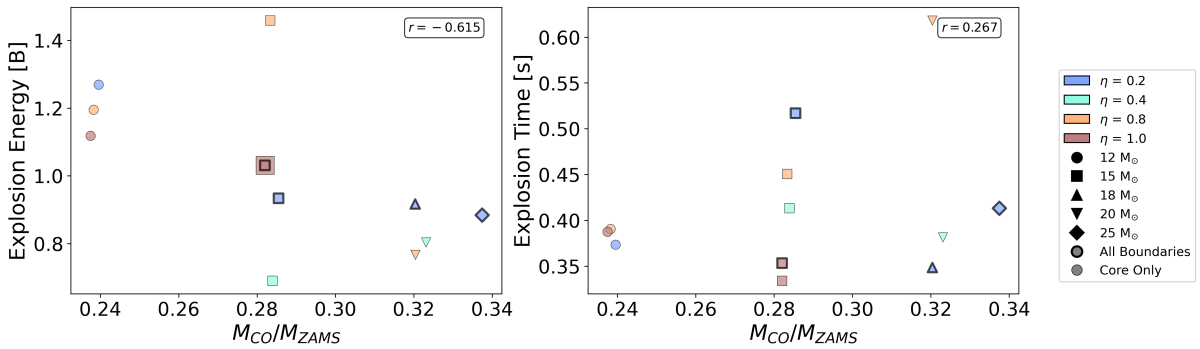

Figure 4.10: Left: the correlation of the ratio of the CO core mass to the ZAMS mass with the explosion energy. Right: The correlation of ZAMS mass to the CO core mass. Note that for both treatments of the convective overshooting in the 15 $M_\odot$, $\eta = 1.0$ models, they have nearly identical CO core masses and explosion energies. This is denoted by the enlarged point on the left panel of this plot.

the onset of collapse and its ZAMS mass. The relationship between ZAMS mass and ejecta mass is not more strongly correlated due to the effects of the mass-loss rate. Some models in Figure 4.2 with high values of η for a given ZAMS mass actually have less mass remaining at collapse than those of a lesser ZAMS mass with a weaker wind efficiency parameter. We find that compactness, explosion time, and remnant mass are all uncorrelated with the ZAMS mass.

The middle column displays the correlations of η with the remnant properties. The only relationship of note is the negative correlation that appears between values of η and ejecta mass. For a larger wind efficiency parameter, the mass ejected from a supernova is reduced in our models. This is consistent with our earlier finding that an increased wind efficiency parameter in the mass loss prescription of these models reduces the overall mass of the hydrogen envelope, which in turn reduces the amount of material that can be ejected from the supernova. Because the remnant mass is uncorrelated with η, then it must be that the effects on the progenitor mass by η at time of collapse are influencing the ejecta mass. Outside of the ejecta mass, there is no correlation between η and any of the other supernova properties shown.

Both ZAMS mass and η are not strong indicators of supernova outcomes with the strongest correlation either of them has is $|r| < 0.6$. The final column of Figure 4.7 shows the correlations with compactness and demonstrate the strongest correlations in the data. The compactness of a progenitor is directly correlated with the remnant mass. For a higher value of $\xi_{2.0}$ at bounce a higher mass neutron star remnant will remain after the explosion. Fur-

ther there is no indication that the convective overshooting treatment has impacted the remnant mass. The explosion time in these models also has a strong dependence on the compactness. This correlation is caused by the parabolic calibration of PUSH. For larger sample sizes, one expects a parabolic trend when more values of $\xi_{2.0}$ are included in the data (see Figure 4 in [11]).

Figure 4.8 is a plot of the correlation between the mass of the CO core (M_{CO}) and two of the properties of the resultant supernovae, explosion energy and explosion time. In the left panel there is a moderate negative correlation between the CO core mass and the explosion energy of the supernova. This correlation closely tracks the correlation seen between the ZAMS mass and the explosion energy of Figure 4.7. The r values for both of these correlations are within 0.011 of one another. Indeed we find almost a perfect 1-to-1 correlation between the ZAMS mass and the CO core mass for our data, shown in Figure 4.9, indicating that the correlation of the M_{CO} with explosion energy stems from the relationship of the explosion energy to the ZAMS mass. This finding of a linear relationship is in good agreement with results for non-rotating, solar-metallicity progenitors of comparable ZAMS mass [44, 45, 46].

However, in Figure 4.10 we control for the dependence of the CO core mass on the ZAMS mass by looking at the fraction of ZAMS mass the CO core mass represents. When controlling for this, a moderate negative correlation of $r = -0.615$ is still present in our data, as seen in the left panel. This finding indicates that the mass of the CO core is a potential indicator of the explosion energy independent of its ZAMS mass. Further, this correlation with explosion energy contrasts starkly to the lack of correlation we see between compactness and explosion energy in Figure 4.7. [9] have indicated that the progenitor CO core mass can be a predictor of some explosion properties, and can be used to gain information where the compactness is unable to make predictions, consistent with what we see here. For our models, a correlation does not appear in the explosion time when accounting for the ZAMS mass. In fact, the ZAMS mass and the M_{CO}/M_{ZAMS} ratio are similarly uncorrelated with the explosion time.

4.5 Summary and Conclusions

In this paper we have simulated the collapse and explosion of 12 of the nonrotating stellar progenitors of [26] for different values of ZAMS mass, the wind efficiency parameter, and different treatments of convective overshooting. We explode models with $M_{\mathrm{ZAMS}} =$

12, 15, 18, 20, and 25 $M_\odot$ and $\eta = 0.2, 0.4, 0.8, 1.0$ for two treatments of the convective overshooting, and compute the properties of the corresponding supernova explosion and remnant.

The main results of this study are:

1. We find that the neutrino luminosities of the simulations correspond to the mass of the iron core of the progenitor models, and that an increase in the iron core mass can be attributed to the extended burning periods in the RSG phase of stellar evolution. The extended burning periods arise from increased nuclear fuel in the burning layers, driven by the enhanced convection introduced by the all-bounds overshooting treatment.

2. We also find that while most of our models begin shock revival around the same time that the Si/O interface crosses the shock front, in agreement with [40] and [41], we do not see this for all of our models. There exist drops in density below the Si/O interface in these models, which are imprints of the extent of the convective core during core silicon burning.

3. The CO core mass, when controlled for ZAMS mass, has a negative correlation (r = -0.615) with the explosion energy. This exceeds the correlation of the explosion energy with ZAMS mass, suggesting that the CO core is potentially a more reliable predictor of this quantity. Similarly, this correlation is stronger than the correlation of $\xi_{2.0}$ with the explosion energy, agreeing with the findings of [9] that CO core masses can act as indicators of explosion properties in regimes where the compactness fails to make a prediction.

4. The wind efficiency parameter has a moderate negative linear correlation (r = -0.574) with the ejecta mass of the supernova due to a reduced hydrogen envelope at the start of the simulation. Otherwise, there appears to be no general trend relating the wind efficiency parameter to any of the supernova properties we calculated.

5. Both the ZAMS mass and wind efficiency parameters do not correlate with the compactness $\xi_{2.0}$ directly. There is a clear impact on the compactness via both the wind efficiency parameter and different treatments of the convective overshooting in our data. This has been seen by [15] and [23] for different progenitor models. The relationship between our parameters and the compactness is not immediately clear based on our data.

6. The ZAMS mass shows a negative linear correlation (r = -0.561) with the explosion energy. This is consistent with the findings of [9], [10], and [11], who use PUSH to explode the s and w series KEPLER 2007 progenitor models of [32].

7. The compactness of these pre-supernova models is the strongest predictor of the supernova outcomes and correlates very strongly with the explosion time (r = 0.892) and the remnant mass (r = 0.945), consistent with other works [5, 8, 41].

4.6 Acknowledgments

The work at NC State was supported by United States Department of Energy, Office of Science, Office of Nuclear Physics (award number DE-FG02-02ER41216). This work is also supported by the National Science Foundation Windows on the Universe: the Era of Multi-Messenger Astrophysics Program: WoU-MMA: Collaborative Research: A Next-Generation SuperNova Early Warning System for Multimessenger Astronomy through Grant No 2209449.

Software: *AGILE [33], IDSA [34], PUSH [27, 9], MESA [28], Matplotlib [47], NumPy [48]*

REFERENCES

[1] S. E. Woosley, A. Heger, and T. A. Weaver. The evolution and explosion of massive stars. *Reviews of Modern Physics*, 74(4):1015–1071, November 2002. Publisher: American Physical Society.

[2] S. J. Smartt, J. J. Eldridge, R. M. Crockett, and J. R. Maund. The death of massive stars - I. Observational constraints on the progenitors of Type II-P supernovae. *Monthly Notices of the Royal Astronomical Society*, 395:1409–1437, May 2009. Publisher: OUP ADS Bibcode: 2009MNRAS.395.1409S.

[3] S. E. Woosley and Alexander Heger. The Remarkable Deaths of 9-11 Solar Mass Stars. *The Astrophysical Journal*, 810:34, September 2015. Publisher: IOP ADS Bibcode: 2015ApJ...810...34W.

[4] Ken'ichi Nomoto and Masa-aki Hashimoto. Presupernova evolution of massive stars. *Physics Reports*, 163(1):13–36, June 1988.

[5] Evan O'Connor and Christian D. Ott. Black Hole Formation in Failing Core-Collapse Supernovae. *The Astrophysical Journal*, 730:70, April 2011. Publisher: IOP ADS Bibcode: 2011ApJ...730...70O.

[6] Adam Burrows and James M. Lattimer. Neutrinos from SN 1987A. *The Astrophysical Journal*, 318:L63, July 1987. Publisher: IOP ADS Bibcode: 1987ApJ...318L..63B.

[7] Chris L. Fryer. Mass Limits For Black Hole Formation. *The Astrophysical Journal*, 522(1):413, September 1999. Publisher: IOP Publishing.

[8] Marcella Ugliano, Hans-Thomas Janka, Andreas Marek, and Almudena Arcones. PROGENITOR-EXPLOSION CONNECTION AND REMNANT BIRTH MASSES FOR NEUTRINO-DRIVEN SUPERNOVAE OF IRON-CORE PROGENITORS. *The Astrophysical Journal*, 757(1):69, September 2012. Publisher: The American Astronomical Society.

[9] K. Ebinger, S. Curtis, C. Fröhlich, M. Hempel, A. Perego, M. Liebendörfer, and F.-K. Thielemann. PUSHing Core-collapse Supernovae to Explosions in Spherical Symmetry. II. Explodability and Remnant Properties. *ApJ*, 870:1, January 2019.

[10] Kevin Ebinger, Sanjana Curtis, Somdutta Ghosh, Carla Fröhlich, Matthias Hempel, Albino Perego, Matthias Liebendörfer, and Friedrich-Karl Thielemann. PUSHing Core-collapse Supernovae to Explosions in Spherical Symmetry. IV. Explodability, Remnant Properties, and Nucleosynthesis Yields of Low-metallicity Stars. *ApJ*, 888(2):91, January 2020.

[11] Somdutta Ghosh, Noah Wolfe, and Carla Fröhlich. PUSHing Core-collapse Supernovae to Explosions in Spherical Symmetry. V. Equation of State Dependency of Explosion Properties, Nucleosynthesis Yields, and Compact Remnants. *ApJ*, 929(1):43, April 2022.

[12] Tuguldur Sukhbold and S. E. Woosley. THE COMPACTNESS OF PRESUPERNOVA STELLAR CORES. *The Astrophysical Journal*, 783(1):10, February 2014.

[13] Luca Boccioli, Mariam Gogilashvili, Jeremiah Murphy, and Evan P. O'Connor. Quantifying the Impact of the Si/O Interface in CCSN Explosions Using the Force Explosion Condition, January 2025. arXiv:2410.17232 [astro-ph].

[14] G. Meynet, V. Chomienne, S. Ekström, C. Georgy, A. Granada, J. Groh, A. Maeder, P. Eggenberger, E. Levesque, and P. Massey. Impact of mass-loss on the evolution and pre-supernova properties of red supergiants. *Astronomy and Astrophysics*, 575:A60, March 2015. Publisher: EDP ADS Bibcode: 2015A&A...575A..60M.

[15] M. Renzo, C. D. Ott, S. N. Shore, and S. E. de Mink. Systematic survey of the effects of wind mass loss algorithms on the evolution of single massive stars. *Astronomy and Astrophysics*, 603:A118, July 2017. Publisher: EDP ADS Bibcode: 2017A&A...603A.118R.

[16] D. C. Abbott and L. B. Lucy. Multiline transfer and the dynamics of stellar winds. *The Astrophysical Journal*, 288:679–693, January 1985. Publisher: IOP ADS Bibcode: 1985ApJ...288..679A.

[17] C. de Jager, H. Nieuwenhuijzen, and K. A. van der Hucht. Mass loss rates in the Hertzsprung-Russell diagram. *Astronomy and Astrophysics Supplement Series*, 72:259–289, February 1988. Publisher: EDP ADS Bibcode: 1988A&AS...72..259D.

[18] H. Nieuwenhuijzen and C. de Jager. Parametrization of stellar rates of mass loss as functions of the fundamental stellar parameters M, L, and R. *Astronomy and Astrophysics*, 231:134–136, May 1990. Publisher: EDP ADS Bibcode: 1990A&A...231..134N.

[19] J. S. Vink, A. de Koter, and H. J. G. L. M. Lamers. New theoretical mass-loss rates of O and B stars, October 2000. ISSN: 0004-6361 Volume: 362 ADS Bibcode: 2000A&A...362..295V.

[20] E. Böhm-Vitense. In *Theory of the hydrogen convection zone*, volume 12, pages 338–345, January 1960. ADS Bibcode: 1960IAUS...12..338B.

[21] I. Brott, S. E. de Mink, M. Cantiello, N. Langer, A. de Koter, C. J. Evans, I. Hunter, C. Trundle, and J. S. Vink. Rotating massive main-sequence stars. I. Grids of evolutionary models and isochrones. *Astronomy and Astrophysics*, 530:A115, June 2011. Publisher: EDP ADS Bibcode: 2011A&A...530A.115B.

[22] A. Schootemeijer, N. Langer, N. J. Grin, and C. Wang. Constraining mixing in massive stars in the Small Magellanic Cloud. *Astronomy and Astrophysics*, 625:A132, May 2019. Publisher: EDP ADS Bibcode: 2019A&A...625A.132S.

[23] D. Temaj, F. R. N. Schneider, E. Laplace, D. Wei, and Ph Podsiadlowski. Convective-core overshooting and the final fate of massive stars. *Astronomy & Astrophysics*, 682:A123, February 2024. Publisher: EDP Sciences.

[24] B. Freytag, H.-G. Ludwig, and M. Steffen. Hydrodynamical models of stellar convection. The role of overshoot in DA white dwarfs, A-type stars, and the Sun. *Astronomy and Astrophysics*, 313:497–516, September 1996. Publisher: EDP ADS Bibcode: 1996A&A...313..497F.

[25] Falk Herwig. The evolution of AGB stars with convective overshoot, July 2000. arXiv:astro-ph/0007139.

[26] Kenzie Myers, Claire Campbell, Kelly Patton, and James Kneller. The Effect of Mass Loss and Convective Overshooting on the Pre-Collapse Structure, Composition, and Neutrino Emission of Red Supergiants. in prep.

[27] A. Perego, M. Hempel, C. Fröhlich, K. Ebinger, M. Eichler, J. Casanova, M. Liebendörfer, and F.-K. Thielemann. PUSHing Core-collapse Supernovae to Explosions in Spherical Symmetry I: the Model and the Case of SN 1987A. *Astrophys. J.*, 806:275, June 2015.

[28] Bill Paxton, Lars Bildsten, Aaron Dotter, Falk Herwig, Pierre Lesaffre, and Frank Timmes. Modules for Experiments in Stellar Astrophysics (MESA). *The Astrophysical Journal Supplement Series*, 192:3, January 2011. Publisher: IOP ADS Bibcode: 2011ApJS..192....3P.

[29] R. Farmer, C. E. Fields, I. Petermann, Luc Dessart, M. Cantiello, B. Paxton, and F. X. Timmes. ON VARIATIONS OF PRE-SUPERNOVA MODEL PROPERTIES. *The Astrophysical Journal Supplement Series*, 227(2):22, December 2016. Publisher: The American Astronomical Society.

[30] M. Renzo, J. A. Goldberg, A. Grichener, O. Gottlieb, and M. Cantiello. Progenitor Stars Calculated with Small Reaction Networks should not be Used as Initial Conditions for Core Collapse. *Research Notes of the American Astronomical Society*, 8(6):152, June 2024.

[31] Jorick S. Vink, A. de Koter, and H. J. G. L. M. Lamers. Mass-loss predictions for O and B stars as a function of metallicity. *Astronomy & Astrophysics*, 369(2):574–588, April 2001. Publisher: EDP Sciences.

[32] S. E. Woosley and A. Heger. Nucleosynthesis and remnants in massive stars of solar metallicity. *Physics Reports*, 442:269–283, April 2007. ADS Bibcode: 2007PhR...442..269W.

[33] Matthias Liebendörfer, Stephan Rosswog, and Friedrich-Karl Thielemann. An Adaptive Grid, Implicit Code for Spherically Symmetric, General Relativistic Hydrodynamics in Comoving Coordinates. *The Astrophysical Journal Supplement Series*, 141:229–246, July 2002. Publisher: IOP ADS Bibcode: 2002ApJS..141..229L.

[34] M. Liebendörfer, S. C. Whitehouse, and T. Fischer. THE ISOTROPIC DIFFUSION SOURCE APPROXIMATION FOR SUPERNOVA NEUTRINO TRANSPORT. *The Astrophysical Journal*, 698(2):1174, May 2009. Publisher: The American Astronomical Society.

[35] S. Curtis, K. Ebinger, C. Fröhlich, M. Hempel, A. Perego, M. Liebendörfer, and F.-K. Thielemann. PUSHing Core-collapse Supernovae to Explosions in Spherical Symmetry. III. Nucleosynthesis Yields. *ApJ*, 870:2, January 2019.

[36] Matthias Liebendörfer. A Simple Parameterization of the Consequences of Deleptonization for Simulations of Stellar Core Collapse. *The Astrophysical Journal*, 633:1042–1051, November 2005. Publisher: IOP ADS Bibcode: 2005ApJ...633.1042L.

[37] A. Perego, R. M. Cabezón, and R. Käppeli. AN ADVANCED LEAKAGE SCHEME FOR NEUTRINO TREATMENT IN ASTROPHYSICAL SIMULATIONS. *The Astrophysical Journal Supplement Series*, 223(2):22, April 2016. Publisher: The American Astronomical Society.

[38] Matthias Hempel and Jürgen Schaffner-Bielich. A statistical model for a complete supernova equation of state. *Nuclear Physics A*, 837:210–254, June 2010. Publisher: Elsevier ADS Bibcode: 2010NuPhA.837..210H.

[39] S. Typel, G. Röpke, T. Klähn, D. Blaschke, and H. H. Wolter. Composition and thermodynamics of nuclear matter with light clusters. *Physical Review C*, 81:015803, January 2010. Publisher: APS ADS Bibcode: 2010PhRvC..81a5803T.

[40] T. Ertl, H. Th. Janka, S. E. Woosley, T. Sukhbold, and M. Ugliano. A two-parameter criterion for classifying the explodability of massive stars by the neutrino-driven mechanism. 818(2):124, February 2016. arXiv: 1503.07522 [astro-ph.SR] Number: 124 tex.adsnote: Provided by the SAO/NASA Astrophysics Data System.

[41] Tuguldur Sukhbold, T. Ertl, S. E. Woosley, Justin M. Brown, and H.-T. Janka. Core-collapse Supernovae from 9 to 120 Solar Masses Based on Neutrino-powered Explosions. *The Astrophysical Journal*, 821:38, April 2016. Publisher: IOP ADS Bibcode: 2016ApJ...821...38S.

[42] Bernhard Müller, Alexander Heger, David Liptai, and Joshua B. Cameron. A simple approach to the supernova progenitor-explosion connection. *Monthly Notices of the Royal Astronomical Society*, 460:742–764, July 2016. Publisher: OUP ADS Bibcode: 2016MNRAS.460..742M.

[43] Tianshu Wang, David Vartanyan, Adam Burrows, and Matthew S B Coleman. The essential character of the neutrino mechanism of core-collapse supernova explosions. *Monthly Notices of the Royal Astronomical Society*, 517(1):543–559, November 2022.

[44] Marco Limongi and Alessandro Chieffi. Presupernova evolution and explosion of massive stars. volume 202, page 012002. IOP, January 2010. ADS Bibcode: 2010JPhCS.202a2002L.

[45] Alessandro Chieffi and Marco Limongi. The presupernova core mass-radius relation of massive stars: understanding its formation and evolution. *The Astrophysical Journal*, 890(1):43, February 2020. arXiv:1911.08988 [astro-ph].

[46] Cristiano Ugolini, Marco Limongi, Raffaella Schneider, Alessandro Chieffi, Ugo Niccolò Di Carlo, and Mario Spera. The initial mass-remnant mass relation for core collapse supernovae. *Astronomy & Astrophysics*, 695:A122, March 2025.

[47] J. D. Hunter. Matplotlib: A 2d graphics environment. *Computing in Science & Engineering*, 9(3):90–95, 2007.

[48] Charles R. Harris, K. Jarrod Millman, Stéfan J. van der Walt, Ralf Gommers, Pauli Virtanen, David Cournapeau, Eric Wieser, Julian Taylor, Sebastian Berg, Nathaniel J. Smith, Robert Kern, Matti Picus, Stephan Hoyer, Marten H. van Kerkwijk, Matthew Brett, Allan Haldane, Jaime Fernández del Río, Mark Wiebe, Pearu Peterson, Pierre Gérard-Marchant, Kevin Sheppard, Tyler Reddy, Warren Weckesser, Hameer Abbasi, Christoph Gohlke, and Travis E. Oliphant. Array programming with NumPy. *Nature*, 585(7825):357–362, September 2020.

CHAPTER

5

CONCLUSIONS

The extreme and highly dynamical nature of core-collapse supernovae (CCSNe) makes them vital probes of the physical processes that shape the chemical composition of the universe. Their scientific value is obscured by our lack of understanding of the nuances behind the mechanisms that drive these events. Modeling CCSNe can thus uncover the complexities of their evolution and allow us to peer into the engine that drives one of the most energetic events in the cosmos. Their multi-physics nature necessitates a deep understanding of many branches of physics to accurately capture their behavior. Therefore there exists a wide parameter space to explore within these models and a dearth of data to calibrate these models to. This dissertation explores the effects of a subset of these parameters on the dynamics of CCSNe evolution, namely magnetic fields, rotation, and stellar evolution properties.

We first perform an in-depth analysis into the impact of turbulence in the gain region on the evolution of CCSNe. We utilize a 3D magnetohydrodynamics code ELEPHANT [1, 2] to simulate four solar metallicity progenitors of [3] with $M_{\mathrm{ZAMS}} = 15,20,23,27\ \mathrm{M}_{\odot}$ and no initial magnetic field or rotation. Our analysis found that the standard method of quantifying turbulence in 3D CCSNe simulations, an extension of the method used in 1D, is not necessarily well suited to 3D models. Metrics used to quantify turbulence and turbulent energy

in CCSNe generally rely on a choice of averaging method to capture turbulent behavior. We find that using the spherical average (SSA) in the case of highly asymmetric CCSNe does not appear to capture the turbulent energy, but the energy stored in convective plumes. We propose instead the local spatial average (LSA) method of averaging that seeks to capture deviations from the small-scale local behavior of the fluid. The vorticity ($\vec{\omega} = \nabla \times \vec{v}$), and by extension the enstrophy ($\epsilon = \frac{\vec{\omega} \cdot \vec{\omega}}{2}$), is commonly used as an indicator of turbulence. Leveraging this, we found that spatial maps of the turbulent energy agree much more closely with spatial maps of enstrophy when using the LSA method as opposed to the SSA method. We also found that the SSA method calculates a higher ratio of turbulent kinetic energy to total kinetic energy than the LSA method. In the investigation we compared these methods to a 3rd method, known as the spectral method, that is independent of averaging choices through the utilization of a Fourier decomposition. Our findings indicate that the total turbulent energy calculated via the spectral method much more closely aligns with our proposed LSA method than the SSA method, indicating that the SSA method may not be capturing the small scale turbulent behavior that we aim to study.

With a new metric to study turbulence of CCSNe available, our next investigation in chapter 3 studies the relationship between the magnetic fields of CCSNe and the turbulence in the gain region. To do this we once again utilized ELEPHANT to simulate two of the same solar metallicity progenitors with $M_{\mathrm{ZAMS}} = 15{,}20\ \mathrm{M}_{\odot}$ and introduced magnetic fields. We apply a purely toroidal initial field of magnitudes 10^{10} G (T10) and 10^{12} G (T12) for both progenitors and compare them to our simulations with no magnetic fields (Control), resulting in 6 simulations to analyze. The investigation found no strong connection between the magnetic field and the turbulence in the gain region of CCSNe. Our main finding of this work is that the magnetic field quickly becomes complicated and does not appear to influence, or be influenced by, the turbulent motion of the fluid in a substantial way. We found that the magnetic field growth rate is overwhelmingly driven by flux tube compression and does not see a substantial contribution from magnetic dynamo effects of turbulent vortices. Contrary to [4], we do not find a co-production of vorticity and magnetic fields and presume that the inclusion of neutrino heating in our models breaks the relationship. We also find that, consistent with [5], the magnetic field energy, even at late times in the case of the T12 simulation, is of only $\mathcal{O}(1\%)$ of the total kinetic energy within the gain region. However, the growth of the magnetic field is exponential until it reaches a saturation value near 10^{15} G, at which point it remains mostly constant. We see an indication that the turbulent energy may be reduced in the case of the 15 $\mathrm{M}_{\odot}$ T12 simulation, but we do not have a sufficient data set to conclusively make that claim. What can be seen

for that simulation is a reduction in the amount of enstrophy generated compared to the total kinetic energy, indicating that the amount of turbulence present may be lower under these conditions. This agrees with the data of the 20 $M_\odot$ model, where the lowest total enstrophy when compared with the kinetic energy occurs in the T12 simulation(s) as well. Yet we do not see a strong indication of the spatial co-production of magnetic field and enstrophy from the rate equations that govern both, suggesting that the magnetic field growth is not localized to regions of high turbulence. We find that the angle of the vorticity and the magnetic field in the gain region are close to a random alignment once the shock has stalled.

The final investigation in this work explores the impact of varying the treatment of stellar evolution parameters on explosion properties of CCSNe. This work builds upon the previous study of [6] that indicates that variations to these stellar parameters alters the compactness of the progenitors, a quantity used as an indicator of supernova outcomes. Here we use AGILE-IDSA with PUSH [7, 8, 9, 10] to evolve several collapsing progenitor models generated with MESA [11] through core-collapse to explosion. These progenitor models are varied in two parameters, the stellar wind efficiency parameter of the mass loss treatment from [12], and the implementation of the exponential convective overshooting treatment of [13]. We find that of our exploding models there is a moderately strong (r = -0.57) negative correlation between the wind efficiency parameter η and the ejecta mass of the CCSN. We indicate that this finding comes from the reduced mass of the hydrogen envelope, and ultimately reduced total mass, that is seen in progenitor models with high wind efficiency. We also see that there is a moderate negative correlation (r = -0.561) between the ZAMS mass of a given model and the explosion energy. This finding is consistent with the work in [14, 15], which performs a similar analysis using the progenitors of [3]. Further, we found no correlation between the stellar wind efficiency parameter and the compactness, indicating that while this parameter alters the compactness, one cannot make consistent predictions in how the compactness will be affected from this parameter alone. Additionally, we find that the ratio of the CO core mass to the ZAMS mass shares a moderate correlation (r = -0.615) with the explosion energy of the simulations, serving as an indicator of supernova outcomes. [10] suggested similarly that the mass of the CO core can be used as a predictor of supernova quantities in the realm of degenerate compactness parameters. Finally, we also find that, in our models, the point at which the Si/O interface crosses the shock correlates with the shock revival for most of our models, but for several of them the crossing is either well beyond revival or does not cross at all. This is attributed to the increased mixing that occurs in some of the models, resulting in a semi-stable ra-

tio of the ^{28}Si and ^{16}O mass fractions for a much longer period ahead of the Si/O interface that correspond to a significant density drop, thus promoting shock revival. The inclusion of these properties shows potential to break from the accepted trend of relating the Si/O interface crossing to the shock revival [16, 17, 18, 19, 20].

We have shown in this work that the parameter space for CCSNe is vast and understanding their dynamics requires exploring as many aspects of this space as possible. While this work focuses on a few particular aspects of CCSNe, we still have not explored in depth several aspects of CCSNe as they relate to these projects. Analyzing the ejecta composition and light curves of the supernova generated from the MESA progenitors can tell us more about how much of a role convective overshooting plays in the composition of CCSNe and provide insight into the origin of nuclei. More data is also needed regarding magnetic field configurations and strengths in CCSNe models. Due to the computationally expensive nature of 3D models, there are limited systematic studies of magnetic field strengths in CCSNe. Constraining the magnetic field behavior could provide information about the source of magnetars and long gamma ray bursts. It is the hope that this work is a valuable step towards a deeper understanding of supernovae, and that work in the coming years will continue to shed light on the physical processes that make these explosions so extraordinary.

REFERENCES

[1] R. Käppeli, S. C. Whitehouse, S. Scheidegger, U.-L. Pen, and M. Liebendörfer. FISH: A THREE-DIMENSIONAL PARALLEL MAGNETOHYDRODYNAMICS CODE FOR ASTROPHYSICAL APPLICATIONS. *The Astrophysical Journal Supplement Series*, 195(2):20, August 2011.

[2] Rubén M. Cabezón, Kuo-Chuan Pan, Matthias Liebendörfer, Takami Kuroda, Kevin Ebinger, Oliver Heinimann, Albino Perego, and Friedrich-Karl Thielemann. Core-collapse supernovae in the hall of mirrors. A three-dimensional code-comparison project. *åp*, 619:A118, November 2018. _eprint: 1806.09184.

[3] S. E. Woosley and A. Heger. Nucleosynthesis and remnants in massive stars of solar metallicity. *Physics Reports*, 442:269–283, April 2007. ADS Bibcode: 2007PhR...442..269W.

[4] E Endeve, C Y Cardall, R D Budiardja, A Mezzacappa, and J M Blondin. Turbulence and magnetic field amplification from spiral SASI modes in core-collapse supernovae. *Physica Scripta*, 2013(T155):014022, July 2013. Publisher: IOP Publishing.

[5] Bailey Sykes and Bernhard Müller. Long-time 3D supernova simulations of non-rotating progenitors with magnetic fields, December 2024. Publication Title: arXiv e-prints ADS Bibcode: 2024arXiv241201155S.

[6] Kenzie Myers, Claire Campbell, Kelly Patton, and James P. Kneller. The Effect of Mass Loss and Convective Overshooting on the Pre-Collapse Structure, Composition, and Neutrino Emission of Red Supergiants.

[7] Matthias Liebendörfer, Stephan Rosswog, and Friedrich-Karl Thielemann. An Adaptive Grid, Implicit Code for Spherically Symmetric, General Relativistic Hydrodynamics in Comoving Coordinates. *The Astrophysical Journal Supplement Series*, 141:229–246, July 2002. Publisher: IOP ADS Bibcode: 2002ApJS..141..229L.

[8] M. Liebendörfer, S. C. Whitehouse, and T. Fischer. THE ISOTROPIC DIFFUSION SOURCE APPROXIMATION FOR SUPERNOVA NEUTRINO TRANSPORT. *The Astrophysical Journal*, 698(2):1174, May 2009. Publisher: The American Astronomical Society.

[9] A. Perego, M. Hempel, C. Fröhlich, K. Ebinger, M. Eichler, J. Casanova, M. Liebendoerfer, and F.-K. Thielemann. Pushing 1D CCSNe to explosions: model and SN 1987A. *The Astrophysical Journal*, 806(2):275, June 2015. arXiv:1501.02845 [astro-ph].

[10] K. Ebinger, S. Curtis, C. Fröhlich, M. Hempel, A. Perego, M. Liebendörfer, and F.-K. Thielemann. PUSHing core-collapse supernovae to explosions in spherical symmetry. II. Explodability and remnant properties. 870:1, January 2019. arXiv: 1804.03182

[astro-ph.SR] Number: 1 tex.adsnote: Provided by the SAO/NASA Astrophysics Data System.

[11] Bill Paxton, Lars Bildsten, Aaron Dotter, Falk Herwig, Pierre Lesaffre, and Frank Timmes. Modules for Experiments in Stellar Astrophysics (MESA). *The Astrophysical Journal Supplement Series*, 192:3, January 2011. Publisher: IOP ADS Bibcode: 2011ApJS..192....3P.

[12] C. de Jager, H. Nieuwenhuijzen, and K. A. van der Hucht. Mass loss rates in the Hertzsprung-Russell diagram. *Astronomy and Astrophysics Supplement Series*, 72:259–289, February 1988. Publisher: EDP ADS Bibcode: 1988A&AS...72..259D.

[13] B. Freytag, H.-G. Ludwig, and M. Steffen. Hydrodynamical models of stellar convection. The role of overshoot in DA white dwarfs, A-type stars, and the Sun. *Astronomy and Astrophysics*, 313:497–516, September 1996. Publisher: EDP ADS Bibcode: 1996A&A...313..497F.

[14] Kevin Ebinger, Sanjana Curtis, Somdutta Ghosh, Carla Fröhlich, Matthias Hempel, Albino Perego, Matthias Liebendörfer, and Friedrich-Karl Thielemann. PUSHing core-collapse supernovae to explosions in spherical symmetry IV: Explodability, remnant properties and nucleosynthesis yields of low metallicity stars. *The Astrophysical Journal*, 888(2):91, January 2020. arXiv:1910.08958 [astro-ph].

[15] Somdutta Ghosh, Noah Wolfe, and Carla Fröhlich. PUSHing core-collapse supernovae to explosions in spherical symmetry V: Equation of state dependency of explosion properties, nucleosynthesis yields, and compact remnants. *The Astrophysical Journal*, 929(1):43, April 2022. arXiv:2107.13016 [astro-ph].

[16] T. Ertl, H. Th. Janka, S. E. Woosley, T. Sukhbold, and M. Ugliano. A two-parameter criterion for classifying the explodability of massive stars by the neutrino-driven mechanism. 818(2):124, February 2016. arXiv: 1503.07522 [astro-ph.SR] Number: 124 tex.adsnote: Provided by the SAO/NASA Astrophysics Data System.

[17] Tuguldur Sukhbold, T. Ertl, S. E. Woosley, Justin M. Brown, and H.-T. Janka. Core-collapse Supernovae from 9 to 120 Solar Masses Based on Neutrino-powered Explosions. *The Astrophysical Journal*, 821:38, April 2016. Publisher: IOP ADS Bibcode: 2016ApJ...821...38S.

[18] Bernhard Müller, Alexander Heger, David Liptai, and Joshua B. Cameron. A simple approach to the supernova progenitor-explosion connection. *Monthly Notices of the Royal Astronomical Society*, 460:742–764, July 2016. Publisher: OUP ADS Bibcode: 2016MNRAS.460..742M.

[19] Tianshu Wang, David Vartanyan, Adam Burrows, and Matthew S. B. Coleman. The Essential Character of the Neutrino Mechanism of Core-Collapse Supernova Explosions, September 2022. arXiv:2207.02231.

[20] Luca Boccioli, Mariam Gogilashvili, Jeremiah Murphy, and Evan P. O'Connor. Quantifying the Impact of the Si/O Interface in CCSN Explosions Using the Force Explosion Condition, January 2025. arXiv:2410.17232 [astro-ph].